The role and analysis of molecular systems in electrocatalysis

Dijk, B. van

Citation

Dijk, B. van. (2021, March 10). *The role and analysis of molecular systems in electrocatalysis*. Retrieved from https://hdl.handle.net/1887/3151631

Cover Page

Universiteit Leiden

Author: Dijk, B. van
Title: The role and analysis of molecular systems in electrocatalysis
Issue Date: 2021-03-10

The role and analysis of molecular systems in electrocatalysis

Proefschrift

ter verkrijging van
de graad van Doctor aan de Universiteit Leiden,
op gezag van Rector Magnificus Prof.dr.ir. H. Bijl,
volgens besluit van het College voor Promoties
te verdedigen op woensdag 10 maart 2021
klokke 11:15 uur

door

Bas van Dijk

geboren te Heemskerk in 1992

Promotiecommissie:

Promotoren

dr. D. G. H. Hetterscheid

prof. dr. M. T. M. Koper

Overige commissieleden

prof. dr. H. S. Overkleeft (voorzitter)

prof. dr. E. Bouwman (secretaris)

dr. M. Costa Figueiredo (Technische Universiteit Eindhoven)

prof. dr. A. Macchioni (Università degli Studi di Perugia)
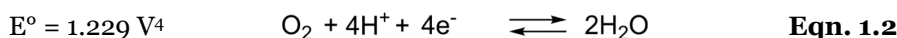
Table of contents

Chapter 1

Introduction to the role and analysis of molecular systems as electrochemical catalysts

Efficient water splitting and fuel cell technology will greatly determine the success of the energy transition from fossil fuels to renewable energy such as solar and wind power. This introductory chapter discusses the role of molecular complexes as electrocatalysts in these reactions. The high tunability of the ligands of these complexes allows for structural diversity. Thereby, these complexes can be used as structural mimics to unravel the catalytic mechanisms of enzymes, or be used as catalysts designed by taking inspiration from the active site of these enzymes. In addition, structure–activity studies can be performed with molecular systems giving direct information about what factors improve the rate determining step and catalysis as a whole. These factors include the electronic withdrawing or donating effect of the ligand, steric bulk or the absence thereof, or the importance of proton coupled electron transfer steps that avoid charge build-up. However, the major drawback of molecular complexes is the stability. Several degradation pathways are discussed and their impact on catalysis. In cases where the parent complexes has degraded, the ligand can still have an influence. Beneficial concepts from homo- and heterogeneous catalysis could then lead to new strategies to improve catalysts. Lastly, the analysis of molecular systems by various electrochemical techniques is discussed which can give information regarding the kinetics, product distribution, and stability of the complexes. In addition, any pitfalls accompanying the use of these techniques are discussed as these can easily lead to over- or misinterpretation. This thesis discusses various molecular complexes for O_2 reduction and H_2O oxidation and will show how the techniques, introduced in this chapter, allow for proper characterization of the active species, identify any decomposition pathways and aid in structure–activity relationship studies.

1.1　The role of electrochemistry in renewable energy

1.1.1　H_2O oxidation to O_2 and *vice versa*

On an almost daily basis, the news confronts us with the global climate crisis. The large scale use and dependence on fossil fuels is leading to global temperature rises with many negative consequences such as climate change and rising seawater levels.[1] Currently, a large share of the renewable energy is consisting of electricity generated from solar and wind power. However, these energy sources are not available 24 hours a day. Diminishing the intermittency effects of these energy sources by large scale energy storage is still a major challenge. One solution, mostly beneficial for short distance mobility, is electricity storage in batteries. However, batteries have a low energy density implicating that the ratio of stored energy to weight is low. For applications that require a high amount of energy storage, such as long and large scale transit, batteries that can store enough energy will simply be too heavy.[2] H_2 is often chosen as an energy carrier in those cases. Even though the energy density of H_2 is lower than that of organic fossil- or biofuels,[2] producing H_2 is in principle as simple as running a current through water with electrolyte. It is not so surprising that water electrolysis has been known since 1789.[3] In detail, water electrolysis is the splitting of water in H_2 and O_2 according to half reactions in Equations 1.1 and 1.2.

$$E° = 0.00 \text{ V} \qquad 4H^+ + 4e^- \;\rightleftharpoons\; 2H_2 \qquad \textbf{Eqn. 1.1}$$

$$E° = 1.229 \text{ V}[4] \qquad O_2 + 4H^+ + 4e^- \;\rightleftharpoons\; 2H_2O \qquad \textbf{Eqn. 1.2}$$

The equilibrium potential ($E°$) is the potential at which the reaction is at the thermodynamic equilibrium. At more positive potentials, the oxidation (H_2 to H^+/ H_2O to O_2) is favored and at negative potentials the reduction (H^+ to H_2/O_2 to H_2O). In principle, 1.229 V is required to oxidize water to H_2 and O_2 as this is the difference in $E°$ of Equations 1.1 and 1.2. However, there is always a kinetic barrier, the activation energy, that requires an additional energy input. For that reason, catalysis generally does not occur at the equilibrium potential. The potential difference between the potential that needs to be applied for catalysis to occur and the equilibrium potential is also called the overpotential (η). A higher energy barrier will result in a higher η. Whereas the $E°$ is often well defined, the actual potential where catalysis starts (also called the onset potential) is not. Often, it is defined as the

potential where a pre-determined magnitude of current is reached, but this gives rise to discrepancies in the definition of onset potentials between different studies.

The extra energy input required due to the overpotential can be considered as energy loss. A low overpotential is therefore highly desired. The overpotential is linked to the height of the activation energy barrier of the reaction. Catalysts are able to lower this barrier by binding the substrate and thereby providing a new thermodynamic route for the making and breaking of bonds. These routes have steps with lower activation barriers than the uncatalyzed reaction. Not every catalyst will lower the energy barrier of any reaction. The binding strength between the catalyst and the substrate is of importance. The Sabatier principle is a general description of the ideal properties of a catalyst. It states that a catalyst that binds the substrate too strongly, will not be able to release intermediates or products. On the other hand, if the substrate has a very weak interaction with the catalyst, no reaction might occur. The ideal catalyst is in the middle of that. As each possible catalyst material has a different binding strength with a substrate, each catalytic reaction can have a unique ideal catalyst that lowers the energy barriers most efficiently for that particular reaction.

Two different catalysts are used for the electrochemical production of H_2 by polymer electrolyte membrane electrolyzers. For the hydrogen evolution reaction (HER) (reductive part of Eqn. 1.1), state of the art catalysts are composed of platinum nanoparticles dispersed on carbon black supports. These achieve outstanding current densities at a low overpotential.[5, 6] Platinum catalysts carry out both the HER and the H_2 oxidation reaction (HOR) close to the equilibrium potential with high forward and backward rates. When a catalyst performs both the oxidation and the reduction of a catalytic reaction with barely any overpotential (reversible electrocatalysis), it is considered as an ideal catalyst. In terms of minimal energy losses, platinum can be considered as ideal catalyst for the HER (and HOR). In fact, the OER (O_2 evolution reaction, Eqn. 1.2) is the bottleneck of electrolyzers. Currently, iridium oxide achieves the lowest overpotentials with a considerable OER rate, but is not an ideal catalyst such as Pt is for HER since there is significant energy loss due to the overpotential at which iridium oxide has to operate.[6] In addition, iridium is, along with platinum, rhodium, and palladium, one of the most scarce metals on earth (Figure 1.1).[7] Moreover, the even distribution in the earth's crust limits the amount of Ir-rich sources.[8] Therefore, most research has focused on increasing the active surface area so that iridium loadings can be reduced.[6] To date, the research goals are finding better dispersing supports that are stable under oxidative conditions and/or better catalysts preferably using less scarce metals.
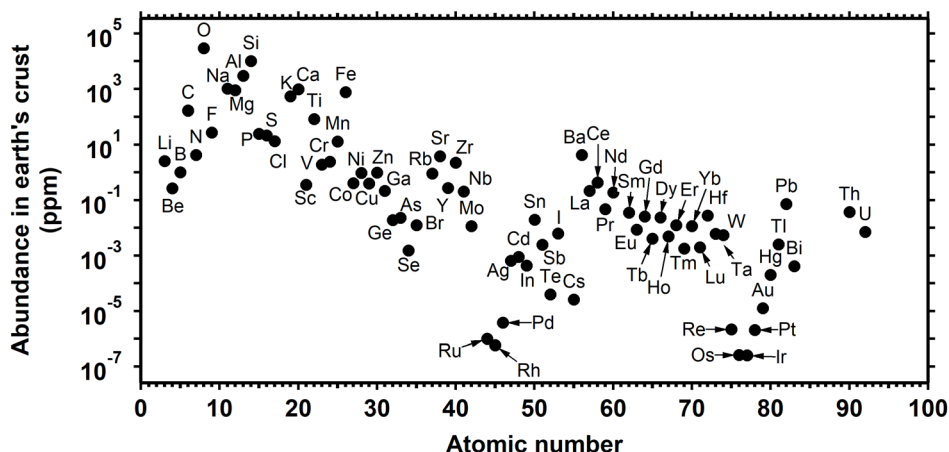
Figure 1.1. Average natural abundance of elements in the earth's crust.[7] The abundance (ppm in weight) was corrected for the atomic weight of the elements.

Apart from producing H_2, electrochemistry is important for utilizing the energy that is released when H_2 is oxidized. This is achieved in fuel cells. Here, the HOR at the anode and the O_2 reduction reaction (ORR) at the cathode are performed resulting in an electric current. Obviously, highly dispersed Pt catalysts are used for the HOR since it is the ideal catalyst. Again, it is the half reaction of Eqn. 1.2 that is the bottleneck. The most energy efficient catalyst for ORR is actually Pt as well.[9] Nonetheless, platinum catalysts cannot operate at the thermodynamic potential of 1.23 V thus reducing the efficiency significantly.[10] Scaling relations prevent predominantly the optimization of heterogeneous catalysts such as platinum. In brief, scaling relations suggest that catalyst binding strength of intermediates is dependent on each other.[11, 12] As a consequence, optimizations of the binding strength for a specific intermediate according to Sabatier's principle, will negatively affect the binding strength of another intermediate. Therefore, most heterogeneous catalyst development is only focused on mass transport optimization to reduce catalyst loadings.[13] To illustrate the challenge that is faced in reducing catalyst loadings, the requirements for the replacement of fossil fuel driven cars by fuel cell driven cars is given as example. Currently, at least 50 g of platinum for a medium-sized vehicle would be required to be able to power it via a fuel cell.[14] Due to the scarcity and costs associated with that amount of platinum, it is estimated that there must be a more than 8 fold reduction of catalyst (maximum of 6 g per vehicle) in order to have feasible large scale fuel cell car production.[15] In this scenario, only medium-sized vehicles are considered. One can imagine that replacing all fossil fuel

driven processes by fuel cells is basically impossible considering the scarcity and costs of platinum. Thus, the need for intrinsically more efficient catalysts for both electrolyzers and fuel cells is high.

1.1.2 H_2O_2 production from O_2

The ORR is generally considered and investigated as the reaction in Eqn. 1.2: the full 4 electron reduction of O_2 to H_2O. However, the 2 electron reduction to H_2O_2 is possible as well (Eqn. 1.3). For fuel cells, H_2O_2 as the product of O_2 reduction is undesired since it is highly corrosive. Moreover, the E° of O_2 to H_2O_2 is 0.695 V (Equation 1.3), which is lower than that of the full 4 electron reduction to water (1.229 V).[4] Thus, the theoretical maximum output potential of a fuel cell, when H_2O_2 is the product, is lowered to 0.695 V instead of 1.229 V. Nevertheless, H_2O_2 is a valuable product. In fact, H_2O_2 is a bulk chemical that is used in applications varying from organic synthesis,[16] waste water treatment,[17, 18] to, most importantly, bleaching of wood or paper pulp.[19, 20] H_2O_2 is a very environmentally friendly reagent following that only H_2O or O_2 are generated as waste. This is in sharp contrast to the production method of H_2O_2. The anthraquinone process is responsible for over 90% of the global H_2O_2 production.[21, 22] This process relies on the reduction of O_2 with H_2 by anthraquinones. These redox mediators have limited life cycles and have to operate in organic solvent mixtures. Obtaining highly concentrated, pure aqueous H_2O_2 solutions requires energy intensive purification steps that increase the waste and costs significantly. Using the electrochemical O_2 to H_2O_2 reduction in aqueous media with electricity from renewable sources is a worthwhile alternative that can also be used as "on-site" production method.

$$E° = 0.695\ V \qquad O_2 + 2H^+ + 2e^- \ \rightleftharpoons\ H_2O_2 \qquad \textbf{Eqn. 1.3}$$
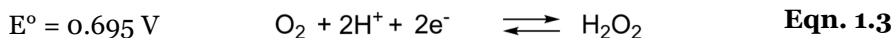
The electrocatalytic reduction of O_2 to H_2O_2 can be carried out by various catalysts such as metal alloys[23-26] or carbon based electrodes.[26-35] The latter category includes electrodes such as pyrolytic graphite (PG) and glassy carbon (GC) that have an intrinsic high selectivity for the 2 electron reduction of O_2 to H_2O_2. Yet, defects and heteroatoms (such as nitrogen), introduced via *in-situ* electrode degradation, can change the selectivity towards the 4 electron reduction. Also, the overpotential is still significantly high. Therefore, research into selective H_2O_2 producing electrocatalysts is of high interest, especially as such a production process would be suitable for on-demand and on-site production of H_2O_2.

1.1.3 Homogeneous *versus* heterogeneous catalysis

Overall, the reactions in Equations 1.2 and 1.3 will play a very important role in a sustainable energy infrastructure and an important contribution lies in the field of electrocatalysis. As will be elaborated, this thesis is focused on molecular complexes. Often, these are seen as homogeneous catalysts. A generalized difference between homo- and heterogeneous catalysts is whether the catalyst is in the same phase (homogeneous), or in a different phase (heterogeneous) as the reactants. Interestingly, electrocatalysis will always require an electrode which is inherently in a different phase (solid) than the substrate such as O_2 (gas) or H_2O (liquid). Heterogeneous electrocatalysts are often either the electrode material itself, or a deposited catalyst layer on a conductive substrate such as GC or a metal. In this perspective, homogeneous catalysts are performing electrocatalysis in the electrolyte itself, but only close to the surface of an (heterogeneous) electrode where these are able to exchange electrons. They might even have to adsorb on the electrode for that purpose. For that reason, concepts from heterogeneous catalysis such as surface area, diffusion constants and mass-transport become important. Moreover, the bulk of the solution is not (entirely) involved in catalysis which is all in contrast with classic homogeneous catalysis. Also, molecular catalysts might have different activity and/or selectivity when they are heterogenized (attached to the electrode surface). An example are Fe^{II} porphyrins that perform electrochemical O_2 reduction both homogeneously and, when adsorbed on the electrode surface, heterogeneously.[36] A small difference in selectivity for H_2O_2 production was observed which was ascribed to faster formation and protonation of the $Fe^{II}–O_2$ adduct when the Fe porphyrin was adsorbed on the electrode. In some cases, molecular catalysts can have such high affinity with the electrode surface that homogeneous electrocatalysis is not possible. An example are planar cobalt porphyrins that adsorb readily and irreversibly on the surface of glassy carbon electrodes.[37] Homogeneous electrocatalysis thus borders heterogeneous catalysis. Various electrochemical techniques derived from that latter field can be (partially) applied to homogeneous electrocatalysis. *Vice versa*, lessons from homogeneous catalysis, such as structure–activity correlations and mechanistic studies, can enhance knowledge about catalyst improvements and perhaps help to uncover new and improved catalytic cycles.

The rest of the introduction will introduce the concepts of electrocatalysis by molecular complexes, examples of structure–activity relationships, pitfalls that are related to catalyst degradation and the use of electrochemical techniques to study kinetics, product distribution and catalyst stability.

1.2   Molecular complexes for redox catalysis

1.2.1   Advantages of molecular complexes in redox catalysis

Molecular complexes are generally highly customizable by ligand modifications resulting in interesting scaffolds for studying catalytic reactions.[38-41] Even though the aforementioned scaling relationships must apply to homogeneous catalysis as well,[42] ligand modifications can still greatly enhance the efficiency of catalysts, but also provide mechanistic insight. One use of complexes is as structural mimic for enzymatic active sites, thereby offering insight and spectroscopic reference for the *modus operandi* of enzymes and perhaps mimic the enzymatic reactivity in catalysis. Another great use of molecular complexes is the ability for systematic structural modifications such as placing electron donating or withdrawing substituents on the backbone of the ligand or the synthesis of multi-metallic systems that both give vital clues to their influence on the rate determining step. In that way, identifying factors that improve rate, but also unraveling the catalytic mechanism can become straightforward. Yet, the structural diversity can come with a price. Ligand oxidation by reactive intermediates can result in the loss of the ligand and/or electrodeposition. These problems will not always be clear in advance and thus various spectroscopic and electrochemical techniques must be employed to identify what is initiating the catalytic activity: the parent complex or, in fact, the degraded (and deposited) complex. At first sight, the latter case seems highly undesirable. Yet, ligand effects may still play a role and could eventually be put to use showcasing where benefits from homo- and heterogeneous catalysis can be combined.

1.2.2   Molecular complexes as structural mimics of enzymes

One of the uses of molecular complexes is as structural mimic for enzymatic active sites. For example, molecular model systems can be a spectroscopic reference to determine the structure of the active site. Likewise, the geometry and coordination environment of the enzyme can serve as inspiration to design catalysts with similar reactivity and activity. A group of enzymes often used as inspiration for performing the ORR efficiently are multi-copper oxidases (MCOs). The active site of these MCOs contains copper clusters including type 1 ("blue copper"), type 2 ("normal copper") and/or type 3 (dinuclear) copper cores.[43] MCO's reduce O_2 to H_2O to be able to oxidize a substrate. One of the most profound examples of an MCO is laccase that has a trinuclear copper active site that reduces O_2 (Figure 1.2). Immobilization studies found that not only O_2 reduction, but also H_2O oxidation could be performed close to the equilibrium potential of 1.23 V.[44-51] Pathways that are inaccessible to
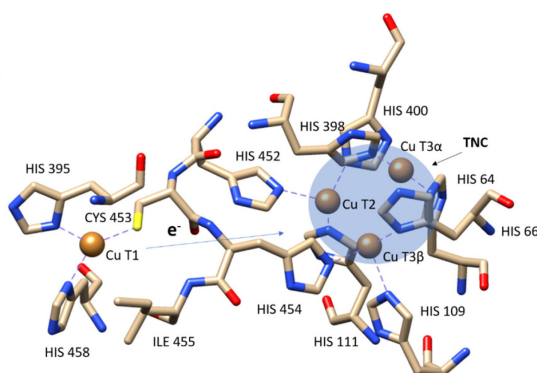
Figure 1.2. Illustration of the active sites of laccase showing the T1 and T2/T3 copper sites. Adapted from Wasak *et al*.[53] (CC BY 4.0 license)

traditional heterogeneous catalysts such as the destabilization of water by carboxylate groups from the second coordination sphere and the irreversible formation of a triangular $\mu_3\text{-}O_2$ bond that facilitates fast electron transfer are suggested to be responsible for this low overpotential.[52]

Long term stability and the low number of active sites are drawbacks of enzymatic catalysis hindering direct application in fuel cells.[49-51, 54]. Here, copper complexes that are structural mimics have played a large role to extract spectroscopic information of key intermediates in the activation of oxygen so that these lessons could lead to the design of better electrocatalysts.[55-61] For example, the interconversion of side-on peroxodicopper and bis-μ-oxo dicopper cores in enzymes have been spectroscopically identified by linking the spectroscopy of model copper complexes for which this behavior had been unambiguously proven. Crystallographic studies would not have been able to reveal this dynamic equilibrium.[62] UV-vis, Raman and electronic paramagnetic resonance (EPR) data have been extensively used to character the active site and the intermediates in MCO driven O_2 reduction.

Another enzyme that has sparked interest is the oxygen-evolving complex of Photosystem II. This enzymatic OER catalyst contains a manganese active site. The oxygen-bridged tetranuclear core contains three manganese and one calcium site (Figure 1.3).[63] A simple complex with a di-μ-oxo dimanganese core and terpyridine ligands (Chart 1.1A) was suggested as catalytic mimic since the complex also achieved high oxidation states.[64] However, under electrochemical conditions a tetranuclear complex is formed that is catalytically inactive.[65, 66] Specifically designed tetranuclear Mn_4O_4-cubane clusters (Chart 1.1B) were found to be inactive under homogeneous conditions as well, but with Nafion-assisted immobilization the clusters had water
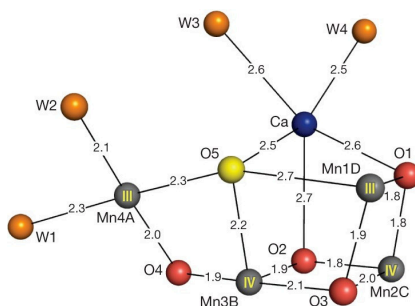
Figure 1.3. Tetranuclear core of the active site of the oxygen evolving complex of Photosystem II. Adapted from Suga *et al.*[63]

oxidation activity.[67] The authors suggested that this could be due to a more efficient distribution of the clusters on the electrode and simultaneous protection from the bulk aqueous electrolyte, though no further investigations to support these hypotheses were conducted.

1.2.3   Mechanistic insight from redox catalysis with sacrificial reagents

The reactivity of most molecular complexes for redox catalysis is studied initially with sacrificial reagents. For water oxidation, cerium(IV) ammonium nitrate (CAN) is often used as sacrificial oxidant which supplies the thermodynamic oxidative power for water oxidation. However, the pH range is limited with CAN
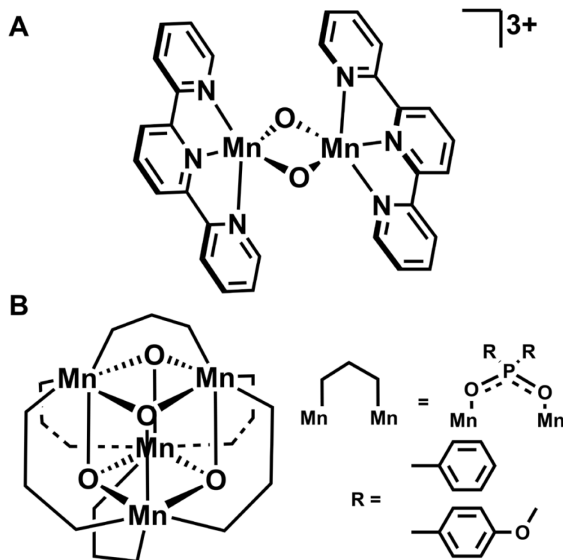

Chart 1.1. The structures of dinuclear manganese complex (A) and a cubane cluster with a Mn_4O_4 core (B) proposed as mimics for the active site of photosystem II.

since it is only stable at low pH.[68] Among other oxidants, sodium periodate is an often used oxidant especially since it can operate at neutral pH as well. One field where the OER has extensively been studied with sacrificial oxidants, is the field of ruthenium based OER that started with the first known molecular water oxidation catalyst (the blue dimer).[69] Often, the ruthenium complexes are studied electrochemically to establish redox potentials, while the catalytic activity is assessed with sacrificial oxidants. The advantage of using oxidants is that, in principle, all catalyst in solution can participate in the reaction. As a result, the turnover number (TON, amount of catalytic cycles per catalyst) and turnover frequency (TOF, TON per time unit) can be easily determined. Moreover, the concentration of Ce^{IV} can be actively tracked by UV-vis allowing for detailed kinetic studies.[70] An important lesson that was learned from ruthenium based OER, was the importance of proton coupled electron transfers (PCET).[71] A PCET step in a catalytic mechanism is the simultaneous transfer of an electron and a proton. The result of a PCET is that there is no net effect on the charge of the active species after oxidation or reduction. Charge build-up is avoided and the redox potentials of higher oxidation states of molecular complexes will be closer together.[72] Ruthenium complexes generally need to reach the high Ru^V state to generate a metal-oxo species and can do so by starting with a $Ru^{III}-OH_2$ moiety that can undergo two consecutive PCET steps to a $Ru^{IV}-OH$ and $Ru^V=O$ species. Another insight gained from ruthenium based water oxidation chemistry is that there are two mechanisms for O−O bond formation: the water nucleophilic attack or the intermolecular coupling of two metal-oxyl radicals (Scheme 1.1).[73, 74]
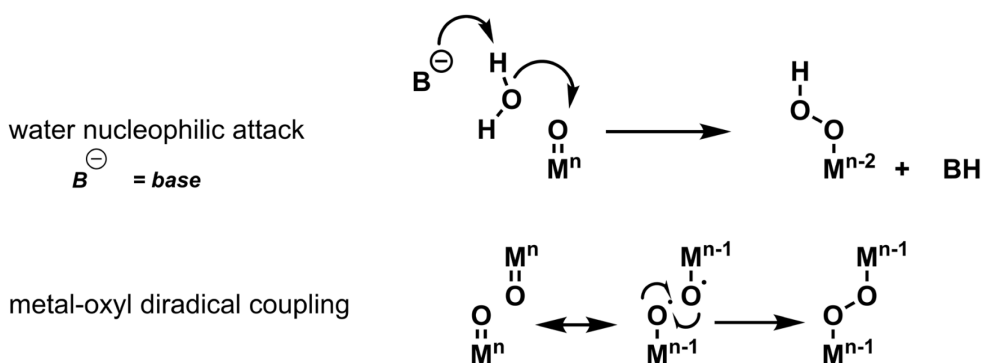
Scheme 1.1. Schematic representation of the water nucleophilic attack or intermolecular coupling of two metal-oxyl radical species.

An important ligand modification that enhanced the activity of ruthenium complexes, is the addition of anionic carboxylate groups on a bipyridine ligand

(Chart 1.2A) that resulted in a distorted octahedral geometry of the complex. That way, a 7-coordinate dinuclear intermediate became more accessible to facilitate O–O bond formation via the metal–oxyl coupling mechanism which in turn increased the turnover frequency for OER significantly.[75] Furthermore, the redox potential for the Ru^V species that is required for OER catalysis can, in general, be lowered by various adjustments to the ligand[76] and specifically by introducing electron withdrawing groups.[77-79] In addition, attractive non-covalent interactions of the ligand can also positively impact the rate of water oxidation. However, having electron withdrawing groups will not always improve the OER. For example, a series of terpyridine ruthenium complexes with substituted bipyridine ligands (Chart 1.2B) showed reversed trends as in that electron donating groups improve the catalytic rate.[80]
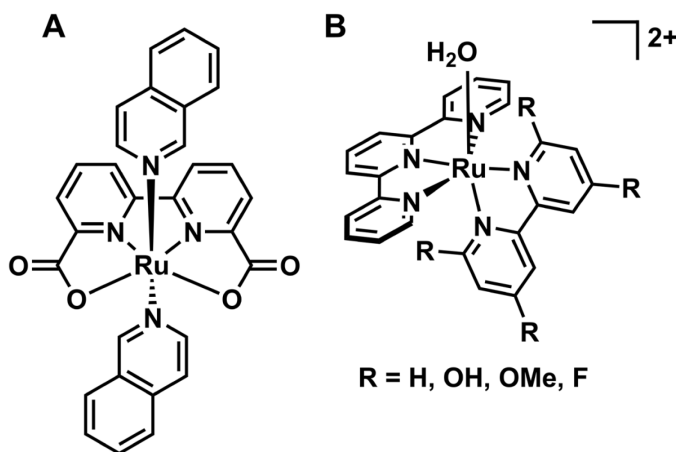

Chart 1.2. Ruthenium complex with dicarboxylate substituents on the bipyridine ligand (A) and ruthenium terpyridine complexes with substituted bipyridine ligands (B).

The ruthenium OER chemistry has laid a good foundation for fast catalysts and mechanistic insight. Nevertheless, results and insight obtained by catalysis with sacrificial oxidants cannot unconditionally be transferred to electrocatalytic conditions. Regularly, electrochemically studied redox potential and catalytic onset potential shifts due to substituent induced electronic differences between complexes are compared to catalytic TOF's derived from sacrificial reagent studies. However, these sacrificial reagents might actually participate in the catalytic cycle,[81] or the oxygen atoms of the nitrate of CAN might be incorporated in the formed O_2 molecule.[82] In the latter case, there is actually no formal water oxidation. Oxygen labeling studies could be used to investigate this possibility, though for sodium periodate this is not possible, since it readily exchanges oxygen atoms with water.[83] In addition, the oxidative potential of these sacrificial reagents is completely

dependent on their concentration according to the Nernst equation and will thus vary uncontrollably during catalysis. To illustrate, at the start of an experiment with CAN there is only cerium (IV) and no cerium (III) present yet. Hence, the potential at the start is, in theory, infinitely high which would translate to an infinite overpotential under electrocatalytic conditions. In addition, care has to be taken into translating results to electrochemical conditions as structure–activity relationships might not prevail. When sacrificial reagents participate in the catalytic mechanism the rate determining step can be different under electrochemical conditions. In some cases, the influence might actually be inversed. A good example is that of a study into Cp* (Cp* = pentamethyl cyclopentadienyl) iridium complexes with tunable carbene ligands (Chart 1.3A).[84] This study reported a clear correlation between electron donating substituents and an enhancement of the catalytic TOF with sacrificial reagents. In contrast, the best performing electrocatalytic system was the unsubstituted complex.

A last word of caution includes the stability of complexes under electrochemical conditions. A series of Cp* iridium picolinate catalysts (Chart 1.3B) previously showed a good correlation between the electron donating ability of the picolinate ligands and the water oxidation activity with sacrificial reagents. Later, electrochemical studies showed that these relationships did not translate to those conditions because of catalyst degradation (see Chapter 2).[85, 86] Sacrificial reagents are often, especially in the field of OER catalysis, used to easily study the catalytic performance of molecular complexes. However, these examples show that without actual electrocatalytic studies, one to one translation of the results of sacrificial reagent driven catalysis to electrocatalytic conditions is not possible.

R^1 = H, OMe
R^2 = H, OMe, ^{t}Bu, NMe$_2$
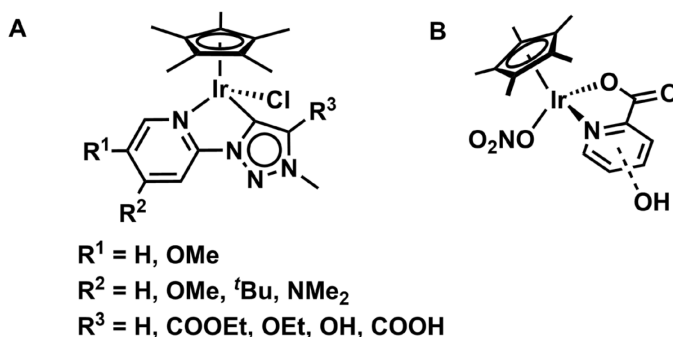R^3 = H, COOEt, OEt, OH, COOH

Chart 1.3. The structures of the carbene iridium complexes (A) and iridium picolinate complexes (B) used for comparative sacrificial and electrochemical structure–activity studies.

1.2.1   Structure–activity relationships in electrocatalysis

Structure–activity relationships (SAR's) are a powerful tool to gain mechanistic insight and to design better catalysts. The ligand framework of molecular complexes can be tuned in such a way that the geometry and/or the electronic properties of a complex are altered. In the previous section, SAR's with sacrificial reagents have been discussed, but SAR's can be found under electrocatalytic conditions as well. Often, the equilibrium redox potential of the metal (the $E_{1/2}$) has a clear relationship, especially when substituents, that have an electron donating or withdrawing effect, are placed on the ligand. This electronic effect can be described by the Hammett parameter. Originally, this parameter was derived for the rate of reactions involving substituted aromatic compounds, such as esterification/hydrolysis and bromination, but also the pK_a of benzoic acids and phenols.[87, 88] For electrocatalysis, the Hammett parameter can correlate to the $E_{1/2}$ of the complex or even to the catalytic rate and/or onset potential. Even in cases without clear correlations, structural diversity can give clues regarding the rate determining step.

One example of SAR studies for O_2 reduction encompasses closely related bis- and tris-pyridyl Cu^{II} complexes (Chart 1.4A). The difference in linker length between the central amine and pyridine or the number of pyridines (2 or 3) shifted the $E_{1/2}$ of the $Cu^{I/II}$ redox couple. Interestingly, the O_2 reduction rate differed among the complexes, but with no clear relation to the $E_{1/2}$.[89] Another study claimed that substituents on the *ortho*-position of the pyridines had no significant influence on the onset potential for O_2 reduction.[90] A first conclusion was that Cu^{II} to Cu^{I} reduction nor protonation of a superoxo species would be the rate determining step. Of note, this latter study studied these *ortho*-substituted complexes at pH 1 where the pyridines might be protonated and not able to coordinate to copper resulting in free copper ions in the solution. In addition, the lessons learned from this set of ligands cannot be extrapolated to all copper complexes. In contrast to the previously mentioned copper series, linear relationships between the $E_{1/2}$ of the redox couple and the O_2 reduction rate were in fact found for several (substituted) bipyridine and phenanthroline copper complexes (Chart 1.4B). In detail, the half wave potential of the catalytic wave corresponded linearly with the redox couple whereas the rate constant had an inverse correlation with the redox couples.[91] Later, the linear dependence was pinpointed to the electron withdrawing nature and the steric demands of the substituent which both result in a higher half wave potential but lower catalytic rate.[92] For the ORR, cobalt porphyrins had a clear substituent effect on the redox couple (Chart 1.5).[93, 94] More electron donating sulfonate groups *versus*
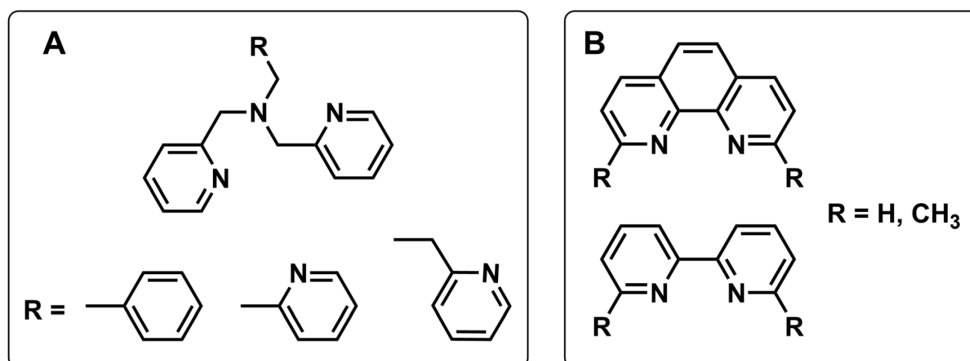
Chart 1.4. Ligands used for the study of Cu^{II} complexes with variable linker length between the pyridine and the central amine, as well as the variable presence of a pyridinic moiety (A) and the structure of the bipyridine and terpyridine ligands (B).

electron withdrawing N-methylpyridine clearly shifted the redox couple to lower potentials. The most interesting observation was that in the case of the N-methylpyridine porphyrins, the $E_{1/2}$ of the redox couple occurred before the catalytic wave whereas the $E_{1/2}$ of the sulfonate substituted porphyrin complex was lower than that of the onset of O_2 reduction. A change of mechanism where O_2 is reduced either by a Co^I or a Co^{II} species was proposed and related to a positive shift of the O_2 reduction onset for the latter. Interestingly, these porphyrins are non-planar which prevented adsorption on glassy carbon electrodes as opposed to the earlier discussed planar analogues.[37]
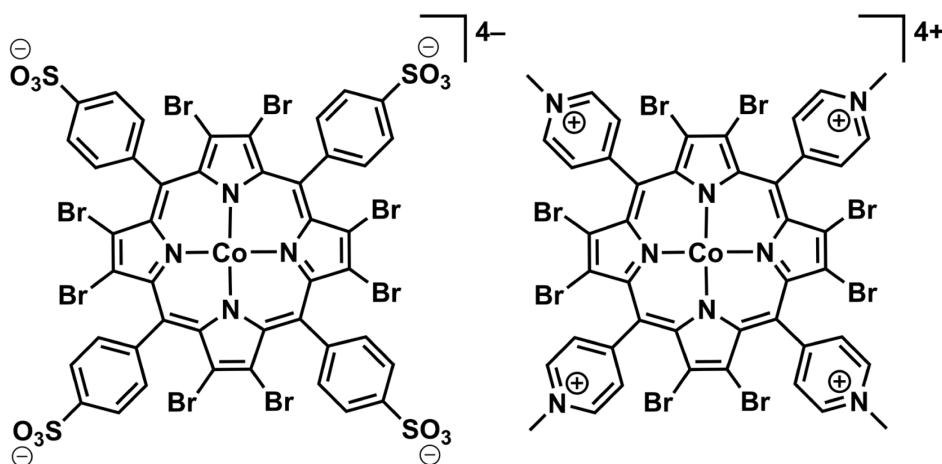

Chart 1.5. The planar cobalt complexes studied for electrochemical O_2 reduction.

The performance of catalysts for electrocatalytic water oxidation can also be boosted with ligand modifications. Electron donating substituents on tetra-anionic tetradentateamidate copper complexes (Chart 1.6A) resulted in a reduction of the overpotential down to 170 mV. Additionally, computational studies suggested that within the catalytic cycle, the ligand stabilizes a peroxo intermediate via hydrogen bonds after O−O bond formation without the presence of a formal metal−O bond.[95] For a series of dinuclear manganese terpyridine complexes (Chart 1.6B), electron donating substituents on the terpyridine resulted in a decrease the $E_{1/2}$ of their respective complexes as well as a decrease of the second order rate constant for the OER. Interestingly, some of the bulkier substituents increased the rate more than expected based on their respective Hammett parameters.[96] However, the $E_{1/2}$ correlated linearly with the catalytic rate constant. Interesting to note here, is that terpyridine based ruthenium complexes actually catalyzed the water oxidation with higher rates with electron donating substituents on the terpyridine backbone.[80]

SAR's under electrocatalytic conditions are not always as straightforward as SAR's from sacrificial reagent studies would predict. Generally, the $E_{1/2}$ of a complex has a good relationship with the electron donating or withdrawing effect of a ligand and might even be correlating to the corresponding Hammett parameter. Interestingly, when the overpotential can be reduced by in- or decreasing the $E_{1/2}$ of a complex, the catalytic rate is often lowered as well. Often, inverse linear relationships can be found under electrocatalytic conditions, but not exclusively. Also, there might be no clear relationship between the electronic effects of the ligand and the catalytic rate. Lastly, these electronic effects might even change the mechanism. All of these mechanistic features can only be revealed by SAR studies.
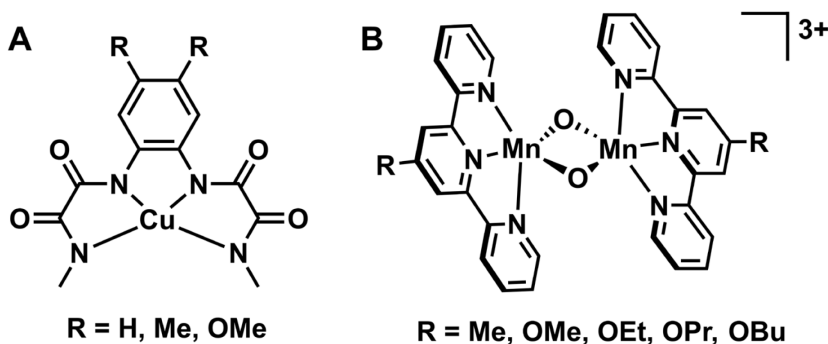

A R = H, Me, OMe

B R = Me, OMe, OEt, OPr, OBu

Chart 1.6. Ligands of the tetra-anionic copper complexes (A) and the terpyridine manganese complexes (B) for electrochemical water oxidation.

1.2.2 Stability of molecular complexes under electrochemical conditions

A major issue of molecular complexes is their stability under electrochemical conditions.[97-99] They can degrade by forming an electrodeposition of metallic layers or metal oxides depending on reductive or oxidative conditions. One origin for this type of degradation can be a very fast ligand exchange rate.[100] Cu^{2+} in particular has very fast exchange rates. For example, exchange rates in the order 10^7 to 10^9 s^{-1} for the exchange of the ligand in $[Cu(1,2-diaminoethane)_3]^{2+}$ and $[Cu(H_2O)_6]^{2+}$ complexes have been determined, respectively. For comparison, $[Ir(H_2O)_6]^{3+}$ has an exchange rate of 1.1×10^{-10} s^{-1} at room temperature. As these reactions are equilibriums, a very low concentration of unchelated metal is present at all times, despite high binding constants of a ligand. Under reductive potentials, this could form a metallic deposit which disturbs the equilibrium with the chelated complex. For copper complexes, this equilibrium is re-established within the order of nanoseconds. As the deposited, solid metallic copper is not included in the equilibrium, the overall concentration of the chelated copper complex is lowered. Therefore, copper complexes can easily degrade by deposition in the time scale of a short cyclic voltammogram. The actual rate of deposition would be dependent on potential and the binding strength of the ligand to copper, but at low reductive potentials this is a very likely process. Apart from electrochemical conditions, this fast ligand exchange rate can also affect sacrificial reagent driven water oxidation. For copper catalysts, ligand chelation to Ce^{IV} can take place through the same route as described above thereby lowering the copper complex concentration and inhibiting reactivity from Ce^{IV}. For other complexes, such as the aforementioned iridium aqua complex, ligand exchange rate is so slow that this deposition pathway is not applicable. In those cases, other decomposition pathways are of importance. Generally, ligand oxidation by reactive (radical) intermediates is the major degradation pathway, but the formation of an inactive complex is also possible. One example is the electrochemical study that compared Cp* versus Cp iridium complexes (Cp = cyclopentadienyl). Cp complexes had a rather low activity,[101] later suggested[38] to stem from the formation of an inactive dimerized μ-oxo complex that cannot be formed when Cp* was used as ligand. As will be discussed next, the Cp* ligand can degrade itself and the remaining iridium moieties can dimerize to form μ-oxo-bridged species,[102] which is in contrast to this proposed hypothesis of deactivation of Cp iridium complexes by dimerization. Some studies report ligand degradation or even the formation of iridium oxide (IrO$_x$) nanoparticles during or after catalysis.[103-128] The high water oxidation activity found by studies involving the

simple $[Cp*Ir(H_2O)_3]^{2+}$ complex initiated research into the, now well-established, breakdown routes of the Cp* ligand for various complexes.[103-119, 129] For $[Cp*Ir(H_2O)_3]^{2+}$, this results in IrO_x electrodeposition as after Cp* degradation only iridium aqua species remain that easily deposit.[122] Also, (substituted) bipyridine Cp* complexes oxidatively degrade into inert deposits under electrochemical conditions as opposed to some structure-activity relationships observed with chemical oxidants.[117]

1.2.3   Influence of the ligand on heterogenized systems

Often, complexes are intentionally immobilized on the surface of an electrode to be able to combine the advantages of homo- and heterogeneous catalysis. Here, a distinction between two strategies has to be made. Immobilizing a complex onto the electrode surface has the goal to use the intact complex whereas some strategies merely use this complex as a pre-catalyst for a transformation to the active and heterogenized species by for example (intentional) ligand oxidation or electrodeposition. For the first strategy, many studies utilize an anchor group (thiol, pyrene linker) on the ligand that serves as a tether between the electrode surface and the complex. General methods are covalent bonding with metal oxo surfaces,[130, 131] self-assembled monolayers of thiol moieties with a gold surface,[132] electrografting of diazonium salts to carbon or metal surfaces,[133] π-π stacking based adsorption with pyrene linkers or Nafion-assisted dropcasting.[134, 135] Notably, bringing complexes in close contact with the electrode can change intrinsic properties such as the redox couples which inherently influences the catalytic activity as opposed to the homogeneous complex. An example is a trispyridyl Cu^{II} complex that was found to be more stable in the Cu^{I} state when tethered on the electrode via a thiol moiety.[136] On the other hand, adsorbed cobalt hangman corroles (Chart 1.7) still benefited from electron withdrawing substituents for water oxidation, thus structure–activity relationships can still prevail.[135]
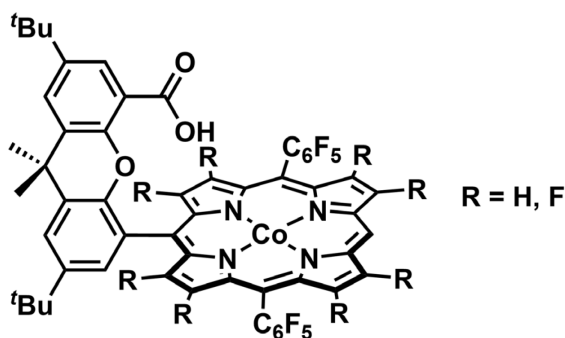
Chart 1.7. Substituted cobalt hangman corroles.

An interesting alternative to the aforementioned immobilization strategies, are pyrazine linkages between graphitic electrodes and the complex. In contrast to traditional, tether-based anchoring, this method is suggested to allow for fast electron-transfer kinetics by incorporating the catalysts as part of the electrode thereby facilitating conjugation through the pyrazine linkage (Scheme 1.2).[137]
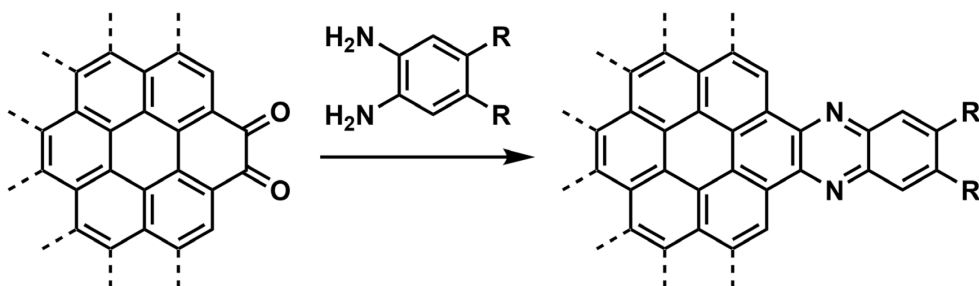
Scheme 1.2. Immobilization of catalysts through pyrazine conjugation with graphitic carbon electrodes.

The second strategy is using molecular complexes as pre-catalysts. Basically, this strategy includes an expected (as often claimed) decomposition of the parent complex (or pre-catalyst) that results in the desired catalyst. For example, after oxidation of the Cp* moiety of [Cp*Ir(pyalc)(Cl)] (pyalc = 2-(2'pyridyl)-2-propanolate)[102, 109, 115, 116, 122] the complex turns into a dinuclear species with the pyalc ligands still coordinating to the iridium cores (Scheme 1.3). This species has later been immobilized on a metal oxide and it was shown that over 90% of the iridium atoms were involved in catalysis.[102] Such an approach could be very beneficial for reducing catalyst loadings in electrolyzers.
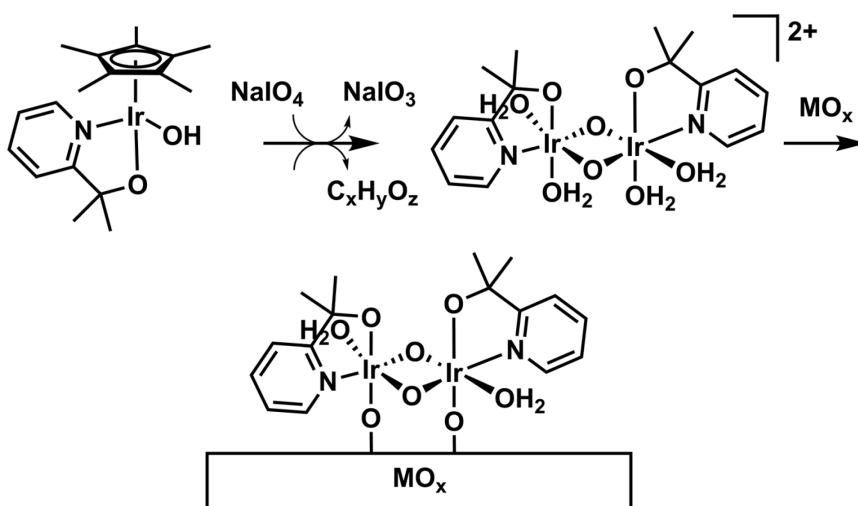
Scheme 1.3. Oxidative degradation and subsequent immobilization of the active species formed by [Cp*Ir(pyalc)(OH)].[102]

Another example shows that by picking the right potential and under the influence of the ligand a copper complex could be transformed to copper oxide with increased water oxidation activity and inhibited copper stripping at high oxidative potentials.[138] Optimizing nanoparticle sizes is another field where molecular-pre-catalysts or ligands play a role. Sometimes ligands are used to "cap" nanoparticles to control the nanoparticle size. However, ligands might actually participate in nanoparticle catalysis and thereby influencing selectivity and activity.[139, 140] Striking examples include ligand induced inhibition of undesired phosphate adsorption on the surface of platinum nanoparticles,[141] or actually improving the ORR activity of platinum nanoparticles with electron withdrawing ligands. In the study of Zhou *et al.*, a clear Hammett correlation with the ORR activity could be found emphasizing the power of the synthetic versatility of ligands (Figure 1.4).[142]

1.3 Electrochemical techniques for the analysis of molecular complexes

1.3.1 Analyzing the kinetics of the catalytic reaction

The practice of studying electrocatalysis by molecular complexes has been well described in many reviews and tutorials.[143-149] Most often, the current response when the potential is cycled with a three-electrode setup is recorded in a cyclic voltammogram (CV) that reveals redox couples and catalytic currents. In addition,
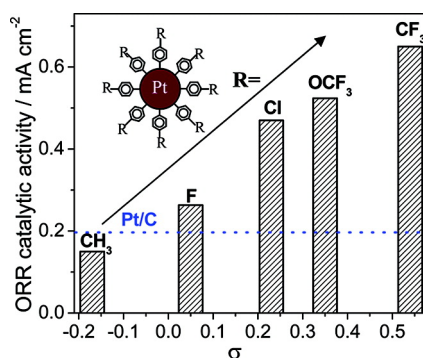
Figure 1.4. Concept of *para*-substituted phenyl groups capping Pt nanoparticles and the correlation between the Hammett parameter and the ORR activity. Adapted from Zhou *et al.*[142]

there are several other electrochemical techniques that can be used. Though a lot of information can be extracted from these techniques, the underlying theory is often based on certain assumptions. This section discusses both the application of these techniques towards the study of molecular complexes including any pitfalls that may lead to a wrong interpretation when the theoretical background is not considered completely.

Analyzing the kinetics of an electrocatalytic reaction catalyzed by a homogeneous, molecular complex is different than in traditional homogeneous catalysis with sacrificial reagents, because catalysis is only taking place near the electrode surface. Nevertheless, it is possible to establish the rate of catalysis. The current enhancement method can be used to directly determine the observed rate constant of a reaction (k_{obs}).[150] It uses the ratio between the maximum current of the catalytic wave i_{cat} and the peak current of the reduction or oxidation of the complex i_p (depending on the catalytic reaction). From this ratio, k_{obs} can be calculated according to Equation 1.4 with n being the number of electrons, R the gas constant, T the temperature (in Kelvin), F Faradays constant, and v the scan rate (in V/s).

$$\frac{i_{cat}}{i_p} = \frac{n}{0.4463}\sqrt{\frac{RTk_{obs}}{Fv}}$$
Eqn. 1.4

A downside of using the current enhancement method is that the catalytic peak current is used. This current can be heavily affected by mass transport limitations resulting in cases where for example the catalyst might be intrinsically very fast, but the k_{obs} is low due to fast substrate consumption. One way to overcome

this problem, is to use the foot of the wave analysis (FOWA).[145-148] The FOWA is elaborated in Chapter 5, but in short, the FOWA allows to determine the (theoretical) maximum TOF (TOF$_{max}$) of the catalyst by analyzing the catalytic current close to the onset potential where it is assumed that the current is purely kinetic in nature. The downside is that precise knowledge of the mechanism is required to be able to correctly apply the FOWA. Also, the TOF$_{max}$ is a theoretical rate which might never truly be obtained for instance due to catalyst degradation.

Another technique for studying the kinetics is to construct a Tafel plot. This plot can, in an ideal case, be used to benchmark catalysts and to get mechanistic insight. A Tafel plot is a plot of the overpotential (or potential) *versus* the logarithm of the current density (current per active surface area). In an ideal case, the linear part of the obtained plot is described by the Tafel equation (Equation 1.5 in a simple form).[151] The major assumption, and pitfall when used incorrectly, is that the Tafel equation is only valid for a situation where the concentration of the substrate near the electrode is equal to the bulk concentration. In other words, the mass transport rate should be far larger than the kinetic rate. The current used for the Tafel plot should be the kinetic current I_k, which may be derived by using Equation 1.6 (see next section). In a heterogeneous system, the Tafel slope (A, V/dec) can be used to compare catalytic behavior. With a lower the magnitude of the slope, more catalytic current will be generated when the overpotential is increased which is characteristic for a better catalyst. i_o is the exchange current density, which is the intersection with the x-axis when the linear part of a Tafel plot is extrapolated. In simple terms, this current is the theoretical current at 0 V potential. The higher this number, the better the catalyst. Even for heterogeneous catalysts, ideal conditions may not be met when the current is not a 100% Faradaic current for the reaction of interest. Instead, catalyst decomposition or unwanted side reactions can contribute to the overall current as well. For homogeneous systems, the applicability might be limited since the diffusion of the catalyst itself plays a role. The theoretical background of the Tafel equation assumes that the catalyst is a heterogeneous and stationary surface. Nevertheless, Tafel plots might still be useful for catalyst benchmarking or mechanistic insight. The next section gives an example the use of the rotating ring disk electrode (RRDE) setup in combination with a Tafel analysis.

$$\eta = A \times \log\left(\frac{i}{i_0}\right) \qquad\qquad \textbf{Eqn. 1.5}$$

Another technique that can be used is (chrono)amperometry in which the applied potential is fixed and the current monitored over time. This would reveal any activation/deactivation processes but it also allows for bulk electrolysis (also called controlled potential electrolysis). The latter technique affects the entire bulk solution by employing large surface area electrodes, stirring of the solution, and separating the counter and work electrodes. This way, one might be able to replicate sacrificial reagent conditions where the bulk of the solution is utilized as well and TON/TOF calculations might be made. In addition, post-catalytic spectroscopic studies of the bulk solution become possible. These studies can help to detect intermediates/products and any degraded catalyst. Of note, it is impossible to accurately determine after what period of time bulk electrolysis has affected the entire solution which can lead to wrong interpretations. If one performs bulk electrolysis to check whether the catalyst remains intact, the post-catalytic spectroscopic observation of intact catalyst does not necessarily indicate that the catalyst is stable nor could any ratio of degraded *versus* intact complex be determined. Instead, it might be that this portion of intact catalyst has never been in contact with the electrode during the duration of the experiment. Nevertheless, bulk electrolysis can allow for the qualitative detection of any intermediate, product, or degraded complex in combination with other techniques that are discussed in the next section.

1.3.2 Determining the product distribution

One of the most powerful electrochemical techniques to study the product distribution of a catalytic reaction is the RRDE setup. This electrochemical setup allows for control over the diffusion of electrolyte towards the electrode. By rotating a disk electrode, a laminar flow of electrolyte towards the surface of that electrode is established (Figure 1.5). That way, the obtained current is no longer dependent on time and thus on the scan rate (as would be predict by for instance the Randles-Sevcik equation, see next section) but purely on the electrode rotation speed as variable. In addition, a ring electrode could be used around the disk to detect products that are formed on the disk and thus the product selectivity could be derived. Most often, this ring electrode is a Pt electrode. In O_2 reduction, H_2O_2 can be detected by setting a ring potential of 1.2 V where H_2O_2 is oxidized to O_2, but H_2O is not oxidized. Central to its usage is the collection efficiency (N_{coll}). Not 100% of the products formed at the disk will be detected at the ring due to geometrical constraints. Therefore, a well-defined redox couple such as the $[Fe(CN)_6]^{4-}/[Fe(CN)_6]^{3-}$ redox couple is often used to determine the ring to disk
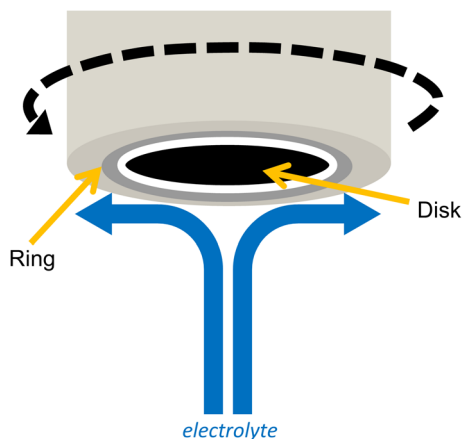
Figure 1.5. Schematic representation of a rotating ring disk electrode.

ratio which is N_{coll} in that case (Figure 1.6). Importantly, Pt is not always the best ring electrode as, for example, H_2O_2 oxidation was found to be not mass transport limited under alkaline conditions.[152] Instead, Au was suggested as better a better option for the ring electrode under those conditions. As discussed in Appendix C of this thesis, the Pt ring is also not a steady sensor for H_2O_2 at pH 7 in phosphate buffer, especially for longer measurements (hours). The N_{coll} can become less during the measurement due to, for instance, PtO_x formation. Also, the polish method of the electrode plays a role and the N_{coll} may vary after each polish. A good practice would be to determine the N_{coll} before each catalytic experiment preferably with the substrate of interest, instead of the $[Fe(CN)_6]^{4-}/[Fe(CN)_6]^{3-}$ redox couple. For longer experiments, such as bulk electrolysis, the RRDE setup is less reliable for quantitative assessment of the product distribution and the RRDE measurement could be complemented with other techniques to determine the product ratio such as gas chromatography, mass spectrometry, or by titration of the formed products such as the titration of H_2O_2 with $KMnO_4$.

The current that is obtained with the disk electrode, where catalysis takes place, is generally described by Equations 1.6 and 1.7 which are the Koutecký-Levich and Levich equations, respectively.[151] In an ideal case, the contributions of the kinetic current I_k (in absence of mass transport limitations) and diffusion limited current I_L are described by Equation 1.6. The diffusion limited current is the maximum current that can be obtained at a certain rotation rate ω (in rad/s) and is only dependent on physical constants. Apart from earlier mentioned physical constants, the current is
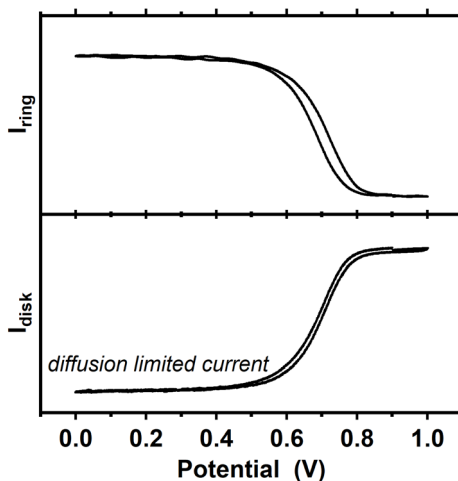
Figure 1.6. Typical RRDE response of the reduction of $[Fe(CN)_6]^{3-}$ to $[Fe(CN)_6]^{4-}$ on the disk (bottom panel) and the re-oxidation to $[Fe(CN)_6]^{3-}$ on the ring (top panel).

also dependent on v_k which is the kinematic viscosity of the electrolyte in cm²/s, the electrode surface area A (in cm²), the bulk concentration of the complex C_0 (in mol/cm³), the diffusion coefficient of the complex D_0 (in cm²/s).

$$\frac{1}{I} = \frac{1}{I_k} + \frac{1}{I_L} \qquad \textbf{Eqn. 1.6}$$

$$I_L = 0.62nFAD_0^{2/3}C_0v_k^{-1/6}\omega^{1/2} \qquad \textbf{Eqn. 1.7}$$

These equations have many uses, but an important use is to determine n: the number of electrons transferred in the reaction. This number can give information about the product selectivity of the reaction. For example, an electron transfer number of 2 would indicate that H_2O_2 is the major product for O_2 reduction whereas a number of 4 would point towards H_2O as product. Any number in between will tell something about the selectivity. When performing RRDE in the potential window of I_L, n can be determined by varying the rotation rate. Important to realize is that these equations have been developed for single-step, one-way reactions. In reality, most catalysis is not. For example, a study by Qiao and co-workers in alkaline electrolyte showed that n for the O_2 reduction reaction depended on the rotation rate ω which opposes Equation 1.7 that states it should remain constant.[152] Another key aspect is that homogeneous catalysts are freely diffusive species as well. Equations 1.6 and 1.7 are tailored for a heterogeneous electrocatalysts that are, or situated on, the disk

electrode. If the catalytic rate (TOF) of a homogeneous complex is not fast enough, the catalyst might not complete a full catalytic cycle before it has passed the electrode surface and is thus interrupted. Very slow rotation could help, but in that case steady state conditions will only be achieved at very low scan rates[151] and considerable lag between the disk and ring current response is observed.[153] The exact limit of the TOF is not known, since it would depend on, among others, the diffusion coefficient and whether or not the complex can adsorb on the electrode. In that sense, even fast catalysts could even be affected.

The kinetic current I_k that can be obtained by Equation 1.6 can be used for the construction of a Tafel plot, as described in the previous section. As said, the Tafel analysis can be used to benchmark catalysts and for mechanistic studies. For example, a Tafel analysis was performed for the electrochemical O_2 and H_2O_2 reduction by a copper trispyridyl complex.[154] In this study, the Tafel plot for O_2 reduction had two linear regions with different Tafel slopes. One of the slopes corresponded to the slope of the linear region of the Tafel plot for H_2O_2 reduction. This finding, combined with observation of H_2O_2 on the ring electrode in specific potential windows, led to the conclusion that O_2 was reduced in a stepwise 2+2 reduction with H_2O_2 as intermediate and thus that O_2 was reduced by two, consecutive catalytic cycles.

1.3.3   Techniques to determine the homogeneity of the active species

Several techniques can be employed to determine whether degradation of the molecular complex has taken place, which new species are formed and whether they are the active catalyst. The simple rinse-test is the most often mentioned control experiment showing that no deposit has formed on the electrode. In this test, the electrode is rinsed after being in contact with the catalyst (and optionally having performed electrocatalysis) and subsequently tested in catalyst-free electrolyte. This test will give a first indication whether a deposit is formed and if it is catalytically active. Mistakenly, this test is often the sole evidence for the presence or absence of any deposit (and thus catalyst degradation). This would either ignore cases with catalytically inactive deposits or deposits that reversibly desorb as soon the potential is lifted.[155-157] Moreover, discrepancies between the before and after voltammograms could be incorrectly be assigned to catalyst degradation. The latter case is especially important in the case of glassy carbon. This electrode is widely employed for studying homogeneous complexes. However, electrode corrosion can alter its voltametric response even in the absence of catalyst. At high potential and depending on pH, glassy carbon can severely degrade and as a result increase the double layer

capacitance and significantly affect the CV or amperogram (see also Chapter 2 and Appendix A).[158] In general, electrodes are not inert substances and, depending on conditions, can actually degrade during the experiment.[159] Therefore, a rinse test should always be complemented with other techniques to establish whether catalyst degradation and/or deposition takes place.

Another often used simple technique is to record CV's at different scan rates and plot the peak current of the redox couples against the scan rate or the square root of the scan rate. The idea behind this technique is that homogeneous species will give a linear relationship with the square root of the scan rate, which is based on the Randles-Sevcik equation (Equation 1.8).[151] The equation describes the relationship between the scan rate at which the potential is swept v (in V/s) and the peak current i_p (in A) of a redox reaction. Important to note, is that this equation considers the peak current of a redox process in which diffusion plays a role. In this case, there is a diffusion layer between unaffected species in the bulk of the electrolyte and electrochemically converted species near the electrode surface. The size of diffusion layer determines how quickly unreacted species can diffuse to the electrode and subsequently converted. The size of this layer is dependent on the scan rate: a faster scan rate yields a smaller diffusion layer. As a consequence, at a higher scan rate more unreacted species can diffuse to the electrode and thus the peak current of the reduction or oxidation is larger.[143] The Randles-Sevcik equation can be put to use in several ways to investigate molecular complexes. First of all, the diffusion coefficient of a diffusive species can be calculated when the electron transfer number is known. In addition, if the reduction/oxidation of the complex corresponds to diffusive process, the peak current of that redox reaction is proportional to $v^{1/2}$. If diffusion does not play a role, the peak current is directly proportional to v.[151] Usually, the diffusive species is the homogeneous complex. This equation is therefore often used to prove that a species is homogeneous. However, finding that a redox couple is related to a diffusive process does not necessarily prove this. For example, complexes that have been tethered on the surface of electrodes can also be regarded as diffusive species when they have freedom of movement due to flexible tethers and will give a peak current *versus* $v^{1/2}$ relationship. As a consequence, one could wrongly conclude that heterogenization by ligand tethering has failed.

$$i_p = 0.4463 nFAC_0 \left(\frac{nFvD_0}{RT}\right)^{\frac{1}{2}} \qquad \textbf{Eqn. 1.8}$$

A direct method to study deposition *in operando* is the electrochemical quartz crystal microbalance (EQCM). This technique can monitor the weight changes of the electrode during the measurement. In the ideal case, features of the cyclic voltammogram can be directly linked to electrodeposition, deposit stripping, or the absence of these phenomena and thus direct evidence for the homogeneity of a molecular complex under electrochemical conditions.[86, 122, 128, 138, 160] This technique is based on the vibration of a quartz crystal on which the electrode surface resides. Key to EQCM is the Sauerbrey equation (Equation 1.9).[161]

$$\Delta f = -\frac{2f_0{}^2}{A\sqrt{\rho_q \mu_q}} \Delta m \qquad\qquad \textbf{Eqn. 1.9}$$

Here, the frequency change Δf of the quartz crystal is measured and can be linked to the mass change of the electrode Δm (g/cm²) by the surface area of the crystal (A, cm²), the nominal frequency resonant frequency of the crystal (f_0, 6 MHz for the setup used), the density of quartz (ρ_q, g/cm³), and the shear modulus of quartz (μ_q, g/cm s²). In practice, $\frac{2f_0{}^2}{A\sqrt{\rho_q \mu_q}}$ can be replaced by a sensitivity coefficient that can be experimentally determined with a known electrochemical deposition process such as Pb deposition.[128, 162] Of note, a relative negative frequency change with respect to the pre-experimental oscillation frequency corresponds to a mass increase.

Importantly, Equation 1.9 was originally derived for crystals that are in contact with air. For liquid interfaces, the density and viscosity of the liquid affect the oscillation frequency.[163] Under catalytic conditions, where substrates are consumed at a fast pace and possibly gaseous products are formed, the frequency can change without any actual deposit forming or stripping by, for example, changes in hydrophobicity of the electrode surface or the viscosity of the electrolyte.[164] Moreover, small frequency changes can relate to catalyst adsorption/desorption rather than electrodeposition and catalyst degradation. For these reasons, results of EQCM data are best combined with *ex-situ* spectroscopic surface studies. Several spectroscopic techniques are available that can detect the size of the deposit (tunneling or scanning electron microscopy), soluble colloidal particles (dynamic light scattering), and the elemental composition of the electrode surface (various X-ray techniques such as X-ray photoelectron microscopy, energy-dispersive X-ray spectrometry, X-ray absorption spectroscopy).[97-99] These techniques complement

each other and provide a powerful tool as is demonstrated in Chapters 2 and 3. EQCM is a quick technique for a first *in operando* check of electrodeposition and more informative than the above-mentioned simple rinse test and scan rate dependence studies. Determination of the homogeneity and the nature of the active species is very important to avoid incorrect conclusions and these studies should be done with several techniques instead of relying on just one.

1.4   Scope of thesis

The brief review of molecular catalysts in electrocatalysis shows that structure–activity relationships can be found within electrocatalysis by molecular complexes. On the other hand, decomposition of these molecular catalysts is a significant issue in electrocatalytic studies and should always be kept in mind when studying new catalysts. Chapters 2 and 3 discuss such electrochemical decomposition studies for several iridium complexes for water oxidation and a copper based oxygen reduction catalyst, respectively. Chapters 4 and 5 discuss molecular copper complexes for which the active species is the complex itself. Here, structural adjustments such as linking active sites (Chapter 4) and placing electron withdrawing substituents (Chapter 5) are shown to directly affect catalytic rates and selectivity.

In Chapter 2, the electrochemical study of several known molecular iridium complexes for OER is elaborated. Structure–activity relationships that were previously obtained under sacrificial reagent conditions did not prevail. By using a combination of spectroscopic techniques such as XPS, UV-vis and NMR, and electrochemical techniques such as EQCM we have been able to show that these complexes suffer from ligand oxidation, such as Cp* degradation, and form catalytically active deposits on the electrode. Nevertheless, small, ligand-induced differences in activity were observed and, combined with XPS characterization, led to the suggestion that small IrO_x clusters with incorporated ligand residues were responsible for the catalytic activity.

In Chapter 3, it is shown that a triazole based copper complex, previously regarded as the benchmark for O_2 reduction for molecular copper complexes, disintegrates to form a metallic copper layer under electrochemical conditions. This result was obtained by simply mixing the salt and ligand with a carbon support (the previously reported procedure), as well as for an *in situ* generated complex. Again, a combination of spectroscopic techniques (EPR, SQUID, UV-vis, XPS) and EQCM was employed to identify the copper deposition as the active species. In addition, we

were able to show that the triazole ligand still influences the deposit as it prevents this metallic layer from being oxidatively stripped close to the onset of O_2 reduction.

In Chapter 4, a molecular copper complex, consisting of two fused mononuclear copper complexes through a covalent bond, is reported to drastically change the O_2 reduction selectivity to H_2O_2 instead of H_2O. Furthermore, high Faradaic efficiencies for the formation of H_2O_2 were obtained over prolonged measurements. For the first time, elaborate bulk electrolysis experiments for H_2O_2 production with a molecular complex have been performed for which factors that negatively affect catalyst stability were identified. The experimental design was optimized by, for instance, applying Cu^0 stripping intervals, to directly improve the Faradaic efficiency.

In the last experimental chapter, Chapter 5, substituted copper trispyridyl complexes are discussed. The effect of electron donating or withdrawing substituents on the electrochemical O_2 and H_2O_2 reduction was investigated. Remarkably, the onset potential of O_2 reduction was not affected leading to a new insight into the observed O_2 to H_2O_2 reduction mechanism that was taking place on the time scale of the experiment. On the other hand, we found that electron withdrawing substituents substantially improved both the onset potential and rate for H_2O_2 reduction.

Overall, this thesis focusses on ligand effects in electrocatalysis by molecular (pre)catalysts and proper characterization of the active species. In all cases, the ligand plays a role in catalytic activity of the complex, its decomposition, and/or in the catalytic activity of the deposited active species.

1.5   References

1.   IPCC, *Climate Change 2013: The Physical Science Basis. Contribution of Working Group I to the Fifth Assessment Report of the Intergovernmental Panel on Climate Change*. Cambridge University Press: Cambridge, United Kingdom and New York, NY, USA, 2013; p 1535.
2.   Cano, Z. P.; Banham, D.; Ye, S.; Hintennach, A.; Lu, J.; Fowler, M.; Chen, Z., *Nat. Energy* **2018**, *3*, 279–289.
3.   Paets van Troostwyk, A.; Deiman, J. R., *Obser phys hist na* **1789**, *35*, 369–378.
4.   Bratsch, S. G., *J. Phys. Chem. Ref. Data* **1989**, *18*, 1–21.
5.   Dau, H.; Limberg, C.; Reier, T.; Risch, M.; Roggan, S.; Strasser, P., *ChemCatChem* **2010**, *2*, 724–761.
6.   Carmo, M.; Fritz, D. L.; Mergel, J.; Stolten, D., *Int. J. Hydrogen Energy* **2013**, *38*, 4901–4934.
7.   Hans Wedepohl, K., *Geochim. Cosmochim. Acta* **1995**, *59*, 1217–1232.
8.   Parry, S. J., *Chem. Geol.* **1984**, *43*, 115–125.
9.   Gasteiger, H. A.; Kocha, S. S.; Sompalli, B.; Wagner, F. T., *Appl. Catal., B* **2005**, *56*, 9–35.
10. Gewirth, A. A.; Thorum, M. S., *Inorg. Chem.* **2010**, *49*, 3557–3566.
11. Koper, M. T. M., Catalysis of Redox Reactions. In *Comprehensive Inorganic Chemistry II (Second Edition)*, Reedijk, J.; Poeppelmeier, K., Eds. Elsevier: Amsterdam, 2013; Vol. 8, pp 459–474.
12. Abild-Pedersen, F.; Greeley, J.; Studt, F.; Rossmeisl, J.; Munter, T. R.; Moses, P. G.; Skúlason, E.; Bligaard, T.; Nørskov, J. K., *Phys. Rev. Lett.* **2007**, *99*, 016105.
13. Orfanidi, A.; Madkikar, P.; El-Sayed, H. A.; Harzer, G. S.; Kratky, T.; Gasteiger, H. A., *J. Electrochem. Soc.* **2017**, *164*, F418–F426.

14. Gröger, O.; Gasteiger, H. A.; Suchsland, J.-P., *J. Electrochem. Soc.* **2015,** *162*, A2605–A2622.
15. Kongkanand, A.; Mathias, M. F., *J. Phys. Chem. Lett.* **2016,** *7*, 1127–1137.
16. Goor, G., *Catalytic Oxidations with Hydrogen Peroxide as Oxidant*. Kluwer Academic Publishers: The Netherlands, 1992.
17. Legrini, O.; Oliveros, E.; Braun, A. M., *Chem. Rev.* **1993,** *93*, 671–698.
18. Metcalf & Eddy Inc.; Tchobangolous, G., *Wastewater Engineering: Treatment and Resource Recovery*. 5th edition ed.; Mcgraw-Hill Education: 2014.
19. Hage, R.; Lienke, A., *Angew. Chem. Int. Ed.* **2006,** *45*, 206–222.
20. Süss, H. U., Bleaching. In *Ullmann's Encyclopedia of Industrial Chemistry*, 2012.
21. Campos-Martin, J. M.; Blanco-Brieva, G.; Fierro, J. L. G., *Angew. Chem. Int. Ed.* **2006,** *45*, 6962–6984.
22. Eul, W.; Moeller, A.; Steiner, N., Hydrogen Peroxide. In *Kirk-Othmer Encyclopedia of Chemical Technology* [Online] John Wiley & Sons, Inc.: 2000. http://dx.doi.org/10.1002/0471238961.0825041808051919.a01.pub2.
23. Siahrostami, S.; Verdaguer-Casadevall, A.; Karamad, M.; Deiana, D.; Malacrida, P.; Wickman, B.; Escudero-Escribano, M.; Paoli, E. A.; Frydendal, R.; Hansen, T. W.; Chorkendorff, I.; Stephens, I. E. L.; Rossmeisl, J., *Nat. Mater.* **2013,** *12*, 1137–1143.
24. Verdaguer-Casadevall, A.; Deiana, D.; Karamad, M.; Siahrostami, S.; Malacrida, P.; Hansen, T. W.; Rossmeisl, J.; Chorkendorff, I.; Stephens, I. E. L., *Nano Lett.* **2014,** *14*, 1603–1608.
25. Jirkovský, J. S.; Panas, I.; Ahlberg, E.; Halasa, M.; Romani, S.; Schiffrin, D. J., *J. Am. Chem. Soc.* **2011,** *133*, 19432–19441.
26. Jiang, Y.; Ni, P.; Chen, C.; Lu, Y.; Yang, P.; Kong, B.; Fisher, A.; Wang, X., *Adv. Energy Mater.* **2018,** *8*, 1801909.
27. Song, C.; Zhang, J., Electrocatalytic Oxygen Reduction Reaction. In *PEM Fuel Cell Electrocatalysts and Catalyst Layers: Fundamentals and Applications*, Zhang, J., Ed. Springer London: London, 2008; pp 89–134.
28. Chen, S.; Chen, Z.; Siahrostami, S.; Kim, T. R.; Nordlund, D.; Sokaras, D.; Nowak, S.; To, J. W. F.; Higgins, D.; Sinclair, R.; Nørskov, J. K.; Jaramillo, T. F.; Bao, Z., *ACS Sustainable Chem. Eng.* **2018,** *6*, 311–317.
29. Liu, Y.; Quan, X.; Fan, X.; Wang, H.; Chen, S., *Angew. Chem. Int. Ed.* **2015,** *54*, 6837–6841.
30. Kim, H. W.; Ross, M. B.; Kornienko, N.; Zhang, L.; Guo, J.; Yang, P.; McCloskey, B. D., *Nat. Catal.* **2018,** *1*, 282–290.
31. Lu, Z.; Chen, G.; Siahrostami, S.; Chen, Z.; Liu, K.; Xie, J.; Liao, L.; Wu, T.; Lin, D.; Liu, Y.; Jaramillo, T. F.; Nørskov, J. K.; Cui, Y., *Nat. Catal.* **2018,** *1*, 156–162.
32. Iglesias, D.; Giuliani, A.; Melchionna, M.; Marchesan, S.; Criado, A.; Nasi, L.; Bevilacqua, M.; Tavagnacco, C.; Vizza, F.; Prato, M.; Fornasiero, P., *Chem* **2018,** *4*, 106–123.
33. Chen, S.; Chen, Z.; Siahrostami, S.; Higgins, D.; Nordlund, D.; Sokaras, D.; Kim, T. R.; Liu, Y.; Yan, X.; Nilsson, E.; Sinclair, R.; Nørskov, J. K.; Jaramillo, T. F.; Bao, Z., *J. Am. Chem. Soc.* **2018,** *140*, 7851–7859.
34. Han, L.; Sun, Y.; Li, S.; Cheng, C.; Halbig, C. E.; Feicht, P.; Hübner, J. L.; Strasser, P.; Eigler, S., *ACS Catal.* **2019,** *9*, 1283–1288.
35. Fellinger, T.-P.; Hasché, F.; Strasser, P.; Antonietti, M., *J. Am. Chem. Soc.* **2012,** *134*, 4072–4075.
36. Costentin, C.; Dridi, H.; Savéant, J.-M., *J. Am. Chem. Soc.* **2015,** *137*, 13535–13544.
37. Chan, R. J. H.; Su, Y. O.; Kuwana, T., *Inorg. Chem.* **1985,** *24*, 3777–3784.
38. Blakemore, J. D.; Crabtree, R. H.; Brudvig, G. W., *Chem. Rev.* **2015,** *115*, 12974–13005.
39. Singh, A.; Spiccia, L., *Coord. Chem. Rev.* **2013,** *257*, 2607–2622.
40. Limburg, B.; Bouwman, E.; Bonnet, S., *Coord. Chem. Rev.* **2012,** *256*, 1451–1467.
41. Pegis, M. L.; Wise, C. F.; Martin, D. J.; Mayer, J. M., *Chem. Rev.* **2018,** *118*, 2340–2391.
42. Anand, M.; Nørskov, J. K., *ACS Catal.* **2020,** *10*, 336–345.
43. Solomon, E. I.; Sundaram, U. M.; Machonkin, T. E., *Chem. Rev.* **1996,** *96*, 2563–2606.
44. Soukharev, V.; Mano, N.; Heller, A., *J. Am. Chem. Soc.* **2004,** *126*, 8368–8369.
45. Mano, N.; Soukharev, V.; Heller, A., *J. Phys. Chem. B* **2006,** *110*, 11180–11187.
46. Blanford, C. F.; Heath, R. S.; Armstrong, F. A., *Chem. Commun.* **2007,** 1710–1712.
47. Pita, M.; Mate, D. M.; Gonzalez-Perez, D.; Shleev, S.; Fernandez, V. M.; Alcalde, M.; De Lacey, A. L., *J. Am. Chem. Soc.* **2014,** *136*, 5892–5895.
48. Thorum, M. S.; Anderson, C. A.; Hatch, J. J.; Campbell, A. S.; Marshall, N. M.; Zimmerman, S. C.; Lu, Y.; Gewirth, A. A., *J. Phys. Chem. Lett.* **2010,** *1*, 2251–2254.
49. Cracknell, J. A.; Vincent, K. A.; Armstrong, F. A., *Chem. Rev.* **2008,** *108*, 2439–2461.
50. Calabrese Barton, S.; Gallaway, J.; Atanassov, P., *Chem. Rev.* **2004,** *104*, 4867–4886.
51. Davis, F.; Higson, S. P. J., *Biosens. Bioelectron.* **2007,** *22*, 1224–1235.

36

52. Solomon, E. I.; Augustine, A. J.; Yoon, J., *Dalton Trans.* **2008**, 3921–32.
53. Wasak, A.; Drozd, R.; Jankowiak, D.; Rakoczy, R., *Scientific Reports* **2019,** *9*, 3707.
54. Bullen, R. A.; Arnot, T. C.; Lakeman, J. B.; Walsh, F. C., *Biosens. Bioelectron.* **2006,** *21*, 2015–2045.
55. Thorseth, M. A.; Tornow, C. E.; Tse, E. C. M.; Gewirth, A. A., *Coord. Chem. Rev.* **2013,** *257*, 130–139.
56. Rulíšek, L.; Ryde, U., *Coord. Chem. Rev.* **2013,** *257*, 445–458.
57. Mirica, L. M.; Ottenwaelder, X.; Stack, T. D. P., *Chem. Rev.* **2004,** *104*, 1013–1046.
58. Lewis, E. A.; Tolman, W. B., *Chem. Rev.* **2004,** *104*, 1047–1076.
59. Haack, P.; Limberg, C., *Angew. Chem. Int. Ed.* **2014,** *53*, 4282–4293.
60. Serrano-Plana, J.; Garcia-Bosch, I.; Company, A.; Costas, M., *Acc. Chem. Res.* **2015,** *48*, 2397–2406.
61. Hong, S.; Lee, Y.-M.; Ray, K.; Nam, W., *Coord. Chem. Rev.* **2017,** *334*, 25–42.
62. Solomon, E. I.; Ginsbach, J. W.; Heppner, D. E.; Kieber-Emmons, M. T.; Kjaergaard, C. H.; Smeets, P. J.; Tian, L.; Woertink, J. S., *Faraday Discuss.* **2011,** *148*, 11–39.
63. Suga, M.; Akita, F.; Hirata, K.; Ueno, G.; Murakami, H.; Nakajima, Y.; Shimizu, T.; Yamashita, K.; Yamamoto, M.; Ago, H.; Shen, J.-R., *Nature* **2015,** *517*, 99–103.
64. Limburg, J.; Vrettos, J. S.; Liable-Sands, L. M.; Rheingold, A. L.; Crabtree, R. H.; Brudvig, G. W., *Science* **1999,** *283*, 1524–1527.
65. Collomb, M.-N.; Deronzier, A., *Eur. J. Inorg. Chem.* **2009,** *2009*, 2025–2046.
66. Baffert, C.; Romain, S.; Richardot, A.; Leprêtre, J.-C.; Lefebvre, B.; Deronzier, A.; Collomb, M.-N., *J. Am. Chem. Soc.* **2005,** *127*, 13694–13704.
67. Brimblecombe, R.; Bond, A. M.; Dismukes, G. C.; Swiegers, G. F.; Spiccia, L., *Phys. Chem. Chem. Phys.* **2009,** *11*, 6441–6449.
68. Parent, A. R.; Crabtree, R. H.; Brudvig, G. W., *Chem. Soc. Rev.* **2013,** *42*, 2247–2252.
69. Gersten, S. W.; Samuels, G. J.; Meyer, T. J., *J. Am. Chem. Soc.* **1982,** *104*, 4029–4030.
70. Koelewijn, J. M.; Lutz, M.; Dzik, W. I.; Detz, R. J.; Reek, J. N. H., *ACS Catal.* **2016,** *6*, 3418–3427.
71. Gagliardi, C. J.; Vannucci, A. K.; Concepcion, J. J.; Chen, Z.; Meyer, T. J., *Energy Environ. Sci.* **2012,** *5*, 7704–7717.
72. Huynh, M. H. V.; Meyer, T. J., *Chem. Rev.* **2007,** *107*, 5004–5064.
73. Geselowitz, D.; Meyer, T. J., *Inorg. Chem.* **1990,** *29*, 3894–3896.
74. Shaffer, D. W.; Xie, Y.; Concepcion, J. J., *Chem. Soc. Rev.* **2017,** *46*, 6170–6193.
75. Duan, L.; Bozoglian, F.; Mandal, S.; Stewart, B.; Privalov, T.; Llobet, A.; Sun, L., *Nature Chem.* **2012,** *4*, 418–423.
76. Zhang, B.; Sun, L., *Chem. Soc. Rev.* **2019,** *48*, 2216–2264.
77. Duan, L.; Araujo, C. M.; Ahlquist, M. S. G.; Sun, L., *Proc. Natl. Acad. Sci.* **2012,** *109*, 15584–15588.
78. Duan, L.; Wang, L.; Inge, A. K.; Fischer, A.; Zou, X.; Sun, L., *Inorg. Chem.* **2013,** *52*, 7844–7852.
79. Wasylenko, D. J.; Ganesamoorthy, C.; Koivisto, B. D.; Henderson, M. A.; Berlinguette, C. P., *Inorg. Chem.* **2010,** *49*, 2202–2209.
80. Marelius, D. C.; Bhagan, S.; Charboneau, D. J.; Schroeder, K. M.; Kamdar, J. M.; McGettigan, A. R.; Freeman, B. J.; Moore, C. E.; Rheingold, A. L.; Cooksy, A. L.; Smith, D. K.; Paul, J. J.; Papish, E. T.; Grotjahn, D. B., *Eur. J. Inorg. Chem.* **2014,** *2014*, 676–689.
81. Codolà, Z.; Gómez, L.; Kleespies, S. T.; Que Jr, L.; Costas, M.; Lloret-Fillol, J., *Nat. Commun.* **2015,** *6*, 5865.
82. Wasylenko, D. J.; Ganesamoorthy, C.; Henderson, M. A.; Berlinguette, C. P., *Inorg. Chem.* **2011,** *50*, 3662–3672.
83. Pecht, I.; Luz, Z., *J. Am. Chem. Soc.* **1965,** *87*, 4068–4072.
84. Olivares, M.; van der Ham, C. J. M.; Mdluli, V.; Schmidtendorf, M.; Müller-Bunz, H.; Verhoeven, T. W. G. M.; Li, M.; Niemantsverdriet, J. W.; Hetterscheid, D. G. H.; Bernhard, S.; Albrecht, M., *Eur. J. Inorg. Chem.* **2020,** *2020*, 801–812.
85. Menendez Rodriguez, G.; Bucci, A.; Hutchinson, R.; Bellachioma, G.; Zuccaccia, C.; Giovagnoli, S.; Idriss, H.; Macchioni, A., *ACS Energy Lett.* **2017,** *2*, 105–110.
86. van Dijk, B.; Rodriguez, G. M.; Wu, L.; Hofmann, J. P.; Macchioni, A.; Hetterscheid, D. G. H., *ACS Catal.* **2020,** *10*, 4398–4410.
87. Hammett, L. P., *J. Am. Chem. Soc.* **1937,** *59*, 96–103.
88. Hansch, C.; Leo, A.; Taft, R. W., *Chem. Rev.* **1991,** *91*, 165–195.
89. Asahi, M.; Yamazaki, S.-i.; Itoh, S.; Ioroi, T., *Dalton Trans.* **2014,** *43*, 10705–10709.
90. Thorseth, M. A.; Letko, C. S.; Tse, E. C. M.; Rauchfuss, T. B.; Gewirth, A. A., *Inorg. Chem.* **2013,** *52*, 628–634.

1

91.   Zhang, J.; Anson, F. C., *Electrochim. Acta* **1993,** *38*, 2423–2429.
92.   McCrory, C. C. L.; Ottenwaelder, X.; Stack, T. D. P.; Chidsey, C. E. D., *J. Phys. Chem. A* **2007,** *111*, 12641–12650.
93.   D'Souza, F.; Deviprasad, R. G.; Hsieh, Y.-Y., *J. Electroanal. Chem.* **1996,** *411*, 167–171.
94.   D'Souza, F.; Hsieh, Y.-Y.; Deviprasad, G. R., *J. Electroanal. Chem.* **1997,** *426*, 17–21.
95.   Garrido-Barros, P.; Funes-Ardoiz, I.; Drouet, S.; Benet-Buchholz, J.; Maseras, F.; Llobet, A., *J. Am. Chem. Soc.* **2015,** *137*, 6758–6761.
96.   Yamazaki, H.; Igarashi, S.; Nagata, T.; Yagi, M., *Inorg. Chem.* **2012,** *51*, 1530–1539.
97.   Crabtree, R. H., *Chem. Rev.* **2015,** *115*, 127–150.
98.   Artero, V.; Fontecave, M., *Chem. Soc. Rev.* **2013,** *42*, 2338–2356.
99.   Crabtree, R. H., *Chem. Rev.* **2012,** *112*, 1536–1554.
100.   Helm, L.; Merbach, A. E., *Chem. Rev.* **2005,** *105*, 1923–1960.
101.   Blakemore, J. D.; Schley, N. D.; Balcells, D.; Hull, J. F.; Olack, G. W.; Incarvito, C. D.; Eisenstein, O.; Brudvig, G. W.; Crabtree, R. H., *J. Am. Chem. Soc.* **2010,** *132*, 16017–16029.
102.   Sheehan, S. W.; Thomsen, J. M.; Hintermair, U.; Crabtree, R. H.; Brudvig, G. W.; Schmuttenmaer, C. A., *Nat. Commun.* **2015,** *6*, 6469.
103.   Blakemore, J. D.; Schley, N. D.; Olack, G. W.; Incarvito, C. D.; Brudvig, G. W.; Crabtree, R. H., *Chem. Sci.* **2011,** *2*, 94–98.
104.   Savini, A.; Belanzoni, P.; Bellachioma, G.; Zuccaccia, C.; Zuccaccia, D.; Macchioni, A., *Green Chem.* **2011,** *13*, 3360–3374.
105.   Grotjahn, D. B.; Brown, D. B.; Martin, J. K.; Marelius, D. C.; Abadjian, M.-C.; Tran, H. N.; Kalyuzhny, G.; Vecchio, K. S.; Specht, Z. G.; Cortes-Llamas, S. A.; Miranda-Soto, V.; van Niekerk, C.; Moore, C. E.; Rheingold, A. L., *J. Am. Chem. Soc.* **2011,** *133*, 19024–19027.
106.   Zuccaccia, C.; Bellachioma, G.; Bolaño, S.; Rocchigiani, L.; Savini, A.; Macchioni, A., *Eur. J. Inorg. Chem.* **2012,** *2012*, 1462–1468.
107.   Hong, D.; Murakami, M.; Yamada, Y.; Fukuzumi, S., *Energy Environ. Sci.* **2012,** *5*, 5708–5716.
108.   Wang, C.; Wang, J.-L.; Lin, W., *J. Am. Chem. Soc.* **2012,** *134*, 19895–19908.
109.   Hintermair, U.; Sheehan, S. W.; Parent, A. R.; Ess, D. H.; Richens, D. T.; Vaccaro, P. H.; Brudvig, G. W.; Crabtree, R. H., *J. Am. Chem. Soc.* **2013,** *135*, 10837–10851.
110.   Blakemore, J. D.; Mara, M. W.; Kushner-Lenhoff, M. N.; Schley, N. D.; Konezny, S. J.; Rivalta, I.; Negre, C. F. A.; Snoeberger, R. C.; Kokhan, O.; Huang, J.; Stickrath, A.; Tran, L. A.; Parr, M. L.; Chen, L. X.; Tiede, D. M.; Batista, V. S.; Crabtree, R. H.; Brudvig, G. W., *Inorg. Chem.* **2013,** *52*, 1860–1871.
111.   Codolà, Z.; M. S. Cardoso, J.; Royo, B.; Costas, M.; Lloret-Fillol, J., *Chem. - Eur. J.* **2013,** *19*, 7203–7213.
112.   Graeupner, J.; Hintermair, U.; Huang, D. L.; Thomsen, J. M.; Takase, M.; Campos, J.; Hashmi, S. M.; Elimelech, M.; Brudvig, G. W.; Crabtree, R. H., *Organometallics* **2013,** *32*, 5384–5390.
113.   Zuccaccia, C.; Bellachioma, G.; Bortolini, O.; Bucci, A.; Savini, A.; Macchioni, A., *Chem. - Eur. J.* **2014,** *20*, 3446–3456.
114.   Savini, A.; Bucci, A.; Bellachioma, G.; Rocchigiani, L.; Zuccaccia, C.; Llobet, A.; Macchioni, A., *Eur. J. Inorg. Chem.* **2014,** *2014*, 690–697.
115.   Ingram, A. J.; Wolk, A. B.; Flender, C.; Zhang, J.; Johnson, C. J.; Hintermair, U.; Crabtree, R. H.; Johnson, M. A.; Zare, R. N., *Inorg. Chem.* **2014,** *53*, 423–433.
116.   Thomsen, J. M.; Sheehan, S. W.; Hashmi, S. M.; Campos, J.; Hintermair, U.; Crabtree, R. H.; Brudvig, G. W., *J. Am. Chem. Soc.* **2014,** *136*, 13826–13834.
117.   Zhang, T.; deKrafft, K. E.; Wang, J.-L.; Wang, C.; Lin, W., *Eur. J. Inorg. Chem.* **2014,** *2014*, 698–707.
118.   Lewandowska-Andralojc, A.; Polyansky, D. E.; Wang, C.-H.; Wang, W.-H.; Himeda, Y.; Fujita, E., *Phys. Chem. Chem. Phys.* **2014,** *16*, 11976–11987.
119.   Wan, X.; Wang, L.; Dong, C.-L.; Menendez Rodriguez, G.; Huang, Y.-C.; Macchioni, A.; Shen, S., *ACS Energy Lett.* **2018,** *3*, 1613–1619.
120.   Dzik, W. I.; Calvo, S. E.; Reek, J. N. H.; Lutz, M.; Ciriano, M. A.; Tejel, C.; Hetterscheid, D. G. H.; de Bruin, B., *Organometallics* **2011,** *30*, 372–374.
121.   Brewster, T. P.; Blakemore, J. D.; Schley, N. D.; Incarvito, C. D.; Hazari, N.; Brudvig, G. W.; Crabtree, R. H., *Organometallics* **2011,** *30*, 965–973.
122.   Schley, N. D.; Blakemore, J. D.; Subbaiyan, N. K.; Incarvito, C. D.; D'Souza, F.; Crabtree, R. H.; Brudvig, G. W., *J. Am. Chem. Soc.* **2011,** *133*, 10473–10481.
123.   Blakemore, J. D.; Schley, N. D.; Kushner-Lenhoff, M. N.; Winter, A. M.; D'Souza, F.; Crabtree, R. H.; Brudvig, G. W., *Inorg. Chem.* **2012,** *51*, 7749–7763.

124. Hintermair, U.; Hashmi, S. M.; Elimelech, M.; Crabtree, R. H., *J. Am. Chem. Soc.* **2012,** *134*, 9785–9795.
125. Junge, H.; Marquet, N.; Kammer, A.; Denurra, S.; Bauer, M.; Wohlrab, S.; Gärtner, F.; Pohl, M.-M.; Spannenberg, A.; Gladiali, S.; Beller, M., *Chem. - Eur. J.* **2012**, *18*, 12749–12758.
126. Diaz-Morales, O.; Hersbach, T. J. P.; Hetterscheid, D. G. H.; Reek, J. N. H.; Koper, M. T. M., *J. Am. Chem. Soc.* **2014,** *136*, 10432–10439.
127. Hetterscheid, D. G. H.; van der Ham, C. J. M.; Diaz-Morales, O.; Verhoeven, M. W. G. M.; Longo, A.; Banerjee, D.; Niemantsverdriet, J. W.; Reek, J. N. H.; Feiters, M. C., *Phys. Chem. Chem. Phys.* **2016,** *18*, 10931–10940.
128. Abril, P.; del Rı́o, M. P.; Tejel, C.; Verhoeven, T. W. G. M.; Niemantsverdriet, J. W. H.; van der Ham, C. J. M.; Kottrup, K. G.; Hetterscheid, D. G. H., *ACS Catal.* **2016,** *6*, 7872–7875.
129. Corbucci, I.; Ellingwood, K.; Fagiolari, L.; Zuccaccia, C.; Elisei, F.; Gentili, P. L.; Macchioni, A., *Catal. Today* **2017,** *290*, 10–18.
130. Materna, K. L.; Crabtree, R. H.; Brudvig, G. W., *Chem. Soc. Rev.* **2017,** *46*, 6099–6110.
131. Zhang, L.; Cole, J. M., *ACS Appl. Mater. Interfaces* **2015,** *7*, 3427–3455.
132. Love, J. C.; Estroff, L. A.; Kriebel, J. K.; Nuzzo, R. G.; Whitesides, G. M., *Chem. Rev.* **2005,** *105*, 1103–1170.
133. Pinson, J.; Podvorica, F., *Chem. Soc. Rev.* **2005,** *34*, 429–439.
134. Blakemore, J. D.; Gupta, A.; Warren, J. J.; Brunschwig, B. S.; Gray, H. B., *J. Am. Chem. Soc.* **2013,** *135*, 18288–18291.
135. Dogutan, D. K.; McGuire, R.; Nocera, D. G., *J. Am. Chem. Soc.* **2011,** *133*, 9178–9180.
136. Smits, N. W. G.; den Boer, D.; Wu, L.; Hofmann, J. P.; Hetterscheid, D. G. H., *Inorg. Chem.* **2019,** *58*, 13007–13019.
137. Jackson, M. N.; Surendranath, Y., *Acc. Chem. Res.* **2019,** *52*, 3432–3441.
138. van der Ham, C. J. M.; Işık, F.; Verhoeven, T. W. G. M.; Niemantsverdriet, J. W.; Hetterscheid, D. G. H., *Catal. Today* **2017,** *290*, 33–38.
139. Rossi, L. M.; Fiorio, J. L.; Garcia, M. A. S.; Ferraz, C. P., *Dalton Trans.* **2018,** *47*, 5889–5915.
140. Kunz, S., *Top. Catal.* **2016,** *59*, 1671–1685.
141. Chung, Y.-H.; Chung, D. Y.; Jung, N.; Sung, Y.-E., *J. Phys. Chem. Lett.* **2013,** *4*, 1304–1309.
142. Zhou, Z.-Y.; Kang, X.; Song, Y.; Chen, S., *J. Phys. Chem. C* **2012,** *116*, 10592–10598.
143. Elgrishi, N.; Rountree, K. J.; McCarthy, B. D.; Rountree, E. S.; Eisenhart, T. T.; Dempsey, J. L., *J. Chem. Educ.* **2018,** *95*, 197–206.
144. Martin, D. J.; McCarthy, B. D.; Rountree, E. S.; Dempsey, J. L., *Dalton Trans.* **2016,** *45*, 9970–9976.
145. Costentin, C.; Drouet, S.; Robert, M.; Savéant, J.-M., *J. Am. Chem. Soc.* **2012,** *134*, 11235–11242.
146. Rountree, E. S.; McCarthy, B. D.; Eisenhart, T. T.; Dempsey, J. L., *Inorg. Chem.* **2014,** *53*, 9983–10002.
147. Costentin, C.; Savéant, J.-M., *ChemElectroChem* **2014,** *1*, 1226–1236.
148. Costentin, C.; Savéant, J.-M., *J. Am. Chem. Soc.* **2017,** *139*, 8245–8250.
149. Hetterscheid, D. G. H., *Chem. Commun.* **2017,** *53*, 10622–10631.
150. Bullock, R. M.; Appel, A. M.; Helm, M. L., *Chem. Commun.* **2014,** *50*, 3125–3143.
151. Bard, A. J.; Faulkner, L. R., *Electrochemical Methods: Fundamentals and Applications.* Wiley: New York, 2000.
152. Zhou, R.; Zheng, Y.; Jaroniec, M.; Qiao, S.-Z., *ACS Catal.* **2016,** *6*, 4720–4728.
153. Kottrup, K. G.; D'Agostini, S.; van Langevelde, P. H.; Siegler, M. A.; Hetterscheid, D. G. H., *ACS Catal.* **2018,** *8*, 1052–1061.
154. Langerman, M.; Hetterscheid, D. G. H., *Angew. Chem. Int. Ed.* **2019,** *58*, 12974–12978.
155. Li, M.; Takada, K.; Goldsmith, J. I.; Bernhard, S., *Inorg. Chem.* **2016,** *55*, 518-526.
156. Hessels, J.; Yu, F.; Detz, R.; Reek, J., *ChemSusChem* **2020,** *in press*.
157. D'Agostini, S. Mechanistic studies of the water oxidation reaction with molecular iron catalysts. PhD dissertation, Leiden University, Leiden, 2020.
158. Yi, Y.; Weinberg, G.; Prenzel, M.; Greiner, M.; Heumann, S.; Becker, S.; Schlögl, R., *Catal. Today* **2017,** *295*, 32–40.
159. Benck, J. D.; Pinaud, B. A.; Gorlin, Y.; Jaramillo, T. F., *PLoS One* **2014,** *9*, e107942.
160. van Dijk, B.; Hofmann, J. P.; Hetterscheid, D. G. H., *Phys. Chem. Chem. Phys.* **2018,** *20*, 19625–19634.
161. Sauerbrey, G., *Z. Phys.* **1959,** *155*, 206–222.
162. Deakin, M. R.; Melroy, O., *J. Electroanal. Chem. Interfacial Electrochem.* **1988,** *239*, 321-331.
163. Kanazawa, K. K.; Gordon, J. G., *Anal. Chem.* **1985,** *57*, 1770–1771.
164. Buttry, D. A.; Ward, M. D., *Chem. Rev.* **1992,** *92*, 1355–1379.

1

Chapter 2

The influence of the ligand in the iridium mediated electrocatalytic water oxidation

Electrochemical water oxidation is the bottleneck of electrolyzers as even the best catalysts, iridium and ruthenium oxides, have to operate at significant overpotentials. Previously, the position of a hydroxyl on a series of hydroxylpicolinate ligands was found to significantly influence the activity of molecular iridium catalysts in sacrificial oxidant driven water oxidation. In this study, these catalysts were tested under electrochemical conditions and benchmarked to several other known molecular iridium catalysts under the exact same conditions. This allowed us to compare these catalysts directly and observe whether structure–activity relationships would prevail under electrochemical conditions. Using both electrochemical quartz crystal microbalance experiments and X-ray photoelectron spectroscopy, we found that all studied iridium complexes form an iridium deposit on the electrode with binding energies ranging from 62.4 to 62.7 eV for the major Ir $4f_{7/2}$ species. These do not match the binding energies found for the parent complexes which have a broader binding energy range from 61.7 to 62.7 eV and show a clear relationship to the electronegativity induced by the ligands. Moreover, all catalysts performed the electrochemical water oxidation in the same order of magnitude as the maximum currents ranged from 0.2 to 0.6 mA cm^{-2} once more without clear structure–activity relationships. In addition, by employing ^1H NMR spectroscopy we found evidence for Cp* breakdown products such as acetate. Electrodeposited iridium oxide from ligand free $[Ir(OH)_6]^{2-}$ or a colloidal iridium oxide nanoparticles solution produces currents almost 2 orders of magnitude higher with a maximum current of 11 mA cm^{-2}. Also, this deposited material contains, apart from an Ir $4f_{7/2}$ species at 62.4 eV, an Ir species at 63.6 eV which is not observed for any deposit formed by the molecular complexes. Thus, the electrodeposited material of the complexes cannot be directly linked to bulk iridium oxide. Small IrO_x clusters containing a few Ir atoms with partially incorporated ligand residues are the most likely option for the catalytically active electrodeposit. Our results emphasize that structure–activity relationships obtained with sacrificial oxidants do not necessarily translate to electrochemical conditions. Furthermore, other factors, such as electrodeposition and catalyst degradation, play a major role in the electrochemically driven water oxidation and should thus be considered when optimizing molecular catalysts.

2.1   Introduction

Electrolysis of water has been put forward as an interesting method for the storage of renewable energy, thereby countering intermittency problems of, for instance, sunlight and wind energy. Polymer electrolyte membrane (PEM) electrolyzers can achieve high H_2 production via proton reduction in water. Nevertheless, the efficiency of electrolysis should still massively be improved, considering that substantial overpotentials and very high loadings of precious metals are required. Specifically, the electrochemical water oxidation reaction is the main bottleneck of electrolyzers. A strategy to potentially improve the water oxidation reaction is the use of molecular iridium and ruthenium (pre-) catalysts.[1-11] First of all, the ligand system around the active metal center can be altered to enhance activity and lower the overpotential. For example, the water oxidation overpotential of ruthenium based molecular catalysts has improved significantly over the years by various ligand–alterations.[11] In detail, the use of an anionic carboxylate containing backbone was found to be the key to substantially lower the overpotential and increase the turnover frequency.[12] Second, by using highly active molecular complexes significantly lower catalyst loadings can be achieved. Conventional heterogeneous catalysts that consist of nanoparticles have inaccessible metal atoms that are not directly involved in catalysis. Ideally, all these metal sites would be exposed to the electrolyte solution where catalysis occurs, for example by incorporating iridium in an inert support.[13] In this context, the active molecular iridium catalyst $[Ir(pyalc)(H_2O)_2(\mu\text{-}O)]_2^{2+}$ (pyalc = 2-(2'pyridyl)-2-propanolate) has been heterogenized on a metal oxide support previously by the groups of Sheehan *et al.*[14] That way, 90% of the iridium in the formed monolayer on the surface was involved in water oxidation, producing 0.5 mA cm^{-2} current densities at an overpotential <160 mV. Given that organic ligands are still coordinated to the iridium site, it is likely that modifications of the pyalc ligand could further optimize the catalytic performance.

Since the first report of a molecular iridium water oxidation catalyst by Bernhard and co-workers[15], many other iridium complexes with structural adjustments have been investigated to improve the water oxidation activity.[16-30] Nevertheless, general structure–activity relationships for optimizing these catalysts have not been established yet for several reasons. First of all, most of the water oxidation performance of molecular iridium catalysts was explored with sacrificial oxidants such as ceric ammonium nitrate (CAN) or $NaIO_4$ (periodate), and the structure/activity relationship was found to be strongly affected by the nature of the

sacrificial oxidant.[31, 32] Only a few studies focused on the electrochemical performance of complexes, which is closer to electrolysis operating conditions. In addition, the activity of molecular iridium complexes has been studied in a broad range of experimental conditions such as pH, buffer, or electrolyte. Moreover, the stability and homogeneous nature of molecular iridium catalysts has been under debate. As it happens, a number of studies report the observation of ligand breakdown products or even the presence of iridium oxide (IrO$_x$) nanoparticles during or after catalysis.[29, 30, 33-56] Especially the degradation of the anionic pentamethyl cyclopentadienyl (Cp*) ligand has been widely observed, and its breakdown mechanism has been extensively investigated.[29, 30, 33-47, 57] These degradation routes take place both with sacrificial reagents as well as under electrochemical conditions. Under the latter conditions, electrodeposits may be formed when the parent complexes are subjected to oxidative potentials.[50, 56, 58] Whether an actual deposit is formed is highly dependent on the experimental conditions. For establishing structure–activity relationships, it is desirable to study complexes with the exact same electrochemical conditions and to investigate any possible degradation pathways.

Recently, we showed that the presence and position of a hydroxyl substituent on deprotonated #-hydroxypicolinic acid ligands of a series of [Cp*Ir^{III}(L)(NO$_3$)] complexes (**[H]1** and **[#-OH]1** in Chart 2.1 where L is the picolinate ligand) had a major influence on their respective sacrificial oxidant driven water oxidation activity.[18, 22, 28] pH was an important variable as the complexes had negligible activity at pH 1 but high activity at pH 7. The highest turnover number and frequency were obtained with **[H]1** using NaIO$_4$ as an oxidant. The trend in activity could be explained by the trend in electron-donating character of the ligands of the complexes. In addition, evidence for Cp* degradation was found based on NMR studies. Nevertheless, these NMR studies also indicated that the hydroxypicolinate ligands most likely remained intact and coordinated to the iridium center. In a later study, the activity of these picolinate complexes was benchmarked to several other known iridium complexes (including **2 − 5**, [Ir(OH)$_6$]$^{2-}$ and IrO$_x$·nH$_2$O nanoparticles, having a mean diameter of 2 nm) under the exact same conditions, and the nature of the generated active species was discussed.[27] [Ir(OH)$_6$]$^{2-}$ was found to be significantly more active than all other catalysts, at pH 7 with periodate as an oxidant. On the basis of that and other results, it was concluded that the active species has to be molecular, containing a few iridium atoms, though its exact nature was not completely disclosed, in particular as far as the possibility that it contains a residual Cp*-fragment and/or other ligands derived from the precursors.

In this study, we explored complexes **1 – 5** (Chart 2.1) electrochemically to see whether structurally induced electronic differences of the ligand would translate into different electrochemical water oxidation activity as well. Furthermore, spectroscopic NMR and XPS studies were used to study the active species in more detail. In contrast to the studies with sacrificial oxidants, we found that previously determined structure–activity relationships do not prevail under electrochemical conditions. In fact, only marginal differences in activity between the complexes were found.
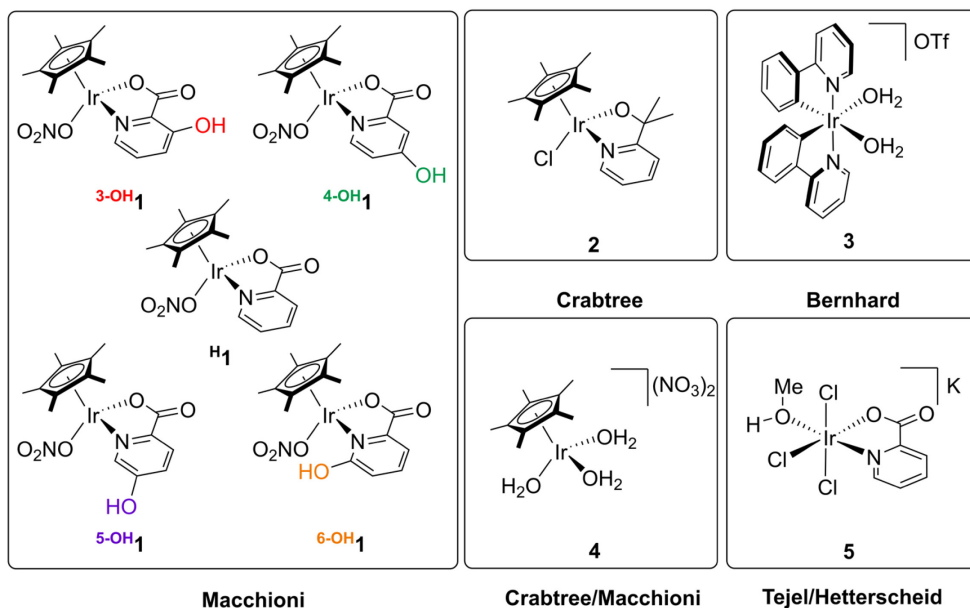

Chart 2.1. Structure and nomenclature of iridium complexes of (hydroxy)picolinate (**1**) and other benchmark (**2 – 5**) complexes herein discussed.

2.2   Results and discussion

2.2.1   Electrocatalytic O_2 evolution

Cyclic voltammetry (CV) is the first tool used for studying the electrochemical response of a homogeneous catalyst wherein the potential of the work electrode is cycled and plotted versus the current response. For this purpose, a glassy carbon (GC) working electrode and 1 mM solutions of catalyst in a 0.1 M phosphate buffer of pH 7 with 0.5 M ionic strength by adding $NaClO_4$ were used. The more electron rich complexes $^{4-OH}$**1** and $^{6-OH}$**1** produce an oxidizing current starting at 1.55 V

versus the reversible hydrogen electrode (RHE) when the potential is initially increased from 0.8 V to 2.1 V (Figure A.1). $^H1$, $^{3-OH}1$ and $^{5-OH}1$ start to produce an oxidizing current from a 100 mV higher potential (1.65 V) onward. Interestingly, no redox waves are observed for the Ir^{III}/Ir^{IV} redox couple, which is in line with other iridium complexes studied electrochemically at this pH.[16, 45, 49, 50, 55, 59] Instead, the observed irreversible oxidative wave is most likely catalytic in nature. To prove that water is oxidized to O_2, online electrochemical mass spectrometry (OLEMS) was employed.[60] This technique provides means to measure the types of gases that are evolved at the electrode by the use of a porous Teflon tip closely approaching to the surface of the electrode. This way, the mass traces of gases can be detected as a function of applied potential. Specifically, O_2 and CO_2 with m/z traces of 32 and 44 respectively were of interest. $^{6-OH}1$ and $^H1$ were tested with OLEMS by performing chronoamperometry (CA) at a static potential of 1.8 V (Figure 2.1). All catalysts produce significant currents at this potential (Figure A.1). $^{6-OH}1$ and $^H1$ start to produce oxygen immediately once the potential is switched to 1.8 V. For both complexes, the produced current at 1.8 V is not static and increases over time (Figure 2.1 A and B). The O_2 mass trace follows this trend, which indicates that an activation process takes place over time. Simultaneously, there is CO_2 evolution as well. CO_2 is
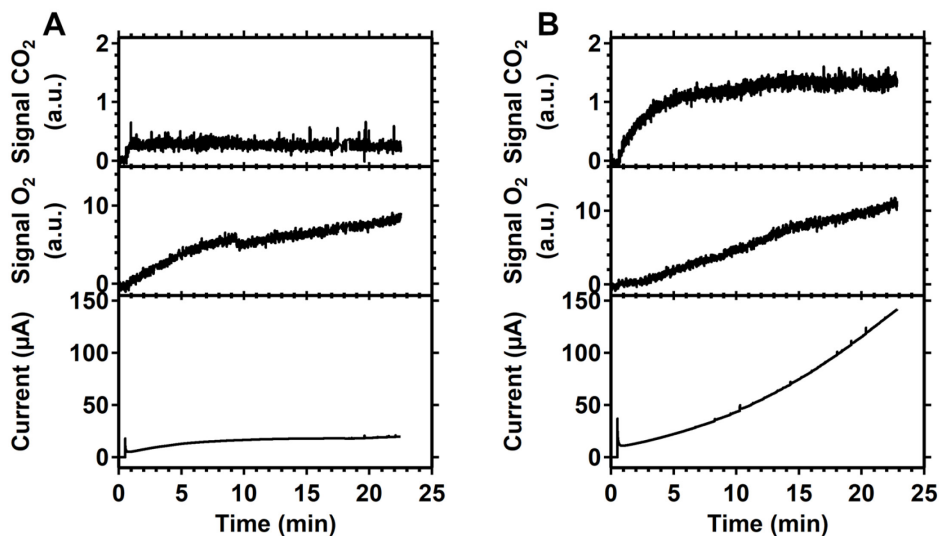

Figure 2.1. Online electrochemical mass spectrometry measurements of $^{6-OH}1$ (A) and $^H1$ (B) in 0.1 M $HClO_4$ (pH 1) with an ionic strength of 0.5 M by adding $NaClO_4$. Chronoamperometry was performed by initially applying 0.8 V versus RHE and subsequently 1.8 V. The resulting amperogram is plotted in the bottom panel. Simultaneously recorded mass traces of m/z 32 (O_2) and m/z 44 (CO_2) are depicted in the top panels. A large surface area Au working electrode (0.14 cm²) was used.

indicative of (oxidative) catalyst degradation. To be sure that CO_2 is not originating from the oxidation of a carbon electrode work electrode, a large surface area gold electrode (0.14 cm²) was used as a working electrode (WE) for this experiment. It has been shown that gold itself will not oxidize water to O_2 below 2.0 V at pH 1.[61] Thus, the electrochemically evolved O_2 is produced by the complex and/or its degradation products.

2.2.2 Deposition of material on the electrode

Electrochemically studied iridium complexes can deposit material on the electrode during catalysis.[21, 33, 45, 50, 51, 56] Often, a simple "electrode-rinse-test" is used to have a quick indication whether a deposit is formed on the electrode. After measuring the complex of interest, the working electrode is rinsed and tested in a catalyst-free electrolyte. Deviations in this CV with respect to the CV of a freshly polished electrode indicate that material has been (electro)deposited on the electrode. Indeed, for all complexes the CV deviated after rinsing the electrode. Specifically, the double layer and maximum current increased significantly for the GC electrodes (for example, see Figure A.2 where the CVs for **6−OH1** are displayed), suggesting that there is electrodeposit in all cases. The produced CVs do not change over the course of 5 scans indicating negligible desorption of the deposited layer. Of note, an increased double layer and maximum current could also originate from electrode degradation as carbon electrodes do corrode at high potentials.[62] The formation of a deposit can be studied in more detail by employing electrochemical quartz crystal microbalance (EQCM) experiments.[50, 58, 63, 64] For this purpose, a quartz crystal with a deposited gold layer is used as working electrode. The quartz crystal is oscillated during the course of the experiment. The frequency of this oscillation is dependent on the mass of the electrode. Specifically, a decrease in this frequency corresponds to an increase of mass. Any potential-related mass changes of the electrode can thus be revealed while monitoring the relative frequency when cyclic voltammetry is performed. The complexes **6−OH1** and **H1** were studied with EQCM while performing cyclic voltammetry in a potential window from 1.3 to 1.9 V (Figure 2.2). For both complexes, the oscillation frequency decreases while the anodic current increases at potentials above 1.55 for **6−OH1** and 1.65 V for **H1**, which is within the catalytic potential window. Thus, the mass of the electrode increases during the water oxidation reaction indicating that a deposit is steadily formed on the electrode. In addition, **H1** shows less deposit than **6−OH1** over the course of 10 scans. The Δ frequency reaches −130 Hz for **H1** as opposed to −320 Hz for **6−OH1** with the lower value being indicative of more deposit. Later, we show that all complexes

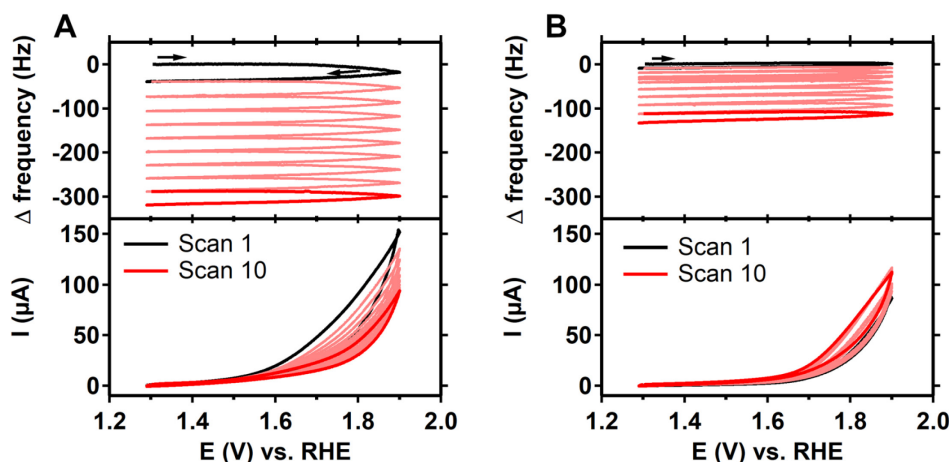**Figure 2.2.** Electrochemical Quartz Crystal Microbalance measurements of $^{6-OH}\mathbf{1}$ (A) and $^{H}\mathbf{1}$ (B) in 0.1 M phosphate buffer at pH 7. The work electrode is a Au working electrode (0.35 cm²) that was oxidized by performing 10 CV scans in a 1.3 to 2.0 V potential window in a catalyst-free electrolyte prior to the measurement. The CVs, taken at a scan rate of 0.1 V/s, are displayed in the bottom panels. Simultaneously, the relative frequency of the oscillating quartz crystal of the work electrode was monitored during the potential cycling in the presence of the catalyst (top panels).

electrodeposit iridium species by analyzing the electrodes with surface-sensitive X-ray photoelectron spectroscopy (XPS).

2.2.3   Spectroscopic studies of electrolyte after bulk electrolysis

The electrodeposition of material might be triggered by complex degradation. Several iridium complexes have been reported to (partially) disintegrate under the oxidative conditions under which water oxidation is performed.[29, 30, 33-56] Degradation products, such as (colloidal) iridium oxide (IrOₓ), have been observed in studies using sacrificial reagents as well as electrochemical studies. The presence of IrO_x in a solution could be indicated by a distinctive absorption at 580 nm in the UV-vis spectrum.[65, 66] Of note, an absorption at 580 nm is not exclusively related to IrO_x but could originate from other iridium species as well.[52] In addition, Cp* in the coordination sphere of iridium in [Cp*IrL$_n$] type complexes is not stable under oxidative conditions.[29, 30, 33-47, 57] The exact mechanism of Cp* degradation was previously elucidated by Macchioni and co-workers for three [Cp*IrL$_n$] type complexes.[30] Several Ir-containing intermediates could be characterized and it was determined that the oxidative degradation of Cp* eventually leads to acetic, formic, and glycolic acids. To study whether any of these breakdown products are observed, we set out a 6-hour bulk electrolysis experiment to allow for nuclear magnetic

resonance (NMR) and UV-vis spectroscopy studies of the electrolyte after catalysis. Bulk electrolysis affects the entire electrolyte as opposed to a regular electrochemical setup where merely a small diffusion layer close to the working electrode is reached. To perform bulk electrolysis, a large, custom-made and preanodized glassy carbon work electrode (0.79 cm²) was used as a working electrode to be able to generate as much current as possible in a 6 hour window of the experiment. Preanodization of the electrode was performed by applying 2.1 V in catalyst-free electrolyte for 25 minutes. Furthermore, a H−cell was used allowing for separation of the electrolyte exposed to the working and counter electrodes by a proton conductive Nafion membrane. A potential of 1.9 V versus RHE was applied for 6 hours while the electrolyte containing 1 mM of $^{4-OH}$**1** was continuously stirred. Furthermore, D_2O instead of H_2O was used to be able to study the electrolyte with ¹H NMR. After bulk electrolysis, the intact complex $^{4-OH}$**1** was found to be the major compound in the electrolyte according to the NMR studies (Figure A.4). However, the observation of unaffected complex cannot be used as an indication of complex stability as not all material might have been in contact with the electrode during the 6-hour experiment. Nonetheless, acetate and other distinctive breakdown products from Cp* were observed as well. Interestingly, no uncoordinated 4-hydroxypicolinate is observed suggesting that the ligand is still coordinated to the remaining iridium complex after Cp* degradation, which is in line with other reports.[29, 30, 33-47, 57] In fact, the Cp* degradation bears resemblance to the previously reported degradation of **1** when sacrificial oxidants are used.[27, 28] The UV-vis spectrum of the electrolyte after bulk electrolysis has not changed significantly (Figure A.5). Notably, no peak at 580 nm has emerged indicating that no IrO_x nanoparticles are present in the solution. As expected, the CV response of the GC electrode in a catalyst-free electrolyte has significantly changed with respect to its freshly polished state (Figure A.6) due to the deposition of iridium material. The fact that there is no IrO_x in the solution and that 4-hydroxypicolinate can exclusively be assigned to $^{4-OH}$**1** indicates that any species that is the result of the degradation of $^{4-OH}$**1** is either a paramagnetic Ir(IV) species or has settled on the electrode.

2.2.4   Comparative chronoamperometry studies

2.2.4.1   *The picolinate catalysts (1)*

It is difficult to draw conclusions from CV experiments with **1** with respect to the water oxidation reaction because of the simultaneous electrodeposit process. There is a clear negative shift of 0.1 V in the onset of the anodic current induced by the more electron donating complexes $^{6-OH}$**1** and $^{4-OH}$**1**. However, the shift in onset

is not exclusively related to enhanced water oxidation performance, but also to a different amount of electrodeposition. The latter case is illustrated by the unequal amount of material that is electrodeposited by the complexes (Figure 2.2). Also, the material that deposits in one CV scan will affect the next CV scan. Therefore, any apparent difference in the CVs of the complexes (Figure A.1) that seems to be performance related might actually be due to inconsistencies caused by electrodeposition (Figure A.2). Moreover, the different magnitude of the currents measured in CV experiments with **1** (Figure A.1) are actually within the experimental error (Figure A.3). Furthermore, glassy carbon electrodes are oxidized at high potentials.[62] This process is reflected in an amperogram by an initial increase of the current until a maximum is reached (Figure A.7). Subsequently, the current decreases slightly to a stable, plateauing current. This process is faster at higher potentials. The magnitude of GC anodization is similar to the magnitude of the currents generated by the complexes under our conditions (Figure A.7A–D). Also, in some cases we observed that the current could suddenly increase to a higher plateauing level. An example can be found in the amperogram of 3^{-OH}**1** recorded at 2.1 V (Figure A.7D). This artifact could not be reproduced when a fresh solution of 3^{-OH}**1** was measured twice (Figure A.8). Instead, the magnitude of the current differed for both measurements. The undesirable changes in surface structure of the GC electrode during anodic corrosion was found as a source of these phenomena.

We therefore studied the most electron poor (3^{-OH}**1**) and electron rich (4^{-OH}**1**) hydroxypicolinate complexes with an elaborate chronoamperometry study which resulted in reproducible data. Moreover, chronoamperometry can visualize processes such as deactivation or activation over time and allows for a better comparison.[56] Specifically, PEEK encapsulated GC electrodes were used to establish that the same geometrical surface area (0.07 cm^2) is exposed to the electrolyte. Furthermore, the GC electrode was preanodized at 2.1 V for 25 minutes in a complex-free pH 7 phosphate buffer. This preanodization treatment ensures that the GC electrode generates a stable, plateauing current at all relevant potentials in the absence of a catalyst.[62] Next, a 10 minute amperogram was taken of the GC electrode at the desired potential and used for background correction. Finally, a 30-minute amperogram was recorded in the electrolyte containing the complex at the desired potential. This process was repeated for each potential that was measured. In an ideal case, the obtained current under steady state conditions is purely kinetic in nature, thus controlled by the catalytic mechanism of the catalyst. A straight line is expected when the potential is plotted *versus* the log of the current. The slope of this fitted line can subsequently be used to compare differences in activity and

mechanism.[67] In our case, the magnitude of the slope is not only dependent on the kinetics of water oxidation but also on mass-transport limitations of the parent complex to the electrode and the kinetics of electrodeposition. Therefore, obtaining direct mechanistic information about water oxidation remains elusive using this method. To start, the background-corrected current that was generated by $3^{-OH}1$ and $4^{-OH}1$ after 30 minutes of amperometry is plotted versus the potential in Figure 2.3A and 2.3B. Notably, the currents at lower potential (below 1.95 V) can be fitted with a
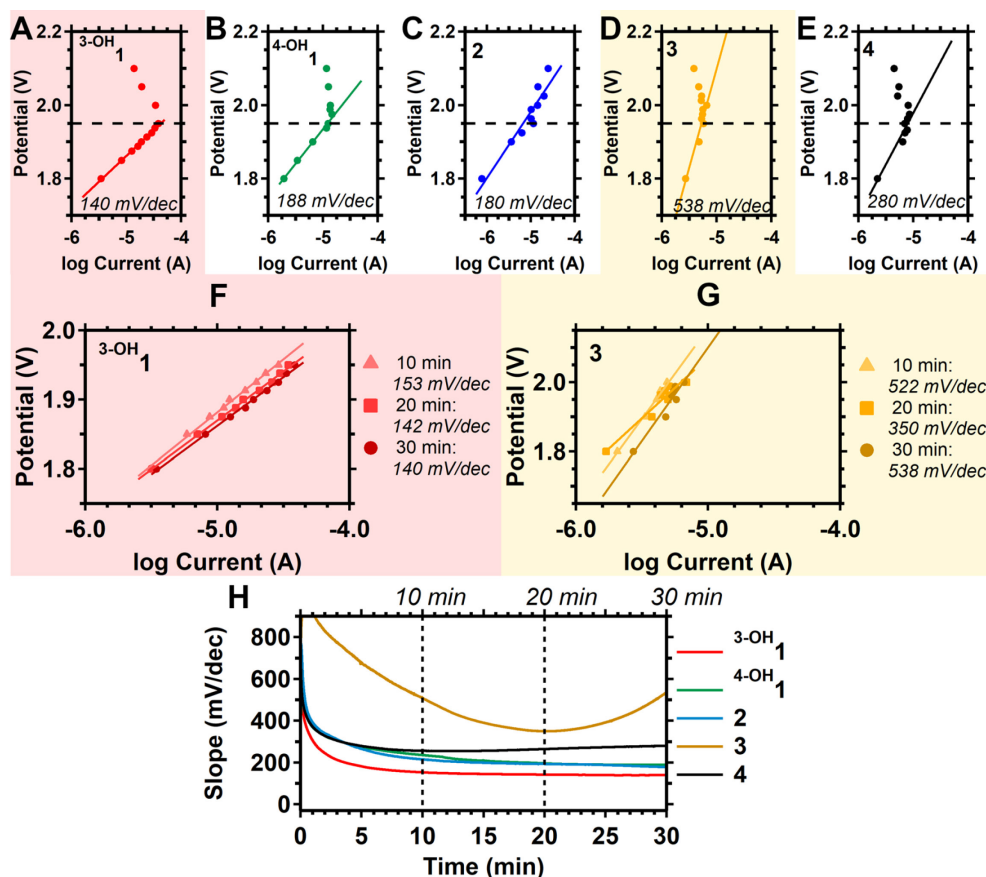
Figure 2.3. The logarithm of the current after 30 minutes of amperometry *versus* the potential for the complexes $3^{-OH}1$ (A), $4^{-OH}1$ (B), **2** (C), **3** (D) and **4** (E). The currents were measured with a GC working electrode that was preanodized by applying a potential of 2.1 V for 25 minutes in a complex-free electrolyte. The current generated by this anodized electrode in the absence of complex was used to normalize the currents generated by the complexes. Linear fits (straight lines) have been applied to the potential window that shows an increase in current with increasing potential. Fits of the current after 10, 20, and 30 minutes are displayed in F ($3^{-OH}1$) and G (**3**). The lines in H represent the slope of this fit of complexes **1 – 4** and its magnitude over time to illustrate the continuous change.

straight line with a positive slope. The currents at higher potential do not follow this trend. The course of the generated currents of the raw amperograms are also potential dependent (Figure A.9). Applying potentials below 1.95 V resulted in generated currents that slowly increase over time. In contrast, the magnitude of the current generally reaches a maximum and decreases subsequently over time at potentials above 1.95 V. The behavior of the current over time might be related to a change in mechanism of the water oxidation reaction, electrodeposition, or a combination thereof. Alternatively, potential dependent aggregation of catalytic particles, thereby reducing the number of active sites, may be an explanation for the kink in the log current versus potential profiles. Second, we found that the slope of the fit is not constant but changes over time. As illustrated in Figure 2.3F for $^{3-OH}\mathbf{1}$, the slope of the fit has a different value after 10, 20 or 30 minutes of chronoamperometry. The continuous change of this fitted slope over time is displayed in Figure 2.3H for the full time scale of the experiment (30 minutes). For both $^{3-OH}\mathbf{1}$ and $^{4-OH}\mathbf{1}$, the magnitude of the slope starts at a high value but decreases over time and reaches a constant value. The slope of $^{3-OH}\mathbf{1}$ decreases more quickly and reaches a lower value (140 mV/dec) as compared to $^{4-OH}\mathbf{1}$ (188 mV/dec). This observed difference might be related to the structural difference of the parent complexes. However, the water oxidation activity of $^{3-OH}\mathbf{1}$ and $^{4-OH}\mathbf{1}$ after 30 minutes is on the same order of magnitude where the highest obtained currents are 0.59 mA cm^{-2} ($^{3-OH}\mathbf{1}$) and 0.30 mA cm^{-2} ($^{4-OH}\mathbf{1}$). This is in contrast to the large difference in activity found in the preceding studies at pH 7 with NaIO$_4$ as a sacrificial oxidant.[28] In that study, turnover frequencies (TOF) up to 300 min^{-1} were found for $^{3-OH}\mathbf{1}$ as opposed to a TOF of around 60 min^{-1} found for $^{4-OH}\mathbf{1}$.

2.2.4.2   *Extension of studies to $\mathbf{2-4}$*

To place the structure–activity relationship of $^{3-OH}\mathbf{1}$ and $^{4-OH}\mathbf{1}$ into a broader perspective, we initially screened the iridium complexes $\mathbf{2-5}$ (Chart 2.1) that have more profound modifications of the ligand system. [Cp*Ir(pyalc)(Cl)] ($\mathbf{2}$)[14, 37, 43, 44, 50] was chosen as the well-known example of a complex that degrades by losing Cp* but forms a homogeneous, dinuclear homogeneous catalyst still bearing its bidentate ligand. $\mathbf{2}$ can be transformed to the active species by either NaIO$_4$ or by electrolysis with gold electrodes above 1.5 V *versus* RHE in Na$_2$SO$_4$ solutions of pH $2-3$. The bidentate pyalc ligand of $\mathbf{2}$ bears structural similarities to the hydroxypicolinate ligands of $\mathbf{1}$. [Ir(ppy)$_2$(H$_2$O)$_2$]OTf ($\mathbf{3}$)[15] was chosen as a benchmark for a homogeneous iridium complex that does not contain Cp* and performs CAN driven water oxidation. [Cp*Ir(H$_2$O)$_3$](NO$_3$)$_2$ ($\mathbf{4}$)[16, 17] has no ligand apart from Cp* and is

known to lead to electrochemical IrO_x deposition at potentials above 1.3 V versus RHE in a KNO_3 solution of pH 3.[33, 50] In addition, $K[Ir(picolinate)(Cl_3)(MeOH)]$ (**5**) is a Cp* lacking complex that electrochemically oxidizes to deposit IrO_x.[56] In that study, the amount of IrO_x deposit was below the detection limit of EQCM, but could be determined with XPS. Water oxidation started with a considerable lag time after the oxidative conversion of **5**. In turn, the lag time was potential dependent: at 2.0 V, O_2 evolution started after 32 seconds, whereas the lag time was 82 seconds at a potential of 1.9 V. Also, the highest activity was found at pH 1, while at pH 7 only negligible activity was observed.[56]

First of all, we screened complexes **1** – **5** by performing chronoamperometry at 1.8, 1.9, 2.0, and 2.1 V under the exact same conditions, specifically at pH 7 in a 0.1 M phosphate buffer. Of note, these conditions are different from the conditions that have been previously reported for complexes **1** – **5**. We found that the water oxidation activity of all complexes is within the same order of magnitude (Figure A.7E–H) under our conditions. Also, there is no clear structure–activity relationship. **5** was excluded from further studies since the activity was marginal similar to the findings of previous studies at this pH.[56] We further subjected **2** – **4** to the elaborate chronoamperometry study as performed for **3**–**OH1** and **4**–**OH1**. The resulting logarithms of current versus potential are displayed in Figure 2.3C to 2.3E. The highest produced current densities of the complexes are close together in a range from 0.2 – 0.6 mA cm^{-2} (**3** – **3**–**OH1**). Similar to **3**–**OH1** and **4OH1**, we found that the fitted slope changes over time. Especially **3** displays large shifts as illustrated in Figure 2.3G and 2.3H. At first sight, the difference between the picolinate series and **2** is rather small. Specifically, the magnitude of the fitted slope for **2** (Figure 2.3C) as well as the progression of the slope over time (Figure 2.3H) are similar to that of **4**–**OH1**. This might be related to the more electron-donating character of both ligands relative to that of **3**–**OH1**. Unlike **3**–**OH1** and **4**–**OH1**, there is no kink in the data above 1.95 V (Figure 2.3C). Instead, the current increases with increasing potential within the full potential window of 1.8 to 2.1 V. In contrast, Cp*-free **3** and IrO_x forming **4** show more profound differences. The fitted slopes are higher (Figures 2.3D and 2.3E) and the progress of the slope over time is different as compared to **1** and **2** (Figures A.3F – A.3H). Specifically, the magnitude of the slope of **4** quickly decreases to a minimum value and subsequently increases slowly. The slope is far higher than that found for IrO_2 nanoparticles,[68] possibly due to the interplay of simultaneous deposition, degradation, activation, and water oxidation under these conditions. The fitted slope of **3** follows the same trend as **4** over time, but the magnitude is higher at all points in time than any of the other catalysts. The large difference displayed by

3 with respect to **1, 2**, and **4** might indicate that the absence of Cp* or the presence of two ligands in the parent complex plays a role. The difference in the progression of the slope of **4** with respect to **1** and **2** over a longer period of time could be caused by the additional presence or absence of a bidentate ligand in combination with Cp* as a ligand, but the differences are less clear. Moreover, the fitted slope that is used here in the analysis is dependent on the kinetic OER, the deposition of catalytic material, and the mass transport of fresh material to the electrode. Therefore, any differences cannot be unambiguously linked to underlying mechanisms based on the structural differences of the parent complexes.

2.2.5   X-ray photoelectron spectroscopy of complexes **1** – **4** and their respective deposit

2.2.5.1   Spectra of parent complexes 1 – 4

The previous experiments strongly suggest the formation of an iridium containing surface-deposit on the electrode that is able to catalyze the water oxidation reaction. Surface-sensitive X-ray photoelectron spectroscopy (XPS) was employed to investigate the nature of these deposits. In addition, XPS can provide information on the electronic environment and any trends therein. The Ir 4f region including both spin–orbit split peaks is displayed in Figure 2.4. For the parent complex **3−OH1**, an iridium species with a binding energy (BE) of 62.3(1) eV was found in the Ir $4f_{7/2}$ spectrum. For **4−OH1**, a species with a lower binding energy of 62.1(1) eV was observed. As expected, the iridium species of **3−OH1** has a slightly higher binding energy as the electron density around the metal ion is lower due to the more electron-withdrawing nature of the picolinate ligand as compared to **4−OH1**. In contrast, the pyridinic ligand of **2** has a more electron donating character with respect to both picolinate ligands. Indeed, an Ir $4f_{7/2}$ species at a lower binding energy of 61.7 eV was found for complex **2** that is in line with a more electron rich metal center. Analogous to **2**, an Ir 4f species at 61.7 eV is found for complex **3**. The identical binding energies indicate that the iridium metal centers are in the same electronic state. Even though Cp* is absent in complex **3**, the two bidentate ligands apparently have a similar electronic character to that of the combined ligand system of **2**. Complex **4** lacks any ligands apart from Cp*. This results in an iridium center that is relatively electron poor with respect to **1** and **2**; an Ir 4f species with a higher binding energy of 62.7 eV is found. For all complexes, species in the N 1s XPS spectrum are observed as well (Figure A.10A). For **3−OH1** and **4−OH1**, two major species can be found at 406.4 eV and 400.2 (**3−OH1**) or 399.7 eV (**4−OH1**). The electronically poor nitrogen of NO_3^- corresponds to the first species, whereas the

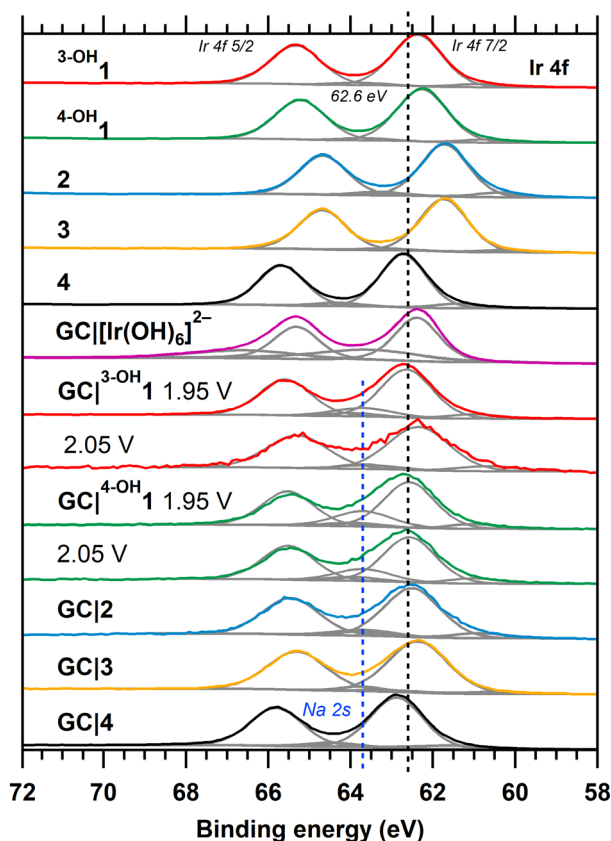**Figure 2.4.** XPS spectra of the Ir 4f region of the compounds 3−OH1 (red), 4−OH1 (green), **2** (blue), **3** (orange), and **4** (black) as well as that of the electrodes subjected to CA in the presence of the complex at 1.95 V for 30 minutes: **GC|3−OH1**, **GC|4−OH1**, **GC|2**, **GC|3**, and **GC|4** or at 2.05 V for **GC|3−OH1** and **GC|4−OH1**. In grey, the fitted species are shown.

pyridinic nitrogen of the picolinate ligand corresponds to the lowest binding energies. Clearly, the electronic effect of the position of the hydroxyl substituent is reflected in the difference in binding energies. Logically, the more electron rich nitrogen of the picolinate ligand of 4−OH1 has a lower binding energy. **2** does not contain NO_3^- but does show a peak for the pyridinic nitrogen at 399.8 eV. The electron donating character of the pyridinic ligand of **2** is mostly due to the isopropyl bridged alcohol that coordinates to the metal center. Thus, the pyridinic nitrogen of **2** has a similar electronic level (399.8 eV) as compared to 4−OH1. This is also the case for **3** where the pyridinic nitrogen is not the most electron donating moiety and has a binding energy of 400.3 eV. The electron donating moiety of the ligand system of **3** is the organometallic Ir−C bond. **4** does not have a pyridinic nitrogen. Instead, the nitrate ions observed at 406.6 eV are close to the 406.4 eV found for 3−OH1 and

4–OH1. Additionally, in all the N 1s spectra of the nitrate containing complexes **3–OH1**, **4–OH1,** and **4**, there is an additional nitrogen species observed at 403.7 eV which we cannot assign at this point. The O 1s spectrum was also recorded for all complexes (Figure A.10B). The different oxygen moieties found in the ligand systems for **1 – 4** cannot be precisely assigned due to overlapping signals in the recorded spectra. For instance, the oxygen of nitrate might be found at binding energies ranging from 531 to 534 eV[69] that fully overlap with the observed O 1s signal. Only for **2**, there is a major species at a lower binding energy of 529.6 eV. This low binding energy indicates an electron-rich oxygen moiety and can be assigned to the metal-coordinated alcohol of the pyridinic ligand of **2**. Overall, the trend of the electronic state of iridium and nitrogen species of complexes **1 – 4** observed in the XPS spectra is in line with the expected trend in structurally induced electronegativity of the ligand.

2.2.5.2   *Spectra of deposited species on GC|1 – GC|4*

In all prolonged chronoamperometry experiments with **1 – 4**, a blue deposition was formed on the GC electrodes. As discussed, EQCM studies for **H1** and **6–OH1** showed that electrodeposition accompanies the electrochemical water oxidation. We used XPS to study the surface of GC electrodes after chronoamperometry was performed in solutions containing **1 – 4**. In detail, these samples are GC electrodes that have been preanodized at 2.1 V and subsequently been used to perform CA at 1.95 V in a solution containing the catalyst. For reference, the XPS spectra of a preanodized GC electrode were recorded as well (Figure A.11). The N 1s regions and O 1s regions showed that this preanodized electrode surface contains nitrogen and oxygen moieties. In fact, the N 1s and O 1s spectra of all investigated preanodized GC electrodes are dominated by these species (Figure A.10). These spectra can thus not be used to find traces of ligand (residues) on the electrodes. XPS analysis of the Ir 4f region of the anodized electrode (Figure A.11) revealed the presence of a Na 2s species with a binding energy of 63.7 eV because the Na 2s and Ir 4f regions overlap. Apparently, the preanodization treatment results in the deposition/entrapment of sodium from the electrolyte on the surface of the GC electrode. This sodium species is present in the spectra of all the electrodes (Figure 2.4). The Na 2s species is only a minor component in the Ir 4f spectrum and thus iridium species can readily be observed and fitted (Figure 2.4). Sample **GC|3–OH1** is a preanodized GC electrode used to perform chronoamperometry in a solution containing **3–OH1** at either 1.95 or 2.05 V. At both potentials, there is a typical iridium doublet signal in the Ir 4f region as well as a sodium species originating from the

preanodization of the GC electrode (Figure 2.4). A second, minor iridium species could be fitted as well. So, there must be a deposit of some sort of iridium species on the electrode. Interestingly, the surface of **GC|4^{-OH}1** contains the same major (62.6 eV) and minor (60.9 eV) iridium species as **GC|3^{-OH}1** in the Ir $4f_{7/2}$ spectrum. Moreover, the applied potential (1.95 or 2.05 V) during chronoamperometry has no influence on the binding energy of these deposited iridium species. Notably, the binding energies of the major and minor iridium species of **GC|3^{-OH}1** and **GC|4^{-OH}1** do not match with the binding energy of iridium in the respective parent complexes **3^{-OH}1** and **4^{-OH}1**. The electrodes used for chronoamperometry at 1.95 V in the presence of complexes **2 – 4** (**GC|2 – GC|4**) show deposited iridium species on the surface as well. The surface of **GC|2** contains a species with a BE of 62.6 eV. This BE is identical to that of the iridium species on **GC|3^{-OH}1** and **GC|4^{-OH}1** but does not match the parent complex **2**. The deposited iridium species on **GC|3** has a slightly lower BE of 62.4 eV, whereas **GC|4** has a deposited species with a higher BE of 62.9 eV. Overall, the difference in BE of the deposited Ir 4f species on the GC electrodes is smaller than the difference in BE of the parent complexes. Thus, the ligand of the parent complex barely influences the electronic state of iridium in the deposit as opposed to its effect on the parent complexes.

2.2.6 Activity and XPS analysis of IrO$_x$ deposited by [Ir(OH)$_6$]$^{2-}$ and IrO$_x$ nanoparticles

2.2.6.1 *Water oxidation activity*

IrO$_x$ nanoparticles are sometimes suggested or observed to be the active water oxidation species. Therefore, we tested the electrochemical water oxidation activity of these nanoparticles. Either as an electrodeposited *in situ* formed layer on the electrode surface or as a colloidal IrO$_x$ solution. [Ir(OH)$_6$]$^{2-}$ is a precursor for the generation of thin nanoparticle films of IrO$_x$ by electrodeposition.[66] An exact pH of 12.1 is required in the preparation of a 2 mM [Ir(OH)$_6$]$^{2-}$ solution as otherwise a deep blue, colloidal solution of IrO$_x$ nanoparticles is obtained. Specifically, pH 12.1 corresponds to a concentration of 12 mM of OH$^-$ required for the hydrolysis of a 2 mM K$_2$IrCl$_6$ to 2 mM solution of [Ir(OH$_6$)]$^{2-}$. Both solutions ([Ir(OH$_6$)]$^{2-}$ and colloidal IrO$_x$) were tested for their water oxidation activity. These solutions yield a black precipitate when mixed with phosphate buffer. Therefore, electrochemical tests were performed with 0.5 M NaClO$_4$ as the supporting electrolyte. The water oxidation currents that were obtained with a GC electrode in these solutions (containing 1 mM iridium) were 2 orders of magnitude higher than those obtained with **1 – 5** (Figure A.12 and Figure A.7). Bubble formation is clearly observed and

causes noisy amperograms (Figure A.12). Moreover, maximum activity is obtained at 1.9 V for $[Ir(OH)_6]^{2-}$ with currents reaching up to 11 mA cm^{-2}. The colloidal IrO$_x$ solution produces lower currents with a maximum of 4 mA cm^{-2} at 1.8 V. Remarkably, at higher potentials (2.0 and 2.1 V) the activity dramatically declines and becomes an order of magnitude lower at 2.1 V for both $[Ir(OH)_6]^{2-}$ and colloidal IrO$_x$. This apparent potential related maximum in activity is similar to what is observed for the catalysts **1**, **3**, and **4** (Figure 2.3), but not **2**. Furthermore, the water oxidation activity increases over time, in particular for $[Ir(OH)_6]^{2-}$ (Figure A.12A). In a solution of colloidal IrO$_x$ as well as in a $[Ir(OH)_6]^{2-}$ solution a deposit is formed on the electrode while performing chronoamperometry. This electrodeposition becomes evident from the electrode rinse test when pre- and post-CVs are compared (Figure A.12C and D). These CVs after amperometry in Figure A.12C and D have similar features and reach currents up to 36 mA cm^{-2} at 2.1 V. Only the first scan of the electrode tested in the colloidal IrO$_x$ solution (Figure A.12D) deviates as it has an additional oxidative event at 1.6 V. In terms of water oxidation activity, the IrO$_x$ deposits produce 1 to 2 orders of magnitude higher currents than **GC|1 – GC|4**. The formation of a deposit from a $[Ir(OH)_6]^{2-}$ solution is also dependent on the aging of the solution. When the solution is a day old, deposition and catalytic water oxidation start immediately after a potential is applied (Figure A.12A). However, a considerable lag time of 45 minutes is observed between the application of 1.95 V on the GC electrode and the start of the catalytic current (Figure A.12E) in a $[Ir(OH)_6]^{2-}$ solution just 1.5 hours after its preparation. Moreover, the lag time decreases with increasing aging of the solution (Figure A.12E). This suggests that the concentration of the species responsible for depositing the active species on the GC electrode slowly increases over time. It is very likely that a small IrO$_x$ cluster is boosting deposition and water oxidation in this case, as a fresh solution initially contains $[Ir(OH)_6]^{2-}$ but over time gradually contains large colloidal IrO$_x$ particles.[66] The color change of the solution from colorless to purplish blue over the course of these experiments strengthens this hypothesis. When 1 mM of ligand (4-hydroxypicolinic acid in particular) is added, the solution turns slightly turbid and green. Comparing the amperogram of a $[Ir(OH)_6]^{2-}$ solution with and without this ligand (Figure A.S12F) reveals that the lag time decreases in the presence of the ligand but the obtained water oxidation current is a fraction of what is obtained without ligand (0.7 versus 5.0 mA cm^{-2} respectively), which is partly due to formation of a black precipitate.

2.2.6.2 *Comparison of electrode surface to GC|1 – GC|4*

XPS was performed on a preanodized electrode on which a potential of 1.95 V was applied for 1 hour and 15 minutes in a $[Ir(OH)_6]^{2-}$ solution 1.5 hour after its preparation. The spectrum of **GC|[Ir(OH)₆]²⁻** reveals that two iridium species are deposited on the surface. An Ir $4f_{7/2}$ species with a binding energy of 62.4 eV and a species with a higher binding energy of 63.6 eV were found in a 1.8 : 1 ratio, respectively. The thickness of the iridium layer is further reflected by the low intensity of the N 1s signal at 400.4 eV originating from the anodized GC electrode (Figure A.10A). Interestingly, the Ir $4f_{7/2}$ signal of bulk IrO_x is usually reported at a binding energy of 61.8 – 61.9 eV.[70, 71] However, the "hydration level" of bulk IrO_x has been shown to increase the binding energy of the surface Ir up to binding energies of 62.4 – 62.5 eV which agrees well with the 62.4 eV species found for **GC|[Ir(OH)₆]²⁻**.[71] Moreover, this 62.4 eV Ir species has the same the binding energy as the Ir species of **GC|3**. In contrast, **4** has been reported as IrO_x depositing precatalyst but deposits Ir species at a significantly higher binding energy of 62.9 eV as found for **GC|4**.[33, 50] This might be due to a different electrochemical treatment (potential of 1.3 V *versus* RHE in a 0.1 M KNO_3 solution of pH 2.9) as compared to previous reports or, more likely, due to remainders of the Cp* moiety since 9% of the electrodeposit was found to contain carbon in the same study under those conditions.[32] Moreover, remainders of the Cp* ligand might diminish the activity of the electrodeposit as we have found 2 orders of magnitude higher activities with the ligand free $[Ir(OH)_6]^{2-}$ precursor. Interestingly, the BE of the minor Ir species at 63.6 eV of **GC|[Ir(OH)₆]²⁻** is higher than any of the other observed species and falls in the range of Ir(IV) salts.[69] In our case, XPS cannot give conclusive distinction between bulk IrO_x, IrO_x with ligand residues, or a different, ligand containing species. First of all, $[Ir(OH)_6]^{2-}$ can only be generated in solution and not isolated as a solid, so the binding energy of the iridium species prior to catalysis cannot be determined. Second, the Ir $4f_{7/2}$ binding energy of bulk IrO_x species can differ as mentioned before and thus cannot be compared directly. However, based on the electrochemical data it can be concluded that the ligand systems of **1 – 4** significantly reduce the water oxidation activity of their respective iridium deposit and/or decrease the amount of electrodeposited active iridium sites as compared to the ligand-free iridium precursor $[Ir(OH)_6]^{2-}$.

2.2.7 Nature of active species generated by **1 – 5**

It is not a new phenomenon that parent iridium complexes (partially) disintegrate like **1 – 5** to a catalytically active deposit.[29, 30, 33-47, 57] It has been

suggested that Cp* based iridium complexes lacking a bidentate ligand degrade to an IrO$_x$ layer.[29, 33, 38] In contrast, iridium complexes bearing Cp* and bidentate ligands may only oxidatively lose Cp* and produce a dinuclear species as active species for water oxidation.[14, 36-38, 40, 44, 54, 55] Acetic acid liberated by Cp* degradation is suggested to prevent IrO$_x$ formation in that case.[72] Nonetheless, in some cases IrO$_x$ nanoparticles were still reported despite the presence of bidentate bipyridine ligands.[35, 46] Indeed, we observed Cp* degradation for **4^{-OH}1** under our conditions. The bidentate hydroxypicolinate ligand (or a residue thereof) could be part of the electrodeposit as there was no indication of noncoordinated hydroxypicolinate ligand in the electrolyte afterward. XPS spectroscopy confirmed the deposition of iridium, but the possible presence of a ligand (or residues thereof) remains elusive due to interference of the electrode material in the C 1s spectrum. Nevertheless, the effect of structural diversity of the ligands of **1 – 5** on their respective water oxidation activity is marginal. Our chronoamperometry data show that there is no clear relationship between the water oxidation activity of the electrodeposit and the ligand system of the parent complex.

The catalytic behavior of all molecular iridium complexes over time appears to be quite similar under our conditions, yet considerably less active than IrO$_x$ generated from [Ir(OH)$_6$]$^{2-}$. Given the complexity of the system, it is difficult to assign the catalytic activity to one predominant species. Nevertheless, we cannot rule out that the same active species is formed for all the complexes **1 – 5**, albeit at significant larger amounts in the case of [Ir(OH)$_6$]$^{2-}$. The organic ligands of **1 – 5** as well as the Cp* degradation products prevent or slow down the formation of IrO$_x$.[72] The lag time observed for water oxidation with freshly prepared solutions of [Ir(OH)$_6$]$^{2-}$ indicates that [Ir(OH)$_6$]$^{2-}$ itself is not the depositing species. Instead, a small IrO$_x$ cluster consistent of merely a few atoms might form over time. Over a prolonged period of time, these small clusters can further aggregate to form larger IrO$_x$ clusters that result in observed blue colloidal IrO$_x$ solutions. The small IrO$_x$ cluster might thus be responsible for the deposition and water oxidation activity on the GC electrode. This would also explain why a slightly aged [Ir(OH)$_6$]$^{2-}$ solution has no lag time since it would contain a higher concentration of aggregated IrO$_x$ clusters. It seems likely that a similar process takes place for the **1 − 5** catalyst precursors. In contrast to ligand-free [Ir(OH)$_6$]$^{2-}$, the ligand is involved in the formation of these small, few-atom containing IrO$_x$ clusters and might stabilize these to prevent agglomeration to large IrO$_x$ clusters. The relatively small effect of the ligand on the binding energy of the Ir 4f$_{7/2}$ species deposited on **GC|1 – GC|4** indicates that any ligand residues must be present in less than 1 ratio with respect to

iridium atoms since the 1:1 or even 2:1 ratio of ligand to iridium in the parent complexes **1 − 4** directly results in larger shifts of the Ir $4f_{7/2}$ binding energies. The small ligand to iridium ratio also would also explain the small difference in water oxidation activity for **GC|1 − GC|4**. In this context, it is interesting to note that the pyalc ligand appears to be most resistive to catalyst deactivation at higher potentials. We believe this is in line with reports by the Crabtree and Brudvig groups that claim that the pyalc ligand is retained in the catalytic species of their chemisorbed pyalc catalyst.[14] This also illustrates that the choice of ligand has, though small, an influence on the outcome of the active species. Even more, with the right knowledge and choice of substituents the size of the IrO_x agglomeration could be more precisely controlled, similar to the isolation of active sites in supports, allowing for enhanced water oxidation activity.[13, 73]

2.3   Conclusion

We set out to benchmark the water oxidation performance of complexes **1 − 5** under the exact same electrochemical conditions. Previous studies with $NaIO_4$ showed that the water oxidation activity of most complexes increased significantly when the pH was increased from 1 to 7. By contrast, these complexes show minimal electrocatalytic activity, just barely above the background current of the glassy carbon electrode at pH 7. Our results show that the structure–activity relationships obtained in studies with sacrificial reagents do not translate under our electrochemical conditions where also the difference in activity between complexes seems to be rather marginal. All complexes do form deposits on the electrode surface, where they produce iridium sites that in terms of their electronic structure are barely influenced by the ligands that were present in the precatalyst. A possible explanation for this phenomenon is that small IrO_x clusters are formed. Ligands of the parent complexes or residues thereof might be incorporated and still influence the properties of these clusters. In terms of catalytic activity, the iridium deposits of the molecular complexes largely fall behind that of $[Ir(OH)_6]^{2-}$, indicating that the remnants of the organic ligands have an inhibitory effect on the catalytic reaction. However, our catalyst screening study does show that the presence of organic ligands may in some cases result in slower catalyst deactivation, and potentially retain more iridium sites available for the water oxidation reaction by preventing aggregation of these active sites.

2.4 Acknowledgements

2.5 Experimental

2.5.1 General

For all aqueous solutions, all experiments, and for cleaning of glassware Milli-Q grade Ultrapure water (>18.2 MΩ cm resistivity) was used unless mentioned otherwise. Chemicals were bought from commercial suppliers and used as received without further purification. The pH 7 (6.9) electrolyte was prepared with NaH_2PO_4, Na_2HPO_4 (both Merck Suprapur 99.99%), and $NaClO_4 \cdot H_2O$ (Merck Emsure) in the right ratio to obtain an aqueous 0.1 M phosphate buffer with an ionic strength of 0.5 M. This strengthened buffer was used for every experiment with a pH 7 phosphate buffer. To obtain the 0.1 M $HClO_4$ solution with an ionic strength of 0.5 M, $HClO_4$ (Merck Suprapur) and $NaClO_4$ were used. D_2O was obtained from Eurisotop and used as received. The pH was measured with a Hannah Instruments HI 4222 pH meter that was calibrated with five IUPAC standard buffers. UV-vis measurements were performed on a Varian Cary 50 UV-vis spectrometer. ^{1}H NMR measurements were performed with a Bruker DPX-300 300 MHz spectrometer.

The complexes ^{H}**1**, $^{5-OH}$**1**, **2**, **3**, **4**, and **5** were all synthesized according to their published procedures.[15, 17, 28, 50, 56] $^{3-OH}$**1**, $^{4-OH}$**1**, and $^{6-OH}$**1** were synthesized using **4** as an iridium precursor instead of $[Cp*IrCl_2]_2$. In particular, 100 mg of **4** (0.198 mmol) was added to a solution of 33.0 mg of the ligand (0.237 mmol) and 13.3 mg of KOH (0.237 mmol) in 20 mL of MeOH. The resulting solution was stirred at r.t. for 15 h. The solvent was removed under vacuum and the residual solid was dissolved/suspended in DCM. The mixture was filtered through a membrane and the resulting solution reduced in volume and the product was crystallized with diethyl ether. The yields were ca. 60-70%. The corresponding ^{1}H NMR spectra (Figure A.13-A.15) in DMSO-d_6 match the spectra that were previously reported for the method using $[Cp*IrCl_2]_2$ as a precursor.[28]

[Ir(OH)$_6$]$^{2-}$ was prepared according to the procedure of Zhao *et al.*[66] As described in their publication, control of pH is of importance. Specifically, we found that mixing the iridium precursor K$_2$IrCl$_6$ (Sigma) and NaOH (Fluka TraceSelect, ≥99.9995%) in water should be in the proper atomic ratio; thus to convert 2 mM K$_2$IrCl$_6$, 12 mM of NaOH is required. Any excess of NaOH will result in a pH which is too high. Actually, in one attempt a blue solution was obtained due to this excess. This deep blue IrO$_x$ nanoparticle solution is the tested solution as described before.

2.5.2 General electrochemistry

Electrochemical experiments were performed with a three-electrode setup in a custom-made, single-compartment glass cell. For EQCM and bulk electrolysis, special cells were used that are described separately. Autolab PGSTAT 204 and 128N potentiostats were used in combination with NOVA 2.1 software. All glassware used for electrochemistry was cleaned by boiling in and copiously rinsing the glassware with water prior to each experiment. Periodically, the glassware was cleaned by immersing the glassware in a 1 g/L KMnO$_4$ solution in 0.5 M H$_2$SO$_4$ (Sigma, reagent grade) for at least a night. Afterward, the glassware was rinsed 10 times with water. Next, water and a few drops of H$_2$O$_2$ (Merck Emprove, 35%) and H$_2$SO$_4$ were added to reoxidize any MnO$_2$ residues. Subsequently, the glassware was rinsed and a 3-fold process of boiling the glassware in water and subsequent rinsing followed to finalize the cleaning.

All solutions were purged with argon (Linde, Ar 5.0) prior to each experiment for at least 30 minutes and the cell was kept under a flow of argon during the experiment.

All potentials are referenced to the reversible hydrogen electrode by utilizing a platinum mesh in H$_2$ (Linde, H$_2$ 5.0) saturated electrolyte that is operated at the same pH as the working electrode. The cell and reference electrode are connected via a Luggin capillary. The counter electrode was a large surface area gold wire that is flame annealed prior to use. The working electrode was generally a glassy carbon electrode (Alfa Aesar type 1, 0.07 cm^2) used in a hanging meniscus configuration or a PEEK encapsulated one (Metrohm, 0.07 cm^2) that was specifically used for the CA studies resulting in the plots of Figure 2.3 and 2.4. Regular polish was applied by mechanically polishing the electrode with 1.0, 0.3 and 0.05 micron alumina slurry (Buehler) for 2 minutes followed by rinsing and sonicating the electrode in water for 15 minutes. It has to be noted that the corrosive conditions under which the electrode was preanodized and used at high potentials for some of the experiments has a major destructive impact on the electrode itself. The surface is roughened extensively,

which is reflected in a large increase in the capacitive current of the double layer.[62] Only extensive polishing with sandpaper to remove a substantial amount of material from the surface and subsequent smoothing of the surface with alumina slurry was found to restore the electrode to an acceptable state. For this purpose, regular polishing was preceded by mechanical polishing with 600 and 2500 grit sandpaper, respectively.

2.5.3   OLEMS

The gaseous products that are detected with OLEMS are collected using a small tip that is in very close proximity to the working electrode.[60] The working electrode is a large surface area (0.14 cm^2) gold working electrode to maximize the current response. The tip was a porous Teflon cylinder (0.5 mm diameter) with an average pore size of $10 - 14$ μm in a KeI-F holder. The mass spectrometer and the tip are interconnected via a PEEK capillary. The tip was cleaned in a solution of $K_2Cr_2O_7$ (0.2 M) in H_2SO_4 (2M) and rinsed with water before use. The measurements were performed with an IviumStat potentiostat operated by Ivium software.

2.5.4   Bulk electrolysis

Bulk electrolysis was performed in a custom-made, two-compartment glass cell that could be separated with a Nafion membrane (Alfa Aesar, Nafion N-117 membrane, 0.180 mm thick, ≥ 0.90 mequiv/g exchange capacity) to allow for separation of the work and counter electrode. The Nafion membrane is cleaned and activated by a 5-fold boiling and rinsing procedure in water, 5% H_2O_2, water, 1.0 M H_2SO_4, and water, respectively. This allows for optimal exchange capacitiy.[74] However, as the final experiment was performed in D_2O the Nafion membrane was dried in a 70 °C oven for 1 hour to avoid contamination by H_2O. The reference electrode was a HydroFlex (Gaskatel) electrode used in a RHE configuration and connected via a Luggin capillary to the compartment with the work electrode. The work electrode was a custom-cut large surface area GC electrode (0.79 cm^2) used in a hanging meniscus configuration which was preanodized in a pH 7 phosphate electrolyte at 2.1 V for 25 minutes. Afterward, the electrode was rinsed thoroughly with water and dried under a stream of N_2. For the bulk electrolysis itself with 1 mM $^{4-OH}\mathbf{1}$ present, a D_2O based solution was used with 0.1 M phosphate buffer and 0.5 M ionic strength. This solution was used in the working electrode compartment. For the Luggin capillary and the counter electrode compartments, a catalyst-free D_2O solution was used. The solution in the compartment for the working electrode was continuously stirred with a Teflon stirring bar that was cleaned according to the

periodic glass cleaning procedure. A potential of 1.9 V was held for 1 hour after which the catalyst solution was removed for further testing by NMR, DLS and UV-vis. For UV-vis, the background was corrected for a catalyst free-solution and the dilution was achieved by adding the appropriate amount of D_2O to both the background and desired solution.

2.5.5 EQCM

EQCM experiments were performed with Autolab gold EQCM electrodes (0.35 cm^2) in an Autolab 3 ml Teflon EQCM cell that consists of a 200 nm gold layer deposited on a quartz crystal. A modified RHE reference electrode was used which prevents interference of continuous hydrogen bubbling to the sensitive microbalance signal.[56]

2.5.6 XPS

X-ray photoelectron spectroscopy (XPS) was performed on a Thermo Scientific K-Alpha spectrometer equipped with a monochromatic small-spot X-ray source and a double focusing hemispherical analyzer with a 128-channel delay line detector. Spectra were obtained by using an aluminum anode (Al Kα = 1486.6 eV) operated at 72 W and a spot size of 400 µm. Survey scans were measured at a constant pass energy of 200 eV, and high-resolution scans of the separate regions were measured at 50 eV pass energy. The background pressure of the ultrahigh vacuum (UHV) chamber was 2×10^{-8} mbar. Sample charging was compensated using an electron flood gun, and binding energy (BE) calibration was done by setting the C 1s peak of sp^3 (CH, CC) carbon to BE (C 1s) = 284.8 eV. For proper fitting of the data of **1** and **2**, two different iridium species had to be fitted. For $^{3-OH}$**1**, species at binding energies of 62.3(1) eV and 60.8(1) eV in a respective ratio of 17:1 were fitted. For $^{4-OH}$**1**, a ratio of 21:1 between a fitted species at 62.1(1) eV and 60.7(1) eV was fitted. Last, 61.7 and 60.4 eV (with a ratio of 11:1 respectively) were the fitted species for **2**. The numbers in parentheses are standard errors. Electrode samples for XPS analysis were prepared by performing amperometry at the desired potential (1.95 or 2.05 V) with a GC electrode (0.07 cm^2) in a hanging meniscus configuration for 30 minutes. The electrode was preanodized for 25 minutes at 2.1 V in a catalyst-free pH 7 phosphate buffer electrolyte. After subsequent rinsing with water, the electrode was held in electrolyte that contained 1 mM of the complex of interest. After amperometry, the electrode was rinsed with water and air dried before being subjected to XPS analysis.

2.6   References

1.   Blakemore, J. D.; Crabtree, R. H.; Brudvig, G. W., *Chem. Rev.* **2015,** *115*, 12974–13005.
2.   Fukuzumi, S.; Hong, D., *Eur. J. Inorg. Chem.* **2014,** *2014*, 645–659.
3.   Hetterscheid, D. G. H.; Reek, J. N. H., *Angew. Chem. Int. Ed.* **2012,** *51*, 9740–9747.
4.   Kärkäs, M. D.; Verho, O.; Johnston, E. V.; Åkermark, B., *Chem. Rev.* **2014,** *114*, 11863–12001.
5.   Liu, X.; Wang, F., *Coord. Chem. Rev.* **2012,** *256*, 1115–1136.
6.   Macchioni, A., *Eur. J. Inorg. Chem.* **2019,** *2019*, 7–17.
7.   Seidler-Egdal, R. K.; Nielsen, A.; Bond, A. D.; Bjerrum, M. J.; McKenzie, C. J., *Dalton Trans.* **2011,** *40*, 3849–3858.
8.   Thomsen, J. M.; Huang, D. L.; Crabtree, R. H.; Brudvig, G. W., *Dalton Trans.* **2015,** *44*, 12452–12472.
9.   Wu, X.; Li, F.; Zhang, B.; Sun, L., *Journal of Photochemistry and Photobiology C: Photochemistry Reviews* **2015,** *25*, 71–89.
10.   Yagi, M.; Syouji, A.; Yamada, S.; Komi, M.; Yamazaki, H.; Tajima, S., *Photochem. Photobiol. Sci.* **2009,** *8*, 139–147.
11.   Zhang, B.; Sun, L., *Chem. Soc. Rev.* **2019,** *48*, 2216–2264.
12.   Duan, L.; Fischer, A.; Xu, Y.; Sun, L., *J. Am. Chem. Soc.* **2009,** *131*, 10397–10399.
13.   Fagiolari, L.; Zaccaria, F.; Costantino, F.; Vivani, R.; Mavrokefalos, C.; Patzke, G.; Macchioni, A., *Dalton Trans.* **2020**.
14.   Sheehan, S. W.; Thomsen, J. M.; Hintermair, U.; Crabtree, R. H.; Brudvig, G. W.; Schmuttenmaer, C. A., *Nat. Commun.* **2015,** *6*, 6469.
15.   McDaniel, N. D.; Coughlin, F. J.; Tinker, L. L.; Bernhard, S., *J. Am. Chem. Soc.* **2008,** *130*, 210–217.
16.   Blakemore, J. D.; Schley, N. D.; Balcells, D.; Hull, J. F.; Olack, G. W.; Incarvito, C. D.; Eisenstein, O.; Brudvig, G. W.; Crabtree, R. H., *J. Am. Chem. Soc.* **2010,** *132*, 16017–16029.
17.   Savini, A.; Bellachioma, G.; Ciancaleoni, G.; Zuccaccia, C.; Zuccaccia, D.; Macchioni, A., *Chem. Commun.* **2010,** *46*, 9218–9219.
18.   Bucci, A.; Savini, A.; Rocchigiani, L.; Zuccaccia, C.; Rizzato, S.; Albinati, A.; Llobet, A.; Macchioni, A., *Organometallics* **2012,** *31*, 8071–8074.
19.   DePasquale, J.; Nieto, I.; Reuther, L. E.; Herbst-Gervasoni, C. J.; Paul, J. J.; Mochalin, V.; Zeller, M.; Thomas, C. M.; Addison, A. W.; Papish, E. T., *Inorg. Chem.* **2013,** *52*, 9175–9183.
20.   Savini, A.; Bucci, A.; Bellachioma, G.; Giancola, S.; Palomba, F.; Rocchigiani, L.; Rossi, A.; Suriani, M.; Zuccaccia, C.; Macchioni, A., *J. Organomet. Chem.* **2014,** *771*, 24–32.
21.   Li, M.; Takada, K.; Goldsmith, J. I.; Bernhard, S., *Inorg. Chem.* **2016,** *55*, 518–526.
22.   Bucci, A.; Dunn, S.; Bellachioma, G.; Menendez Rodriguez, G.; Zuccaccia, C.; Nervi, C.; Macchioni, A., *ACS Catal.* **2017,** *7*, 7788–7796.
23.   Li, M.; Bernhard, S., *Catal. Today* **2017,** *290*, 19–27.
24.   Mahanti, B.; González Miera, G.; Martínez-Castro, E.; Bedin, M.; Martín-Matute, B.; Ott, S.; Thapper, A., *ChemSusChem* **2017,** *10*, 4616–4623.
25.   Navarro, M.; Li, M.; Bernhard, S.; Albrecht, M., *Dalton Trans.* **2018,** *47*, 659–662.
26.   Navarro, M.; Smith, C. A.; Li, M.; Bernhard, S.; Albrecht, M., *Chem. - Eur. J.* **2018,** *24*, 6386–6398.
27.   Menendez Rodriguez, G.; Gatto, G.; Zuccaccia, C.; Macchioni, A., *ChemSusChem* **2017,** *10*, 4503–4509.
28.   Menendez Rodriguez, G.; Bucci, A.; Hutchinson, R.; Bellachioma, G.; Zuccaccia, C.; Giovagnoli, S.; Idriss, H.; Macchioni, A., *ACS Energy Lett.* **2017,** *2*, 105–110.
29.   Grotjahn, D. B.; Brown, D. B.; Martin, J. K.; Marelius, D. C.; Abadjian, M.-C.; Tran, H. N.; Kalyuzhny, G.; Vecchio, K. S.; Specht, Z. G.; Cortes-Llamas, S. A.; Miranda-Soto, V.; van Niekerk, C.; Moore, C. E.; Rheingold, A. L., *J. Am. Chem. Soc.* **2011,** *133*, 19024–19027.
30.   Savini, A.; Belanzoni, P.; Bellachioma, G.; Zuccaccia, C.; Zuccaccia, D.; Macchioni, A., *Green Chem.* **2011,** *13*, 3360–3374.
31.   Bucci, A.; Menendez Rodriguez, G.; Bellachioma, G.; Zuccaccia, C.; Poater, A.; Cavallo, L.; Macchioni, A., *ACS Catal.* **2016,** *6*, 4559–4563.
32.   Corbucci, I.; Zaccaria, F.; Heath, R.; Gatto, G.; Zuccaccia, C.; Albrecht, M.; Macchioni, A., *ChemCatChem* **2019,** *11*, 5353–5361.
33.   Blakemore, J. D.; Schley, N. D.; Olack, G. W.; Incarvito, C. D.; Brudvig, G. W.; Crabtree, R. H., *Chem. Sci.* **2011,** *2*, 94–98.

2

34. Zuccaccia, C.; Bellachioma, G.; Bolaño, S.; Rocchigiani, L.; Savini, A.; Macchioni, A., *Eur. J. Inorg. Chem.* **2012,** *2012*, 1462–1468.
35. Hong, D.; Murakami, M.; Yamada, Y.; Fukuzumi, S., *Energy Environ. Sci.* **2012,** *5*, 5708–5716.
36. Wang, C.; Wang, J.-L.; Lin, W., *J. Am. Chem. Soc.* **2012,** *134*, 19895–19908.
37. Hintermair, U.; Sheehan, S. W.; Parent, A. R.; Ess, D. H.; Richens, D. T.; Vaccaro, P. H.; Brudvig, G. W.; Crabtree, R. H., *J. Am. Chem. Soc.* **2013,** *135*, 10837–10851.
38. Blakemore, J. D.; Mara, M. W.; Kushner-Lenhoff, M. N.; Schley, N. D.; Konezny, S. J.; Rivalta, I.; Negre, C. F. A.; Snoeberger, R. C.; Kokhan, O.; Huang, J.; Stickrath, A.; Tran, L. A.; Parr, M. L.; Chen, L. X.; Tiede, D. M.; Batista, V. S.; Crabtree, R. H.; Brudvig, G. W., *Inorg. Chem.* **2013,** *52*, 1860–1871.
39. Codolà, Z.; M. S. Cardoso, J.; Royo, B.; Costas, M.; Lloret-Fillol, J., *Chem. - Eur. J.* **2013,** *19*, 7203–7213.
40. Graeupner, J.; Hintermair, U.; Huang, D. L.; Thomsen, J. M.; Takase, M.; Campos, J.; Hashmi, S. M.; Elimelech, M.; Brudvig, G. W.; Crabtree, R. H., *Organometallics* **2013,** *32*, 5384–5390.
41. Zuccaccia, C.; Bellachioma, G.; Bortolini, O.; Bucci, A.; Savini, A.; Macchioni, A., *Chem. - Eur. J.* **2014,** *20*, 3446–3456.
42. Savini, A.; Bucci, A.; Bellachioma, G.; Rocchigiani, L.; Zuccaccia, C.; Llobet, A.; Macchioni, A., *Eur. J. Inorg. Chem.* **2014,** *2014*, 690–697.
43. Ingram, A. J.; Wolk, A. B.; Flender, C.; Zhang, J.; Johnson, C. J.; Hintermair, U.; Crabtree, R. H.; Johnson, M. A.; Zare, R. N., *Inorg. Chem.* **2014,** *53*, 423–433.
44. Thomsen, J. M.; Sheehan, S. W.; Hashmi, S. M.; Campos, J.; Hintermair, U.; Crabtree, R. H.; Brudvig, G. W., *J. Am. Chem. Soc.* **2014,** *136*, 13826–13834.
45. Zhang, T.; deKrafft, K. E.; Wang, J.-L.; Wang, C.; Lin, W., *Eur. J. Inorg. Chem.* **2014,** *2014*, 698–707.
46. Lewandowska-Andralojc, A.; Polyansky, D. E.; Wang, C.-H.; Wang, W.-H.; Himeda, Y.; Fujita, E., *Phys. Chem. Chem. Phys.* **2014,** *16*, 11976–11987.
47. Wan, X.; Wang, L.; Dong, C.-L.; Menendez Rodriguez, G.; Huang, Y.-C.; Macchioni, A.; Shen, S., *ACS Energy Lett.* **2018,** *3*, 1613–1619.
48. Dzik, W. I.; Calvo, S. E.; Reek, J. N. H.; Lutz, M.; Ciriano, M. A.; Tejel, C.; Hetterscheid, D. G. H.; de Bruin, B., *Organometallics* **2011,** *30*, 372–374.
49. Brewster, T. P.; Blakemore, J. D.; Schley, N. D.; Incarvito, C. D.; Hazari, N.; Brudvig, G. W.; Crabtree, R. H., *Organometallics* **2011,** *30*, 965–973.
50. Schley, N. D.; Blakemore, J. D.; Subbaiyan, N. K.; Incarvito, C. D.; D'Souza, F.; Crabtree, R. H.; Brudvig, G. W., *J. Am. Chem. Soc.* **2011,** *133*, 10473–10481.
51. Blakemore, J. D.; Schley, N. D.; Kushner-Lenhoff, M. N.; Winter, A. M.; D'Souza, F.; Crabtree, R. H.; Brudvig, G. W., *Inorg. Chem.* **2012,** *51*, 7749–7763.
52. Hintermair, U.; Hashmi, S. M.; Elimelech, M.; Crabtree, R. H., *J. Am. Chem. Soc.* **2012,** *134*, 9785–9795.
53. Junge, H.; Marquet, N.; Kammer, A.; Denurra, S.; Bauer, M.; Wohlrab, S.; Gärtner, F.; Pohl, M.-M.; Spannenberg, A.; Gladiali, S.; Beller, M., *Chem. - Eur. J.* **2012,** *18*, 12749–12758.
54. Diaz-Morales, O.; Hersbach, T. J. P.; Hetterscheid, D. G. H.; Reek, J. N. H.; Koper, M. T. M., *J. Am. Chem. Soc.* **2014,** *136*, 10432–10439.
55. Hetterscheid, D. G. H.; van der Ham, C. J. M.; Diaz-Morales, O.; Verhoeven, M. W. G. M.; Longo, A.; Banerjee, D.; Niemantsverdriet, J. W.; Reek, J. N. H.; Feiters, M. C., *Phys. Chem. Chem. Phys.* **2016,** *18*, 10931–10940.
56. Abril, P.; del Rı́o, M. P.; Tejel, C.; Verhoeven, T. W. G. M.; Niemantsverdriet, J. W. H.; van der Ham, C. J. M.; Kottrup, K. G.; Hetterscheid, D. G. H., *ACS Catal.* **2016,** *6*, 7872–7875.
57. Corbucci, I.; Ellingwood, K.; Fagiolari, L.; Zuccaccia, C.; Elisei, F.; Gentili, P. L.; Macchioni, A., *Catal. Today* **2017,** *290*, 10–18.
58. van Dijk, B.; Hofmann, J. P.; Hetterscheid, D. G. H., *Phys. Chem. Chem. Phys.* **2018,** *20*, 19625–19634.
59. Joya, K. S.; Subbaiyan, N. K.; D'Souza, F.; de Groot, H. J. M., *Angew. Chem. Int. Ed.* **2012,** *51*, 9601–9605.
60. Wonders, A. H.; Housmans, T. H. M.; Rosca, V.; Koper, M. T. M., *J. Appl. Electrochem.* **2006,** *36*, 1215–1221.
61. Diaz-Morales, O.; Calle-Vallejo, F.; de Munck, C.; Koper, M. T. M., *Chem. Sci.* **2013,** *4*.
62. Yi, Y.; Weinberg, G.; Prenzel, M.; Greiner, M.; Heumann, S.; Becker, S.; Schlögl, R., *Catal. Today* **2017,** *295*, 32–40.
63. van der Ham, C. J. M.; Işık, F.; Verhoeven, T. W. G. M.; Niemantsverdriet, J. W.; Hetterscheid, D. G. H., *Catal. Today* **2017,** *290*, 33–38.

2

64. Hetterscheid, D. G. H., *Chem. Commun.* **2017,** *53*, 10622–10631.
65. Zhao, Y.; Hernandez-Pagan, E. A.; Vargas-Barbosa, N. M.; Dysart, J. L.; Mallouk, T. E., *J. Phys. Chem. Lett.* **2011,** *2*, 402–406.
66. Zhao, Y.; Vargas-Barbosa, N. M.; Hernandez-Pagan, E. A.; Mallouk, T. E., *Small* **2011,** *7*, 2087–2093.
67. Bard, A. J.; Faulkner, L. R., *Electrochemical Methods: Fundamentals and Applications*. Wiley: New York, 2000.
68. Diaz-Morales, O.; Raaijman, S.; Kortlever, R.; Kooyman, P. J.; Wezendonk, T.; Gascon, J.; Fu, W. T.; Koper, M. T. M., *Nat. Commun.* **2016,** *7*, 12363.
69. NIST X-ray Photoelectron Spectroscopy Database. National Institute of Standards and Technology: Gaithersburg, 2012; Vol. Version 4.1.
70. Rubel, M.; Haasch, R.; Mrozek, P.; Wieckowski, A.; De Pauli, C.; Trasatti, S., *Vacuum* **1994,** *45*, 423–427.
71. Kötz, R.; Neff, H.; Stucki, S., *J. Electrochem. Soc.* **1984,** *131*, 72–77.
72. Huang, D. L.; Beltrán-Suito, R.; Thomsen, J. M.; Hashmi, S. M.; Materna, K. L.; Sheehan, S. W.; Mercado, B. Q.; Brudvig, G. W.; Crabtree, R. H., *Inorg. Chem.* **2016,** *55*, 2427–2435.
73. Corbucci, I.; Petronilho, A.; Müller-Bunz, H.; Rocchigiani, L.; Albrecht, M.; Macchioni, A., *ACS Catal.* **2015,** *5*, 2714–2718.
74. Jiang, B.; Yu, L.; Wu, L.; Mu, D.; Liu, L.; Xi, J.; Qiu, X., *ACS Appl. Mater. Interfaces* **2016,** *8*, 12228–12238.

2

Chapter 3

Pinpointing the active species of the Cu(DAT) catalyzed oxygen reduction reaction

*Dinuclear Cu^{II} complexes bearing two 3,5-diamino-1,2,4-triazole (DAT) ligands have gained considerable attention as a potential model system for laccase due to their low overpotential for the oxygen reduction reaction (ORR). In this study, the active species for the ORR was investigated. The water soluble dinuclear copper complex (**Cu(DAT)**) was obtained by mixing a 1 : 1 ratio of Cu(OTf)$_2$ and DAT in water. The electron paramagnetic resonance (EPR) spectrum of **Cu(DAT)** showed a broad axial signal with a g factor of 2.16 as well as a low intensity M_s = ±2 absorption characteristic of the Cu$_2$(μ-DAT)$_2$ moiety. Monitoring the typical 380 nm peak with UV-Vis spectroscopy revealed that the Cu$_2$(μ-DAT)$_2$ core is extremely sensitive to changes in pH, copper to ligand ratios and the presence of anions. Electrochemical quartz crystal microbalance experiments displayed a large decrease in frequency below 0.5 V versus the reversible hydrogen electrode (RHE) in a **Cu(DAT)** solution implying the formation of deposition. Rotating ring disk electrode experiments showed that this deposition is an active ORR catalyst which reduces O$_2$ all the way to water at pH 5. The activity increased significantly in the course of time. X-ray photoelectron spectroscopy was utilized to analyze the composition of the deposition. Significant shifts in the Cu 2p$_{3/2}$ and N 1s spectra were observed with respect to **Cu(DAT)**. After ORR catalysis at pH 5, mostly Cu^I and/or Cu^0 species are present and the deposition corresponds to previously reported electrodepositions of copper. This leads us to conclude that the active species is of a heterogeneous nature and lacks any structural similarity with laccase.*

3.1 Introduction

Hydrogen is considered the fuel of the future as it can be produced from sustainable energy sources such as sunlight and wind. In a fuel cell, electricity can be regenerated by electrochemical oxidation of hydrogen at the anode (Eqn. 3.1) and an oxygen reduction reaction (ORR) at the cathode (Eqn. 3.2). Thus far, platinum is the catalyst of choice at the cathode.[1] Nonetheless, platinum catalysts cannot operate at the thermodynamic equilibrium potential of water at 1.23 V *versus* the reversible hydrogen electrode (RHE) and require an additional energy input of approximately 400 mV. This limits the overall efficiency of the fuel cell.[1-3] Moreover, platinum is too expensive and too scarce to be applied on a scale required for a sustainable hydrogen economy.[4, 5] Hence, viable alternatives must be found.

$E° = 0.00$ V $\qquad H_2 \longrightarrow 2H^+ + 2e^-$ **Eqn. 3.1**

$E° = 1.229$ V[6] $\qquad O_2 + 4H^+ + 4e^- \longrightarrow 2H_2O$ **Eqn. 3.2**
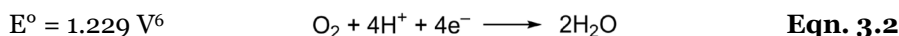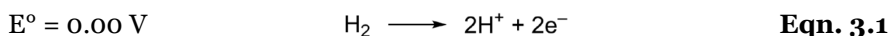
The family of multi-copper oxidases (MCOs) catalyzes the oxidation of various substrates while simultaneously reducing oxygen to water.[7-9] An extensively studied MCO is laccase which bears a trinuclear copper ORR site consisting of type 2 ("normal copper") and type 3 (dinuclear) copper nuclei.[10] Electrochemical studies on immobilized laccase have shown that both dioxygen reduction as well as water oxidation are performed close to the equilibrium potential.[11-17] How laccase is able to perform the ORR close to the equilibrium potential of water is still a very intriguing question.[18, 19]

Synthetic laccase mimics are important for the elucidation of the mechanism wherein dioxygen can be reduced efficiently. Structural and electronic information of key intermediates in the activation of dioxygen by model copper complexes are very valuable references to explain the enzymatic process.[20-25] Yet, the ORR performance of the majority of these copper based model systems is relatively unexplored.

The dinuclear copper complex bearing two 3,5-diamino-1,2,4-triazole (DAT) ligands[26] is considered to be a benchmark system for the ORR as it has been proposed to be a very active synthetic catalyst.[27] The onset potential for the ORR, when deposited on a carbon support, was claimed to be one of the highest reported yet for synthetic copper complexes; that is 0.86 V *versus* RHE at pH 13. For this reason, it was proposed that the structure and ORR activity of this copper complex make the

complex an interesting model for laccase. Nonetheless, the mechanism wherein dioxygen is reduced has not been fully clarified yet.[28-35] No detailed structure of the active species is known. This signifies the relevance of pinpointing the active structure of these species in order to be able to define any catalyst design principles for copper mediated ORR.

In this study, we have investigated the active species of the ORR mediated by the molecular DAT coordinated copper complex and found that not the complex but rather electrodeposited Cu^I and/or Cu^o appears to be the active species.

3.2   Results and discussion

3.2.1   Complex characterization by electron paramagnetic resonance and UV-vis spectroscopy

It was shown in previous studies that the structure of the DAT coordinated copper complex is strongly dependent on the method wherein it is prepared.[26] The first crystal structure of a dinuclear copper complex was obtained by Aznar *et al.*[26] Crystals of $[Cu_2(DAT)_2(\mu-OH_2)(H_2O)_4(SO_4)](SO_4)\cdot3.5H_2O$ (Figure 3.1) were obtained from the supernatant of a poorly soluble 1 : 1 mixture of $CuSO_4$ and DAT. However, when $CuCl_2$ was added to the suspension, a trinuclear species with a bridging sulfate anion was also found. Our first goal was to obtain a water-soluble dinuclear copper complex with DAT and to fully establish its structure in solution by several spectroscopic techniques. The solubility of the complex was significantly enhanced when anions such as triflate (OTf^-) or perchlorate (ClO_4^-) were used instead of sulfate. Figure 3.2 shows the electron paramagnetic resonance (EPR) spectrum of an aqueous solution containing a 1 : 1 ratio of $Cu(OTf)_2$ and DAT. The complex that is formed by this mixture will be further referred to as **Cu(DAT)**. A broad axial signal, corresponding to the triplet state, is observed at g = 2.16
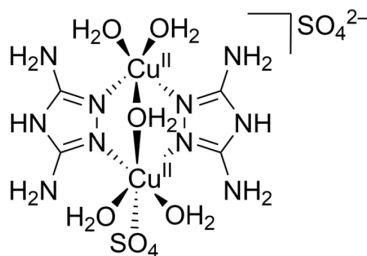
Figure 3.1. Representation of $[Cu_2(DAT)_2(\mu-OH_2)(H_2O)_4(SO_4)](SO_4)\cdot3.5H_2O$ as determined by X-ray crystallography by Ferrer and co-workers.[26]
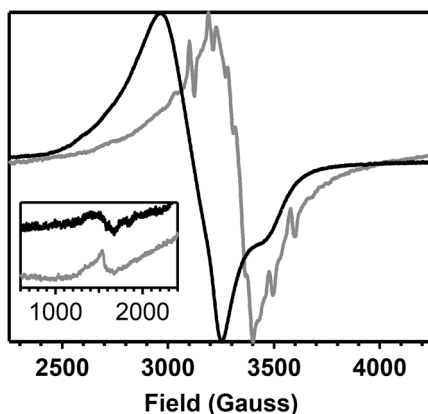
Figure 3.2. A superimposed and normalized EPR spectrum of a 0.02 M aqueous solution of a 1:1 mixture of $Cu(OTf)_2$ and DAT (in black, obtained at 9.36 GHz) and a normalized solid state spectrum of Vulcan|**Cu(DAT)** (in grey, obtained at 9.37 GHz). The inset depicts a zoom of the spectra between 600 and 2400 Gauss. Both spectra were obtained at 77 K.

consistent with the solid-state spectrum of $[Cu_2(DAT)_2(\mu\text{-}OH_2)(H_2O)_4(SO_4)](SO_4)\cdot 3.5H_2O$[26] and typical for a $Cu_2(\mu\text{-triazole})_2$ core.[36-41] In addition, the lack of observable hyperfine interactions is a common feature for these compounds. Moreover, the characteristic weak half field signal corresponding to the forbidden $M_s = \pm 2$ transition was observed, belonging to the thermally populated S = 1 state of the dinuclear Cu^{II} species at temperatures above 20 K. The Cu^{II} sites are antiferromagnetically coupled (S = 0) in the ground state below 20 K.[26] No signals of a S = ½ species, and in particular $Cu(OTf)_2$, were observed [42] This suggests that complete product formation has taken place and that **Cu(DAT)** is indeed a water soluble copper complex with the same $Cu_2(\mu\text{-DAT})_2$ core structure as $[Cu_2(DAT)_2(\mu\text{-}OH_2)(H_2O)_4(SO_4)](SO_4)\cdot 3.5H_2O$. Structurally, it will thus only differ at the position of the sulfate anions. These positions will most likely be taken up by triflate, H_2O, OH^- or buffer. A green solid could be obtained from a **Cu(DAT)** solution by removing water under reduced pressure. The EPR spectrum of the powder showed the same characteristic features as compared to **Cu(DAT)** in solution (Figure B.1) suggesting that the structure of **Cu(DAT)** is retained upon the removal of water. This was further confirmed by SQUID (Superconducting Quantum Interference Device) data (Figure B.2, see appendix). These data confirmed the presence of antiferromagnetically coupled, closely spaced Cu^{II} sites in the solid state with a *J*-coupling constant, isotropic g-factor, and temperature independent (orbital) paramagnetism value of -115.8 cm^{-1}, 2.11, and 5.2×10^{-4} cm^3 mol^{-1}, respectively. Moreover, the a negligibly small intermolecular coupling constant of

1.0×10^{-4} cm^{-1} was found indicating that the formation of polymeric chain structures could be excluded. The structure of **Cu(DAT)** in solution was further validated by the observation of two distinctive peaks in the corresponding UV-Vis spectrum (Figure B.3 and B.4B). The 380 nm absorption correlates to either a charge-transfer band or a high-energy absorption of the Cu^{II} dimer. The exact assignment of this band has been under debate.[26, 40, 41, 43, 44] In addition, a broad signal was observed at circa 740 nm arising from the d-d transition of copper. The stability and solubility of **Cu(DAT)** is very susceptible to changes in the conditions applied. A **Cu(DAT)** solution is not stable over prolonged periods of time (Figure B.3) and therefore must always be freshly prepared. An aqueous solution of 6.6 mM DAT and Cu(OTf)$_2$ in water or 0.1 M NaClO$_4$ has a pH of 4.8 due to the formation of the **Cu(DAT)** complex. Upon protonation of the ligand (pK_a of HDAT$^+$ is 4.4)[45-47], the Cu$_2$(μ-DAT)$_2$ core is disrupted (Figure B.3). At high pH, an insoluble coordination polymer is formed (Figure B.5) as is common for aqueous copper complexes.[48-50] Likewise, changing DAT : Cu(OTf)$_2$ ratios has a large effect as well (Figures B.6 – B.9). The instability of a **Cu(DAT)** solution affects the tolerance towards buffers. Only the Good's buffer 2-(*N*-morpholino)ethanesulfonic acid (MES) was found suitable as it did not disrupt the Cu$_2$(μ-DAT)$_2$ core (Figures B.10 and B.11) and has a buffering capacity close to pH 4.8.[51-53]

3.2.2   Electrochemical quartz crystal microbalance experiments

Cyclic voltammetry (CV) was performed with the same concentration (6.6 mM) **Cu(DAT)** as the UV-vis experiments in a 0.1 M NaClO$_4$ solution to keep conditions identical. Redox couples that are typically found for homogeneous species were not observed (Figure 3.3). Instead, a broad cathodic peak from 0 to 0.8 V was observed as well as an anodic peak with an onset at 0.8 V. Electrochemical quartz crystal microbalance (EQCM) experiments were employed to investigate whether deposition of material on the electrode takes place and thus whether the active species is actually heterogeneous.[54-56] In EQCM experiments, a gold-deposited quartz crystal is used which is oscillated during the electrochemical experiment. Frequency changes of this oscillation can be related directly to the change in mass of the electrode.[57] A decrease in the observed frequency corresponds to an increase in mass. The EQCM data for **Cu(DAT)** show a decrease in frequency when the cathodic region is reached during repeated CV scans (Figure 3.3A). Starting at 0.8 V, a typical scan begins with a positive sweep towards 1.0 V. An anodic peak with an onset of 0.9 V can be observed. This peak was also found in a 6.6 mM solution of DAT in the absence of Cu(OTf)$_2$ (Figure B.12) and is thus related to the oxidation of the ligand.
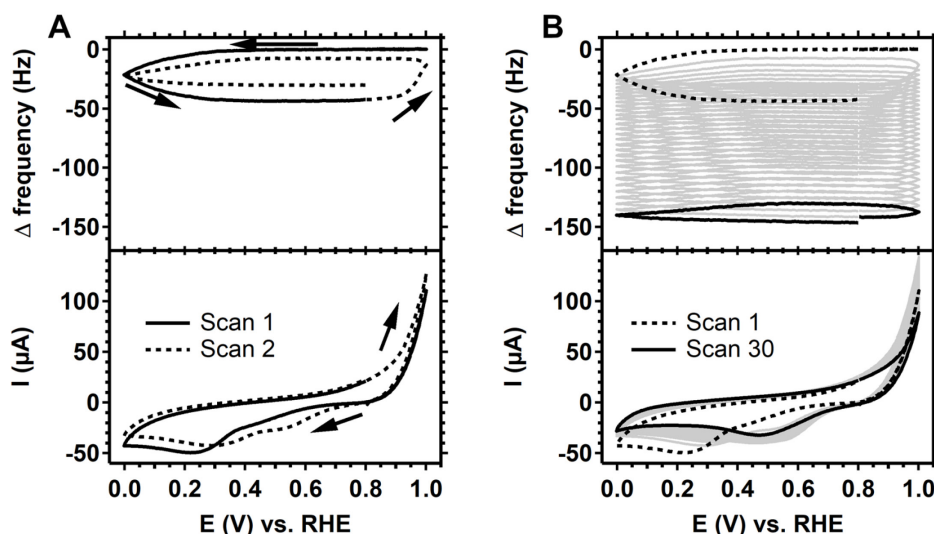
Figure 3.3. A cyclic voltammogram (bottom panel) of a gold electrode in a 0.1 M NaClO$_4$ solution (pH 4.8) containing 6.6 mM of a 1:1 mixture of Cu(OTf)$_2$ and DAT performed at a scan rate of 100 mV s^{-1}. The measurement was combined with a quartz crystal microbalance experiment (top panel). For clarity, only the first two scans are shown in A whereas B shows the full measurement of 30 scans.

When 1.0 V is reached in the first scan, a negative sweep is started and a broad cathodic peak is observed between 0.3 and 0 V. Simultaneously, a decrease in frequency, thus increase in mass, is observed suggesting that the electrochemical reduction triggers deposition of material on the electrode. In subsequent scans, the anodic peak has shifted to 0.8 V and is accompanied by loss of part of the deposition. Also, the cathodic region shifts to 0.5 V. Figure 3.3B shows that after multiple scans, the CV apprehends a stable shape and the overall mass has increased significantly. Thus, a deposition is formed on the electrode by performing CV in this potential window. Likewise, the deposition can be formed potentiostatically when a potential of 0.2 V is applied (Figure B.13). Hence, the oxidative events above 0.8 V are not required for the deposition to occur. Moreover, the activity towards the ORR is roughly the same for electrodes modified by CV or chronoamperometry (Figure B.14). Expanding the potential window up to 1.3 V strips off most of the deposition in one single scan (Figure B.15).

3.2.3   Rotating ring disk electrode experiments

The catalytic activity of the deposition of **Cu(DAT)** was investigated using rotating ring disk electrode (RRDE) experiments. The activity was studied at both pH 5.2 and pH 13 for the reason that we found that the **Cu(DAT)** complex is stable at pH 5.2 but the highest activity has previously been reported at pH 13.[27, 29-31] For these tests, a pyrolytic graphite (PG) working electrode was chosen since gold is active in the same potential window for the ORR (Figure B.16) compared to **Cu(DAT)** and a clear distinction between activity from gold and **Cu(DAT)** cannot be made. Nevertheless, the electrochemistry of **Cu(DAT)** on PG shows qualitatively the same CV as on gold (Figure B.17). As mentioned previously, MES was used as buffer as it leaves the $Cu_2(\mu\text{-DAT})_2$ core intact. PG|**Cu(DAT)** was prepared by cyclic voltammetry between 0 and 1 V for 30 cycles at a 100 mV s^{-1} scan rate in a 0.1 M $NaClO_4$ solution of pH 4.8 containing **Cu(DAT)** followed by thorough rinsing with water. At pH 5.2, the onset for the ORR on a PG|**Cu(DAT)** electrode was found to have shifted to a more positive potential with respect to unmodified PG (Figure 3.4A). The observed current increased considerably upon repetitive potential cycling suggesting that further activation of the catalyst takes place. When the mass
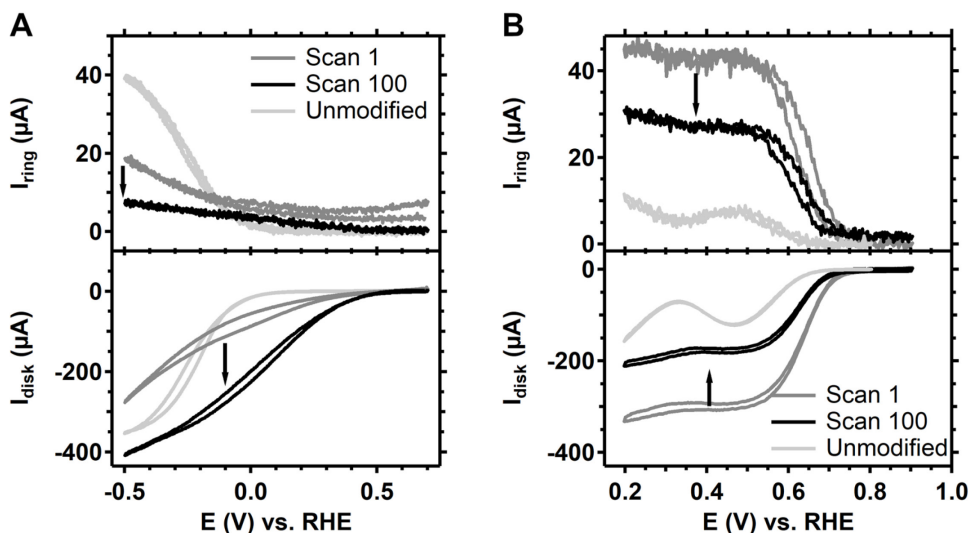
Figure 3.4. Shown here are the cyclic voltammograms (bottom panel) of the PG|**Cu(DAT)** disk rotated at 2000 rpm taken in an oxygen-saturated (a) 0.03 M MES buffer (pH 5.2) in 0.1 M $NaClO_4$ and (b) 0.1 M NaOH (pH 13) solution. In the graphs, the 1st (dark grey line) and 100th scan (black line) of the CV of the disk taken at a 100 mV s^{-1} scan rate are shown. The light grey line depicts the current response of an unmodified PG disk electrode. In addition, the current response of the platinum ring, which was held at a potential of 1.2 V, is shown in the top panel.

transport of dioxygen towards the electrode becomes the limiting factor, a peak current (plateau like region) is expected. However, such a diffusion-limited disk current was not observed. For PG electrodes, it is known that dioxygen is reduced via a 2-electron pathway to H_2O_2 or HOO^- depending on pH (pK_a of H_2O_2 is 11.8).[58, 59] These products are readily oxidized at the platinum ring electrode which is set at a fixed potential of 1.2 V. The ring current for PG|**Cu(DAT)** is significantly lower compared to unmodified PG. Moreover, the ring current decreases over time, which indicates an improvement of selectivity upon prolonged reaction times. An oxidizing ring current can already be observed prior to any ORR taking place at the disk (E > 0.5 V), suggesting that part of the ring current should be attributed to decomposition of the catalyst. Presumably, remnants of the DAT ligand are leaching away from the disk and are being oxidized on the ring as DAT is oxidized at potentials above 0.9 V (Figure B.12). This is in line with a decreasing ratio of nitrogen to copper of the catalytic material at the disk as we will discuss later (Table 3.1). The observed increase in activity and selectivity at pH 5.2 is thus linked to decomposition of PG|**Cu(DAT)**. This increase in activity over time can also be observed with non-rotating Au|**Cu(DAT)** electrodes (Figure B.14 and B.19).

At pH 13, the onset for dioxygen reduction with PG|**Cu(DAT)** was found to shift to a higher potential on the RHE reference scale compared to the ORR at pH 5.2 (Figure 3.4B). Furthermore, a limiting disk current was observed. The activity rapidly decreases over the course of repeated CV scans, and stabilizes after circa 100 scans. A Koutecky-Levich analysis was conducted on the stable limiting catalytic current (see Figure B18A and supporting information). 1.2 electrons are transferred during the electrochemical reduction of dioxygen by PG|**Cu(DAT)**. Apparently, the selectivity of dioxygen reduction has shifted to the formation of mainly superoxide and partly peroxide species. This is further supported by the ring current that has a ratio of almost 100% with respect to the disk current (corrected for the collection efficiency, Figure B.18B).

3.2.4 Electrode characterization with X-ray photoelectron spectroscopy

To determine the composition of the material that is deposited on the electrode, X-ray photoelectron spectroscopy (XPS) was performed on selected samples. An XPS spectrum of the well-defined **Cu(DAT)** powder was measured as reference for the dinuclear $Cu_2(\mu\text{-DAT})_2$ core found for **Cu(DAT)** in solution. In addition, three modified gold electrodes (^CVAu|**Cu(DAT)**, ^CAAu|**Cu(DAT)** and ^CatAu|**Cu(DAT)**) and a modified PG electrode (PG|**Cu(DAT)**) were prepared. Gold

electrodes were used since pyrolytic graphite overlaps with the ligand carbon signals in the C 1s region. Both CVAu|**Cu(DAT)** and CatAu|**Cu(DAT)** were modified under the same conditions as the preparation of PG|**Cu(DAT)** using cyclic voltammetry. However, for the preparation of the XPS sample of PG|**Cu(DAT)** more CV cycles were necessary to obtain a sufficient XPS signal intensity. CAAu|**Cu(DAT)** was prepared potentiostatically for comparison (Figure B.13). CatAu|**Cu(DAT)** was further prepared as post-catalytic reference by performing ORR under at pH 5.2 (Figure B.19).

The Cu $2p_{3/2}$ region of the XPS spectrum of a $Cu(OTf)_2$ reference sample contains two copper species with binding energies of BE (Cu $2p_{3/2}$) 933.5 eV and 936.8 eV that lie in the range typically found for Cu^{II} compounds such as CuO and $Cu(OH)_2$ (Figure 3.5).[60] Moreover, pronounced shake-up satellite features typically observed for Cu^{II} species are present as well between 939 and 950 eV. Additionally, the Auger peak maximum in the Cu $L_3M_{4,5}M_{4,5}$ spectrum with a kinetic energy (KE) of 914.0 eV corresponds to Cu^{II} species. In the C 1s spectrum, four additional peaks can be observed with a BE of 284.8, 286.2, 288.6 and 293.0 eV with the latter being the major species (Figure B.20). This major species corresponds to the $-CF_3$ group of triflate as it has a high BE and a ratio of 1:3 (C:F) with a fluorine species observed at a F 1s BE of 688.7 eV. The Cu 2p region of **Cu(DAT)** also contains the characteristic satellite features and two Cu^{II} species with BE of 936.2 eV and 933.2
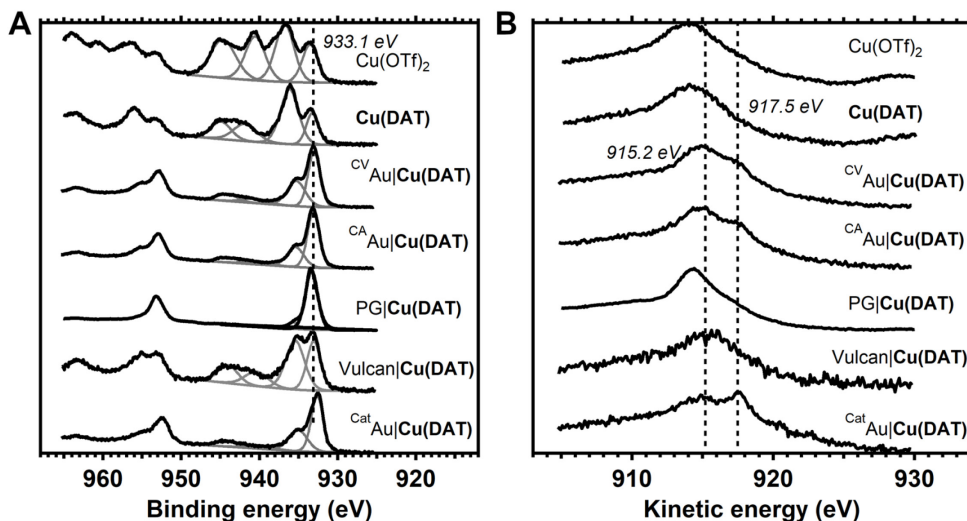
Figure 3.5. XPS spectra (black lines) of the modified electrodes CVAu|**Cu(DAT)**, CAAu|**Cu(DAT)**, CatAu|**Cu(DAT)**, PG|**Cu(DAT)** and the reference compounds **Cu(DAT)**, $Cu(OTf)_2$ and Vulcan|**Cu(DAT)**. A shows the Cu 2p region of the spectra and B shows the Cu $L_3M_{4,5}M_{4,5}$ Auger spectra. In grey, the deconvolution of the Cu $2p_{3/2}$ region is depicted.

eV. The Auger peak at KE = 914.5 eV is correspondingly indicative for the presence of Cu^{II} species. Four carbon species can be observed in the C 1s spectrum of **Cu(DAT)**: two minor species with a BE of 284.8 and 286.5 eV and two major components at 288.6 and 292.6 eV. The latter species matches with the $-CF_3$ group of Cu(OTf)$_2$. In the N 1s region, a major species with a BE of 400.2 eV and a minor species with a BE of 401.6 eV were observed. The nitrogen to carbon ratio of these two nitrogen species with respect to the carbon species with a BE of 288.6 eV is 5:2 (Table 3.1 and Table B.1). This equals the expected 5:2 ratio of DAT; so the C 1s 288.6 eV and the two N 1s species are ascribed to DAT. Also, the ratio of the N 1s species with respect to the Cu 2p$_{3/2}$ species is close to 5:1 (Table 3.1).

Table 3.1. The ratio of nitrogen species with respect to the copper species of the modified electrodes and the reference compound **Cu(DAT)** as determined by XPS.

Sample	Elemental ratio N : Cu[a]
Cu(DAT)	5.6
^{CV}Au|**Cu(DAT)**	3.0
^{CA}Au|**Cu(DAT)**	2.6
PG|**Cu(DAT)**	4.2
^{Cat}Au|**Cu(DAT)**	2.1
Vulcan|**Cu(DAT)**	3.9
^{Cat}GC|Vulcan|**Cu(DAT)**	3.7

[a]The full areas of all species in the N 1s region and in the Cu 2p$_{3/2}$ region are used to determine the ratio.

The XP spectra of the deposition on the modified electrodes ^{CV}Au\|**Cu(DAT)** and ^{CA}Au\|**Cu(DAT)** are almost identical. Thus, the formation of the deposition is not dependent on the preparation method being potentiostatic or potentiodynamic. Clearly, this deposition contains copper species as two Cu^{II} features in the Cu 2p$_{3/2}$ region are observed: a major species with a BE of 933.1 eV and a minor species with shoulder at 935.3 eV. Additionally, the Auger peak has shifted to a KE of 915.2 eV. Both spectra are clearly not identical to **Cu(DAT)**. Rather, the copper species might be associated with the presence of CuO and Cu(OH)$_2$.[60-63] The presence of Cu^{II} species is also confirmed by the existence of shake-up satellite features. For both electrodes, a noteworthy shift has taken place in the C 1s region. A major species with a BE of 287.1 eV and two minor species at 286.2 eV and 288.4 eV are present. The component at 284.8 eV can be ascribed to sp^2 or sp^3 carbon species but also adventitious carbon could contribute to the intensity of this peak. Both carbon species relating to triflate and to DAT are not observed further implying that

78

Cu(DAT) is not present. Moreover, the N 1s species have shifted to a BE of 399.5 eV and 401.1 eV. None of the carbon species has a 5 : 2 ratio with the nitrogen species. Furthermore, the nitrogen to copper ratio has decreased and does not correspond to the expected 5 : 1 ratio anymore. These N 1s peaks still fall in the region previously ascribed to DAT[64, 65], but are distinctively different from those observed in the **Cu(DAT)** reference and do not correspond to DAT anymore.

The modified electrode PG|**Cu(DAT)** has a different composition in the Cu $2p_{3/2}$ spectrum with respect to the Au|**Cu(DAT)** electrodes. Clearly, one major species is present with a BE of 933.3 eV. A minor species with a BE of 935.7 eV can be observed as well, yet less intense than in the Au supported samples. The binding energies fall still in the range expected for Cu^{II} species, and also the Cu $L_3M_{4,5}M_{4,5}$ spectrum contains a relatively sharp peak at a kinetic energy of 914.3 eV suggesting the presence of Cu^{II} species. However, the typical shake-up satellite features supporting formation of a Cu^{II} state are absent in the case of PG|**Cu(DAT)**. Apparently, the electrode material but also film thickness and different leaching rates have some influence on the exact identity of the copper deposition as the Cu 2p spectra differ for PG and Au. The N 1s spectrum contains one species at 399.5 eV at the same position as the major N 1s species found for all Au|**Cu(DAT)** electrodes. Clearly, none of the deposited samples has an electronic structure similar to molecular **Cu(DAT)**.

The spectra of the post-catalysis reference [Cat]Au|**Cu(DAT)** are considerably different from [CV]Au|**Cu(DAT)** and [CA]Au|**Cu(DAT)** indicating a change in composition of the deposition. A major species at 932.6 eV and a minor 934.9 eV species (shoulder) are observed in the Cu $2p_{3/2}$ region. The low BE of the 932.6 eV species is indicative of a more reduced, electron rich species and correlate with Cu^{I} and/or Cu^{o} although exact differentiation cannot be done by XPS solely as Cu^{II} species are observed as well.[60-62] Their presence is indicated by the 934.9 eV species and the minor satellite feature. This is further supported by the Cu $L_3M_{4,5}M_{4,5}$ Auger spectrum that seems to consist of two components with KE of 914.0 eV and 917.5 eV, the latter being indicative of Cu^{I} species.[60-62] The carbon composition has changed as at least four carbon signals are observed at 284.8, 286.3 eV, 287.2 eV and 288.5 eV. However, the intensities of these peaks have decreased with respect to [CA]Au|**Cu(DAT)** and [CV]Au|**Cu(DAT)** (Table B.1). No significant shift is observed for the species in the N 1s region. Notably, both the N : Cu and C : Cu ratios have decreased significantly as compared to [CV]Au|**Cu(DAT)** and [CA]Au|**Cu(DAT)** (Table 3.1 and B.1). Most important is the resemblance of [Cat]Au|**Cu(DAT)** with the XPS spectrum of a previously reported electrodeposited amorphous Cu^{o} film

(Figure 3.6).[63] This amorphous film was prepared galvanostatically in 0.1 M $CuSO_4$ with 10 mM DAT as additive. The film contains considerably more Cu^{II} species than ^{Cat}Au|**Cu(DAT)** based on the shake-up satellite features observed in both spectra (Figure 3.6). Nonetheless, the activity of ^{Cat}Au|**Cu(DAT)** is different from polycrystalline copper in the presence of DAT (Figures B.21 – B.23).
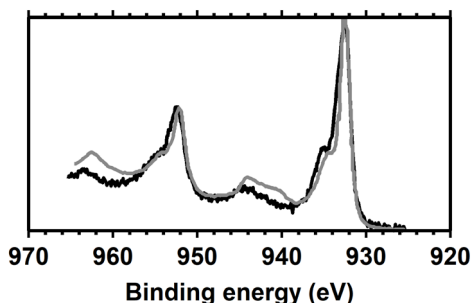

Figure 3.6. Superimposed XPS spectra of the Cu 2p region of ^{Cat}Au|**Cu(DAT)** (solid black line) and of an amorphous electrodeposited copper film formed in the presence of DAT (grey line) as obtained by Hoang *et al.*[63] The spectral data of the dashed line was reprinted and adapted with permission from ref 63. Copyright 2017 American Chemical Society. The data was extracted using ScanIt.[66]

3.2.5   Comparison to previous catalytic studies

Previously, attempts to study the ORR activity of **Cu(DAT)** were made by sequential immobilization of $CuSO_4$ and DAT on a carbon support (Vulcan).[27] This strategy for catalytic studies was chosen as the use of $CuSO_4$ leads to an insoluble analogue of **Cu(DAT)**. Particularly, a suspension of this Vulcan|**Cu(DAT)** catalyst could be dropcasted on a GC electrode for electrochemical ORR measurements (GC|Vulcan|**Cu(DAT)**).[27] In order to relate these results to ours (Scheme 3.1), Vulcan|**Cu(DAT)** was prepared according to the reported procedure (see supporting information).[27] First of all, we essayed the nature of Vulcan|**Cu(DAT)** before any electrochemical survey or contact with buffers (Scheme 3.1). In previous studies no experiments to prove the presence of **Cu(DAT)** within Vulcan|**Cu(DAT)** have been undertaken.[28-35]

A powder EPR spectrum was recorded of Vulcan|**Cu(DAT)** (Figure 3.2). The EPR spectrum of Vulcan|**Cu(DAT)** is very different compared to the EPR spectrum of **Cu(DAT)**. Like **Cu(DAT)**, the spectrum of Vulcan|**Cu(DAT)** does show the $M_s = \pm 2$ transitions indicative of closely spaced Cu^{II} centers. Nonetheless, the low g-factor of 2.00 observed in case of Vulcan|**Cu(DAT)** is very close to that of the free electron (g=2.0023) rather than to values of 2.08 – 2.16 that are typical for triazole

bridged copper sites, including **Cu(DAT)**.[26, 38-41, 67, 68] This suggests that the electronic structure of **Cu(DAT)** and the copper sites in Vulcan|**Cu(DAT)** are largely different and that Vulcan|**Cu(DAT)** does not contain the $Cu_2(\mu\text{-DAT})_2$ core. Whereas the hyperfine coupling in **Cu(DAT)** is not resolved due to the close proximity of both copper sites[26], clear coupling patterns are visible in case of the Vulcan|**Cu(DAT)** sample. These latter splitting patterns are very difficult to simulate. Most likely, Vulcan|**Cu(DAT)** consists from a mixture of different species. Furthermore, XPS analysis shows a clear difference between Vulcan|**Cu(DAT)** and **Cu(DAT)** (Figures 3.5, B.24, and B.25). Instead, the Cu $2p_{3/2}$ and N 1s spectra of
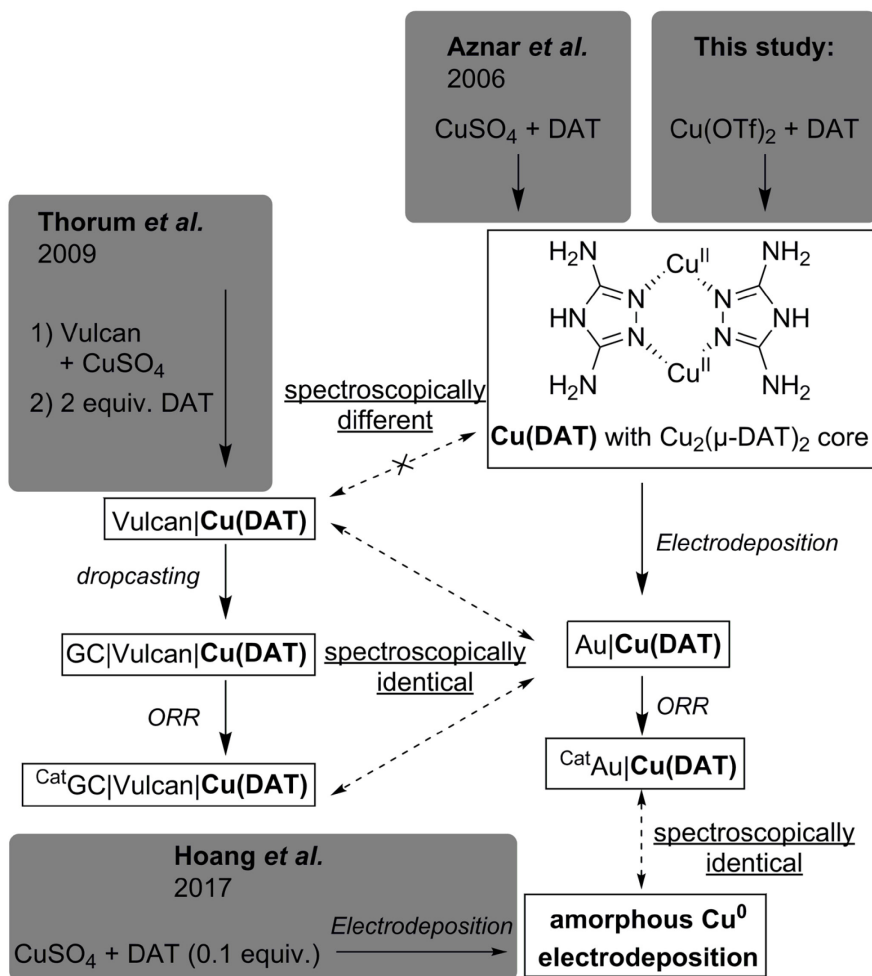
Scheme 3.1. Overview of samples prepared in this study and their spectroscopic similarity with previously reported **Cu(DAT)** related samples from literature.[26, 27, 63]

Vulcan|**Cu(DAT)** are identical to the spectra of the modified electrodes [CA]Au|**Cu(DAT)** and [CV]Au|**Cu(DAT)**. It is remarkable that Vulcan|**Cu(DAT)** already resembles these **Cu(DAT)** deposits prior to any electrochemical treatment (Scheme 3.1).

Analogous to the original study of Thorum *et al.*,[27] a GC electrode (GC|Vulcan|**Cu(DAT)**)) was prepared for catalytic and *post*-catalytic studies by dropcasting Vulcan|**Cu(DAT)** and subsequently studying ORR in a pH 7 Britton-Robinson buffer and a pH 5 MES buffer (Figure B.26 and B.27). The activity of GC|Vulcan|**Cu(DAT)** is significantly higher under RRDE conditions than that of PG|**Cu(DAT)**. The XPS spectra of the Cu $2p_{3/2}$ and N 1s regions of a post catalytic sample [Cat]GC|Vulcan|**Cu(DAT)** were found to be identical to Vulcan|**Cu(DAT)** (Figures B.24 and B.25). In contrast to [CV]Au|**Cu(DAT)**, the composition of the dropcasted [Cat]GC|Vulcan|**Cu(DAT)** does not change upon performing ORR catalysis (Scheme 3.1).

Apparently, Vulcan plays a significant role in the activity of Vulcan|**Cu(DAT)** by stabilizing the structure of the active species, and preventing the formation of Cu⁰. This is in line with previous findings.[27, 28, 32] Instead of forming a $Cu_2(\mu\text{-DAT})_2$ species, the DAT ligand may play a different role in the redox chemistry of GC|Vulcan|**Cu(DAT)**, Au|**Cu(DAT)** and PG|**Cu(DAT)** as it is known to have a corrosion inhibitive effect on copper electrodes (Figure B.22).[69-71]

3.3   Conclusion

We have obtained a water soluble **Cu(DAT)** complex containing the $Cu_2(\mu\text{-DAT})_2$ core identical to the previously reported crystal structure (Scheme 3.1).[26] The **Cu(DAT)** complex in solution is very labile and its structure is extremely dependent on the precise reaction conditions. During electrocatalysis a deposition on the electrode surface is formed, which was found to be the active ORR catalyst. XPS studies showed that the structural integrity of the deposit has significantly changed with respect to the **Cu(DAT)** precursor and, on gold electrodes, is identical to Cu⁰ deposits in the presence of remnants of DAT as found by Hoang *et al.* (Scheme 3.1).[63] XPS analysis has shown that the copper and nitrogen species found in Vulcan|**Cu(DAT)** are the same species found in the electrodeposition that is formed by **Cu(DAT)** on gold electrodes. Neither the deposition formed by **Cu(DAT)**, nor Vulcan|**Cu(DAT)** contains the $Cu_2(\mu\text{-DAT})_2$ core (Scheme 3.1). Consequently, we have shown that the true active species is a copper deposition, which lacks a structural similarity with laccase. Most importantly, our findings signify that, in

order to acquire more precise catalytically active laccase model systems for unraveling detailed structure-activity relationships, it is of vital importance to verify that the catalyst remains intact and does form a copper deposition instead.

3.4   Acknowledgements

3

3.5   Experimental

3.5.1   General

Milli-Q Ultrapure grade water (>18.2 MΩ·cm resistivity) was used for all experiments and for the preparation of aqueous solutions. All chemicals were bought from commercial sources and used without any further purification. 0.1 M aqueous electrolyte solutions were prepared from $NaOH \cdot H_2O$ (TraceSelect ≥99.9995%, Fluka), $NaClO_4 \cdot H_2O$ (EMSURE®, Merck), and 70% $HClO_4$ (Suprapur®, Merck). The 0.03 M 2-(N-morpholino)ethanesulphonic acid (MES buffer, High Purity Grade, VWR) buffer contains 0.1 M $NaClO_4$ to obtain a proper ionic strength and was adjusted to pH 5.2 using NaOH. A 0.04 M pH 7 Britton-Robinson buffer was prepared from H_3PO_4 (85%, Suprapur®, Merck), glacial acetic acid (Honeywell, ≥99.99%), and H_3BO_3 (Sigma Aldrich, ≥99.999%) and adjusted with NaOH to obtain the correct pH. The ionic strength was increased with 0.1 M $NaClO_4$. Electrolytes containing DAT or a 1 : 1 mixture of $Cu(OTf)_2$ and DAT (the complex that is formed by this mixture is further referred to as **Cu(DAT)**) were prepared from $Cu(OTf)_2$ (Alfa Aesar) and/or 3,5-diamino-1,2,4-triazole (Acros). Generally, a 6.6 mM solution of these precursors was prepared by dissolving the appropriate amount of $Cu(OTf)_2$ and/or DAT (simultaneously) in the electrolyte. Other concentrations have been obtained in a similar manner. **Cu(DAT)** solutions were always freshly prepared prior to the measurement because the solution is not stable over a prolonged period of time (Figure B.3). Vulcan|**Cu(DAT)** was prepared according to the reported procedure[27] (see Appendix B).

pH measurements and titrations were performed with either a Hanna Instruments HI 4222 or a Radiometer PHM220 pH meter that were calibrated using standard IUPAC buffers. UV-Vis measurements were performed on a Varian Cary 50 UV-Vis spectrophotometer. Electron paramagnetic resonance (EPR) spectra were recorded on a Bruker EMXplus X-band spectrometer. SQUID measurements were performed on a Quantum Design MPMS-XL 7T SQUID magnetometer employing the settle approach with activated No-overshoot mode om the 300-2K temperature range with varying increment: 5K (300-150K), 2K (150-50K), 1K (50-25K), and 0.5K (25-2K) at constant 5 kOe magnetic field. An automatic diamagnetic correction was applied for a sample holder that was measured separately point-to-point in the same temperature range beforehand. Each data point was averaged over 4 consecutive scans.

3.5.2   Electrochemical experiments

All electrochemical experiments apart from the rotating ring disk electrode (RRDE) experiments and electrochemical quartz crystal microbalance (EQCM) experiments were performed in custom-made single-compartment glass cells using a three-electrode set-up. All glassware used in electrochemical measurements was routinely cleaned by boiling in a 3:1 mixture of concentrated sulfuric and nitric acid. Prior to each experiment, the glassware was cleaned by at least twofold boiling and rinsing with Milli-Q water. Autolab PGSTAT 12, 204 and 128N potentiostats operated by NOVA software were used. All potentials are reported *versus* RHE.

All solutions were purged by argon (Linde, Ar 5.0) for at least 30 minutes prior to each experiment and the cell was kept under a flow of argon during the experiment. Oxygen-saturated solutions were prepared by purging the solution with O_2 (Linde, O_2 5.0) for at least 20 minutes and an oxygen atmosphere was sustained during the experiment.

The counter electrode was a large surface area gold wire that was flame annealed and rinsed with water prior to use. The reference electrode was a platinum mesh in H_2 (Linde, H_2 5.0) saturated electrolyte or a HydroFlex (GasKatel) electrode working at the same pH as the working electrode. Any unbuffered solutions were acidified with $HClO_4$ to obtain the correct pH. The cell and reference electrode were connected via a Luggin capillary. The working electrode (WE) was either a pyrolytic graphite (PG) electrode or a gold electrode used in hanging meniscus configuration. PG was sanded with 600 and 1000 grit sandpaper followed by 10 minutes sonication in water prior to use. The gold working electrode was a gold plate that was cleaned prior to use by applying 10 V between the gold WE and a graphite counter electrode

for 30 seconds in a 10% H_2SO_4 solution. This was followed by dipping the gold WE in 6 M HCl for 30 seconds. Next, the electrode was rinsed with water and flame annealed. The electrode was subsequently electrochemically polished by cyclic voltammetry (CV) between 0 and 1.75 V *versus* RHE for 200 cycles at a 1 V s^{-1} scan rate in a 0.1 M $HClO_4$ solution.

RRDE experiments were performed in a custom-made two-compartment cell using a three-electrode set-up. The counter electrode was used in a different compartment from the rotating disk electrode separated by a water permeable glass frit. A platinum (0.196 cm^2), gold (0.196 cm^2), pyrolytic graphite (0.12 cm^2), glassy carbon (0.196 cm^2) or copper disk (0.196 cm^2) was used. All disk electrodes and the platinum ring were obtained from Pine Instruments and used in a ChangeDisk configuration using a Pine MSR rotator. Prior to use, the copper, gold, glassy carbon or platinum disk and platinum ring electrodes were mechanically polished for 2 minutes with subsequent rinsing and sonication in water for 10 minutes with 1.0, 0.3 and 0.05 micron alumina slurry respectively. The pyrolytic graphite disk was polished for 20 seconds with each alumina slurry. Next, electrochemical polishing was applied. The copper electrode was repeatedly electrochemically polished by applying 3 V for 10 seconds between the disk and a copper counter electrode in a 66% H_3PO_4 solution after which 0 V was applied for at least 30 seconds.[72] Gold was cleaned by cyclic voltammetry as previously mentioned. Platinum was cleaned by cyclic voltammetry between 1.8 V and −0.2 V at 500 mV s^{-1} for 50 cycles in a 0.5 M H_2SO_4 solution.

EQCM experiments were performed in an Autolab 3 ml Teflon EQCM cell using an Autolab gold EQCM electrode (0.35 cm^2) as working electrode that consists of a 200 nm gold layer deposited on a quartz crystal. A modified RHE reference electrode was used which prevents interference of continuous hydrogen bubbling to the sensitive microbalance signal.[73]

3.5.3   X-ray photoelectron spectroscopy

X-ray photoelectron spectroscopy (XPS) was performed on a Thermo Scientific K-Alpha spectrometer equipped with a monochromatic small-spot X-ray source and a double focusing

hemispherical analyzer with a 128-channel delay line detector. Spectra were obtained by using an aluminum anode (Al K_α = 1486.6 eV) operated at 72 W and a spot size of 400 μm. Survey scans were measured at constant pass energy of 200 eV, and high-resolution scans of the separate regions were measured at 50 eV pass energy. The background pressure of the ultra-high vacuum (UHV) chamber was

2×10^{-8} mbar. Sample charging was compensated for by the use of an electron flood gun, and binding energy (BE) calibration was done by setting the C 1s peak of sp^3 (CH, CC) carbon to BE(C 1s) = 284.8 eV. Electrode samples for XPS analysis with electrochemical deposition from **Cu(DAT)** were prepared by either cyclic voltammetry (^{CV}Au|**Cu(DAT)** and ^{Cat}Au|**Cu(DAT)**, PG|**Cu(DAT)**) or chronoamperometry (^{CA}Au|**Cu(DAT)**). Further details of the preparation of these samples can be found Appendix B. After modification by cyclic voltammetry, oxygen reduction catalysis was performed with ^{Cat}Au|**Cu(DAT)** before subjecting the electrode to XPS analysis. The electrodes were consistently kept under an inert atmosphere during transfer, handling and introduction to the XPS apparatus. For sample ^{Cat}Au|**Cu(DAT)**, no special care was taken to prevent contact with air. ^{Cat}GC|Vulcan|**Cu(DAT)** for XPS analysis was prepared by dropcasting Vulcan|**Cu(DAT)** onto a freshly polished GC electrode (0.07 cm^2) according to the reported procedure.[27]

The XP spectra of the powders Vulcan|**Cu(DAT)** and **Cu(DAT)** were obtained by containing the powder in a powder sample holder (ThermoScientific). The **Cu(DAT)** powder was obtained from a 6.6 mM solution of a 1 : 1 ratio of Cu(OTf)$_2$ and DAT in water. A green powder could be retrieved after removing water under reduced pressure.

3.6   References

1.   Gasteiger, H. A.; Kocha, S. S.; Sompalli, B.; Wagner, F. T., *Appl. Catal., B* **2005,** *56*, 9–35.
2.   Gewirth, A. A.; Thorum, M. S., *Inorg. Chem.* **2010,** *49*, 3557–3566.
3.   Nørskov, J. K.; Rossmeisl, J.; Logadottir, A.; Lindqvist, L.; Kitchin, J. R.; Bligaard, T.; Jónsson, H., *J. Phys. Chem. B* **2004,** *108*, 17886–17892.
4.   Gröger, O.; Gasteiger, H. A.; Suchsland, J.-P., *J. Electrochem. Soc.* **2015,** *162*, A2605–A2622.
5.   Kongkanand, A.; Mathias, M. F., *J. Phys. Chem. Lett.* **2016,** *7*, 1127–1137.
6.   Bratsch, S. G., *J. Phys. Chem. Ref. Data* **1989,** *18*, 1–21.
7.   Bullen, R. A.; Arnot, T. C.; Lakeman, J. B.; Walsh, F. C., *Biosens. Bioelectron.* **2006,** *21*, 2015–2045.
8.   Calabrese Barton, S.; Gallaway, J.; Atanassov, P., *Chem. Rev.* **2004,** *104*, 4867–4886.
9.   Cracknell, J. A.; Vincent, K. A.; Armstrong, F. A., *Chem. Rev.* **2008,** *108*, 2439–2461.
10.   Solomon, E. I.; Sundaram, U. M.; Machonkin, T. E., *Chem. Rev.* **1996,** *96*, 2563–2606.
11.   Soukharev, V.; Mano, N.; Heller, A., *J. Am. Chem. Soc.* **2004,** *126*, 8368–8369.
12.   Mano, N.; Soukharev, V.; Heller, A., *J. Phys. Chem. B* **2006,** *110*, 11180–11187.
13.   Blanford, C. F.; Heath, R. S.; Armstrong, F. A., *Chem. Commun.* **2007,** 1710–1712.
14.   Pita, M.; Mate, D. M.; Gonzalez-Perez, D.; Shleev, S.; Fernandez, V. M.; Alcalde, M.; De Lacey, A. L., *J. Am. Chem. Soc.* **2014,** *136*, 5892–5895.
15.   Thorum, M. S.; Anderson, C. A.; Hatch, J. J.; Campbell, A. S.; Marshall, N. M.; Zimmerman, S. C.; Lu, Y.; Gewirth, A. A., *J. Phys. Chem. Lett.* **2010,** *1*, 2251–2254.
16.   Davis, F.; Higson, S. P. J., *Biosens. Bioelectron.* **2007,** *22*, 1224–1235.
17.   Koper, M. T. M., Catalysis of Redox Reactions. In *Comprehensive Inorganic Chemistry II (Second Edition)*, Reedijk, J.; Poeppelmeier, K., Eds. Elsevier: Amsterdam, 2013; Vol. 8, pp 459–474.
18.   Solomon, E. I.; Augustine, A. J.; Yoon, J., *Dalton Trans.* **2008,** 3921–32.
19.   Rulíšek, L.; Ryde, U., *Coord. Chem. Rev.* **2013,** *257*, 445–458.

20. Thorseth, M. A.; Tornow, C. E.; Tse, E. C. M.; Gewirth, A. A., *Coord. Chem. Rev.* **2013,** *257*, 130–139.
21. Mirica, L. M.; Ottenwaelder, X.; Stack, T. D. P., *Chem. Rev.* **2004,** *104*, 1013–1046.
22. Lewis, E. A.; Tolman, W. B., *Chem. Rev.* **2004,** *104*, 1047–1076.
23. Haack, P.; Limberg, C., *Angew. Chem. Int. Ed.* **2014,** *53*, 4282–4293.
24. Serrano-Plana, J.; Garcia-Bosch, I.; Company, A.; Costas, M., *Acc. Chem. Res.* **2015,** *48*, 2397–2406.
25. Hong, S.; Lee, Y.-M.; Ray, K.; Nam, W., *Coord. Chem. Rev.* **2017,** *334*, 25–42.
26. Aznar, E.; Ferrer, S.; Borrás, J.; Lloret, F.; Liu-González, M.; Rodríguez-Prieto, H.; García-Granda, S., *Eur. J. Inorg. Chem.* **2006,** 5115–5125.
27. Thorum, M. S.; Yadav, J.; Gewirth, A. A., *Angew. Chem. Int. Ed.* **2009,** *48*, 165–167.
28. Brushett, F. R.; Thorum, M. S.; Lioutas, N. S.; Naughton, M. S.; Tornow, C.; Jhong, H.-R.; Gewirth, A. A.; Kenis, P. J. A., *J. Am. Chem. Soc.* **2010,** *132*, 12185–12187.
29. Goenaga, G. A.; Belapure, A.; Zhang, C.; Papandrew, A.; Foister, S.; Zawodzinski, T., *ECS Trans.* **2011,** *41*, 1193–1205.
30. Kato, M.; Kimijima, K. i.; Shibata, M.; Notsu, H.; Ogino, K.; Inokuma, K.; Ohta, N.; Uehara, H.; Uemura, Y.; Oyaizu, N.; Ohba, T.; Takakusagi, S.; Asakura, K.; Yagi, I., *Phys. Chem. Chem. Phys.* **2015,** *17*, 8638–8641.
31. Kato, M.; Oyaizu, N.; Shimazu, K.; Yagi, I., *J. Phys. Chem. C* **2016,** *120*, 15814–15822.
32. Thorum, M. S.; Hankett, J. M.; Gewirth, A. A., *J. Phys. Chem. Lett.* **2011,** *2*, 295–298.
33. Barile, C. J.; Tse, E. C. M.; Li, Y.; Sobyra, T. B.; Zimmerman, S. C.; Hosseini, A.; Gewirth, A. A., *Nat. Mater.* **2014,** *13*, 619–623.
34. Koshikawa, H.; Nakanishi, S.; Hashimoto, K.; Kamiya, K., *Electrochim. Acta* **2015,** *180*, 173–177.
35. Tse, E. C. M.; Barile, C. J.; Kirchschlager, N. A.; Li, Y.; Gewargis, J. P.; Zimmerman, S. C.; Hosseini, A.; Gewirth, A. A., *Nat. Mater.* **2016,** *15*, 754–759.
36. Koomen-Van Oudenniel, W. M. E.; De Graaff, R. A. G.; Haasnoot, J. G.; Prins, R.; Reedijk, J., *Inorg. Chem.* **1989,** *28*, 1128–1133.
37. van Koningsbruggen, P. J.; Haasnoot, J. G.; Kooijman, H.; Reedijk, J.; Spek, A. L., *Inorg. Chem.* **1997,** *36*, 2487–2489.
38. Slangen, P. M.; van Koningsbruggen, P. J.; Haasnoot, J. G.; Jansen, J.; Gorter, S.; Reedijk, J.; Kooijman, H.; Smeets, W. J. J.; Spek, A. L., *Inorg. Chim. Acta* **1993,** *212*, 289–301.
39. Slangen, P. M.; van Koningsbruggen, P. J.; Goubitz, K.; Haasnoot, J. G.; Reedijk, J., *Inorg. Chem.* **1994,** *33*, 1121–1126.
40. Ferrer, S.; J. van Koningsbruggen, P.; G. Haasnoot, J.; Reedijk, J.; Kooijman, H.; L. Spek, A.; Lezama, L.; M. Arif, A.; S. Miller, J., *J. Chem. Soc., Dalton Trans.* **1999,** 4269–4276.
41. Prins, R.; Birker, P. J. M. W. L.; Haasnoot, J. G.; Verschoor, G. C.; Reedijk, J., *Inorg. Chem.* **1985,** *24*, 4128–4133.
42. Santangelo, M. G.; Medina-Molner, A.; Schweiger, A.; Mitrikas, G.; Spingler, B., *J. Biol. Inorg. Chem.* **2007,** *12*, 767–775.
43. Nonoyama, K.; Ojima, H.; Nonoyama, M., *Inorg. Chim. Acta* **1984,** *84*, 13–18.
44. Reedijk, J.; Knetsch, D.; Nieuwenhuijse, B., *Inorg. Chim. Acta* **1971,** *5*, 568–572.
45. Antolini, L.; Fabretti, A. C.; Gatteschi, D.; Giusti, A.; Sessoli, R., *Inorg. Chem.* **1991,** *30*, 4858–4860.
46. Fabretti, A. C., *J. Crystallogr. Spectrosc. Res.* **1992,** *22*, 523–526.
47. Kröger, G. F.; Freiberg, W., *Z. Chem.* **1965,** *5*, 381–382.
48. Zhang, T.; Wang, C.; Liu, S.; Wang, J.-L.; Lin, W., *J. Am. Chem. Soc.* **2014,** *136*, 273–281.
49. Gomez, V.; Benet-Buchholz, J.; Martin, E.; Galan-Mascaros, J. R., *Eur. J. Inorg. Chem.* **2014,** *2014*, 3125–3132.
50. Boland, Y.; Tinant, B.; Safin, D. A.; Marchand-Brynaert, J.; Clerac, R.; Garcia, Y., *CrystEngComm* **2012,** *14*, 8153–8155.
51. Good, N. E.; Winget, G. D.; Winter, W.; Connolly, T. N.; Izawa, S.; Singh, R. M. M., *Biochemistry* **1966,** *5*, 467–477.
52. Kandegedara, A.; Rorabacher, D. B., *Anal. Chem.* **1999,** *71*, 3140–3144.
53. Mash, H. E.; Chin, Y.-P.; Sigg, L.; Hari, R.; Xue, H., *Anal. Chem.* **2003,** *75*, 671–677.
54. Schley, N. D.; Blakemore, J. D.; Subbaiyan, N. K.; Incarvito, C. D.; D'Souza, F.; Crabtree, R. H.; Brudvig, G. W., *J. Am. Chem. Soc.* **2011,** *133*, 10473–10481.
55. van der Ham, C. J. M.; Işık, F.; Verhoeven, T. W. G. M.; Niemantsverdriet, J. W.; Hetterscheid, D. G. H., *Catal. Today* **2017,** *290*, 33–38.
56. Hetterscheid, D. G. H., *Chem. Commun.* **2017,** *53*, 10622–10631.
57. Sauerbrey, G., *Z. Phys.* **1959,** *155*, 206–222.

3

58. Paliteiro, C.; Hamnett, A.; Goodenough, J. B., *J. Electroanal. Chem. Interfacial Electrochem.* **1987,** *233*, 147–159.
59. Eul, W.; Moeller, A.; Steiner, N., Hydrogen Peroxide. In *Kirk-Othmer Encyclopedia of Chemical Technology* [Online] John Wiley & Sons, Inc.: 2000. http://dx.doi.org/10.1002/0471238961.0825041808051919.a01.pub2.
60. Biesinger, M. C.; Lau, L. W. M.; Gerson, A. R.; Smart, R. S. C., *Appl. Surf. Sci.* **2010,** *257*, 887–898.
61. Poulston, S.; Parlett, P. M.; Stone, P.; Bowker, M., *Surf. Interface Anal.* **1996,** *24*, 811–820.
62. NIST X-ray Photoelectron Spectroscopy Database. National Institute of Standards and Technology: Gaithersburg, 2012; Vol. Version 4.1.
63. Hoang, T. T. H.; Ma, S.; Gold, J. I.; Kenis, P. J. A.; Gewirth, A. A., *ACS Catal.* **2017,** *7*, 3313–3321.
64. Finšgar, M., *Corros. Sci.* **2013,** *77,* 350–359.
65. Vasimalai, N.; John, S. A., *J. Mater. Chem. A.* **2013,** *1*, 4475–4482.
66. Balen, J. v. *ScanIt*, 2.05; AmsterCHEM: 2017.
67. Hathaway, B. J.; Billing, D. E., *Coord. Chem. Rev.* **1970,** *5*, 143–207.
68. Solomon, E. I.; Heppner, D. E.; Johnston, E. M.; Ginsbach, J. W.; Cirera, J.; Qayyum, M.; Kieber-Emmons, M. T.; Kjaergaard, C. H.; Hadt, R. G.; Tian, L., *Chem. Rev.* **2014,** *114*, 3659–3853.
69. Guo, L.; Dong, W.; Zhang, S., *RSC Adv.* **2014,** *4*, 41956–41967.
70. El Ibrahimi, B.; Soumoue, A.; Jmiai, A.; Bourzi, H.; Oukhrib, R.; El Mouaden, K.; El Issami, S.; Bazzi, L., *J. Mol. Struct.* **2016,** *1125*, 93–102.
71. Zarrouk, A.; Hammouti, B.; Al-Deyab, S. S.; Salghi, R.; Zarrok, H.; Jama, C.; Bentiss, F., *Int. J. Electrochem. Sci.* **2012,** *7*, 5997–6011.
72. P. Schouten, K. J.; Gallent, E. P.; Koper, M. T. M., *J. Electroanal. Chem.* **2013,** *699*, 6–9.
73. Abril, P.; del R1´o, M. P.; Tejel, C.; Verhoeven, T. W. G. M.; Niemantsverdriet, J. W. H.; van der Ham, C. J. M.; Kottrup, K. G.; Hetterscheid, D. G. H., *ACS Catal.* **2016,** *6*, 7872–7875.

3

Chapter 4

A selective molecular dinuclear copper oxygen reduction catalyst for the electrochemical synthesis of H_2O_2 at neutral pH

*H_2O_2 is a bulk chemical used in a variety of applications as, for example, bleaching, or as a disinfecting agent. The anthraquinone process is the sole bulk production method of H_2O_2 which inherently has a negative effect on the energy and cost requirements as various purifications steps are required. The electrochemical O_2 reduction to H_2O_2 is viable alternative with examples of the direct production of up to 20% H_2O_2 solutions. We found that H_2O_2 over-reduction was significantly blocked for the dinuclear copper complex **Cu₂(btmpa)** (btmpa = 6,6'-bis[[bis(2-pyridylmethyl)amino]methyl]-2,2'-bipyridine) due to slow electron transfer in the Cu^{II} to Cu^{I} reduction. Electrochemically, **Cu₂(btmpa)** was found to reduce O_2 with a selectivity in the start of a measurement up to 90% towards H_2O_2 according to rotating ring disk electrode (RRDE) measurements. Quartz crystal microbalance measurements showed that reduction of the complex leads to an adsorption on the electrode. This adsorption results in accumulation of active sites on the carbon electrode thereby increasing the O_2 reduction current from –0.2 to –0.4 mA at 0.0 V which is close to the theoretical diffusion limited current. In addition, the Faradaic efficiency for H_2O_2 remained up to 60 to 70% for 2 hours during chronoamperometry experiments at 0.0 V as was determined by periodic enzyme based photometric measurements. After 2 hours, rising concentrations of H_2O_2 intensify Cu^0 deposition that progressively lowers the Faradaic efficiency by over-reduction of H_2O_2. Nevertheless, we found that the efficiency can be improved by introducing high potential intervals to strip Cu^0. Moreover, we showed that H_2O_2 interception by re-oxidation in a RRDE setup plays an important role in tempering Cu^0 deposition. Fine-tuning the operating potential, interval timing and being able to intercept formed H_2O_2 all could help to retain the high Faradaic efficiency. For the first time, extensive studies into the long term electrochemical O_2 to H_2O_2 reduction by a molecular complex have been performed which allowed to retain the high intrinsic selectivity of **Cu₂(btmpa)** towards electrochemical H_2O_2 production.*

4.1　Introduction

H₂O₂ is a bulk chemical that is produced on a 4.5 million ton scale[1] and used in many applications[2] such as bleaching (largest single use),[3, 4] waste water treatment,[5, 6] disinfecting, and industrial organic synthesis.[7] It is one of the most environmentally friendly chemical oxidants because the decomposition products are water and/or O₂. Moreover, up to 50% of the oxygens in H₂O₂ are used in the oxidation thereby enhancing the atomic efficiency with respect to other chemical oxidations such as $NaIO_4$ and tBuOOH.[8] Even though H₂O₂ is considered as environmentally friendly, its current production method is certainly not. Over 90% of the worldwide H₂O₂ production is via the anthraquinone process.[2, 8] Here, anthraquinones are used as redox mediators that first undergo reduction with H₂, followed by a separate re-oxidation in the presence of air (O₂) which produces H₂O₂ selectively. Liquid-liquid extractions are required to extract H₂O₂ given that these reactions take place in organic solvent. Consequently, the obtained H₂O₂ is contaminated with organic impurities. As a result, most of the cost and energy of producing H₂O₂ result from the purification of this extract.

The electrochemical reduction of O₂ to H₂O₂ is a viable alternative for the anthraquinone process and was first reported in 1939 by Berl.[9] In fact, it has been industrialized in the Huron-Dow process which is mostly used for on-site production of alkaline peroxide mixtures for the paper bleaching industry. Nevertheless, this only covers a negligible fraction of the total H₂O₂ production.[2, 8] To overcome the problem of separating the H₂O₂ from the aqueous electrolyte, solid electrolyte cells in combination with flow cell chemistry have recently been proposed as a feasible option.[10] Specifically, H₂O₂ solutions up to 20% with higher purity than the anthraquinone process could be directly obtained. The cathode, where O₂ reduction takes place, can be made of several materials. Noble metals are usually not the best choice since they either catalyze the full 4 electron reduction to H₂O, or they interact weakly with O₂ resulting in low rates and a high overpotential.[11] Attempts to combine these characteristics in alloys have resulted in better catalysts,[11] such as Pt–Hg,[12] Pd–Hg,[13] and Pd–Au[14] alloys. Another interesting approach is the use of carbon based catalysts. In general, carbon electrodes have an intrinsic selectivity towards the formation of H₂O₂ when performing O₂ reduction.[15] Their reactivity is however quite poor, and application of such materials therefore requires large overpotentials.[11] Improvements can be made by increasing the defect[16] [17] and/or oxygen content,[18, 19] doping with heteroatoms,[20-23] or doping with metals as single-site catalysts. For the latter, molecular complexes can help to establish good adsorption through ligand-

carbon interactions because metal–support interactions for carbon are relatively weak.[11] Most molecular catalysts, that have been reported to perform the reduction of O_2 to H_2O_2, have only been studied in non-aqueous solvents.[24-26] Mechanisms and selectivity depend significantly on the acid type and acid strength and cannot be directly translated to aqueous solutions. Until now, high selectivity for electrocatalytic H_2O_2 production in aqueous solutions is observed only for a few manganese,[27, 28] iron,[29-32] copper,[28, 33] and cobalt complexes.[28, 32, 34-39] The initial high selectivity is often restricted to a small potential window and only observed for a few minutes. Longer measurements are often not performed. If performed, they typically result in an overall 4 electron selectivity either due to over-reduction of H_2O_2 or due to the disproportionation of H_2O_2, also catalyzed by these molecular catalysts.[30] Thus far, there is only one exception of a cobalt tetrakis(*N*-methyl-4-pyridyl)porphyrin complex that was reported with high selectivity (>90%) for H_2O_2 after 2 hours of electrolysis, but apart of this claim no further details were provided.[34]

Our group reported [Cu(tmpa)(L)]$^{2+}$ (**Cu(tmpa)**, Chart 4.1, tmpa = tris(2-pyridylmethyl)amine, L = solvent) for the electrochemical 4 electron reduction of O_2 to H_2O that proceeds in a stepwise mechanism with H_2O_2 as detectable intermediate.[33] At pH 7, two separate catalytic cycles for O_2 to H_2O_2 and H_2O_2 to H_2O reduction take place with onsets of 0.50 and 0.45 V *versus* the reversible hydrogen electrode (RHE), respectively. The suggested O_2 to H_2O_2 reduction mechanism starts with coordination of O_2 to a reduced Cu^I complex resulting in the previously reported end-on copper superoxo complex.[40, 41] Subsequently, a PCET (proton coupled electron transfer) most likely results in formation of a hydroperoxo complex and is followed by a proton transfer to produce H_2O_2. Further reduction of H_2O_2 most likely takes place by Fenton type chemistry which splits H_2O_2 in a copper bound hydroxyl and free hydroxyl radical.[42, 43] Both the reduction of O_2 and H_2O_2 are very fast and mass transport limited in oxygen at almost all conditions. For that reason, high selectivity for H_2O_2 can only be observed close to the onset potential of the reduction of O_2 to H_2O_2. At more negative potentials, the formed H_2O_2 is over-reduced to H_2O.

Even though **Cu(tmpa)** is an intrinsic very fast catalyst for the O_2 to H_2O_2 reduction, the over-reduction of H_2O_2 is equally fast limiting the applicability for H_2O_2 production. For that reason, we set out to investigate **Cu₂(btmpa)** (Chart 4.1): the dicopper complex [Cu₂(btmpa)(L)₄]$^{4+}$ (btmpa = 6,6'-bis[[bis(2-pyridylmethyl)amino]methyl]-2,2'-bipyridine) which is consisting of two **Cu(tmpa)** moieties fused via a covalent bond between one of the three pyridines on each moiety resulting in a bipyridine backbone.[44-46] An earlier report suggested that
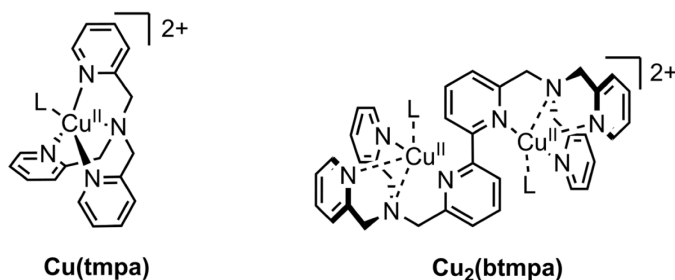
Chart 4.1. Structures of **Cu(tmpa)** and **Cu$_2$(btmpa)**.

the Cu^I complex of **Cu$_2$(btmpa)** had diminished reactivity towards O$_2$ with respect to **Cu(tmpa)** since an O$_2$ purged solution of **Cu$_2$(btmpa)** only showed a very slow color change over the course of several hours.[46] Also, the Cu$^{I/II}$ redox couple potential had shifted positively with respect to **Cu(tmpa)** in organic solvents indicating that the Cu^I state was thermodynamically more favorable. Moreover, the geometry of the Cu^I complex was significantly different from the Cu^I complex of **Cu(tmpa)** as was concluded from ^{1}H NMR data. As these properties could influence the electrochemical O$_2$ and H$_2$O$_2$ reduction significantly, we were interested whether H$_2$O$_2$ selectivity could be improved. Indeed, we found that H$_2$O$_2$ reduction was mostly inhibited resulting in a high selectivity for H$_2$O$_2$. In addition, we performed for the first time a systematic study of long bulk electrosynthesis of H$_2$O$_2$ by a molecular catalyst. By performing long amperometry measurements, we were able to identify factors that limit the Faradaic efficiency, improve the process, and thereby achieve up to 70% Faradaic efficiency for H$_2$O$_2$ over the course of 2 hours.

4.2   Results and Discussion

4.2.1   Synthesis, magnetic properties, and electrochemistry

The dinucleating btmpa ligand was synthesized by the S$_N$2 reaction of 6,6'-(dichloromethyl)-2,2'-bipyridine (**4**) and commercially available 2,2'-dimethylpyridylamine (dmpa) following literature proceedings.[45] The earlier reported synthesis was slightly adjusted by using **4** which bears a chloromethyl instead of bromomethyl moiety (Scheme 4.1). We found that unreacted dmpa was hard to remove by common chromatography methods as both btmpa and dmpa display significant tailing. Therefore, an additional purification method was developed to improve the yield of pure btmpa (for details, see the experimental section). In short, dmpa is selectively converted to an amide by adding hexanoic

anhydride to the crude mixture of dmpa and **4**. This amide can easily be removed by chromatography methods and btmpa was successfully purified with a yield of 21%. Next, the Cu^{II} complex was synthesized by mixing a solution of $Cu^{II}(CF_3SO_3)_2$, and btmpa. After recrystallization by vapor diffusion of diethyl ether in a methanolic solution, blue colored crystals of the complex were obtained with 63% yield with $[Cu_2(btmpa)(CH_3OH)_2](CF_3SO_3)_4$ as molecular formula determined by elemental analysis. Neutral aqueous solutions containing **Cu₂(btmpa)** are blue colored arising from a broad Cu^{II} d-d transition at 675 nm (Figure C.1).

      Cu₂(btmpa) has two copper centra which could interact with each other. A possible magnetic interaction between the copper centra can be investigated with EPR (electron paramagnetic resonance) and SQUID (superconducting quantum interference device) spectroscopy. From fitted SQUID data, a small (ferromagnetic) coupling of 34 cm^{-1} was found and EPR did not show any evidence for large coupling between both copper centers (Figures C.2 and C.3). Another interesting aspect of the dinuclear complex is the equilibrium potential of the $Cu^{I/II}$ redox couple of the two copper centers in aqueous solutions. Previous electrochemical studies of **Cu₂(btmpa)** in organic solvents suggested that the two copper centers are reduced simultaneously because only one redox couple was observed. In addition, their equilibrium potential shifted positively with respect to the mononuclear **Cu(tmpa)**.[46] Therefore, cyclic voltammetry (CV) under an argon atmosphere in a pH 7 phosphate buffer was performed. This revealed only one redox wave for the Cu^{I}/Cu^{II} redox couple (Figure 4.1A) at 0.51 V *versus* the Reversible Hydrogen Electrode (RHE). Interestingly, the $E_{1/2}$ of the redox couple of **Cu₂(btmpa)** has shifted 0.30 V positively with respect to **Cu(tmpa)**. A previously published crystal structure of a $[(btmpa)Cu_2(CH_3\text{-}CN)_2(ClO_4)_2]^{2+}$ complex showed that the Cu–N bond
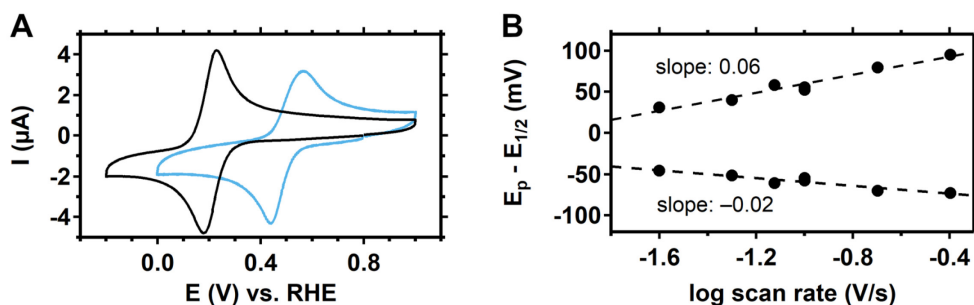
Figure 4.1. (A) Cyclic voltammogram of a 0.15 mM **Cu₂(btmpa)** solution (blue) and a 0.3 mM **Cu(tmpa)**[33] solution (black) under an argon atmosphere in a 0.1 M phosphate buffer of pH 7 with a scan rate of 100 mV/s. (B) Laviron plot of the cathodic and anodic peak positions of **Cu₂(btmpa)** and the slopes of linear fits.

of the bipyridine moiety has longer distances (2.4 Å) than the other pyridines (2.0 Å).[46] As a result, the Cu[II] site is less electron dense than **Cu(tmpa)** which explains the positive shift of the Cu[I/II] redox couple. The Cu[I/II] redox couple has a large peak separation of 0.12 V at 100 mV/s scan rate. Varying the scan rate did not reveal a second redox couple, but instead revealed that the peak separation increases with increasing scan rate (Figure 4.1B). This points to a relative slow electron transfer process due to restricted reorganization of the geometry of **Cu₂(btmpa)** when reduced and re-oxidized. In contrast, the reduction of the mononuclear **Cu(tmpa)** complex is a very fast process[33] due to the easy transition of a trigonal bipyramidal geometry of the Cu[II] complex to the preferred tetragonal geometry for the Cu[I] state by the elongation of Cu–N distance of the tertiary amine from 2.10 to 2.43 Å.[47] In contrast, the Cu[II] geometry of **Cu₂(btmpa)** leans towards a pseudo-octahedral geometry.[46] As mentioned in the introduction, the **Cu[I]₂(btmpa)** geometry was shown to be different from **Cu[I](tmpa)** according to ^{1}H NMR data.[46] Therefore, it seems unlikely that **Cu₂(btmpa)** can easily obtain the preferred tetragonal geometry for the Cu[I] state which hinders fast electron transfer as would also be expected from the Marcus theory in which a higher reorganization energy is linked to slower electron transfer.[48]

Whereas **Cu(tmpa)** was found to be a homogeneous complex under electrochemical conditions,[33] **Cu₂(btmpa)** has a tendency to adsorb on the electrode. This behavior was studied in detail with electrochemical quartz crystal microbalance (EQCM) studies. EQCM is an *in-situ* technique that probes the mass changes of the work electrode by monitoring the change in oscillation frequency of the quartz crystal on which the work electrode resides.[49-52] In EQCM, a negative difference in frequency corresponds to an increase of the mass of the electrode. This technique visualizes any permanent deposit on the electrode as is sometimes formed by molecular complexes (see also Chapters 2 and 3).[49-52] Specifically, a gold electrode on such a quartz crystal was used for this purpose (Figure 4.2). The relative frequency of the oscillation decreases as soon as the complex is reduced electrochemically in the absence of O_2 starting at 0.5 V while scanning negative. In the positive scan, the complex is re-oxidized above 0.5 V which is accompanied by an increase of the frequency back to the starting frequency. Hence, the Cu[I/II] redox couple triggers a reversible change in mass of the electrode. This illustrates that no permanent deposit is formed. The origin of the reversible adsorption might be due to a change in solubility of the complex when changing the charge from 4+ to 2+. The less-charged complex could subsequently adsorb on the electrode more readily.
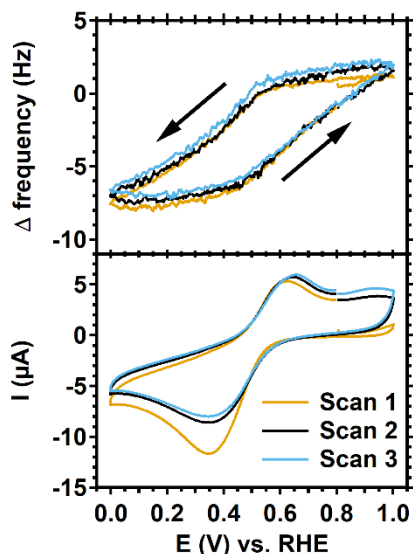
Figure 4.2. Electrochemical quartz crystal microbalance measurement with a gold work electrode of 0.15 mM **Cu₂(btmpa)** in 0.1 M phosphate buffer of pH 7. The bottom panel shows CV cycles at 50 mV/s scan rate under argon atmosphere. The first scan deviates because not all oxygen was completely removed. The top panel shows the relative frequency of the quartz crystal and its response with respect to the applied potential.

4.2.2 O_2 reduction by **Cu₂(btmpa)**

The electrochemical oxygen reduction reaction (ORR) of **Cu₂(btmpa)** was studied by cyclic voltammetry (CV) with a rotating ring disk electrode (RRDE) setup. This setup allows for controlled mass transport due to continuous rotation of the electrode resulting in a laminar flow of O_2 purged electrolyte towards the electrode. Furthermore, a Pt ring around the work electrode can be used as electrochemical sensor for the oxidation of H_2O_2 by applying a potential of 1.2 V. The onset for ORR for the glassy carbon (GC) work electrode itself is at *circa* 0.35 V *versus* RHE under our conditions (Figure 4.3). Generally, polished carbon electrodes such as GC selectively perform the 2 electron reduction of O_2 to H_2O_2.[15] Indeed, the production of H_2O_2 could be derived from the increase in ring current as soon as O_2 was reduced (Figure 4.3). When **Cu₂(btmpa)** was present in solution under an argon atmosphere, the onset for complex reduction was at 0.50 V. In addition, a ring current was observed which corresponds to the re-oxidation of the **Cu^{I}₂(btmpa)** at 1.2 V. When the solution was saturated with O_2, the onset lies at 0.50 V as well. However, the disk current exceeded the current in absence of O_2 pointing to the fact that catalytic O_2 reduction took place. Likewise, the ring current exceeded the current
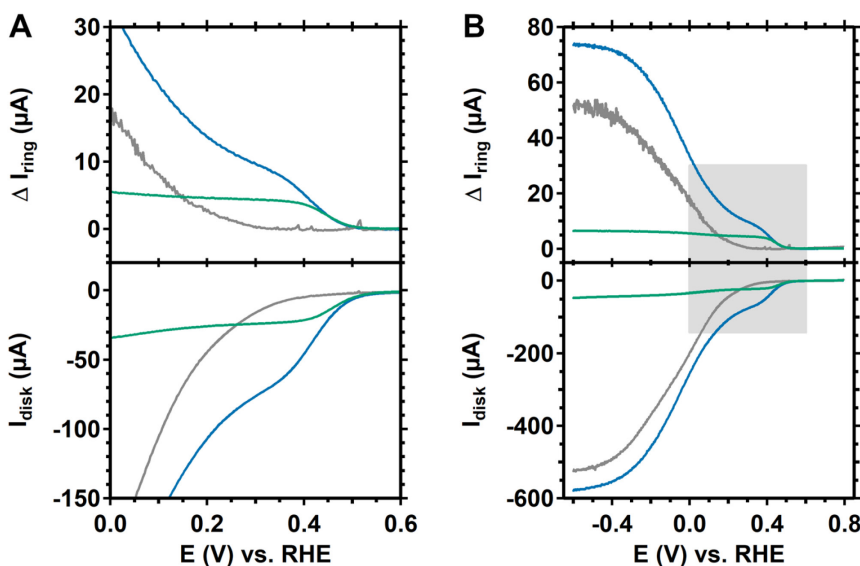
Figure 4.3. Linear sweep voltammograms with a rotating ring disk electrode setup of 0.15 mM **Cu₂(btmpa)** under argon (green) and O₂ atmosphere (blue). The cyclic voltammogram of the GC disk (bottom panel) and the current response of the Pt ring (top panel) are shown. The grey line represents the GC disk in catalyst-free, O₂ purged electrolyte. B shows the full potential window. The voltammograms were recorded at 50 mV/s in a 0.1 M phosphate buffer of pH 7. A rotation rate of 1600 rpm and a Pt ring potential of 1.2 V were applied.

in absence of O_2 indicating that H_2O_2 is formed. In the potential window between 0.50 and 0.35 V, the GC electrode itself is not active for O_2 reduction. Hence, **Cu₂(btmpa)** must perform O_2 reduction and produce H_2O_2. Below 0.35 V, the disk (and ring) current increased significantly because GC reduces O_2 as well in this potential window and a diffusion limited current was reached at −0.6 V. In this potential window, O_2 reduction is mostly performed by GC. Also, the diffusion limited current in presence of **Cu₂(btmpa)** is reached at the same potential as in the absence of **Cu₂(btmpa)**. **Cu₂(btmpa)** clearly reduces O_2 slower as compared to the mononuclear complex **Cu(tmpa)** as the latter reaches a diffusion limited current at 0.2 V.[33] The slow O_2 reduction of **Cu₂(btmpa)** is most likely due to the relative slow electron transfer kinetics of the $Cu^{I/II}$ redox couple.

4.2.1   H₂O₂ selectivity

The RRDE CV of O_2 reduction by **Cu₂(btmpa)** suggested that O_2 is reduced to H_2O_2 based on the observed ring current (Figure 4.3). To quantify the H_2O_2 selectivity, chronoamperometry at a fixed potential was performed. To calculate the H_2O_2 selectivity, the collection efficiency of the ring (N_{CE}) is required. Usually, the

96

one-electron redox couple $[Fe^{II}CN_6]^{4-}/[Fe^{III}CN_6]^{3-}$ is studied for this purpose, but this is not a good reference for multi-electron redox reaction such as H_2O_2 oxidation that includes the formation and breaking of bonds. In that case, the platinum ring is a catalyst whose activity is very susceptible for deactivation. To elaborate, the H_2O_2 oxidation mechanism on Pt is dependent on the number of active sites. This number can be reduced by competition of the phosphate buffer and PtO_x formation during a measurement when applying a potential of 1.2 V. In addition, substrate inhibition decreases H_2O_2 oxidation on Pt at high H_2O_2 concentration.[53] Moreover, we found that the polish method influences the activity of Pt and thereby the N_{CE} value. More information can be found in Appendix C (Figure C.4 and C.5). In short, mechanical polish with silica or alumina slurries will lower the N_{CE} for H_2O_2. A N_{CE} of 12.5% was previously determined under these conditions.[33] When the Pt ring is electropolished as well, the N_{CE} can reach the theoretical maximum value of 22-24% (depending on the ring-disk setup), but will quickly drop during a measurement which leads to a large inaccuracy. Therefore, we did not electropolish the Pt ring and determined the N_{CE} prior to the measurement by performing O_2 reduction with freshly polished GC disk and Pt ring electrodes at −0.3 V in a catalyst-free electrolyte. Since GC is a 100% selective catalyst for H_2O_2,[15] the obtained ring to disk current ratio was used as the N_{CE}.

Chronoamperometry in presence of **Cu₂(btmpa)** was performed at 0.2 V (Figure 4.4). The influence of O_2 reduction by GC is minimized at this potential (Figure 4.3). This establishes a reference for the intrinsic selectivity of **Cu₂(btmpa)** up to 15 minutes. A N_{CE} of 17.5% was determined and used to calculate the% H_2O_2 for this measurement (Figure 4.4B). As expected, the selectivity for H_2O_2 is high as the selectivity starts at 90% but lowers to 70% after 15 minutes. A selectivity below 100% suggests that over-reduction of H_2O_2 takes place. For that purpose, H_2O_2 reduction by **Cu₂(btmpa)** under argon atmosphere was studied (Figure C.6) with non-rotating and rotating electrodes. H_2O_2 is indeed reduced by **Cu₂(btmpa)** and the reducing current do increase with the H_2O_2 concentration. However, the H_2O_2 reduction by **Cu₂(btmpa)** is very sluggish which explains the high selectivity for H_2O_2.

4.2.2 Long-term electrolysis

Over-reduction or disproportionation of H_2O_2 is found for most molecular complexes that have been studied over a longer period of time. Also, catalyst degradation might play a role after a few hours. As was also mentioned in Chapter 1, a very small amount of unchelated copper is present since it is in equilibrium with
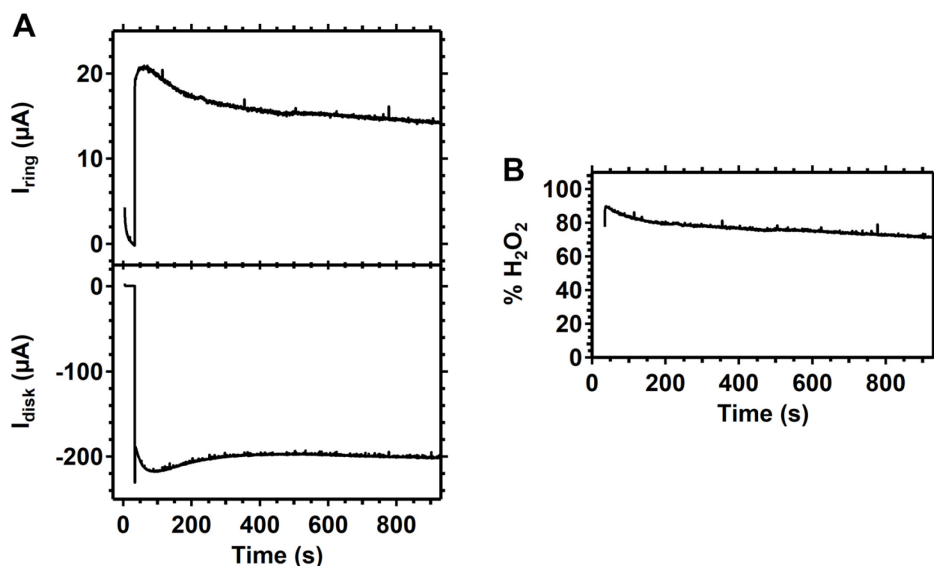
Figure 4.4. Chronoamperometry with a RRDE setup (A) of O_2 reduction in presence of **Cu$_2$(btmpa)** at 0.2 V disk potential (bottom panel) and corresponding Pt ring current (top panel). The calculated H_2O_2 selectivity is shown in B. A 0.1 M phosphate buffer at pH 7 with 0.15 mM catalyst was used. The GC disk was rotated at 1600 rpm. The Pt ring was kept at 1.2 V. The collection efficiency was determined at 17.5% determined by a 3 minute amperometry measurement at −0.3 V in catalyst-free electrolyte.

the chelated copper complex. At low, reductive potentials, this unchelated copper can be deposited as Cu^0 on the electrode. In contrast to most metals, copper has very fast ligand exchange rates. Hence, the tiny amount of unchelated copper is quickly replenished to re-establish the equilibrium with the copper complex. Consequently, the irreversible deposition of Cu^0 may very quickly pull the equilibrium towards dissociation of significant amounts of copper. The pace of the deposition could be influenced by the binding strength of the complex and/or the applied potential.[50, 51] To study these effects, O_2 reduction with **Cu$_2$(btmpa)** was monitored over a >7 hour period in O_2 saturated phosphate buffer. To do so, a rotating disk setup was used for constant diffusion of O_2 saturated electrolyte at 1600 rpm rotation rate. We chose 0.0 V as the most ideal potential because a background hydrogen evolution reaction was not expected, background O_2 reduction reactions on GC were minimal, and significant currents were generated at this potential in presence of **Cu$_2$(btmpa)**. Three different types of measurements were performed (Figure 4.5). First, a GC electrode in absence of **Cu$_2$(btmpa)** was tested as blank measurement (grey line). Second, a GC electrode in 0.15 mM catalyst solution was tested while continuously applying 0.0 V (green line). Last, a GC electrode in catalyst solution was tested with

intervals (orange): after 20 minutes of 0.0 V, the potential at the disk was briefly set at 0.8 V for 4 minutes (see the scheme in the top panel of Figure 4.5). The purpose of the interval measurement was to strip any (possible) Cu^o deposition by briefly applying an oxidizing potential. Of note, H_2O_2 is not re-oxidized to O_2 at this potential (Figure C.6). The results of the continuous measurements with and without catalyst present show that the current is significantly higher in the presence of **Cu₂(btmpa)** (-0.25 mA *versus* -0.05 mA in the first minutes) and increases gradually over the course of 8 hours. In the first half hour, there is a large increase in current from -0.25 to -0.37 mA. This feature of quick increase within the first 30 minutes of the measurement is observed in all cases when catalyst is present but not in absence of the catalyst. Most likely, **Cu₂(btmpa)** accumulates on the electrode. At 0.0 V, O_2 reduction by **Cu₂(btmpa)** is still kinetically limited (Figure 4.3). As a result, the large increase in reductive current can be explained by an increase in active sites due to accumulation of the catalyst. The EQCM measurements hinted towards this behavior as there is some reversible, potential dependent adsorption on gold electrodes (Figure 4.2). Interestingly, the magnitude of the current at 0.0 V after a 4-minute 0.8 V interval is equal to what it ended at the preceding 20 minute amperogram. This indicates that the accumulation effect lasts on the GC electrode even when a potential of 0.8 V is applied. Only thoroughly rinsing the electrode could remove most of the adsorbed catalyst and lower the O_2 reduction current to the same level of GC in catalyst-free electrolyte (see Figure C.7).
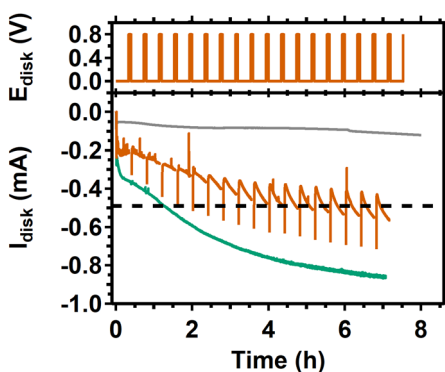
Figure 4.5. Rotating disk chronoamperometry of a GC disk at 0.0 V in a O_2 saturated **Cu₂(btmpa)** solution (bottom panel) in a continuous measurement (green) or a 20 minute interval measurement (orange). For the latter, a 0.8 V potential was briefly applied to re-oxidize accumulated Cu^o deposition every 20 minutes according to the sequence shown in the top panel. The large negative spikes in the bottom panel are an artefact of these intervals. The grey line is a continuous experiment in absence of **Cu₂(btmpa)**. The dotted horizontal line represents the theoretic maximum current for the 2-electron O_2 reduction reaction. The disk was rotated at 1600 rpm in a 0.1 M phosphate buffer of pH 7 with 0.15 mM catalyst.

After 1.5 hours, the reducing current of the continuous measurement became close to the calculated diffusion limited current (-0.49 mA) for O_2 to H_2O_2 reduction under these conditions. The calculation is based on the diffusion limited current that a Pt disk of the same size (0.196 cm²) reaches under the same conditions for the 4 electron reduction of O_2 to H_2O, for which -0.98 mA was obtained.[33] However, the current passed -0.49 mA after 1.5 hours and continued to rise even more. After the full 7 hour continuous measurement, the electrode was taken from the solution and a brown-colored deposit could be observed on the surface of the electrode (Figure C.8). Most likely, this is a Cu^o deposit. As we will show later, this Cu^o deposit can be linked to a gradual shift in selectivity from O_2 to H_2O_2 to the 4 electron reduction of O_2 to H_2O which requires more electrons and thus higher currents. Clearly, Cu^o deposition is undesired and that is the reason for performing the interval measurement. During this measurement (orange line of Figure 4.5), the potential was held at 0.8 V for 4 minutes after every 20 minutes of catalytic amperometry at 0.0 V. Evidently, the current is lower as compared to the continuous measurement. Still, the current steadily increased over time. For the first 2 hours, the current at the start of every 20 minute cycle was of the same magnitude as that of the end of the previous cycle. After 2 hours, this was no longer the case. At that point, the current jumped back to a lower value after the interval than the magnitude it reached during the preceding cycle. Cu^o deposition and the accompanying selectivity change could be the underlying reason as this would explain why the current jumps back after the stripping potential was applied. The observation that this happens after 2 hours might be related to a rise in the H_2O_2 concentration as we will discuss next. Overall, the interval procedure clearly prevented Cu^o deposition to a certain extent with respect to a continuous measurement.

4.2.3   Faradaic efficiency for H_2O_2

The selectivity of **Cu₂(btmpa)** at 0.0 V for H_2O_2 over a prolonged period of time was monitored to study the effect of over-reduction of H_2O_2 by either **Cu₂(btmpa)** or Cu^o deposition. Two different methods were used. The first method used the same RRDE set-up as for Figure 4.4 that utilizes the Pt ring as electrochemical H_2O_2 sensor. Here, we found that the ring is not suited as quantitative peroxide sensor during long-term electrolysis (see Figure C.9). As mentioned before, catalytic H_2O_2 oxidation by the Pt ring is very susceptible for deactivation by PtO_x formation and high amounts of H_2O_2 (Figures C.4 and C.5).[53] However, the data did suggest that there was a slow build-up of H_2O_2. Therefore, we applied a second method: bulk electrolysis with an RDE setup for which the bulk

concentration of H_2O_2 was periodically determined with an enzyme based photometric analysis using a reflectometer. The products of H_2O_2 dissociation by a peroxidase will react with an organic dye. The intensity of the color that arises can be used to quantify H_2O_2. Thereby, the Faradaic efficiency could be calculated which is the percentage of charge passing the disk that is used for the O_2 to H_2O_2 reduction.

The Faradaic efficiency was determined for three measurements with long (4 minute), short (30 seconds) and no intervals of 0.8 V. The results of the 4-minute interval measurement are shown in Figure 4.6. Within the first 30 minutes, a Faradaic efficiency of 83% was obtained which is in good agreement with the data obtained from the short-term RRDE experiment at 0.2 V (Figure 4.4). Likewise, in a continuous measurement without intervals, an efficiency of 80% was found after the first 30 minutes (Figure C.10). The measurement with shorter interval times had a lower Faradaic efficiency of 62% after 30 minutes, though a very noisy amperogram might have influenced this result (Figure C.10). Within the first half hour, the selectivity for H_2O_2 is high and the influence of Cu^0 deposition is clearly low. After the first half hour, the Faradaic efficiency of the 4-minute interval measurement lowered to around 60%. The shorter interval measurement had a slightly higher efficiency of 69%. In contrast, the continuous measurement showed a drastic drop in efficiency to 40% 1 hour after the start and stagnated around 10% after 2 hours. The interval experiments kept at 60 to 70% in the same time window clearly

4
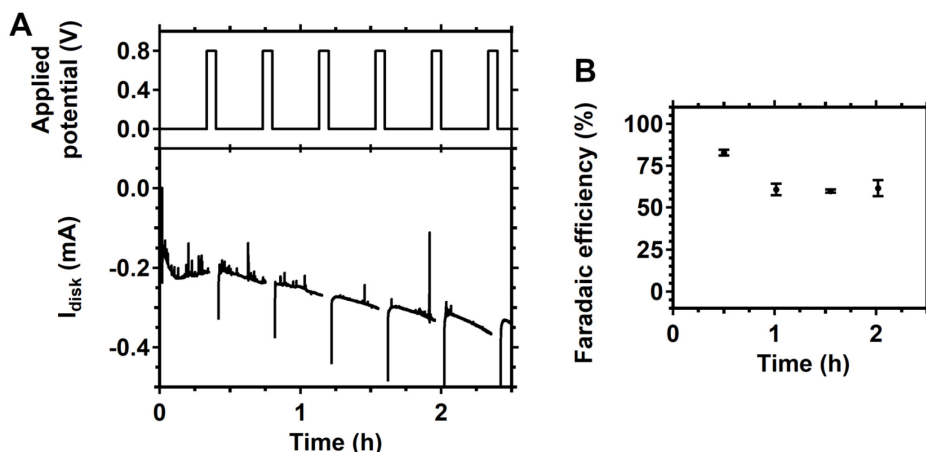
Figure 4.6. Rotating disk electrode chronoamperometry measurement of O_2 reduction at 0.0 V of a GC disk in a **Cu₂(btmpa)** solution (bottom panel, A). The disk current had 4 minute intervals of 0.8 V every 20 minutes according to the scheme in the top panel to be able to strip accumulated Cu^0. The Faradaic efficiency for H_2O_2 is given in B. The black dots represent the Faradaic efficiency of the time window since the last H_2O_2 measurement. The disk was rotated at 1600 rpm in a 0.1 M phosphate buffer of pH 7 with 0.15 mM catalyst.

indicating that the interval procedure greatly enhances the Faradaic efficiency. With the long 4-minute intervals, this efficiency could be kept up to two hours after the start of the measurement and a total Faradaic efficiency of 65% percent was obtained.

After 2 hours, the Faradaic efficiency dropped with every measurement and during the last hour of the 8 hour measurement, only 18% Faradaic efficiency was obtained (Figure C.11 and Table C.1). The total Faradaic efficiency for the entire 7 hour measurement was 34% because of the high efficiency in the first 2 hours. Equally, the efficiency of the short interval experiment dropped after 1.5 hours. In the time window between 5 and 6 hours after the start of the experiment, the calculated Faradaic efficiency was negative. This calculated negative value is a result of an overall decrease in bulk H_2O_2 concentration in that time window and indicates that more H_2O_2 is over-reduced than that H_2O_2 is produced. The same effect was observed for the continuous measurement where it already started in the time window between 4 and 5 hours after the start of the measurement. In the last hour of the short-interval experiment, the interval time was increased to 4 minutes. As a result, the calculated Faradaic efficiency was positive again and the H_2O_2 bulk concentration raised again, which indicated that over-reduction was H_2O_2 was diminished. In addition, the long interval experiment (4 minute intervals) had no decrease in bulk H_2O_2 concentration at any point during the measurement, demonstrating the significance of the duration of the stripping interval.

Even the long stripping interval of 4 minutes did not completely prevent over-reduction after 2 hours of amperometry. We believe that this is due to a steady rise in the bulk H_2O_2 concentration during the measurement. The rate of H_2O_2 over-reduction by **Cu₂(btmpa)** will increase with increasing H_2O_2 concentration as pointed out earlier (Figure C.6). However, it is more likely that that the over-reduction is mostly caused by Cu^0 as this deposits in a faster rate at higher bulk H_2O_2 concentrations. The following observations support this. First of all, the Faradaic efficiency is consistently lower for measurements with shorter or no stripping intervals (Figure C.10) after 2 hours. Also, 2 hours after the start of the measurement, all interval measurements display steeply rising reductive currents during the 20 minute 0.0 V measurement but all fall back after the stripping interval. These observations point to the accumulation of a species on the electrode (Cu^0) that facilitates over-reduction during the 20-minute period which is subsequently stripped after the stripping interval. As mentioned before, **Cu₂(btmpa)** itself seems to be more reluctant to desorb from the surface at 0.8 V. Another observation is the enhancement of the steep increase in current when the H_2O_2 concentration is

manually spiked (Figure C.11). Moreover, this steep increase in current is mostly avoided when the formed H_2O_2 is intercepted. In fact, this was achieved with the 8.5 hour RRDE measurement as the Pt ring, while sensing H_2O_2, is actually continuously converting H_2O_2 back to O_2 thereby limiting H_2O_2 build-up (Figure C.9). To some extent, there is build-up of H_2O_2 in the solution, but the reductive disk current remained remarkably constant over the course of 8 hours as opposed to the other measurements and remained close to the theoretical diffusion limited current of -0.49 mA for O_2 to H_2O_2 reduction. Furthermore, the ring current measurements did indicate that H_2O_2 selectivity remained high throughout the measurement. We therefore conclude that the decrease in Faradaic efficiency after 2 hours is caused by higher rates of Cu^0 deposition induced by a higher H_2O_2 concentration.

The faster deposition rate of Cu^0 after two hours as compared to the start of the measurement might be related to a faster rate of complex degradation. The catalyst-containing electrolyte slowly changes color from blue to green throughout the measurement (Figure C.1B). The same spectral changes in the UV-vis spectrum of the electrolyte could be replicated by adding 1.1 mM H_2O_2 to a 0.15 mM **Cu₂(btmpa)** solution in phosphate buffer (Figure C.1A). Monitoring the UV-vis spectrum over the course of a week showed that the low-intensity absorption at 675 nm remained but a second absorption appears at 359 nm. While this peak increased, another peak at 288 nm decreased and an isosbestic point at 298 nm was observed in between. Since the spectrum only changes upon the addition of H_2O_2 (Figure C.1C), the possibility of H_2O_2 coordination to **Cu₂(btmpa)** was further explored. The absorption at 359 nm could indicate a μ-η^2:η^2-peroxodicopper(II) structure.[54] Typically, complexes and enzymes with such a side-on peroxo dinuclear copper center have a high intensity absorption between 320 and 380 nm as well as a low intensity absorption between 520 and 610 nm. Both absorptions are ascribed to $\pi^* \rightarrow d_{xy}$ peroxo to Cu^{II} charge transfers.[55-58] The band at 610 nm in that case is most likely is obscured by the 675 nm absorption of unreacted **Cu₂(btmpa)**. The possibility of this core was further investigated by Raman spectroscopy (Figure C.12). A low energy O–O stretching band is typically observed for this core in the range of $730 - 760$ cm^{-1}.[54-58] A broad signal at 760 cm^{-1} could be observed, but was also observed in the absence of H_2O_2. Since the Raman spectra with and without H_2O_2 overlap, no evidence for the presence O–O or Cu–O bonds was found. Therefore, the color and spectral changes are most likely due to ligand degradation by oxidation. This would in turn facilitate Cu^0 deposition, especially at higher H_2O_2 concentration. Overall, to achieve a high Faradaic efficiency for a longer period of time the produced H_2O_2 has to be intercepted to prevent Cu^0 deposit, and any formed deposit has to be

stripped of electrochemically. We have shown that the latter approach resulted in a Faradaic efficiency between 60 and 70% for up to 2 hours for the production of H_2O_2.

4.3 Conclusion

The dinuclear copper complex **Cu₂(btmpa)** is able to catalyze the electrochemical O_2 reduction with H_2O_2 as major product. Reduction and re-oxidation of the complex is accompanied by slow electron transfer due to geometrical constrains that are absent in the mononuclear **Cu(tmpa)** complex. That way, the rate of O_2 reduction of **Cu₂(btmpa)** is lower, and, more importantly, the over-reduction of H_2O_2 is largely blocked. The complex produces H_2O_2 with a high Faradaic efficiency of 60 to 70% at 0.0 V over the course of 2 hours. Cu^o deposition lowers the Faradaic efficiency, but can be counteracted by briefly applying a stripping potential periodically. Additionally, the catalytic activity increases significantly in the first half hour of chronoamperometry and the current can stabilize close to the theoretical diffusion limited current for O_2 to H_2O_2 reduction when H_2O_2 is intercepted. Potential dependent accumulation of the catalyst in its reduced dicopper(I) state on the glassy carbon electrode is the most likely explanation for this initial fast increase in activity. This is the first extensive study for prolonged electrochemical O_2 to H_2O_2 reduction by a molecular catalyst. We have successfully identified that fine-tuning the potential, the use of Cu^o stripping intervals, and applying methods to intercept the formed H_2O_2 can significantly improve the Faradaic efficiency. Thereby, we have been able to put the intrinsic high H_2O_2 selectivity of **Cu₂(btmpa)** to use. We anticipate that our results will allow for the next step, which is the incorporating the catalyst in devices for the direct electrochemical production of H_2O_2 from O_2.

4.4 Acknowledgements

4.5   Experimental

4.5.1   General

All chemicals were bought from commercial suppliers and used as received without further purification. The pH was measured with a Hannah Instruments HI 4222 pH meter that was calibrated with five IUPAC standard buffers. UV-vis measurements were performed on a Varian Cary 50 UV-vis spectrometer. ^{1}H NMR measurements were performed with a Bruker DPX-300 spectrometer using deuterated solvents obtained from Eurisotop. $CDCl_3$ was purified by filtration over basic alumina before use. All chemical shifts (δ) are reported with respect to the solvent peak.[59] Elemental analysis was performed by Mikroanalytisch Laboratorium Kolbe in Oberhausen, Germany. Mass spectra were recorded on a Thermo Fisher Scientific MSQ Plus ESI. EPR spectra were recorded on a Bruker EMXplus X-band spectrometer. Reflectance Raman spectra were recorded with a WITech alpha 300 R confocal Raman microscope equipped with a 532 nm laser (1 mW). A 100 x objective with a numeral aperture of 0.9 was used (Zeiss). For preparation of the sample, an aqueous solution of 3 mM **Cu₂(btmpa)** and 22 mM H_2O_2 was dropcasted on a Si/SiO$_2$ wafer (Siegert wafer) with a native silicon oxide layer of 285 nm. SQUID measurements were performed on a Quantum Design MPMS-XL 7T SQUID magnetometer employing the settle approach with activated No-overshoot mode om the 300-2K temperature range with varying increment: 5K (300-150K), 2K (150-50K), 1K (50-25K), and 0.5K (25-2K) at constant 5 kOe magnetic field. An automatic diamagnetic correction was applied for a sample holder that was measured separately beforehand. Each data point was averaged over 4 consecutive scans.

4.5.2   Synthesis

Synthesis of 6,6'-bis(hydroxymethyl)-2,2'-bipyridine (3)

3 (Scheme 4.1) was synthesized with **2** as crude intermediate. **2** was synthesized following the procedure for synthesizing the methyl ester adapted from Forato *et al*.[60] ethanol (EtOH) instead of methanol (MeOH) was used to prepare the ethyl ester. 803.7 mg (3.29 mmol) of 2,2'-bipyridine-6,6'-carboxylic acid (ChemCruz, **1**) was loaded into a dry flask under inert atmosphere. 120 ml degassed EtOH (99.8%, Riedel-de Haën) was added to dissolve the compound. 16 ml of H_2SO_4 (98%, VWR) was added drop-wise over the course of 10 min. The mixture was set to reflux overnight. After cooling the mixture to 0 °C, it was slowly poured into 150 ml of saturated $NaHCO_3$ solution. The resulting mixture was extracted using 4 x 100 ml

DCM (dichloromethane, Honeywell, >99.9%). The organic layers were collected, and the solvent was evaporated under reduced pressure resulting in a crude white solid which was characterized by ^{1}H NMR and ESI MS. Besides peaks belonging to **2**, the monosubstituted by-product was found as well. This and other impurities were removed in the next step of the synthesis. ESI MS of **2** m/z (found (calculated)): 301.1 (301.3 [M + H$^+$]); 323.1 (323.3 [M + Na$^+$]). ^{1}H NMR of **2** (300 MHz, CDCl$_3$) δ 8.88 (dd, 2H, ^3J(H,H) = 7.9 Hz, ^4J(H,H) = 1.1 Hz, Py-NCC-Py-CH), 8.21 (dd, 2H, ^3J(H,H) = 7.8 Hz, ^4J(H,H) = 1.1 Hz), 7.99 (t, 2H, ^3J(H,H) = 7.8 Hz), p-Py-H), 4.53(q, 4H, ^3J(H,H) = 7.1 Hz, CH$_3$CH_2); 1.49 (t, 6H, ^3J(H,H) = 7.1 Hz, CH_3CH$_2$).

  The crude product **2** was further used to synthesize **3** without further purification. **3** was synthesized following the procedure by Ganesan *et al.*[61] 1.1561 g of **2** was dissolved in 40 ml of dry, degassed THF (tetrahydrofuran, Sigma Aldrich) and loaded into a dry flask with inert atmosphere. The solution was further degassed using an N$_2$ flow for 30 min. 1.464 g (38.7 mmol) of NaBH$_4$ (Aldrich) was added to this solution. 9 ml of dry, degassed MeOH (Honeywell, >99.9%) was dropwise added by syringe, resulting in the formation of a large amount of gas. Once the gas production stopped, the mixture was set to reflux overnight. 150 ml of saturated NH$_4$Cl solution, prepared using NH$_4$Cl (Honeywell) and demineralized water, was
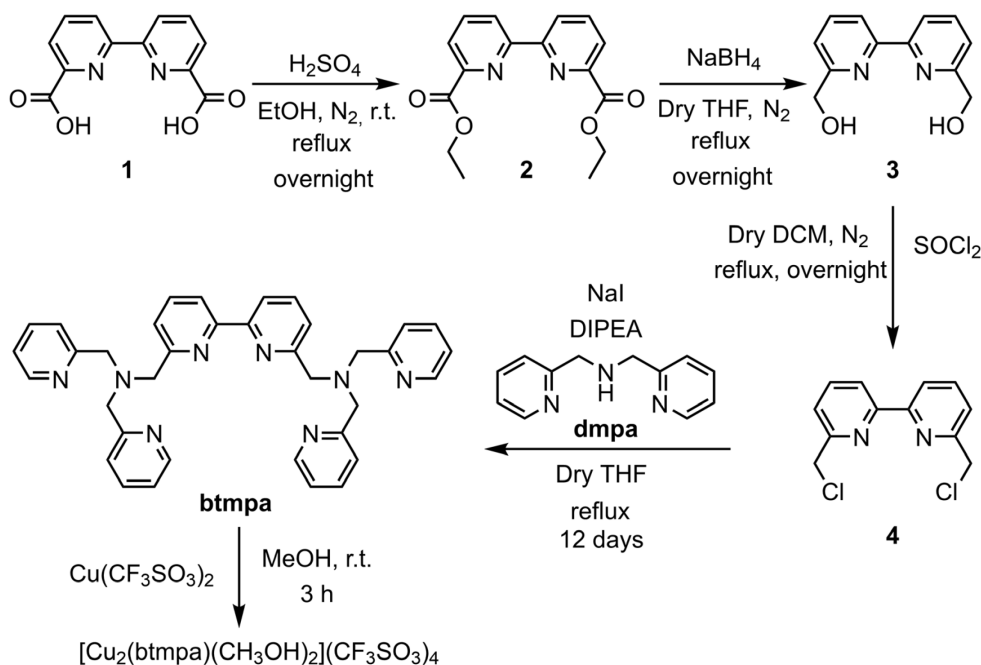
Scheme 4.1. Synthesis of btmpa and [Cu$_2$(btmpa)(CH$_3$OH)$_2$](CF$_3$SO$_3$)$_4$.

added to the reaction mixture to neutralize the remaining $NaBH_4$. The resulting mixture was extracted using 3 x 100 ml EtOAc (ethyl acetate, VWR, Rectapur®). The organic layers were collected, and the solvent was evaporated under reduced pressure. 687.8 mg of product was obtained in the form of a white/yellow solid (3.18 mmol, 97% yield with respect to **1**). ^{1}H NMR matches the values reported by Ganesan *et al.*[61] within 0.2 ppm. ESI MS *m/z* (found (calculated)): 217.0 (217.1 [M + H+]); 239.0 (239.1 [M + Na+]). ^{1}H NMR (300 MHz, $CDCl_3$) δ 8.41 (dd, 2H, [3]*J*(H,H) = 7.8 Hz, [4]*J*(H,H) = 1.0 Hz, Py-NCC-Py-C*H*), δ 7.87 (t, 2H, [3]*J*(H,H) = 7.8 Hz, *p*-Py-*H*), δ 7.52 (dd, 2H, [3]*J*(H,H) = 7.8 Hz, [4]*J*(H,H) = 1.0 Hz, Py-NCC-OH-C*H*), 4.77 (s, 4H, C*H₂*).

Synthesis of 6,6'-bis(chloromethyl)-2,2'-bipyridine (4)

687.8 mg of **3** was dissolved in 60 ml of dry, degassed DCM (Sigma Aldrich) and loaded into a dry flask with inert atmosphere. The resulting solution was further degassed by purging with N_2 for 30 min. 1.2 ml of $SOCl_2$ (Acros Organics) was added dropwise, resulting in a turbid yellow solution. After stirring for 15 minutes the solution had turned clear and yellow. The mixture was left to stir under reflux overnight. After attaching a gas trap filled with 40 ml 10 M NaOH solution, 100 ml of water was carefully added to the reaction mixture to neutralize the remaining $SOCl_2$. The mixture was left stirring vigorously for 1 h to allow the $SOCl_2$ to neutralize completely. The reaction mixture was extracted using DCM (3 x 100 ml). The organic layers were collected, and the solvent was evaporated under reduced pressure resulting in a yellow solid. 643.8 mg of product was obtained (2.54 mmol, 80% yield). The recorded ^{1}H NMR spectrum matches reported values with a maximum 0.05 ppm deviation.[62, 63] MS *m/z* (found (calculated)): 252.9 (253.1 [M + H+]). ^{1}H NMR (300 MHz, $CDCl_3$) δ 8.41 (dd, 2H, [3]*J*(H,H) = 7.9 Hz, [4]*J*(H,H) = 1.0 Hz, Py-NCC-Py-C*H*), δ 7.87 (t, 2H, [3]*J*(H,H) = 7.8 Hz, *p*-Py-*H*), 7.52 (dd, 2H, [3]*J*(H,H) = 7.7 Hz, [4]*J*(H,H) = 1.0 Hz, Py-NCC-Cl-C*H*), 4.77 (s, 4H, C*H₂*)

Synthesis of 6,6'-bis(2,2'-dipicolylamine)-2,2'-bipyridine (btmpa)

Synthesis and initial purification

465.1 mg of **4** and 16.4 mg of NaI were loaded into a dry flask attached to a Schlenk setup. The solids were degassed and subsequently dissolved in 80 ml Degassed, dry THF. 3.2 ml DIPEA (N,N-diisopropylethylamine, Sigma Aldrich) and 0.66 ml 2,2'-dipicolylamine (dmpa, Chemodex) were added to the solution. The resulting yellow solution was refluxed for 12 days, while the progress was checked by

NMR. After 12 days, 200 ml of saturated $NaHCO_3$ solution was added followed by an extraction using 4 x 100 ml DCM. The organic layers were collected, and all volatiles were evaporated under reduced pressure. A silica column (Silica gel 40 – 63 µm, 60 Å, Screening Devices) using a gradient eluent of 0-10% MeOH in DCM was performed as a first purification. Column chromatography alone was not enough to remove unreacted dmpa since it has a very similar Rf value as btmpa and both compounds suffer from tailing and thus mixing. From several recrystallization attempts from 2 : 3 DCM : Et_2O (diethyl ether, Honeywell), part of the crude product could be purified and btmpa was obtained as white crystals. 113.9 mg (0.197 mmol) of btmpa was obtained as first batch.

Purification with hexanoic anhydride

As mentioned, unreacted dmpa is hard to remove from btmpa because the Rf values are very similar and both compounds tail slightly on alumina and largely on silica columns. A large difference in Rf would help to avoid mixing due to tailing of the compounds. Therefore, hexanoic anhydride (Sigma Aldrich) was used to change the Rf of dmpa. This method is based on the reaction of the secondary amine of dmpa with the anhydride to obtain an amide. The aliphatic tail of the amide makes the impurity more hydrophobic and, as a result, increases its Rf value with respect to that of btmpa. btmpa itself has no primary or secondary amines that can react with the anhydride. This way the compounds could be purified successfully. Specifically, 140 mg crude product containing btmpa, which was left after the first purification by column chromatography, was dissolved in 5 ml dry DCM (Sigma Aldrich), 135 µL DIPEA and 60 µL hexanoic anhydride (Sigma Aldrich) were added to the solution. The reaction mixture was stirred at room temperature for 2.5 hours. Next, the mixture was neutralized by adding 1 M HCl till the pH reached 7. The crude mixture was separated in two layers and the aqueous layer was extracted 3 times with DCM. All organic layers were combined, dried over Na_2SO_4 and filtered. All volatiles were removed under reduced pressure. For the purification, the product was dissolved in DCM and loaded on an alumina column (Brockmann Type 1 Basic alumina). A gradient eluent was used from 0.2% triethylamine to 0.5% with additional 0.1% MeOH in DCM. The product fractions were washed with a saturated $NaHCO_3$ solution. Subsequently, this $NaHCO_3$ solution was extracted 3 times with DCM. All organic fractions were combined, dried over Na_2SO_4, and filtered before the volatiles were removed under reduced pressure. The obtained white solid was washed twice with pentane and once with Et_2O. After drying, 108 mg (0.187 mmol) of btmpa was

obtained. ^{1}H NMR and MS confirmed the presence of btmpa and the absence of dmpa and hexanoic amide. The ^{1}H NMR spectra matches reported spectra.[46] The total yield of pure product is 241.9 mg (0.418 mmol, 23%). ESI MS *m/z* (found (calculated)): 601.5 (601.28 [M + Na$^+$]); 579.5 (579.3, [M + H$^+$]); 290.3 (290.15, [M + 2 H$^+$]). ^{1}H NMR (300 MHz, CDCl$_3$) δ 8.53 (dt, 4H, ^3J(H,H) = 4.9 Hz, ^4J(H,H) = 1.4 Hz, *o*-Py-*H*), 8.30 (dd, 2H ^3J(H,H) = 7.8 Hz, ^4J(H,H) = 1.1 Hz, Py-NCC-Py-C*H*), 7.77 (t, 2H, ^3J(H,H) = 7.7 Hz, *p*-biPy-*H*), 7.72 – 7.58 (m, 8H, *p*-Py-*H* and *m*-Py-*H*), 7.54 (dd, 2H, ^3J(H,H) = 7.7 Hz, ^4J(H,H) = 1.1 Hz, biPy-NCCN-C*H*), 7.14 (m, 4H, Py-NCHCH$_2$N-C*H*), 3.95 (overlapping singlets, 12H, C*H*$_2$).

In total, both batches (113.9 and 108 mg) gave a total yield of 221.9 mg (0.383 mmol, 21%).

Synthesis of [Cu$_2$(btmpa)(CH$_3$OH)$_2$](CF$_3$SO$_3$)$_4$ (Cu$_2$(btmpa))

108 mg of **btmpa** was dissolved in 5 ml MeOH yielding a yellow solution. Next, 136 mg of Cu(II)(CF$_3$SO$_3$)$_2$ (Alfa Aesar) was dissolved in 1 ml MeOH and added to the ligand solution. The solution turned from green to dark blue upon addition. The mixture was stirred for 3 hours at room temperature after which the solvent was removed under reduced pressure. The remaining solid residue was redissolved in 2 ml MeOH and Et$_2$O was slowly added by vapor diffusion at 4 °C temperature. The obtained blue crystals were filtered and washed with cold Et$_2$O and dried. After repeating the crystallization, 162 mg (0.118 mmol, 63%) blue crystals of the complex were obtained. The calculated (%) elemental analysis ratio (%) for [Cu$_2$(btmpa)(MeOH)$_2$](OTf)$_4$ (C$_{42}$H$_{42}$Cu$_2$N$_8$O$_{14}$S$_4$) + 2.5 H$_2$O : C 35.75, H 3.36, N 7.94; found: C 35.48, H 3.10, N 7.78. UV-vis λ$_{max}$: 228 nm, 675 nm (0.15 mM in water); 632 nm, 816 nm (2.0 mM in MeCN). EPR 0.6 mM in H$_2$O: g$_{||}$ = 2.21, g$_\perp$ = 2.08; phosphate buffer: g$_{||}$ = 2.23, g$_\perp$ = 2.06; in dimethyl formamide: g$_{||}$ = 2.23 (A$_{Cu}$ = 500 Hz), g$_\perp$ = 2.06. (Figure C.2).

4.5.3   General electrochemistry

For all aqueous solutions, all experiments and for cleaning of glassware Milli-Q grade Ultrapure water (>18.2 MΩ cm resistivity) was used unless mentioned otherwise. The pH 7 electrolyte was prepared with NaH$_2$PO$_4$ (Merck Suprapur ©, 99.99%) and Na$_2$HPO$_4$ (Fluka Traceselect© 99.995%) with 0.1 M phosphate strength. Electrochemical experiments were performed with a three-electrode setup in a custom-made, single-compartment glass cell. For EQCM, RRDE and bulk electrolysis, special cells were used that are described separately. Autolab PGSTAT 12, 204, 128N and IVIUM CompactStat potentiostats were used in combination with

NOVA 2.1 or IVIUM software. All glassware used for electrochemistry was cleaned by boiling in and copiously rinsing the glassware with water prior to each experiment. Periodically and before each RRDE measurement, the glassware was cleaned by immersing the glassware in a 1 g/l $KMnO_4$ solution in 0.5 M H_2SO_4 (Sigma, reagent grade) overnight. Afterwards, the glassware was rinsed 5–10 times with water. To re-oxidize any MnO_2 traces, water, a few drops of H_2O_2 (Merck Emprove, 35%) and H_2SO_4 (Merck) were added. Finally, the glassware was rinsed 5-10 times and boiled in water for a total of three times

All electrolytes solutions were purged by argon (Linde, Ar 5.0) prior to each experiment for at least 30 minutes and the cell was kept under a flow of argon during the experiment. For experiments under O_2 (Linde, O_2 5.0), the electrolyte was purged with O_2 for at least 10 minutes prior to the measurement and was purged continuously during RRDE measurements.

In all cases, the reference electrode was the reversible hydrogen electrode by utilizing a platinum mesh in H_2 (Linde, H_2 5.0) saturated electrolyte that is operated at the same pH as the working electrode or by using a HydroFlex (Gaskatel). The cell and reference electrode are connected via a Luggin capillary. The counter electrode was a large surface area gold wire that was flame annealed prior to use. The working electrode was glassy carbon (GC, Metrohm, 0.07 cm²) encapsulated in PEEK (polyether ether ketone). The GC electrode was polished before each measurement. Either manual or mechanical polish methods were used. Manual polishing was applied with 1.0, 0.3 and 0.05 micron alumina slurry (Buehler) on MicroCloth (Buehler) polishing cloths for 2 minutes followed by rinsing and sonicating the electrode in water for 10 minutes. Mechanical polishing was applied with a Labopol-20 polishing machine on Dur type polishing cloths with 1.0 micron diamond and 0.04 micron silica suspensions for 1 minute (Struers). After the diamond polishing, the electrode was rinsed with water and 2-propanol to remove the oily substances from the slurry. The silica polish was followed by a rinse with water. After that, the electrode was sonicated in water for 10 minutes.

4.5.4   EQCM

EQCM experiments were performed with an Autolab gold EQCM electrode (0.35 cm²) that consist of a 200 nm thick gold layer deposited on a quartz crystal. An adjusted Autolab PEEK EQCM cell was used that was able to contain up to 5 ml of electrolyte.

4.5.5   RRDE

RRDE experiments were performed in a three electrode setup with custom-made two-compartment cells that could separate the working electrodes from the counter electrode via a water permeable glass frit. A glassy carbon disk (0.196 cm^2) surrounded by a platinum ring in a ChangeDisk configuration was used in a Pine MSR rotator as supplied by Pine Instruments. The GC disk and Pt ring electrodes were, prior to each measurement, separately polished. Both were either manually or mechanically polished. For the GC disk, the same procedure for the PEEK encapsulated disk was used. For Pt, the manual polish was performed with 1.0 and 0.3 micron alumina for 30 seconds and 0.05 micron alumina for 1 minute after which the electrode was sonicated for 10 minutes in water. The mechanical polish was equal to the treatment for the GC disk. When applicable, the Pt ring was further electropolished by performing CV in 0.1 M phosphate buffer of pH 7 for 50 scans at a 500 mV/s scan rate between 1.7 and −0.1 V while the shaft was rotated at 1600 rpm.

4.5.6   Bulk electrolysis and Faradaic efficiency

The Faradaic efficiency was determined by bulk electrolysis in combination with H_2O_2 enzyme based photometric determination of the bulk H_2O_2 concentration with the Reflectoquant® system (Merck) using test strips for 0.2 to 20 mg/l H_2O_2 (Merck). The bulk electrolysis was performed in a custom-made glass cell with glass-frit separated compartments for the reference, work and counter electrode. A HydroFlex (Gaskatel) reference electrode was used as RHE reference. The counter electrode was a high surface area gold wire. The work electrode was a custom-made, mechanically polished GC electrode (0.196 cm^2) in a rotating disk setup from Pine. The electrode was continuously rotated at 1600 rpm. The initial volume of the 0.15 mM **Cu$_2$(btmpa)** solution was 33.6 ml. A circa 1.5 ml aliquot was taken for each H_2O_2 measurement and weighed to correct for the decrease in volume of the bulk solution during the measurement. Each aliquot was tested at least twice with the test strips immediately after removing it from the solution. The theoretical charge required to obtain the measured concentration difference of H_2O_2 in the time between two measurements was calculated. The actual charge that passed in the same time window was obtained by integration of the current over time.

4.6   References

1.   *Hydrogen Peroxide*; 18; Global Industry Analysts: 2020.
2.   Eul, W.; Moeller, A.; Steiner, N., Hydrogen Peroxide. In *Kirk-Othmer Encyclopedia of Chemical Technology* [Online] John Wiley & Sons, Inc.: 2000. http://dx.doi.org/10.1002/0471238961.0825041808051919.a01.pub2.
3.   Hage, R.; Lienke, A., *Angew. Chem. Int. Ed.* **2006**, *45*, 206−222.
4.   Süss, H. U., Bleaching. In *Ullmann's Encyclopedia of Industrial Chemistry*, 2012.
5.   Legrini, O.; Oliveros, E.; Braun, A. M., *Chem. Rev.* **1993,** *93*, 671−698.
6.   Metcalf & Eddy Inc.; Tchobanoglous, G., *Wastewater Engineering: Treatment and Resource Recovery*. 5th edition ed.; Mcgraw-Hill Education: 2014.
7.   Goor, G., *Catalytic Oxidations with Hydrogen Peroxide as Oxidant*. Kluwer Academic Publishers: The Netherlands, 1992.
8.   Campos-Martin, J. M.; Blanco-Brieva, G.; Fierro, J. L. G., *Angew. Chem. Int. Ed.* **2006,** *45*, 6962−6984.
9.   Berl, E., *Trans. Electrochem. Soc.* **1939,** *76*, 359.
10.   Xia, C.; Xia, Y.; Zhu, P.; Fan, L.; Wang, H., *Science* **2019,** *366*, 226.
11.   Jiang, Y.; Ni, P.; Chen, C.; Lu, Y.; Yang, P.; Kong, B.; Fisher, A.; Wang, X., *Adv. Energy Mater.* **2018,** *8*, 1801909.
12.   Siahrostami, S.; Verdaguer-Casadevall, A.; Karamad, M.; Deiana, D.; Malacrida, P.; Wickman, B.; Escudero-Escribano, M.; Paoli, E. A.; Frydendal, R.; Hansen, T. W.; Chorkendorff, I.; Stephens, I. E. L.; Rossmeisl, J., *Nat. Mater.* **2013,** *12*, 1137−1143.
13.   Verdaguer-Casadevall, A.; Deiana, D.; Karamad, M.; Siahrostami, S.; Malacrida, P.; Hansen, T. W.; Rossmeisl, J.; Chorkendorff, I.; Stephens, I. E. L., *Nano Lett.* **2014,** *14*, 1603−1608.
14.   Jirkovský, J. S.; Panas, I.; Ahlberg, E.; Halasa, M.; Romani, S.; Schiffrin, D. J., *J. Am. Chem. Soc.* **2011,** *133*, 19432−19441.
15.   Song, C.; Zhang, J., Electrocatalytic Oxygen Reduction Reaction. In *PEM Fuel Cell Electrocatalysts and Catalyst Layers: Fundamentals and Applications*, Zhang, J., Ed. Springer London: 2008; pp 89−134.
16.   Chen, S.; Chen, Z.; Siahrostami, S.; Kim, T. R.; Nordlund, D.; Sokaras, D.; Nowak, S.; To, J. W. F.; Higgins, D.; Sinclair, R.; Nørskov, J. K.; Jaramillo, T. F.; Bao, Z., *ACS Sustainable Chem. Eng.* **2018,** *6*, 311−317.
17.   Liu, Y.; Quan, X.; Fan, X.; Wang, H.; Chen, S., *Angew. Chem. Int. Ed.* **2015,** *54*, 6837−6841.
18.   Kim, H. W.; Ross, M. B.; Kornienko, N.; Zhang, L.; Guo, J.; Yang, P.; McCloskey, B. D., *Nat. Catal.* **2018,** *1*, 282−290.
19.   Lu, Z.; Chen, G.; Siahrostami, S.; Chen, Z.; Liu, K.; Xie, J.; Liao, L.; Wu, T.; Lin, D.; Liu, Y.; Jaramillo, T. F.; Nørskov, J. K.; Cui, Y., *Nat. Catal.* **2018,** *1*, 156−162.
20.   Iglesias, D.; Giuliani, A.; Melchionna, M.; Marchesan, S.; Criado, A.; Nasi, L.; Bevilacqua, M.; Tavagnacco, C.; Vizza, F.; Prato, M.; Fornasiero, P., *Chem* **2018,** *4*, 106−123.
21.   Chen, S.; Chen, Z.; Siahrostami, S.; Higgins, D.; Nordlund, D.; Sokaras, D.; Kim, T. R.; Liu, Y.; Yan, X.; Nilsson, E.; Sinclair, R.; Nørskov, J. K.; Jaramillo, T. F.; Bao, Z., *J. Am. Chem. Soc.* **2018,** *140*, 7851−7859.
22.   Han, L.; Sun, Y.; Li, S.; Cheng, C.; Halbig, C. E.; Feicht, P.; Hübner, J. L.; Strasser, P.; Eigler, S., *ACS Catal.* **2019,** *9*, 1283−1288.
23.   Fellinger, T.-P.; Hasché, F.; Strasser, P.; Antonietti, M., *J. Am. Chem. Soc.* **2012,** *134*, 4072−4075.
24.   Fukuzumi, S.; Yamada, Y.; Karlin, K. D., *Electrochim. Acta* **2012,** *82*, 493−511.
25.   Fukuzumi, S.; Lee, Y.-M.; Nam, W., *ChemCatChem* **2018,** *10*, 9−28.
26.   Pegis, M. L.; Wise, C. F.; Martin, D. J.; Mayer, J. M., *Chem. Rev.* **2018,** *118*, 2340−2391.
27.   Nagao, K.; Hiroshi, S.; Tetsuo, O., *Chem. Lett.* **1985,** *14*, 1917−1920.
28.   He, Q.; Mugadza, T.; Hwang, G.; Nyokong, T., *Int. J. Electrochem. Sci.* **2012,** *7*, 7045−7064.
29.   Kuwana, T.; Fujihira, M.; Sunakawa, K.; Osa, T., *J. Electroanal. Chem. Interfacial Electrochem.* **1978,** *88*, 299−303.
30.   Bettelheim, A.; Kuwana, T., *Anal. Chem.* **1979,** *51*, 2257−2260.
31.   Costentin, C.; Dridi, H.; Savéant, J.-M., *J. Am. Chem. Soc.* **2015,** *137*, 13535−13544.
32.   Kobayashi, N.; Nishiyama, Y., *J. Phys. Chem.* **1985,** *89*, 1167−1170.
33.   Langerman, M.; Hetterscheid, D. G. H., *Angew. Chem. Int. Ed.* **2019,** *58*, 12974−12978.
34.   Chan, R. J. H.; Su, Y. O.; Kuwana, T., *Inorg. Chem.* **1985,** *24*, 3777−3784.
35.   D'Souza, F.; Deviprasad, R. G.; Hsieh, Y.-Y., *J. Electroanal. Chem.* **1996,** *411*, 167−171.
36.   D'Souza, F.; Hsieh, Y.-Y.; Deviprasad, G. R., *J. Electroanal. Chem.* **1997,** *426*, 17−21.

37.   Geiger, T.; Anson, F. C., *J. Am. Chem. Soc.* **1981,** *103*, 7489–7496.
38.   Kang, C.; Anson, F. C., *Inorg. Chem.* **1995,** *34*, 2771–2780.
39.   Smith, P. T.; Kim, Y.; Benke, B. P.; Kim, K.; Chang, C. J., *Angew. Chem. Int. Ed.* **2020,** *59*, 4902–4907.
40.   Jacobson, R. R.; Tyeklar, Z.; Farooq, A.; Karlin, K. D.; Liu, S.; Zubieta, J., *J. Am. Chem. Soc.* **1988,** *110*, 3690–3692.
41.   Tyeklár, Z.; Jacobson, R. R.; Wei, N.; Murthy, N. N.; Zubieta, J.; Karlin, K. D., *J. Am. Chem. Soc.* **1993,** *115*, 2677–2689.
42.   Haber, F.; Weiss, J.; Pope, W. J., *Proc. R. Soc. London, Ser. A* **1934,** *147*, 332–351.
43.   Garcia-Bosch, I.; Cowley, R. E.; Díaz, D. E.; Siegler, M. A.; Nam, W.; Solomon, E. I.; Karlin, K. D., *Chem. - Eur. J.* **2016,** *22*, 5133–5137.
44.   Døssing, A. H., Alan; Toftlund, H., *Acta Chem. Scand.* **1996,** *50*, 95–101.
45.   Dürr, H.; Zengerle, K.; Trierweiler, H.-P., *Z. Naturforsch. B* **1988,** *43*, 361–368.
46.   Lee, D.-H.; Murthy, N. N.; Karlin, K. D., *Inorg. Chem.* **1997,** *36*, 5785–5792.
47.   Lim, B. S.; Holm, R. H., *Inorg. Chem.* **1998,** *37*, 4898–4908.
48.   Marcus, R. A., *Rev. Mod. Phys.* **1993,** *65*, 599–610.
49.   Schley, N. D.; Blakemore, J. D.; Subbaiyan, N. K.; Incarvito, C. D.; D'Souza, F.; Crabtree, R. H.; Brudvig, G. W., *J. Am. Chem. Soc.* **2011,** *133*, 10473–10481.
50.   van der Ham, C. J. M.; Işık, F.; Verhoeven, T. W. G. M.; Niemantsverdriet, J. W.; Hetterscheid, D. G. H., *Catal. Today* **2017,** *290*, 33–38.
51.   van Dijk, B.; Hofmann, J. P.; Hetterscheid, D. G. H., *Phys. Chem. Chem. Phys.* **2018,** *20*, 19625–19634.
52.   van Dijk, B.; Rodriguez, G. M.; Wu, L.; Hofmann, J. P.; Macchioni, A.; Hetterscheid, D. G. H., *ACS Catal.* **2020,** *10*, 4398–4410.
53.   Hall, S. B.; Khudaish, E. A.; Hart, A. L., *Electrochim. Acta* **1998,** *43*, 579–588.
54.   Mirica, L. M.; Ottenwaelder, X.; Stack, T. D. P., *Chem. Rev.* **2004,** *104*, 1013–1046.
55.   Kitajima, N.; Moro-oka, Y., *Chem. Rev.* **1994,** *94*, 737–757.
56.   Ross, P. K.; Solomon, E. I., *J. Am. Chem. Soc.* **1990,** *112*, 5871–5872.
57.   Ross, P. K.; Solomon, E. I., *J. Am. Chem. Soc.* **1991,** *113*, 3246–3259.
58.   Solomon, E. I.; Tuczek, F.; Root, D. E.; Brown, C. A., *Chem. Rev.* **1994,** *94*, 827–856.
59.   Fulmer, G. R.; Miller, A. J. M.; Sherden, N. H.; Gottlieb, H. E.; Nudelman, A.; Stoltz, B. M.; Bercaw, J. E.; Goldberg, K. I., *Organometallics* **2010,** *29*, 2176–2179.
60.   Forato, F.; Belhboub, A.; Monot, J.; Petit, M.; Benoit, R.; Sarou-Kanian, V.; Fayon, F.; Jacquemin, D.; Queffelec, C.; Bujoli, B., *Chem. - Eur. J.* **2018,** *24*, 2457–2465.
61.   Ganesan, V.; Sivanesan, D.; Yoon, S., *Inorg. Chem.* **2017,** *56*, 1366–1374.
62.   Li, W.; Xie, J.-H.; Yuan, M.-L.; Zhou, Q.-L., *Green Chem.* **2014,** *16*, 4081–4085.
63.   Newkome, G. R.; Kohli, D. K.; Fronczek, F., *J. Chem. Soc., Chem. Commun.* **1980**, 9–11.

4

Chapter 5

Mechanistic insight from structure–activity studies in the electrochemical oxygen reduction by substituted tris(2-pyridylmethyl)amine copper complexes

Structural modifications in the ligand system of molecular complexes can lead to improvement of activity and reduce the overpotential for electrochemical reactions. Many copper complexes with diverse structural differences have been reported for the O_2 reduction reaction, but the influence of electron withdrawing substituents had not yet been clearly investigated by a structure–activity study. To contribute to this field, we have investigated the effect of NH_2 (3^{NH2}), Cl (2^{Cl}), and CF_3 (2^{CF3}) as substituents on the oxygen reduction activity of the tris(2-pyridylmethyl)amine copper complex (1); a recently reported very fast molecular copper complex for the oxygen reduction reaction. We found that the redox couple, as expected, had a clear correlation between the Hammett parameters of the substituents and the $E_{1/2}$ of the redox couple. On the other hand, the onset for O_2 reduction was not affected by the substituents as was determined with rotating ring disk electrode (RRDE) experiments. Non-rotating electrode experiments and a Tafel analysis derived from the RRDE data indicated that only 2^{Cl} had a higher rate for O_2 reduction with respect to 1. In contrast, 2^{CF3} did not have improved reactivity and 3^{NH2} displayed significantly lower reactivity than 1. On the other hand, the electron withdrawing effect of 2^{Cl} and 2^{CF3} shifted the onset potential for H_2O_2 reduction 150 mV positive with respect to 1. Moreover, the rate had increased with respect to 1. The remarkable results of O_2 reduction has led to a new insight in the O_2 reduction mechanism, wherein we propose that a Cu^{II} to $Cu^{II}–O_2^{\bullet-}$ step is the observed potential determining step instead of the $Cu^{I/II}$ redox couple of the complex because the rate of O_2 reduction is very fast compared to the experimental scan rate. The significant outcome is that the onset potential for O_2 reduction cannot be easily adjusted by electronic effects of substituents. On the other hand, we have shown that H_2O_2 reduction is affected by these electronic effects. We found that electron withdrawing groups has a beneficial effect on both the onset potential as well as the catalytic rate.

5.1 Introduction

The electrochemical O_2 reduction reaction is an important and versatile reaction. A major aspect is that two different products can be formed with their own applications and challenges. The 4 electron reduction to H_2O plays a central role in fuel cell chemistry. To electrochemically oxidize (sustainably produced) H_2 for electricity generation, O_2 to H_2O reduction has to take place at the cathode. However, even with the best catalysts to date (Pt-based) there are significant energy losses in the form of 400 mV overpotentials.[1-3] The other possible outcome of O_2 reduction is the 2 electron O_2 to H_2O_2 reduction that is a viable and environmentally friendly alternative for the current anthraquinone process for the production of H_2O_2.[4, 5] The waste generation and energy requirements of the latter process make H_2O_2 one of the most expensive bulk chemicals even though it has diverse (green) applications.[6-9] Obviously, for either goal a highly active and selective catalyst with minimal overpotential would be desired.

Recently, our group has shown that complex **1** (Chart 5.1) displays very high reaction rates for the electrochemical O_2 reduction reaction.[10] It was found that O_2 is reduced in two separate catalytic cycles. In the first cycle, O_2 is reduced to H_2O_2. This cycle was proposed to start with the fast reduction of the complex to Cu^I (Equation 5.1). In the next step, suggested as the rate determining step, the reduced Cu^I complex coordinates O_2 and forms a radical superoxo complex (Equation 5.2). Subsequently, the complex further reduces via a proton coupled electron transfer step to an end-on hydroperoxo complex (Equation 5.3) which will release H_2O_2 after protonation. H_2O_2 was found as a detectable intermediate. In the second cycle, the further two electron reduction of H_2O_2 to H_2O takes place. The difference between the equilibrium potential of the desired reaction and the actual onset potential at which catalysis starts, was still around 0.2 V for O_2 to H_2O_2 reduction. This is not
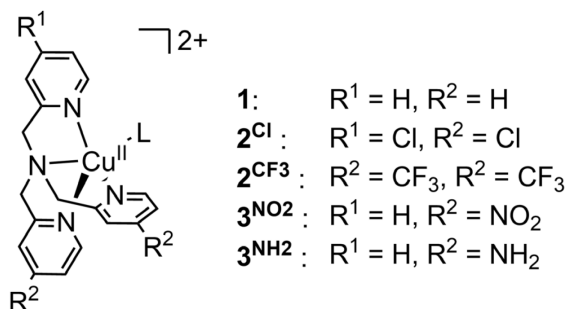
Chart 5.1. Structure and nomenclature of the copper complexes.

based on the standard equilibrium potential of O_2 to H_2O, which is 1.23 V *versus* RHE (reversible hydrogen electrode), but on the 2 electron O_2 to H_2O_2 equilibrium potential of 0.695 V *versus* RHE.[11] The overall rate of the two catalytic cycles for the total 4 electron reduction of O_2 to H_2O was determined at $1.5 \times 10^5 \pm 0.2 \times 10^5$ s^{-1}. The direct determination of the rate constant was possible with the current enhancement method which uses the peak catalytic current and peak current of the reduction the complex to Cu^I (see Chapter 1).[12] Of note, this rate was determined with very low catalyst concentrations (0.1 – 1.0 µM) since the O_2 solubility in water is around 1.2 mM and this way substrate availability does not influence the observed rate significantly. The rate for the O_2 to H_2O_2 reduction, the first catalytic cycle, was calculated with a foot of the wave analysis (FOWA) which is performed close to the onset of the catalytic current to avoid any side-phenomena (such as substrate depletion) so that the current can be assumed to be purely kinetic in nature.[13-16] Of note, the FOWA does not determine the actual rate of catalysis, but estimates the maximum rate, or the maximum turnover frequency (TOF$_{max}$). From the FOWA, a TOF$_{max}$ of $1.8 \times 10^6 \pm 0.6 \times 10^6$ s^{-1} was determined which is in close agreement with the overall rate as obtained with the current enhancement method showing that O_2 reduction catalysis at low catalyst concentrations is close to the maximum rate. For the FOWA, an EC mechanism was assumed in which the rate determining, chemical step is Equation 5.2 which is preceded by fast reduction of **1** with the potential determining step being related to the $E_{1/2}$ of the $Cu^{I/II}$ redox couple. The rate constant for Equation 5.2 (k_2) would actually be the same as the rate of O_2 coordination (k_{O2}) to the Cu^I complex. The rate would be linked via $k_2 = [O_2]k_{O2}$. k_{O2} for the Cu^I complex of **1** has previously been determined to be 1.3×10^9 M^{-1} s^{-1} in THF.[17] When correcting for the 1.2 mM O_2 concentration in phosphate buffer, the same order of magnitude (10^6 s^{-1}) as the TOF$_{max}$ is obtained.

k_1 (ET),
$E_{1/2}$ (Cu$^{I/II}$) $Cu^{II} + e^- \rightleftharpoons Cu^I$ **Eqn. 5.1**

k_2 (k_{O2}) $Cu^I + O_2 \rightleftharpoons Cu^{II}O_2^{\bullet-}$ **Eqn. 5.2**

k_3 $Cu^{II}O_2^{\bullet-} + e^- + H^+ \rightleftharpoons Cu^{II}OOH$ **Eqn. 5.3**
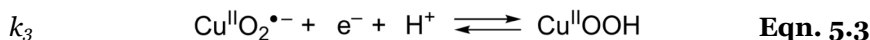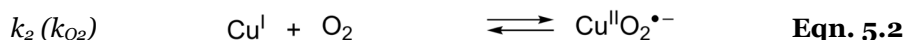
O_2 reduction catalysis by **1** is very fast, but there is still a 0.2 V difference between the equilibrium potential of O_2 to H_2O_2 and the onset potential. Placing substituents on the pyridines of the tmpa ligand (tmpa = tris(2-

pyridylmethyl)amine) of **1** could help to affect the $E_{1/2}$ and the rate of catalysis. A previous study suggested that O_2 coordination to form the end-on superoxo intermediate (Eqn. 5.2) is favored by strong electron donating substituents on the *para* position of the pyridines of the tmpa ligand (tmpa = tris(2-pyridylmethyl)amine) and would thus increase k_1 of Equation 5.2.[18] However, another study reported that electron donating cyclic amine substituents on the tmpa ligand decreased the $E_{1/2}$ and thereby increasing the energy of the HOMO.[19] The latter was found to increase the rate of atom transfer radical polymerization reactions by facilitating the formation of Cu–X species (X = halogen). Interestingly, one studied claimed that NH_2 in the *ortho* position did not affect the onset nor the Tafel slope of O_2 reduction with respect to **1**.[20] This remarkable result was explained as that not the $Cu^{I/II}$, nor a protonation step would be rate determining, but the O–O bond cleavage step would be. However, this specific electrocatalytic study was performed at pH 1. At this pH, the pyridines are protonated at the nitrogen and are unable to coordinate to copper.[21] Essentially, the molecular complexes cannot exist under the experimental conditions. Since the other studies did suggest that substitution of **1** (or related complexes) affects the catalytic activity and the $E_{1/2}$, we placed NO_2, NH_2, CF_3, and Cl[19] substituents on the *para* positions of the pyridines of **1** (Chart 5.1) to understand if and how substituents could improve the rate of electrocatalytic O_2 and H_2O_2 reduction and the onset potential.

5.2   Results

5.2.1   Strategy and synthesis of $\mathbf{3^{NO2}}$ and $\mathbf{3^{NH2}}$

Placing electron donating (EDG) or withdrawing groups (EWG) on the ligand framework was expected to electronically steer the reaction rate and/or selectivity. Especially aromatic (heterocyclic) rings allow for the precise position of both electron withdrawing or donating groups. Louis Hammett found that these substituents could be described by a parameter (σ) and linked to properties such as the pK_a of benzoic acids and phenols, the rate of esterification or hydrolysis of aromatic compounds, or the rate of bromination of acetophenone.[22, 23] Based on these Hammett parameters, specific substituents can be chosen to apply the withdrawing or donating effect to a complex and its reactivity in catalysis. The $E_{1/2}$ of the $Cu^{I/II}$ redox couple of the complexes can be shifted depending on the electronic nature of the substituents. Less electron density around the metal center, induced by EWG, will shift the $Cu^{I/II}$ redox couple to higher potentials while an EDG will lower the $E_{1/2}$. We set out to investigate EWG's on the ligand framework of **1** as we expect

118

these to shift the $E_{1/2}$ of the $Cu^{I/II}$ redox couple to higher potentials which is proposed as the potential determining step for O_2 to H_2O_2 reduction (Eqn. 5.1). In that retrospect, we were interested in studying the effect of Cl, CF_3, and NO_2 substituents that have Hammett parameters of 0.23, 0.54, and 0.78, respectively for the *para* position. Complexes **2^{Cl}** and **2^{CF3}** have all three pyridines substituted at the *para* position and were obtained from the laboratory of K. D. Karlin at the John Hopkins University. Likewise, we were interested in synthesizing the NO_2 analogue. As this analogue could be easily converted to the NH_2 analogue by reduction, we also synthesized the NH_2 analogue for comparison since it has a lower (-0.66) Hammett parameter than tmpa (0 by definition).

For the synthesis of a ligand with three pyridines substituted with NH_2 at the *para* position, 2-aminomethyl-4-nitro-pyridine is required as an intermediate. Compound **5** (Scheme 5.1) is the starting material for 2-aminomethyl-4-nitropyridine, but also required for the S_N2 reaction with an amine to obtain the desired tripodal ligand. However, compound **5** was found to be highly unstable in the solid state and was thus immediately used further in the synthesis after purification to minimize the loss in yield. For that reason, 2-aminomethylpyridine instead of 2-aminomethyl-4-nitropyridine was used which resulted in ligand **6** with two instead of three substituted pyridines via an S_N2 reaction. To obtain the unstable intermediate **5**, compound **4** was prepared by the reaction of the commercially available 4-nitro-2-picoline-N-oxide with trifluoroacetic anhydride and subsequent hydrolysis. The hydroxymethyl-pyridine **4** was then converted into the
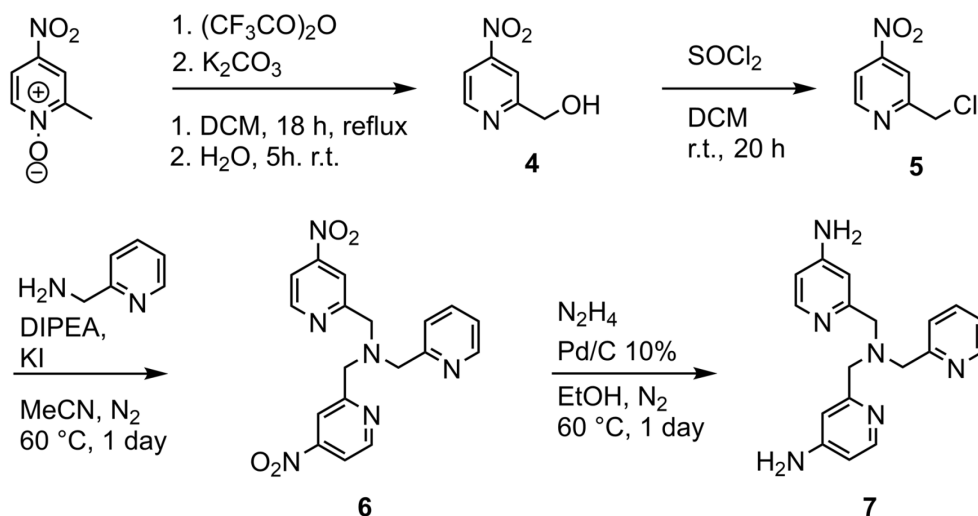
Scheme 5.1. Synthetic route to the ligands **6** and **7**.

chloromethyl-pyridine **5**. Ligand **6** was characterized by ^{1}H nuclear magnetic resonance (NMR), ^{13}C NMR and high resolution mass spectroscopy (HR MS). The NH$_2$ analogue, ligand **7**, was prepared from **6** by catalytic reduction of the nitro groups with Pd/C and hydrazine as reducing agent. **7** was characterized by NMR and MS as well. Next the corresponding copper complexes **3**^{NO2} and **3**^{NH2} were synthesized. **3**^{NO2} was synthesized by mixing Cu(OTf)$_2$ (OTf = CF$_3$SO$_3^-$) and **6** in methanol. The complex was crystallized to produce blue crystals by vapor diffusion of diethyl ether (Et$_2$O) into acetonitrile (MeCN). Unfortunately, no suitable crystals for structure determination by X-Ray diffraction were obtained. Elemental analysis confirmed that [Cu(**6**)(MeCN)](OTf)$_2$ was obtained in purified form. The NO$_2$ groups of **3**^{NO2} were found to electrochemically reduce in the same potential window as where the redox couple and any O$_2$/H$_2$O$_2$ reduction activity would be expected (Figure D.1). Therefore, this complex was not further studied. The complex **3**^{NH2} was synthesized in the same way by mixing **7** and Cu(OTf)$_2$. However, **3**^{NH2} could not be crystallized into a solid form. Probably, hydrogen bonding of the amine with water hinders crystallization. The ligand only dissolves in water and MeOH which limited further crystallization possibilities. When Cu(OTf)$_2$ and **7** are mixed in water (or methanol), the solution turns immediately green in color. This indicates that the complex is formed instantaneous and is characterized by absorptions at 260 nm, 270 nm, *circa* 300 nm (broad), and low intensity, broad absorptions at 700 and 900 nm in the UV-vis spectrum (Figure D.2). Therefore, measurements were performed with the *in situ* formed complex by mixing Cu(OTf)$_2$ and **7** in water in a 1 : 1 ratio and subsequently mixing it with phosphate buffer. Of note, minor impurities are likely still present since purification was not possible which could lead to deposits. Nevertheless, the complex shows a clear redox couple and its cyclic voltammogram (CV) of O$_2$ and H$_2$O$_2$ reduction activity can be compared.

5.2.1   Electrochemistry of **2**^{Cl}, **2**^{CF3}, and **3**^{NH2}

To study the substituent effect on the redox couple, cyclic voltammograms of the complexes in pH 7 phosphate buffer under argon atmosphere were recorded (Figure 5.1). In addition, cyclic voltammograms at 100 mV/s scan rate of **1**, **2**^{Cl}, **2**^{CF3}, and **3**^{NH2} are overlaid in Figure 5.1D. As mentioned before, no data for **3**^{NO2} could be acquired since the NO$_2$ groups are electrochemically reduced in this potential window (Figure D.1). At first sight, the peak current of the substituted complexes is lower than that of **1**. This is caused by lower diffusion coefficients of these complexes as compared to **1** which were determined using the Randles–Sevcik equation (see
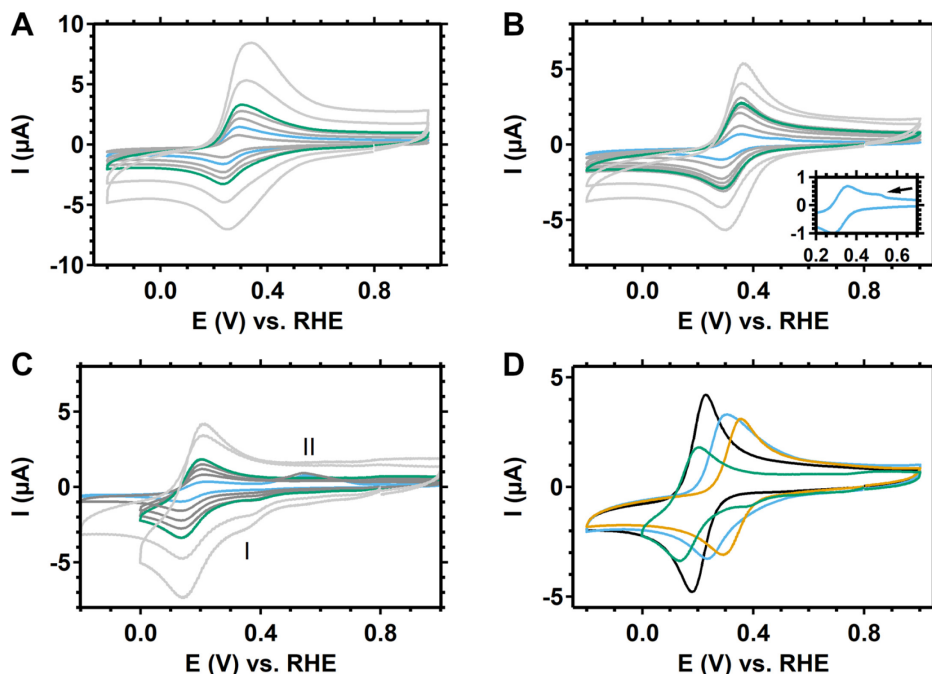
Figure 5.1. Cyclic voltammograms of 2^{Cl} (A), 2^{CF3} (B), and 3^{NH2} (C). The cyclic voltammograms were recorded at scan rates from 25 mV/s (blue) to 100 mV/s (green) in argon purged 0.1 M phosphate buffer of pH 7. Scan rates of 200 and 400 mV/s are depicted in light grey. Catalyst concentration was 0.3 mM. (D) shows 2^{Cl} (blue), 2^{CF3} (orange), and 3^{NH2} (green) with **1** (black) at 100 mV/s. Data of **1** was adapted from reference 10.

Chapter 1).[16] The diffusion coefficients for 2^{Cl} (2.0×10^{-6} cm²/s), 2^{CF3} (1.8×10^{-6} cm²/s), and 3^{NH2} (1.3×10^{-6} cm²/s) are less than half of that of **1** (4.9×10^{-6} cm²/s).[10]

The electron withdrawing or donating capabilities of the substituted complexes **2** and **3** can be best described by the σ_p as Hammett parameter for substituents on the *para* position. As expected, the EWG's of 2^{Cl} and 2^{CF3} shift the $E_{1/2}$ of the redox couple to higher potentials with respect to **1**. Specifically, the $E_{1/2}$ of the complexes shifts from 0.21 V (**1**) to 0.27 V (2^{Cl}) and 0.32 V (2^{CF3}). On the other hand, the $E_{1/2}$ of 3^{NH2} is lower than **1** at 0.17 V due to the electron donating character of NH₂. The $E_{1/2}$ values of the complexes are plotted *versus* the σ_p of the substituents in Figure 5.2A. There is a clear correlation even though the fit is not perfect. Given that the complexes have either 2 or 3 substituted pyridines, Figure 5.2B was constructed where the σ_p of 3^{NH2} was normalized by the number of substituents introduced at the ligand. This normalization of the Hammett parameter gave a better linear fit (Figure 5.2B) which is illustrated by a higher R^2 value.

The peak separation between the reduction and oxidation peaks provides information about the (ir)reversibility of the redox couple. The cyclic voltammogram of 2^{Cl} at scan rates above 100 mV/s appear to be less reversible since both the reductive and oxidative peaks broaden (Figure 5.1A). At those high scan rates, there may be some underlying equilibrium that becomes visible. The electron withdrawing character of the chloride groups might elongate the Cu–N bond of the pyridines. It could be that one, or more of these Cu–N bonds are replaced with H_2O or phosphate in a dynamic equilibrium. However, no second redox couple was found at lower scan rates which would be indicative of the presence of more than one species. A second oxidation did appear at low scan rates in the cyclic voltammogram of 2^{CF3}. In general, the oxidation peak is relatively broad and a second oxidation was observed at 0.52 V at a scan rate of 10 mV/s (Figure 5.1B). No second reduction peak is observed indicating that this second oxidation seems to belong to a species that is formed during the reduction of 2^{CF3}. The cyclic voltammogram of 3^{NH2} has some oxidative peaks that arise from the minor impurities which are indicated by II in Figure 5.1C. These oxidations were not visible when the lower potential limit was set at 0.0 V instead of −0.2V and are possibly related to Cu^0 deposition. In addition, a reductive peak was observed as indicated by I in Figure 5.1C. This reduction relates to the reduction of a small remnant of O_2. Normally, the second scan can be used in that case since all the O_2 has reduced away by the time the second scan starts. However, small impurities in a solution containing 3^{NH2} can electrodeposit on the electrode and thereby influence the cyclic voltammogram significantly in the second scan. Thus, the first scan was used for 3^{NH2}. Interestingly, Laviron plots of the potential of the oxidative and reductive peaks of the complexes *versus* the scan rate show that the peak positions do not shift up to 100 mV/s (Figure D.4) and the peak separation does not widen above 100 mV/s. An increase in peak separation could indicate a
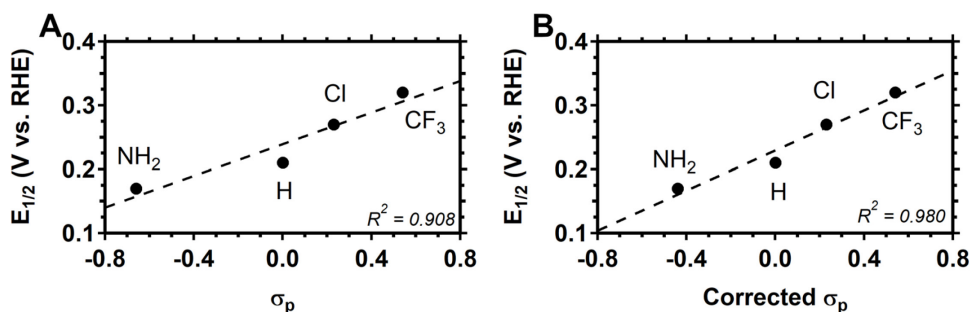
Figure 5.2. Correlation of the Hammett parameter of the substituents and the $E_{1/2}$ of the corresponding complexes. Dashed lines are linear fits. For B, the σ_p of NH_2 was multiplied by 0.667 (2/3).

slower electron transfer,[24] thus it seems that electron transfer for 2^{Cl}, 2^{CF3}, and 3^{NH2} is still fast in contrast to other related complexes such as the dinuclear copper complex described in Chapter 4 and mononuclear copper complex with terpyridine and 2,2'-dimethylpyridylamine ligands.[24]

The magnitude of the peak current varies with the scan rate. As can be derived from the Randles-Sevcik equation (Chapter 1), a linear relationship between the square root of the scan rate and the peak current indicates that diffusive processes play a role for the observed species. Otherwise, there is a direct linear relationship with the peak current. For complexes 2^{Cl}, 2^{CF3}, and 3^{NH2}, the best fit is obtained when the peak current is plotted *versus* the square root of the scan rate rather than directly *versus* the scan rate (Figure 5.3). The fits of 3^{NH2} are of less quality, but for this complex the data fits best when the square root of the scan rate is considered. Therefore, diffusive processes play a role for the (major) redox feature, which belong to the redox couple of the complexes. Following, the complexes themselves are most likely homogeneous in nature.

5.2.2 O₂ and H₂O₂ reduction with non-rotating electrodes

Compound **1** reduces O_2 in a stepwise mechanism wherein H_2O_2 is formed as detectable intermediate before it is further reduced to H_2O. Therefore, both O_2 and H_2O_2 reduction were addressed separately (Figure 5.4). First of all, O_2 reduction is
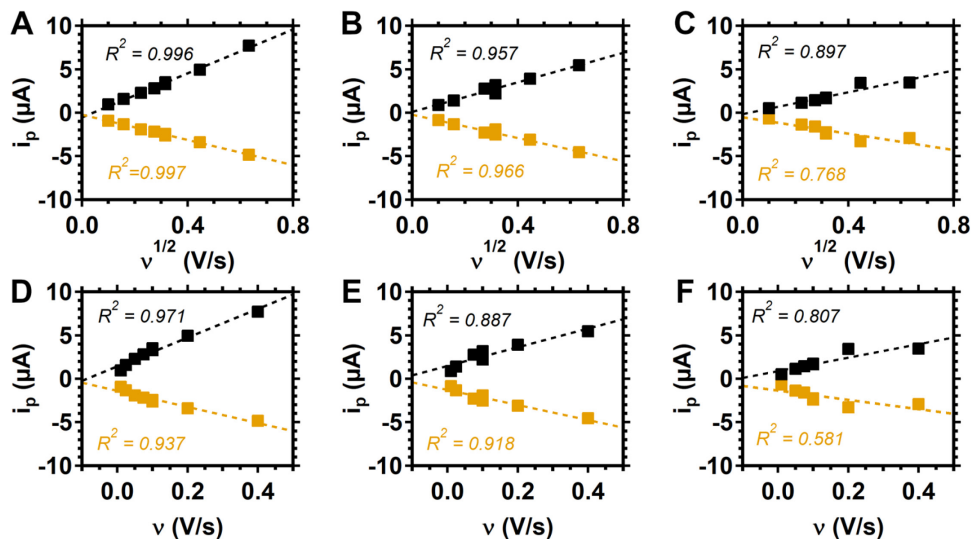
Figure 5.3. Cathodic (orange) and anodic (black) peak currents of the redox couple plotted *versus* either the square root of the scan rate (A–C) or directly *versus* the scan rate (D–F) of the complexes 2^{Cl} (A and D), 2^{CF3} (B and E), and 3^{NH2} (C and F). Dashed lines are linear fits.

considered. Differences in onset potential and peak potential of O_2 reduction by the complexes are visible from the overlay of the voltammograms of complexes **1**, **2^{Cl}**, **2^{CF3}**, and **3^{NH2}** in Figure 5.4. At first sight, the current of **1** and **2^{Cl}** overlap near the onset of O_2 reduction. The same applies to the onset potential for **2^{CF3}** and **3^{NH2}**, but these complexes start reducing O_2 around 50 mV lower. Of note, there is a large experimental error up to 75 mV in the apparent onset potential (Figure D.5). In the next section, the use of rotating electrodes is described whereby the experimental error was smaller and the onset potential is more accurate. The displayed CV's in Figure 5.4 also render information regarding the rate of catalysis. A larger catalytic rate results in higher currents, thus a steeper slope of would indicate faster catalysis.[13] In that sense, **2^{Cl}** (and to a lesser extent **2^{CF3}** as well) seems to catalyze the reduction of O_2 with a higher rate because the reductive current has a steeper slope than **1**. Beware that the catalytic current of the cyclic voltammogram encompasses both O_2 to H_2O_2 and H_2O_2 to H_2O reduction and catalysis is significantly hindered since the O_2 concentration is just one order of magnitude higher than the catalyst concentrations (1.2 mM *versus* 0.3 mM). The lower catalytic rate of **3^{NH2}** is more evident from the CV as its slope is less steep. In addition, a kink can be seen in the reductive current in the presence of O_2 (Figure 5.4 A). This feature could indicate that apart from O_2 reduction, a second reductive process such as catalyst reduction takes at a higher potential than O_2 reduction.

As opposed to the apparent same onset potential for O_2 reduction, H_2O_2 reduction by **2^{Cl}** starts at a 200 mV higher potential than **1**. The other complex bearing an EWG (**2^{CF3}**) has a positive shift in H_2O_2 reduction as well, albeit around 100 mV with respect to **1**. The current profile between the onset and the peak
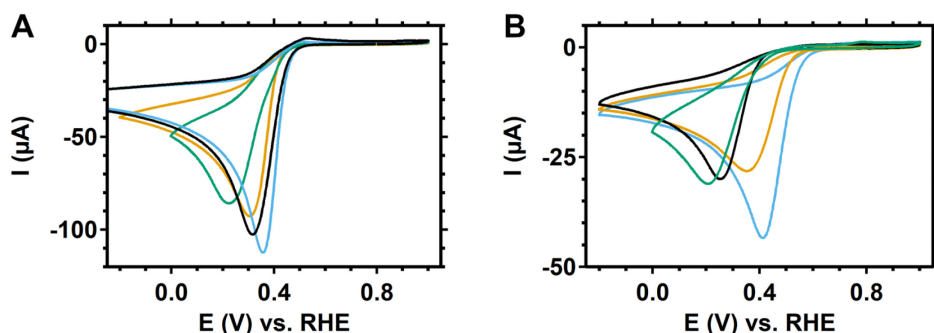
Figure 5.4. Cyclic voltammograms of O_2 reduction (A) and H_2O_2 reduction (B) by 0.3 mM **1** (black), **2^{Cl}** (blue), **2^{CF3}** (orange), and **3^{NH2}** (green). The CV's were recorded at 100 mV/s in 0.1 M phosphate buffer of pH 7 that was either saturated with 1 atm O_2 (A) or argon (B). 1.1 mM H_2O_2 was added to the solution for B. Data of **1** was adapted from reference 10.

catalytic current is considerably steeper in the case of 2^{Cl} than in the case of 2^{CF3} and **1** pointing to faster catalysis. Complex 3^{NH2} with an EDG starts H_2O_2 reduction at the same potential as **1** within the experimental error range. Clearly, the slope of the current is less steep, signifying slower catalysis than **1**. The presence of a second reductive process, as was the case for O_2 reduction, is not clear from the voltammogram, even though the onset potential is around 0.4 V for both O_2 and H_2O_2 reduction.

In general, the onset for O_2 reduction does not change significantly based on the EWG or EDG and is actually within the experimental error. The voltammogram of 2^{Cl} does suggest faster catalysis (overall for the O_2 to H_2O reduction) than **1**. For the H_2O_2 to H_2O reduction, the differences in onset potential are larger and outside the range of the experimental error. H_2O_2 reduction clearly starts at a higher potential for both 2^{Cl} and 2^{CF3} with EWG's with respect to the unsubstituted complex **1**. Moreover, the voltammogram of 2^{Cl} suggests faster catalysis. Interestingly, the Hammett parameter for 2^{Cl} is lower than for 2^{CF3} which might suggest that not only the electron withdrawing character of the chloride group influence the reactivity. In all cases, the onset potential of 3^{NH2} does not significantly differ from **1** and the voltammogram indicates that both O_2 and H_2O_2 reduction is more sluggish.

5.2.3 O_2 and H_2O_2 reduction with rotating (ring) disk electrode

As introduced in Chapter 1, the rotating ring disk electrode (RRDE) is an experimental setup that controls diffusion. Due to the creation of a laminar flow of electrolyte towards the electrode, the diffusion is constant and no longer dependent on the scan rate.[25] This way, the catalytic onset potential can be more accurately compared as the influence of experimental errors could be diminished (Figure D.6). Moreover, the ring electrode around the GC work electrode can be put to use as an electrochemical sensor for H_2O_2 by constantly applying a potential of 1.2 V. O_2 and H_2O_2 reduction were therefore studied by RRDE in a pH 7 phosphate buffer at 1600 rpm electrode rotation rate.

Whereas the results of the non-rotating electrode experiments showed differences in onset potential, the RRDE measurements clearly indicate that these differences should be ascribed to the experimental error. As seen in Figure 5.5A (and the zoom), complexes **1** and 2^{CF3} have the same onset potential. 2^{Cl} seem to start reducing O_2 at a 50 mV lower potential, but again this is within the experimental error limit (Figure D.6). Moreover, the current profiles of **1** and 2^{Cl} overlap almost perfectly. Initially, 2^{CF3} follows the same profile, but deviates at lower potential because a lower diffusion limited current is reached. The catalytic performance of
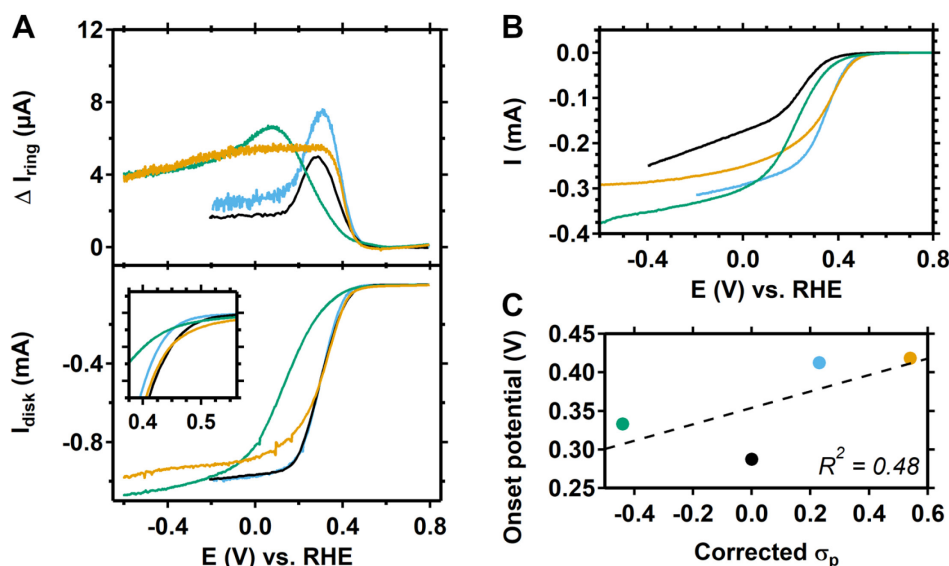
Figure 5.5. Linear sweep voltammograms of O_2 reduction (A, bottom panel) and H_2O_2 reduction (B) by 2^{Cl} (blue), 2^{CF3} (orange), 3^{NH2} (green) and **1** (black), and the onset of H_2O_2 reduction (C, defined as potential where current has reached −50 µA). The Pt ring current (at 1.2 V) is shown in the top panel of A. Scans were recorded at 50 mV/s in a O_2 (A) or Ar (B) saturated 0.1 M phosphate buffer at 0.3 mM catalyst concentration. For B, 1.0 mM H_2O_2 was used. The electrode was rotated at 1600 rpm. Data of **1** was adapted from reference 10.

3^{NH2} is clearly less than that of the other complexes since it only reaches the diffusion limited current at −0.2 V whereas the other complexes do so around 0.2 V. In the potential window between the onset and the diffusion limited current, the ring current indicates that H_2O_2 is partially produced in the case of all complexes. For **1** and 2^{Cl}, a maximum ring current is reached before it levels off.

The maximum ring current differs for **1** and 2^{Cl}, but can be explained by the difference in collection efficiency for H_2O_2 of the ring (12.5% for **1**[10] and pre-determined at 14.8% for 2^{Cl}). As explained in Appendix C, the collection efficiency of the Pt ring for H_2O_2 can be best pre-determined for every experiment to have a reliable collection efficiency. Following, the collection efficiency was determined prior to the measurement of 2^{Cl} by a 3 minute amperogram at −0.1 V disk potential in catalyst-free electrolyte. As the current profiles on the disk overlap for **1** and 2^{Cl}, it is not expected that there is a difference in H_2O_2 selectivity. On the other hand, the ring current profile of 2^{CF3} indicates that H_2O_2 is produced in significant quantities even when the diffusion limited current is reached. In detail, in the potential window between 0.0 and −0.2 V, the average ring current was 5.5 µA where the disk current was 800 µA . Together with a pre-determined collection efficiency of 10.2% prior to

the measurement of 2^{CF3}, the percentage of H_2O_2 was calculated using Eqn. C.1 to be 12.5%.This also explains why the magnitude of the disk current of 2^{CF3} is less than for **1** and 2^{Cl}. A higher selectivity for H_2O_2 inherently results in less electrons that have to be transferred (2 electron *versus* 4 electron reduction of O_2). 3^{NH2} also produces significantly more H_2O_2. Moreover, the diffusion limited current is not reached before the potential limit (<0.0V) where electrodeposition starts to play a role as well (Figure D.3). Also, a new feature is observed on the ring current after prolonged scanning (Figure D.3). Thus, a reliable percentage of H_2O_2 cannot be determined. Nevertheless, it is expected that the selectivity for H_2O_2 is higher than for 2^{CF3} since the ring current is higher and the disk current lower at a potential of 0.0 V for 3^{NH2}.

The current from the RRDE setup is composed of the diffusion limited current I_L and a kinetic current I_k according to the Koutecký-Levich equation (Eqn. 1.6, Chapter 1). As explained in the introduction, the kinetic current is the theoretical current in absence of any mass transport limitations. Since the diffusion limited current is known, I_k can be calculated. When the potential (or overpotential) is plotted *versus* the logarithm of I_k (or the current density) the Tafel plot is obtained.[25] The linear part of this plot can be fitted to obtain the Tafel slope that bears, in theory, information about the mechanism and catalyst performance. Of note, the Tafel plot and slope are usually applied for catalytic reactions that occur at the surface of a heterogeneous electrocatalyst. Since the electrocatalysts in this case (the complexes) are diffusive species as well, any insight from such a Tafel plot should be taken with care. The constructed Tafel plots for O_2 reduction and corresponding slopes for **1**, 2^{Cl}, 2^{CF3}, and 3^{NH2} are depicted in Figure 5.6A. The kinetic currents of all three complexes lie close together. The slopes of the fits of 2^{CF3} and **1** can be considered equal as there is merely a 4 mV/dec difference. The slope of 2^{Cl} is substantially lower at 70 mV/dec which is indicative of faster catalysis. In addition, the slope of 3^{NH2} is substantially higher than the other complexes representing that O_2 catalysis is significantly slower. The Tafel analysis thus supports the visual interpretation of catalytic rates from the non-rotating electrode data for O_2 reduction. In addition, there is no clear correlation to the Hammett parameter (Figure 5.6C). Instead, the data suggests that there is an optimum in reactivity for 2^{Cl}.

Very similar to the non-rotating electrode experiments, there is a large difference in H_2O_2 reduction performance between the complexes bearing EWG's (2^{Cl} and 2^{CF3}) and unsubstituted **1** (Figure 5.5B). The onset potential for H_2O_2 reduction, here defined as the potential at which −50 µA is reached, is plotted *versus* the Hammett parameter of the complexes in Figure 5.5C. There is a positive onset
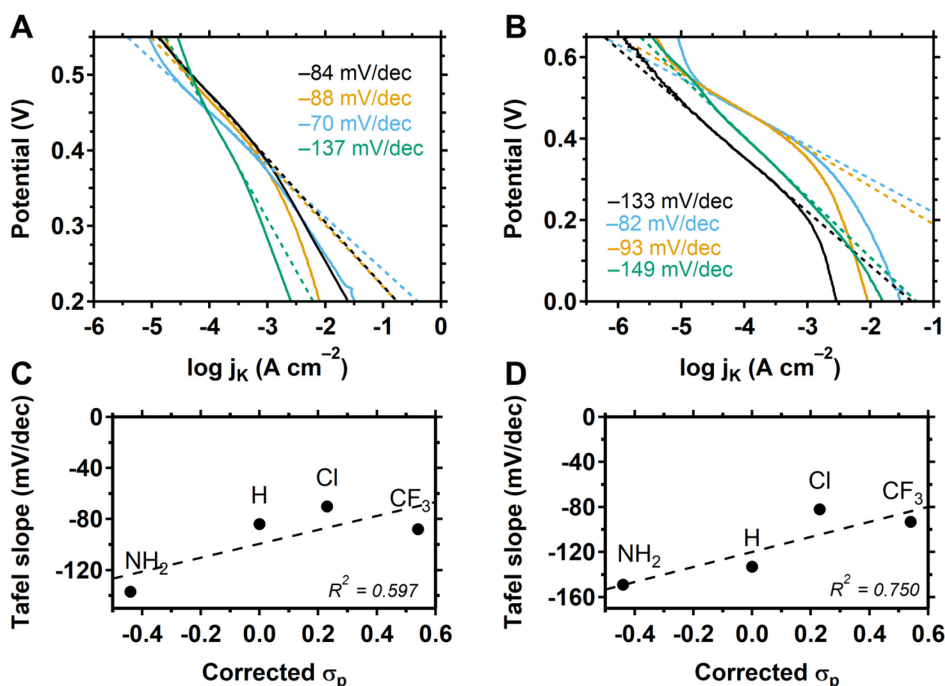
Figure 5.6. Tafel plots of O_2 reduction (A) and H_2O_2 reduction (B) by **1** (black), **2^{Cl}** (blue), **2^{CF3}** (orange), and **3^{NH2}** (green) and the correlation to the Hammett parameter for O_2 (C) and H_2O_2 (D) reduction. The data were obtained in O_2 (A) or argon (B) purged 0.1 M phosphate buffer of pH 7 with 0.3 mM catalyst concentration. The electrode was rotated at 1600 rpm and a scan rate of 50 mV/s was used. 1.0 mM H_2O_2 was used for B. The dashed lines are fits of the linear part of the Tafel plot in A and B. The numbers are the corresponding slopes. Data of **1** was adapted from reference 10.

shift up to 150 mV induced by the EWG's. Interestingly, the onset potential of **3^{NH2}** is slightly above that of **1** as well. The Tafel plot of H_2O_2 reduction (Figure 5.6B) emphasizes the large increase in performance due EWG's (Figure 5.6D). Clearly, **2^{Cl}** and **2^{CF3}** outperform **1** as higher currents at higher potentials are obtained and the respective slopes are significantly lower. For H_2O_2 reduction, the Hammett parameter has a clearer correlation with the catalytic rate (Figure 5.6D) as compared to the results of O_2 reduction, although maximum activity is found for **2^{Cl}** as well. Another similarity is that the performance of **3^{NH2}** is the lowest of all complexes, but the performance of **1** is just slightly higher for H_2O_2 reduction as opposed to the large difference in O_2 reduction activity between **1** and **3^{NH2}**. It has to be noted that no real diffusion limited currents for H_2O_2 reduction are reached in the measured potential window. The exact origin is not known, but substrate/product inhibition or catalyst degradation might be taking place simultaneously. A possibility could be that highly reactive radical species, formed in a Fenton type H_2O_2 reduction mechanism, result

in catalyst degradation whereby the conditions for current purely determined by mass transport limitations are not fulfilled.

The RRDE measurements have shown that there are no significant shifts in onset potential for O_2 reduction with EWG's, whereas the onset did shift positively for H_2O_2 reduction. In addition, the Tafel analysis confirms the observations under non-rotating conditions particularly that 2^{Cl} seems to outperform **1** in both O_2 and H_2O_2 reduction whereas 2^{CF3} only shows improved H_2O_2 reduction activity. Interestingly, the H_2O_2 selectivity of 2^{CF3} is higher than the other complexes which is counterintuitive. The lower diffusion limited current in O_2 reduction also points to the fact that not all H_2O_2 that is formed, is further reduced to H_2O by 2^{CF3}. As the Tafel analysis indicates that the performance close to the onset for H_2O_2 is intrinsically better than **1**, it might be that other processes take place at lower potentials (further from the onset potential), possibly related to the formation of a second, less active species as previous observations (Figure 5.1) did show the existence of a second species after reduction. Also, the complex might also be more prone to degradation at lower potentials.

5.3 Discussion

As demonstrated, EWG's and a EDG can alter the electrochemical and electrocatalytic properties of **1**. First of all, the $E_{1/2}$ of redox the couple had an expected Hammett correlation with the different substituents used in this study. In contrast, the O_2 reduction onset potential was not influenced by electronic character of the substituents. This observation points to an O_2 reduction mechanism wherein the potential determining step is not related to the $E_{1/2}$ of the complex. On the other hand, a slight performance boost for 2^{Cl} with respect to **1** was found. Based on these findings, we suggest that the apparent (observed) mechanism is not best described by Equations 5.1 and 5.2. Based on the immensely fast O_2 reduction by **1**, that can achieve 10^5 turnovers of O_2 per second at micromolar catalyst concentrations,[10] we argue that that the observed potential determining step first is not the 1 electron reduction of the Cu^{II} to the Cu^I complex step (Eqn. 5.1), but rather related to the simultaneous coordination of O_2 and reduction to a superoxo species according to Equation 5.4. The reduction of the Cu^{II} complex (Eqn. 5.1) and the subsequent coordination of O_2 resulting in the superoxo species (Eqn. 5.2) are both very fast and can be considered instantaneous on the time scale of the cyclic voltammograms with scan rates of 50 or 100 mV/s. For that reason, the reduced Cu^I complex might be seen as a transient species and not as an intermediate (Eqn. 5.5). Following, the

overall equilibrium of Equation 5.5 could be covered by Equation 5.6 with a separate $E_{1/2}'$.

$$k_1'/E_{1/2}' \qquad Cu^{II} + O_2 + e^- \;\; \rightleftharpoons \;\; Cu^{II}O_2{}^{\bullet-} \qquad \textbf{Eqn. 5.4}$$

$$k_1 / k_2 \qquad Cu^{II} + e^- \underset{}{\overset{k_1(ET)}{\rightleftharpoons}} \left[Cu^I \right] \overset{k_2(O_2)}{\rightleftharpoons} Cu^{II}O_2{}^{\bullet-} \qquad \textbf{Eqn. 5.5}$$

$$E_{1/2}' \qquad K_{eq}{}^\circ = \frac{Cu^{II}}{Cu^{II}O_2{}^{\bullet-}} \qquad \textbf{Eqn. 5.6}$$
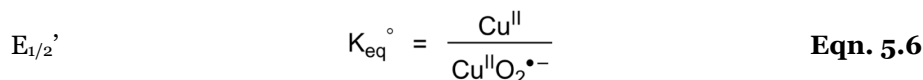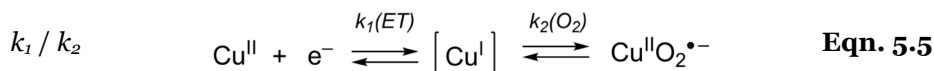
The potential determining step described by Equation 5.4 suggests that the transferred electron ends up in an orbital on the superoxide moiety which is in a remote position and barely influenced by the ligand. Therefore, there is a minimal effect of ligand substitution on the thermodynamic $E_{1/2}'$. The rate constant of this reaction (k_1') could be related to O_2 coordination and thus still be influenced by the electronic effects of the substituent. In this case, filled orbitals of the O_2 moiety have an interaction (overlap) with orbitals of the copper complex to establish the σ-bonds and π-bonding between the complex and O_2 which involves molecular orbitals that can be influenced by the ligand. Remarkably, 2^{Cl} has a higher O_2 reduction rate, as was found by both the non-rotating electrode and Tafel analysis. On the other hand, the reduction rate of O_2 by 2^{CF3} did not improve significantly. This seems to point to an additional effect of the chloride substituents apart from having an electron withdrawing character that does not directly correlate to the Hammett parameter. Examples of correlations between the (electro)catalytic rate and the Hammett parameter are known and will be discussed later. Of note, the Hammett parameter is based on substitution reactions of aromatic C–H bonds. In the case of O_2 coordination and further reduction to H_2O_2, processes such as π-backbonding play an important role. A p-orbital of the chloride substituent can conjugate with the orbitals of the pyridine ring, thereby changing the energy of the pyridinic orbitals via delocalization. Perhaps, this results in better overlap of the orbitals involved in O_2 coordination to facilitate π-backbonding. These processes are more complicated and may not be fully captured in the magnitude of the Hammett parameter and could explain why the reactivity of 2^{Cl} is different from **1** and 2^{CF3}. Apart from the suggested potential and rate determining step linked in Eqn. 5.4, another possibility would be that the potential and rate determining step are related to the step of Equation 5.3. However, we argue that the proton coupled electron transfer involving

$Cu^{II}-O_2^{\bullet-}$ would not be the limiting step in the presence of water and the high concentration (0.1 M) of phosphate buffer.

Applying a FOWA to a catalytic reaction with Equation 5.4 as (observed) potential determining step is problematic. To be able to use the FOWA to calculate the TOF_{max}, the $E_{1/2}$ of the potential determining step is required. In this case for O_2 reduction, that would be the $E_{1/2}'$ of Eqn. 5.4. However, this $E_{1/2}'$ cannot be determined in aqueous solutions since the $Cu^{II}-O_2^{\bullet-}$ species would directly react further because of the presence of protons. As our results show, the $E_{1/2}$ of the complexes differ due to the substituents. In this particular case, where the TOF_{max} can be in the order of 10^6 s^{-1}, as is the case for **1**,[10] a 100 mV shift of the $E_{1/2}$ that is used can in- or decrease the TOF_{max} by 3 orders of magnitude. Therefore, the $E_{1/2}$ of the complexes cannot be used since these would easily lead to over- or underestimation of the TOF_{max}. Interestingly, the order of magnitude (10^6) of the TOF_{max} for O_2 to H_2O_2 reduction as was determined with the FOWA for **1** was actually close to the actual k_{obs} at low catalyst concentrations determined with the current enhancement method.[10] As these values are in good agreement, the FOWA did not over- or underestimate the TOF_{max} to a large extent, even though the $E_{1/2}$ of **1** was used for the calculation. This indicates that the $E_{1/2}$ of **1** must be close to the $E_{1/2}'$ of Eqn. 5.4. The k_1' of the complexes is most likely in the order of **2^{Cl}** > **1** ≈ **2^{CF3}** > **3^{NH2}**.

The mechanism for H_2O_2 reduction has been less well explored. Our results show that the electronic effect of the EWG's of **2^{Cl}** and **2^{CF3}** have shifted the onset positively and significantly improved the rate according to the Tafel analysis. The exact mechanism is unknown, but could be Fenton type chemistry in which H_2O_2 is split in a copper bound hydroxyl ($Cu^{II}-OH$) and free hydroxyl radical ($OH^{\bullet-}$).[26, 27] Another possibility would be a mechanism wherein a copper–oxyl species ($Cu^{II}-O^{\bullet}$) is formed, as is proposed for the *modus operandi* of lytic polysaccharide monooxygenases (LPMO). In the LPMO mechanism, derived from computational research, the O–O bond of H_2O_2 is first split into a copper bound hydroxyl and a hydroxyl radical.[28] In contrast to Fenton type chemistry, the free hydroxyl radical immediately abstracts a hydrogen atom from the copper–hydroxyl species giving rise to a $Cu^{II}-O^{\bullet}$ radical species. The unique hydrogen bonding framework within the enzyme stabilizes this Cu^{II} oxyl radical so that it exclusively oxidizes a substrate instead of causing damage to the amino acid residues that surround the active site. Moreover, this mechanism ensures that the highly reactive free hydroxyl radical is quickly "trapped" to avoid damage. Copper–oxyl species have been proposed as part of H_2O_2 reduction mechanism, though direct evidence for the participation of this species remains elusive.[29] The inductive electron withdrawing effect of the EWG's

used in our study could be important to accommodate the negative charge accompanying the formation of the hydroxyl coordinated copper or copper–oxyl species. The higher rate and onset potential of 2^{Cl} and 2^{CF_3} with respect to **1** is supportive of this theory.

The most remarkable outcome of our study is that influence of the substituents on the onset potential and the catalytic rate differs for O_2 reduction and H_2O_2 reduction. While for O_2 reduction the onset potential was not influenced by EWG's, the onset potential and catalytic rate both increased for H_2O_2 reduction. Nevertheless, correlations between substituted complexes and the corresponding catalytic parameters have been shown to differ significantly depending on the studied system. Generally, the $E_{1/2}$ of the complexes is considered as reference for the electron density around the metal center and its influence on the onset potential and catalytic rate. A typical finding in most cases is that a higher onset potential, induced by substituents or differences in geometry, decreases the catalytic rate in electrocatalytic reductions such as O_2,[30] H_2,[31, 32] and CO_2[33] reduction. For example, the electrochemical O_2 and H_2O_2 reduction by bipyridine or terpyridine chelated copper complexes displays inverse linear relationships between the $E_{1/2}$ and the reduction rate.[34] The higher the $E_{1/2}$, the lower the rate. EWG's on these terpyridine or bipyridine ligands directly increased the $E_{1/2}$,[30] which is in agreement with our findings. In rare cases, a different effect was found. One example includes mononuclear ruthenium water oxidation catalysts for which the $E_{1/2}$ was found to increase with EDG's instead of EWG's. Moreover, the $E_{1/2}$ correlated with the Hammett parameter of the substituents.[35] This remarkable effect was explained by the pK_a of the uncoordinated imidazole moiety of the ligand. That pK_a changed upon substitution and had an overall dominant electronic effect on the $E_{1/2}$ when protonated or deprotonated. Nevertheless, no clear linear correlation between the Hammett parameters ($E_{1/2}$ of the complexes) and the rate of water oxidation was found. It was suggested that EDG's changed the mechanism of water oxidation and thus the rate determining step. The found relationships were therefore not linear but rather a polynomial function. Another aspect to consider, is that the $E_{1/2}$ is not always a direct indication of the electronic nature of the ligand and its influence on the activity. For example, the $E_{1/2}$ of pyridyl alkylamine copper complexes like **1** can be shifted by changing the linker length between the central amine and the pendant pyridine or by substituting a chelating pyridine with a non-chelating benzene arm.[36] In that case, the major influence of the ligand is on the geometry of the resulting complex which in turn affects the $E_{1/2}$ as opposed to electronic effects induced by substituents. However, there was no clear link between the $E_{1/2}$ and the O_2 reduction

activity. Differences in steric hindrance as a result of these diverse geometries could significantly affect the mechanism and even change, for example, the interaction with H_2O_2 from mononuclear to dinuclear.[37] A combination of a higher $E_{1/2}$ and faster catalysis, as we found for H_2O_2 reduction by 2^{Cl} and 2^{CF3} as compared to **1**, is not unique. A series of substituted nickel bis(diphosphine) based electrocatalysts for H_2 reduction showed a similar correlation.[38] In that study, complexes with EWG's had increased H_2 reduction activity while the overpotential decreased as well. In another study that investigated a range of manganese based substituted phthalocyanine complexes, the redox couple of a part of the investigated complexes had a direct linear correlation with the catalytic current, though a small part of the complexes deviated significantly from the fits.[39] Another example is the electrocatalytic CO_2 reduction by iron porphyrins which was improved by EWG's on the porphyrin that increased the rate of catalysis and reduced the required overpotential.[40] In general, correlations between the $E_{1/2}$ of the complex, the catalytic rate, and catalytic onset potential are found. Often, EWG's increase the $E_{1/2}$, can reduce the onset potential (of a reduction), but decrease the catalytic rate. Nevertheless, the mentioned studies clearly show that exceptions to these rules are found frequently. In these cases, the Hammett parameter is too simplistic to fully explain the electron density of the metal active site. Furthermore, secondary effects such as geometry and steric hindrance can significantly influence the $E_{1/2}$ but do not immediately correlate to the catalytic activity. It is therefore not unique that our catalytic results for both O_2 and H_2O_2 reduction by the substituted complexes based on **1** deviate from general expectations due to, for instance, the previously mentioned influence of π-backbonding.

5.4   Conclusion

The electronic influence of electron withdrawing and electron donating groups on **1** have been investigated for both the electrochemical O_2 and H_2O_2 reduction. The Hammett parameter of the substituents correlates directly with the thermodynamic redox potential ($E_{1/2}$) of the $Cu^{I/II}$ redox couple. However, the onset potential for O_2 reduction is not affected. We believe that the observed O_2 to H_2O_2 reduction mechanism does not have a potential determining step related to the $E_{1/2}$ of the complex, but rather to the thermodynamic equilibrium potential of an apparent simultaneous reduction and O_2 coordination of the Cu^{II} complex (Eqn. 5.4) due to the very fast kinetics of O_2 coordination to the copper complexes. The implication of this mechanism would be that the onset potential of O_2 reduction by **1** cannot be

improved by electronic effects of substituents as was found in this study. However, the rate of catalysis was slightly improved as a result of placing a chloride group on the *para* position of the pyridines of **1**. Interestingly, the CF$_3$ group, that is also a EWG and has a higher Hammett parameter than Cl, did not improve the catalytic rate with respect to the unsubstituted complex. The reason for this could be the ability of electron delocalization properties of Cl with the pyridine moiety that influences the π-backbonding with O$_2$. In contrast, H$_2$O$_2$ reduction by the EWG's substituted complexes clearly started at a higher potential than the unsubstituted complex. Remarkably, the rate of reduction improved as well. There is a better correlation of the H$_2$O$_2$ reduction rate to the Hammett parameter as compared to the correlation to the O$_2$ reduction rate. Nevertheless, the reactivity of **1** is lower than expected for H$_2$O$_2$ reduction whereas chloride substitution resulted in the highest catalytic rate again. Once more, delocalization could play a role in stabilizing the transition state of the rate determining step, but requires more studies since the H$_2$O$_2$ reduction mechanism is well understood. Overall, we have shown that by placing EWG groups we have significantly improved the onset potential and catalytic rate of the electrochemical H$_2$O$_2$ to H$_2$O reduction.

5.5   Acknowledgements

5.6   Experimental

5.6.1   General

All chemicals that have been used for synthesis and electrochemistry were purchased from commercial suppliers and used as received, unless mentioned otherwise. The complexes **2^{CF3}** and **2^{Cl}** were synthesized by Austin Herzog from the Karlin group at the John Hopkins University from Baltimore, the United States of America and used as received. Nuclear magnetic resonance (NMR) measurements were performed on a Bruker DPX 300 spectrometer. UV-vis measurements were performed on a Varian Cary UV-vis spectrometer. Mass spectra were obtained on a Thermo Fisher Scientific MSQ Plus ESI. High resolution mass spectra (HR MS) were

obtained on a Thermo Finnigan LTQ Orbitrap. Calibration was performed with a calibration mixture obtained from Thermo Finnigan prior to the measurement. Elemental analysis was performed by Mikroanalytisch Laboratorium Kolbe from Oberhausen, Germany. For pH measurements, a Hannah instruments HI 4222 pH meter was used and calibrated with five different IUPAC standard buffers.

5.6.2   Synthesis

Synthesis of 2-hydroxymethyl-4-nitropyridine (4)

The synthesis was based on a previously reported synthesis.[41] 10.5 g of 4-nitro-2-picoline-N-oxide (Fluorochem) was dissolved in 100 ml dichloromethane (DCM, Honeywell). Over the course of 20 minutes, 22.5 ml trifluoroacetic anhydride (Alfa Aesar) in 25 ml DCM was added dropwise. The mixture turned yellow to red. When finished, the mixture was refluxed for 18 h (overnight). Next, the mixture was concentrated under reduced pressure. 100 ml demineralized water was added. Subsequently, K_2CO_3 was carefully added while stirring until the pH was 8. The mixture was left to stir for 1 hour while the color turned yellow again. The pH was checked, additional K_2CO_3 was added and the mixture was left to stir for 5 more hours. Next, 10 M NaOH was added to raise the pH to circa 10-12 and the mixture was stirred for 30 minutes after which DCM was added. The layers of the mixture were separated subsequently and the aqueous layer was extracted twice with DCM. All organic layers were collected and dried over Na_2SO_4 before being filtered. All volatiles were removed under reduced pressure. A yellow oil was obtained which slowly crystallized into a yellow solid. After column chromatography on silica with 3:1 Et_2O:PetEt as eluent, 2.50 gram of a slightly yellow solid was obtained (16.2 mmol, 25%). ^{1}H NMR matched the values reported in literature of **4** within 0.04 ppm (apart from the hydroxyl, for which the shift depends heavily on the acidity of the solvent).[41]

ESI MS m/z (found (calculated)): 155.2 (155.1 [M + H$^+$]). ^{1}H NMR (300 MHz, CDCl$_3$) δ 8.83 (d, 1H, ^3J(H,H) = 5.4 Hz, m-(NO$_2$-Py)-H), 8.09 (m, 1H, m-HOCH$_2$-(NO$_2$-Py)-H), 7.92 (dd, 1H ^3J(H,H) = 5.5 Hz, ^4J(H,H) = 2.1 Hz, m-(NO$_2$-Py)-H), 4.91 (s, 2H, HOCH_2-(NO$_2$-Py)), 3.79 (s, 1H, HOCH$_2$-(NO$_2$-Py)).

Synthesis of 2-chloromethyl-4-nitropyridine (5)

Compound **5** was prepared by following a procedure for the conversion of a 4-chloro anologue.[18] 2.51 g of 2-hydroxymethyl-4-nitropyridine (**4**) was dissolved in 80 ml DCM. Next, 2 ml SOCl$_2$ was added slowly over the course of 2 minutes. A

precipitation formed. The mixture was stirred at room temperature and followed by TLC. After 20 h, saturated NaHCO$_3$ solution was added to quench the reaction while stirring vigorously until the mixture reached neutral pH. The organic layer was separated and the aqueous layer was extracted 3 times with DCM. All organic fractions were combined and dried over Na$_2$SO$_4$. Volatiles were removed under reduced pressure after filtration. A yellow oil was obtained. This was dissolved in a minimum amount of a 3:1 mixture of pentane:Et$_2$O and a few drops of DCM. This was loaded on a silica (Screening Devices, Silica Gel 40-63 µm) column and the product was obtained with 3:1 pentane:Et$_2$O as eluent. All product fractions were combined and the volatiles were removed under reduced pressure. 2.30 g of yellow oil was obtained (14.9 mmol, 92%). The purity was assessed by TLC and based on experience of the preparation of a smaller batch. No further characterization was performed since the product is very unstable when it is not dissolved. Directly after the yield was determined, the product was immediately used in the next reaction. As said, a smaller batch was prepared and the purity of that batch was assessed by ^{1}H NMR. The spectra matched literature values within 0.03 ppm.[42] ^{1}H NMR (300 MHz, CDCl$_3$) δ 8.87 (dd, 1H, ^3J(H,H) = 5.4 Hz, ^5J(H,H) = 0.6 Hz, o-(NO$_2$-Py)-H), 8.23 (dd, 1H, ^4J(H,H) = 2.1 Hz, ^5J(H,H) = 0.6 Hz, m-ClCH$_2$-(NO$_2$-Py)-H), 7.98 (dd, 1H, ^3J(H,H) = 5.4, ^4J(H,H) = 2.1 Hz, m-(NO$_2$-Py)-H), 4.79 (s, 2H, ClCH_2-(NO$_2$-Py)).

Synthesis of bis[(4-nitro-2-pyridyl)methyl]-2-pyridylmethyl-amine (6)

Directly after the purification of 2-chloromethyl-4-nitropyridine (compound **5**) by column chromatography in the previous step, 2.3 g of the compound was directly dissolved in 30 ml MeCN (dried over molecular sieves, purged with N$_2$, Biosolve HPLC grade) under N$_2$ atmosphere. Next, 654 µL 2-picolylamine (Sigma Aldrich) was dissolved in 20 ml dry MeCN and transferred to the mixture. The mixture became darker yellow. Next, 3.3 ml diisopropylethylamine (DIPEA, Acros) and 95 mg KI (Sigma Aldrich) were added and the mixture was heated at 60 °C. The mixture became dark brown over time. The reaction was followed over time by TLC on alumina with dichloromethane + 2% MeOH as eluent. After 1 day, the reaction was stopped and saturated NaHCO$_3$ solution, water, and ethyl acetate were added. The layers were separated. The aqueous layer was extracted 4 times with ethyl acetate. All organic layers were combined and dried over Na$_2$SO$_4$. After filtration, volatiles were removed under reduced pressure. A thick brown oil was obtained. Purification was performed with alumina column chromatography (Brockmann Type 1). A gradient eluent was used starting with DCM. The product was collected by switching the eluent to 0.4% methanol in DCM. Most product was collected in a pure

fraction: 1.35 g (3.55 mmol) but a second round of column chromatography of a collected mixed fraction increased the yield of the thick brown oil to a total of 1.635 g (4.3 mmol, 68%).

HRMS *m/z* (found (calculated)): 381.13026 (381.13058, [M + H$^+$]), 403.11209 (403.11252, [M + Na$^+$]). ^{1}H NMR (300 MHz, CDCl$_3$) δ 8.84 (d, 2H, ^3J(H,H) = 5.4 Hz, *o*-(NO$_2$-Py)-*H*), 8.57 (ddd, 1H ^3J(H,H) = 4.8 Hz, ^4J(H,H) = 1.7 Hz, ^5J(H,H) = 0.9 Hz, *o*-Py-*H*), 8.31 (d, 2H, ^4J(H,H) = 1.9 Hz, *m*-NCH$_2$(NO$_2$-Py)-*H*), 7.87 (dd, 2H, ^3J(H,H) = 5.4 Hz, ^4J(H,H) = 2.2 Hz, *m*-(NO$_2$-Py)-*H*), 7.69 (td, 1H, ^3J(H,H) = 7.7 Hz, ^4J(H,H) = 1.8 Hz, *p*-Py-*H*), 7.49 (dt, 1H, ^3J(H,H) = 7.8 Hz, $^{4,5}J$(H,H) = 1.2 Hz *m*-NCH$_2$Py-*H*), 7.18 (ddd, 1H, ^3J(H,H) = 7.4 Hz, ^3J(H,H) = 4.9, ^4J(H,H) = 1.1 Hz, *m*-Py-*H*), 4.11 (s, 4H NC*H$_2$*(NO$_2$-Py)), 3.97 (s, 2H, NC*H$_2$*Py). ^{13}C NMR (75 MHz, CDCl$_3$) δ 163.07 (NCH$_2$*C*-(NO$_2$-Py)), 158.18 (NCH$_2$*C*-Py), 154.60 (O$_2$N-*C*-Py), 151.55 (*o*-(NO$_2$-Py)-*C*H), 149.59 (*o*-Py-*C*H), 136.85 (*p*-Py-*C*H), 123.35 (*m*-NCH$_2$Py-*C*H), 122.63 (*m*-Py-*C*H), 115.72 (*m*-NCH$_2$-(NO$_2$-Py)-*C*H), 114.83 (*m*-(NO$_2$-Py)-*C*H), 60.71 (N*C*H$_2$-Py), 60.00 (N*C*H$_2$-(NO$_2$-Py)). See Appendix D Figures D.7 to D.11 for the ^{1}H NMR, ^{13}C APT, COSY, HSQC, and HMBC NMR spectra.

Synthesis of bis[(4-amino-2-pyridyl)methyl]-2-pyridylmethyl-amine (7)

To synthesize **7**, the nitro groups of **6** were catalytically reduced by Pd/C with hydrazine as reducing agent. Of note, other reducing agents did not yield the product. H$_2$ does not react while NaBH$_4$ leads to a mixture of azo compounds. These latter compounds can be further reduced to amines and the desired product with hydrazine. However, it is best to start with Pd/C and hydrazine from start to avoid the formation of by-products. 0.285 g of **6** was dissolved in 15 ml EtOH (Honeywell). Next, 134 mg Pd/C (10%, Sigma Aldrich) was added and rinsed of the sides of the flask with 15 ml extra EtOH. The mixture was stirred and purged with N$_2$ for 1 hours. Next, 3 ml hydrazine hydrate (80%, Sigma Aldrich) was added dropwise and the mixture was heated at 60 ° C under N$_2$ atmosphere. The reaction was followed by thin layer chromatography (TLC) on alumina with CHCl$_3$ with 20% methanol and 1% triethylamine as eluent. Full conversion was obtained after 1 day. The mixture was filtered over celite and washed copiously with EtOH. The filtrate was concentrated under reduced pressure. When *circa* 5 ml remained, water and CHCl$_3$ were added and mixed thoroughly. Subsequently, the layers were separated. The aqueous layer was extracted 3 times with CHCl$_3$. All organic layers were combined, dried over Na$_2$SO$_4$ and filtered. All volatiles were removed under reduced pressure. The remaining pale yellow oil was dried under reduced pressure. Over time, the oil solidified. 131 mg (0.408 mmol, 54%) of **7** was obtained.

ESI MS m/z (found (calculated)): 321.2 (321.2 [M + H$^+$]); 343.2 (343.2 [M + Na$^+$]); 290.3 (290.15, [M + 2 H$^+$]). ^{1}H NMR (300 MHz, MeOD) δ 8.43 (ddd, 1H, ^3J(H,H) = 5.0 Hz, ^4J(H,H) = 1.8 Hz, ^5J(H,H) = 1.0 Hz, o-Py-H), 7.89 (dd, 2H, ^3J(H,H) = 5.9 Hz, ^5J(H,H) = 0.5 Hz, o-(NH$_2$-Py)-H), 7.80 (td, 1H, ^3J(H,H) = 7.8 Hz, ^4J(H,H) = 1.8 Hz, p-Py-H), 7.67 (dt, 1H, ^3J(H,H) = 7.8 Hz, $^{4,5}J$(H,H) = 1.1 Hz, m-NCH$_2$Py-H), 7.28 (ddd, 1H, ^3J(H,H) = 7.5 Hz, ^3J(H,H) = 5.0 Hz, ^4J(H,H) = 1.3 Hz, m-Py-H), 6.82 (d, 2H, ^4J(H,H) = 2.3 Hz, m-NCH$_2$(NH$_2$-Py)-H), 6.46 (dd, 2H ^3J(H,H) = 5.9 Hz, ^4J(H,H) = 2.4 Hz, m-(NH$_2$-Py)-H), 3.79 (s, 2H, NCH_2Py), 3.64 (s, 4H, NCH_2(NH$_2$-Py)),). Signals corresponding to the NH$_2$ protons were not observed possibly due to fast exchange with deuterium from the solvent. ^{13}C NMR (75 MHz, MeOD) δ 160.25 (H2NC-(NH$_2$-Py)), 159.04 (o-NCH$_2$$C$-Py), 157.75 ($o$-NCH$_2$$C$-(NH$_2$-Py)), 149.39 ($o$-Py$C$H), 148.52 ($o$-(NH$_2$-Py)$C$H), 138.69 ($p$-Py$C$H), 124.90 ($m$-NCH$_2PyC$H), 123.85 ($m$-Py$C$H), 109.20 ($m$-NCH$_2$(NH$_2$-Py)$C$H), 109.15 ($m$-(NH$_2$-Py)$C$H), 60.91 (N$CH_2$Py), 60.58 (N$CH_2$(NH$_2$-Py)). See Appendix D Figures D.12 to D.16 for the ^{1}H NMR, ^{13}C APT, COSY, HSQC, and HMBC NMR spectra.

Synthesis of [Cu(2NO$_2$-tmpa)(CH$_3$CN)](CF$_3$SO$_3$)$_2$ (3^{NO2})

108 mg **6** and 99 mg Cu(OTf)$_2$ were dissolved in 10 ml MeOH and stirred for 2 hours at room temperature. Next, all volatiles were removed under reduced pressure. The turquoise colored oil was washed with hexane 3 times and 2 times with Et$_2$O. Next, hexane was added and all volatiles were removed under reduced pressure. The last step was repeated 3 times. Small crystals appeared. Next, the crude solid/oil was dissolved in a minimum amount of MeCN. Vapor diffusion with Et$_2$O at 5 °C resulted in the formation of blue crystals. After filtration, the crystals were washed with a 1:9 MeCN:Et$_2$O mixture. After drying the crystals under reduced pressure, 85.9 mg of crystals (0.112 mmol, 41%) was obtained.

Elemental analysis calculated ratio (%) for [Cu((**6**)(CH$_3$CN)](OTf)$_2$ (C$_{22}$H$_{19}$CuF$_6$N$_7$O$_9$S$_2$)+ 1.6 H$_2$O: C 33.20, H 2.81, N 12.32; found: C 33.01, H 2.63, N 12.21. UV-vis λ$_{max}$: 285 nm, 690 nm, 890 nm (0.3 mM in pH 7 phosphate buffer, Figure D.2).

5.6.3   General electrochemistry

For the preparation of buffers, the cleaning of glassware, cleaning of the electrodes, Milli-Q grade Ultrapure water (>18.2 MΩ cm resistivity) was used. A 0.1 M phosphate buffer of pH 7 was used. This buffer was prepared from NaH$_2$PO$_4$ (Merck Suprapur ©, 99.99%) and Na$_2$HPO$_4$ (Fluka Traceselect© 99.995%). The electrolyte was purged with Ar (Linde, Ar 5.0) for 30 minutes or O$_2$ (Linde, O$_2$ 5.0)

for 20 minutes prior to the experiment. During measurements, a constant flow of O_2 or Ar was kept above the solution. For H_2O_2 reduction measurements, H_2O_2 for ultratrace analysis (Sigma Aldrich) was used and diluted with Milli-Q water. For RRDE measurements, the electrolyte was purged during the measurement as well. Electrochemical measurements were performed in custom-made, single compartment glass cells. For RRDE, a different cell was used that will be described in a separate section. All glassware was cleaned by boiling in water and extensive rinsing prior to each experiment. Periodically, the glassware was cleaned by immersing it in a 1 g/L $KMnO_4$ (Sigma) solution in 0.5 M H_2SO_4 (Sigma, reagent grade) for at least a night. Next, the glassware was extensively rinsed with water and immersed in water with a few drops of concentrated H_2SO_4 and H_2O_2 (Merck Emprove 35%). After all MnO_2 residues had been oxidized, the glassware was rinsed and boiled in water for 3 consecutive times. Prior to each RRDE measurement, this extensive cleaning procedure was performed. A three electrode setup with Autolab PGSTAT 12 and 204 and IVIUM CompactStat potentiostats were used. NOVA 2.1 or IVIUM software were used.

For all measurements, a reversible hydrogen electrode (RHE) was used as reference electrode. This was either a HydroFlex (Gaskatel) or a Platinum mesh in H_2 (Linde, H_2 5.0) saturated electrolyte operating at the same pH as the working electrode and connected to the cell via a Luggin capillary. In all cases, the counter electrode was a large surface area gold wire that was flame annealed prior to each measurement. The working electrode (not for RRDE), was a glassy carbon (GC) electrode (0.07 cm², Metrohm) encapsulated in polyether ether ketone (PEEK). Before each measurement, the electrode was mechanically polished. When extensive polish was required, P2500 sand paper was used for 10 seconds before the usual polishing procedure. For the regular polish, a Labopol 20 polishing machine with 1.0 micron diamond and 0.04 micron silica suspension on Dur-type polishing cloths were used (all from Struers). The GC was polished for 1 minute after which it was rinsed with water and isopropanol (after the diamond slurry) or water only (after the silica suspension). Next, the electrode was sonicated in water for 10 minutes and rinsed copiously with water. Before each measurement, the quality of the polish was checked by running a CV in catalyst-free electrolyte under O_2 and/or Ar.

5.6.4   RRDE

Rotating ring disk electrode experiments were performed in a custom-made glass cell with three different compartments for the reference, counter and work electrode. Water permeable glass frits were used to separate the compartments. The

work electrode was a glassy carbon disk (0.196 cm²) that was used in a ChangeDisk configuration with a Platinum ring all of which were obtained from Pine. A Pine rotator was used. The GC disk was polished as described before and separately from the Pt ring. The Pt ring was polished following the same procedure as glassy carbon. Generally, the setup was rotated at 1600 rpm. For the O_2 and H_2O_2 reduction measurements of 3^{NH2} a 0.05 M phosphate buffer of pH 7 was used.

5.7   References

1.   Gewirth, A. A.; Thorum, M. S., *Inorg. Chem.* **2010,** *49*, 3557−3566.
2.   Nørskov, J. K.; Rossmeisl, J.; Logadottir, A.; Lindqvist, L.; Kitchin, J. R.; Bligaard, T.; Jónsson, H., *J. Phys. Chem. B* **2004,** *108*, 17886−17892.
3.   Gasteiger, H. A.; Kocha, S. S.; Sompalli, B.; Wagner, F. T., *Appl. Catal., B* **2005,** *56*, 9−35.
4.   Campos-Martin, J. M.; Blanco-Brieva, G.; Fierro, J. L. G., *Angew. Chem. Int. Ed.* **2006,** *45*, 6962−6984.
5.   Eul, W.; Moeller, A.; Steiner, N., Hydrogen Peroxide. In *Kirk-Othmer Encyclopedia of Chemical Technology* [Online] John Wiley & Sons, Inc.: 2000. http://dx.doi.org/10.1002/0471238961.0825041808051919.a01.pub2.
6.   Hage, R.; Lienke, A., *Angew. Chem. Int. Ed.* **2006,** *45*, 206−222.
7.   Süss, H. U., Bleaching. In *Ullmann's Encyclopedia of Industrial Chemistry*, 2012.
8.   Legrini, O.; Oliveros, E.; Braun, A. M., *Chem. Rev.* **1993,** *93*, 671−698.
9.   Metcalf & Eddy Inc.; Tchobangolous, G., *Wastewater Engineering: Treatment and Resource Recovery*. 5th edition ed.; Mcgraw-Hill Education: 2014.
10.   Langerman, M.; Hetterscheid, D. G. H., *Angew. Chem. Int. Ed.* **2019,** *58*, 12974−12978.
11.   Bratsch, S. G., *J. Phys. Chem. Ref. Data* **1989,** *18*, 1−21.
12.   Bullock, R. M.; Appel, A. M.; Helm, M. L., *Chem. Commun.* **2014,** *50*, 3125−3143.
13.   Costentin, C.; Drouet, S.; Robert, M.; Savéant, J.-M., *J. Am. Chem. Soc.* **2012,** *134*, 11235−11242.
14.   Costentin, C.; Savéant, J.-M., *ChemElectroChem* **2014,** *1*, 1226−1236.
15.   Costentin, C.; Savéant, J.-M., *J. Am. Chem. Soc.* **2017,** *139*, 8245−8250.
16.   Rountree, E. S.; McCarthy, B. D.; Eisenhart, T. T.; Dempsey, J. L., *Inorg. Chem.* **2014,** *53*, 9983−10002.
17.   Fry, H. C.; Scaltrito, D. V.; Karlin, K. D.; Meyer, G. J., *J. Am. Chem. Soc.* **2003,** *125*, 11866−11871.
18.   Zhang, C. X.; Kaderli, S.; Costas, M.; Kim, E.-i.; Neuhold, Y.-M.; Karlin, K. D.; Zuberbühler, A. D., *Inorg. Chem.* **2003,** *42*, 1807−1824.
19.   Enciso, A. E.; Lorandi, F.; Mehmood, A.; Fantin, M.; Szczepaniak, G.; Janesko, B. G.; Matyjaszewski, K., *Angew. Chem. Int. Ed. n/a*.
20.   Thorseth, M. A.; Letko, C. S.; Tse, E. C. M.; Rauchfuss, T. B.; Gewirth, A. A., *Inorg. Chem.* **2013,** *52*, 628−634.
21.   Ramsey, B. G.; Walker, F. A., *J. Am. Chem. Soc.* **1974,** *96*, 3314-3316.
22.   Hammett, L. P., *J. Am. Chem. Soc.* **1937,** *59*, 96−103.
23.   Hansch, C.; Leo, A.; Taft, R. W., *Chem. Rev.* **1991,** *91*, 165−195.
24.   Smits, N. W. G.; van Dijk, B.; de Bruin, I.; Groeneveld, S. L. T.; Siegler, M. A.; Hetterscheid, D. G. H., *The Influence of Ligand Denticity and Flexibility on the ORR Behavior of Cu-terpy and Cu-bmpa.* **2020,** *Accepted*.
25.   Bard, A. J.; Faulkner, L. R., *Electrochemical Methods: Fundamentals and Applications*. Wiley: New York, 2000.
26.   Haber, F.; Weiss, J.; Pope, W. J., *Proc. R. Soc. London, Ser. A* **1934,** *147*, 332−351.
27.   Garcia-Bosch, I.; Cowley, R. E.; Díaz, D. E.; Siegler, M. A.; Nam, W.; Solomon, E. I.; Karlin, K. D., *Chem. - Eur. J.* **2016,** *22*, 5133−5137.
28.   Wang, B.; Johnston, E. M.; Li, P.; Shaik, S.; Davies, G. J.; Walton, P. H.; Rovira, C., *ACS Catal.* **2018,** *8*, 1346−1351.
29.   Shimoyama, Y.; Kojima, T., *Inorg. Chem.* **2019,** *58*, 9517−9542.
30.   McCrory, C. C. L.; Ottenwaelder, X.; Stack, T. D. P.; Chidsey, C. E. D., *J. Phys. Chem. A* **2007,** *111*, 12641−12650.
31.   Hu, X.; Brunschwig, B. S.; Peters, J. C., *J. Am. Chem. Soc.* **2007,** *129*, 8988−8998.

32. Koca, A.; Özçeşmeci, M.; Hamuryudan, E., *Electroanalysis* **2010,** *22*, 1623–1633.
33. Bernatis, P. R.; Miedaner, A.; Haltiwanger, R. C.; DuBois, D. L., *Organometallics* **1994,** *13*, 4835–4843.
34. Zhang, J.; Anson, F. C., *Electrochim. Acta* **1993,** *38*, 2423–2429.
35. Kärkäs, M. D.; Liao, R.-Z.; Laine, T. M.; Åkermark, T.; Ghanem, S.; Siegbahn, P. E. M.; Åkermark, B., *Catal. Sci. Technol.* **2016,** *6*, 1306–1319.
36. Asahi, M.; Yamazaki, S.-i.; Itoh, S.; Ioroi, T., *Dalton Trans.* **2014,** *43*, 10705–10709.
37. Kunishita, A.; Kubo, M.; Ishimaru, H.; Ogura, T.; Sugimoto, H.; Itoh, S., *Inorg. Chem.* **2008,** *47*, 12032–12039.
38. Kilgore, U. J.; Roberts, J. A. S.; Pool, D. H.; Appel, A. M.; Stewart, M. P.; DuBois, M. R.; Dougherty, W. G.; Kassel, W. S.; Bullock, R. M.; DuBois, D. L., *J. Am. Chem. Soc.* **2011,** *133*, 5861–5872.
39. Sehlotho, N.; Nyokong, T., *J. Electroanal. Chem.* **2006,** *595*, 161–167.
40. Costentin, C.; Robert, M.; Savéant, J.-M., *Acc. Chem. Res.* **2015,** *48*, 2996–3006.
41. Zaman, N.; Guillot, R.; Sénéchal-David, K.; Boillot, M.-L., *Tetrahedron Lett.* **2008,** *49*, 7274–7275.
42. Tamura, M.; Urano, Y.; Kikuchi, K.; Higuchi, T.; Hirobe, M.; Nagano, T., *Chem. Pharm. Bull.* **2000,** *48*, 1514–1518.

5

Chapter 6

Summary and conclusion

6.1 Summary

The storage of electricity that is generated via renewable sources is one of the great challenges of the future because there is no technology available yet that is able to replace all fossil fuel driven processes. As discussed in Chapter 1, water electrolysis into H_2 and O_2 is a method to store electricity, but the half reaction that concerns the oxidation of H_2O to O_2, and *vice versa*, is accompanied with large energy losses. Even the best electrocatalysts to date have to operate far from the equilibrium potential to obtain sufficiently high currents. Electrocatalytic studies of molecular catalytic systems can contribute to reduce overpotentials in several ways. Structural mimics of the active site of highly active enzymes can be synthesized and/or the ligand(s) of molecular complexes can be systematically adjusted to induce differences in the electronic and geometric properties of the metal active site to boost its reactivity. For example, the molecular copper complexes for O_2 reduction that have been described in this thesis are partly inspired on the active site of the enzyme laccase. Laccases performs oxygen reduction close to the equilibrium potential of 1.23 V by utilizing a trinuclear copper active site. Mechanistic structure–activity studies of the (modified) molecular complexes can reveal which factors improve catalysis. On the other hand, molecular systems are generally far less stable than heterogeneous electrocatalysts. In most cases, high ligand exchange rates or ligand degradation due to reactive intermediates lead to metallic or metal oxide deposits on the electrode. With this in mind, there are several tools to attribute the kinetics, product selectivity and stability of these molecular systems under electrocatalytic conditions. Rate constants may be obtained with the current enhancement method and/or the foot of the wave analysis (FOWA). The rotating ring disk electrode (RRDE) setup is a powerful tool to determine product selectivity, for example the selectivity of the O_2 reduction reaction (ORR) to either H_2O_2 or H_2O as product, especially when combined with other tools to quantitatively determine the product distribution. Finally, the stability of molecular systems can be assessed with a range of electrochemical tools such as electrochemical quartz crystal microbalance (EQCM), but also surface sensitive techniques such as X-ray photoelectron spectroscopy (XPS). We have used these tools to investigate several molecular systems. Chapters 2 and 3 discuss molecular complexes that decompose to a heterogeneous active species and the subsequent effect on electrocatalytic water oxidation or ORR, respectively. Also, we have studied molecular copper complexes for the ORR for which we changed the ligand which resulted in a different selectivity (Chapter 4) and/or affected the onset potential and catalytic rate (Chapter 5).

The best electrolyzers to date use iridium oxide as catalyst to oxidize water to O_2. Nevertheless, the overpotential at which these electrolyzers have to operate is still significantly large. Moreover, iridium oxide is expensive and scarce to such an extent, that the current technology will not be able to replace all fossil fuel driven processes. For that reason, molecular iridium complexes can be interesting platforms to study whether ligand effects can increase the activity of iridium and reduce catalyst loadings. A significant portion of studies involving molecular catalysts have been performed with sacrificial reagents, in which the oxidative power for O_2 evolution is delivered by reagents such as $((NH_4)_2[Ce(NO_3)_6])$ and $NaIO_4$. In a previous study that used sacrificial reagents, the turnover frequency (TOF) of a series of Cp* (Cp* = pentamethylcyclopentadienyl) iridium complexes bearing hydroxylpicolinate ligands was found to be the highest for the complex with an unsubstituted picolinate ligand. In Chapter 2, the electrochemical evaluation of the water oxidation activity of these complexes is described. We found with EQCM studies that these complexes, under electrochemical conditions, form a deposit on the electrode that was characterized by XPS. Bulk electrolysis revealed that the Cp* ligand of the parent complexes was oxidatively degraded because breakdown products were found in the electrolyte with ^{1}H nuclear magnetic resonance (NMR) spectroscopy. Interestingly, the XPS studies showed that the influence of the ligand on the electronic environment of the iridium was stronger for the parent complexes than for the corresponding deposits on the electrode. Minimal differences between the electronic properties of the iridium in the deposit were found. Correspondingly, a minimal difference in water oxidation activity of these deposits was observed as well without a clear structure–activity relationship. Equally, other known iridium complexes with different ligand systems were also found to deposit material on the electrode. XPS studies showed that the spectra of these deposits differed only marginally from the spectra of the deposits formed by the iridium picolinate complexes. Likewise, a minimal variation in water oxidation activity of these deposits was observed. In contrast, the deposit formed by ligand-free $[Ir(OH)_6]^{2-}$ produces water oxidation currents that are almost 2 orders of magnitude larger. Based on these results, we suggested that the iridium complexes oxidatively degrade to a small IrO_x type cluster that contains just a few iridium atoms but also some ligand (or residues thereof). The ligand (or residue), might inhibit the water oxidation activity but may be used to prevent catalyst deactivation and, more importantly, prevent aggregation of active iridium sites which could be beneficial for lowering the iridium loading in electrolyzers.

6

Fuel cells are able to generate electricity by the reaction of H_2 and O_2 to H_2O. However, the energy output is limited due to the fact that even state-of-the-art catalysts cannot reduce O_2 close to the equilibrium potential of 1.23 V. Some electrochemical studies into laccase have suggested that this enzyme can perform the ORR close to the equilibrium potential. Inspired on the enzymatic active site that contains a trinuclear copper cluster, many molecular copper complexes for oxygen reduction have been reported. Interestingly, one specific dinuclear copper complex (**Cu(DAT)**) with two bridging 3,5-diamino-1,2,4-triazole (DAT) ligands was reported with a remarkably low overpotential and high activity and was therefore seen as the benchmark for ORR by molecular copper complexes. Notably, the active catalyst used in that study was prepared by mixing a copper salt, the triazole ligand, and a carbon support without any proof that **Cu(DAT)** was actually present as active species. Therefore, we set out to investigate the ORR activity of **Cu(DAT)** as is elaborated in Chapter 3. We found that **Cu(DAT)** precipitates out of aqueous solutions when coordinating anions are used either in the source of the copper salt or in the electrolyte. Therefore, our electrochemical studies were performed with *in situ* generated complex that was prepared from $Cu(CF_3SO_3)_2$ and in $NaClO_4$ as supporting electrolyte. This way, we were able to start with a homogeneous, dinuclear copper complex which was characterized with EPR (electron paramagnetic resonance) and UV-vis spectroscopy. We found with EQCM that the complex forms a deposit on the electrode under electrochemical conditions. We characterized this as a Cu^o deposit with XPS. Thus, the complex itself was found to be unstable under electrochemical conditions. Furthermore, we have shown with EPR and XPS characterization that the previously reported active catalyst (the mixture of carbon support, a copper salt, and DAT) is not **Cu(DAT)**, but in fact the very same Cu^o deposit. Studies with a Cu^o electrode in the presence of the triazole ligand showed that this ligand inhibits corrosion of Cu^o at higher potentials than without the presence of the triazole. This explains why the active species formed by the complex (the Cu^o deposit) did not show any stripping peaks at higher potentials within the catalytic potential window. Even though the molecular system disintegrates, this finding shows that the ligand still beneficially influences the electrocatalysis. This study signifies the need for proper characterization of the active species so that catalyst are not wrongfully benchmarked to molecular systems that are not stable under electrocatalytic conditions.

The electrocatalytic reduction of O_2 can be either the 4 electron reduction to H_2O or the 2 electron reduction to H_2O_2. The electrochemical production of H_2O_2 by the ORR is a promising on-site alternative for the current bulk production method

via the energy intensive and wasteful anthraquinone process which still accounts for over 90% of the worldwide production of H_2O_2. In that retrospect, we studied a water-soluble dinuclear copper complex (**Cu₂(btmpa)**) that bears the btmpa ligand (btmpa = 6,6'-bis[[bis(2-pyridylmethyl)amino]methyl]-2,2'-bipyridine) that links two Cu^{II} sites via the central bipyridine moiety. This complex can be considered as the dinuclear version of the mononuclear copper complex (**Cu(tmpa)**) bearing the tmpa ligand (tmpa = tris(2-pyridylmethyl)amine). **Cu(tmpa)** was previously found to reduce O_2 with a TOF up to 10^6 s^{-1} in a stepwise mechanism with H_2O_2 as intermediate. In Chapter 4, we show that **Cu₂(btmpa)** has very different properties as compared to **Cu(tmpa)**. Characterization by EPR and SQUID (superconducting quantum interference device) showed that the Cu^{II} centers do not antiferromagnetically couple and that each Cu^{II} has a distorted octahedral geometry as opposed to **Cu(tmpa)** that has a trigonal bipyramidal geometry. This difference has a large impact on the electrochemistry of **Cu₂(btmpa)**. First of all, the $Cu^{I/II}$ redox couple potential of both Cu^{II} centra of **Cu₂(btmpa)** shifted 0.3 V positively with respect to **Cu(tmpa)** due to bipyridine moiety of the btmpa ligand which is less able to donate electrons to the Cu^{II} centra of **Cu₂(btmpa)**. Moreover, we found that O_2 reduction was more sluggish as compared to the O_2 reduction by **Cu(tmpa)**. The most important finding was that H_2O_2 (over-)reduction is hindered to such an extent that the selectivity for H_2O_2 was up to 90% according to RRDE measurements. This lead us to investigate the Faradaic efficiency for H_2O_2 in long, bulk electrolysis experiments using a rotating disk electrode. We found that RRDE is not a suitable method for the measurement of the Faradaic efficiency. Instead, a photometric based method that determines the concentration of H_2O_2 by its reaction with an peroxidase enzyme was used to determine the Faradaic efficiency. In the first half hour of bulk electrolysis at 0.0 V, we found that the complex has a Faradaic efficiency up to 80% for the production of H_2O_2. Moreover, potential dependent adsorption of the complex on the electrode surface, as suggested by EQCM measurements, resulted in the accumulation of active catalyst and thereby a steady increase of the catalytic current in the first 20 to 30 minutes. The most important finding of this study, was that we were able to retain a Faradaic efficiency between 60 and 70% for 2 hours by preventing over-reduction of H_2O_2. At higher H_2O_2 concentrations, **Cu₂(btmpa)** is most likely more prone to disintegrate to Cu^o. Consequently, the formed Cu^o deposit over-reduces H_2O_2 to H_2O which lowers the Faradaic efficiency. However, by briefly applying stripping potentials in regular intervals during the bulk electrolysis of O_2, we were able to strip accumulated Cu^o and prevent over-reduction of H_2O_2. The research presented in Chapter 4 is the first intensive study into the long term

production of H_2O_2 by a molecular system showing that optimization of potentials and stripping intervals is beneficial to optimally use this intrinsically highly selective molecular system for the production of H_2O_2.

The mononuclear **Cu(tmpa)** complex was also the inspiration for Chapter 5. In this chapter, the effect of electron donating groups (EDG's) or electron withdrawing groups (EWG's) on the reactivity of **Cu(tmpa)** was explored. NH_2 (EDG), Cl, and CF_3 (both EWG's) substituents were placed at the *para* position of the coordinating pyridines of the tmpa ligand. The resulting effect that the substituted ligand has on the electronic character of the complex can be best described with the Hammett parameter, because a linear correlation between this parameter and the $E_{1/2}$ of $Cu^{I/II}$ redox couple was found for the complexes. Interestingly, the onset potential of O_2 reduction did not change for the complexes with EWG's with respect to **Cu(tmpa)**, even though the corresponding $E_{1/2}$ of the complex had shifted 100 mV more positive in the case of CF_3 as substituent. Additionally, we found that the rate of catalysis was the highest with Cl substituents, whereas CF_3 substituents did not affect the rate with respect to **Cu(tmpa)**. The reduction of Cu^{II} to Cu^{I} and the subsequent coordination of O_2 to the reduced Cu^{I} complex to form the Cu^{II}–$O_2^{\bullet-}$ superoxo species are very fast with respect to the scan rate of a cyclic voltammogram, because the TOF of O_2 reduction by **Cu(tmpa)** is very high (10^6 s^{-1}). Therefore, we believe that the Cu^{I} complex can be considered as a transient species in a fast equilibrium with both Cu^{II} and Cu^{II}–$O_2^{\bullet-}$ and that the observed rate determining step is Cu^{II} to Cu^{II}–$O_2^{\bullet-}$. In addition, the potential determining step is determined by the $E_{1/2}$ of the Cu^{II} to Cu^{II}–$O_2^{\bullet-}$ reduction. As the electron ends up in an orbital at a remote position from the ligand, the ligand does not affect the onset potential significantly. The rate is most likely determined by the binding constant of O_2 to the complex for which π-backbonding plays an important role. The reduction of H_2O_2 is significantly different from O_2 reduction. Here, we found that EWG's increase the onset potential and increase the rate of H_2O_2 reduction. This is not a unique finding, but can be regarded as unusual as many studies find that a decrease of the overpotential is accompanied by a lower rate. Of note, the highest rate was again obtained with the complex that had Cl groups as substituent. As opposed to the CF_3 group, the Cl group can delocalize electrons from p orbitals and thus have secondary effects on, for example, π-backbonding that are not entirely captured by the Hammett parameter. The structure–activity study presented in this chapter shows that this type of study yields valuable insight into the (apparent) mechanism and can help to beneficially increase the reactivity of molecular systems.

6.2   Conclusion and outlook

The high tunability of molecular complexes is an ideal toolbox to study (electro)catalytic reactions. A variety of options, such as structure–activity studies, can greatly aid the understanding of catalytic mechanism. Chapters 4 and 5 both took inspiration from the mononuclear **Cu(tmpa)** complex and show that catalysis can be significantly altered by inducing a different geometry (Chapter 4) or by changing the electronic nature of the complex by introducing EDG's and EWG's on the ligand (Chapter 5). Specifically, we were able to improve the electrochemical reduction of H_2O_2 by a simultaneous increase of the catalytic rate and onset potential by introducing EWG's on the tmpa ligand of moleculer **Cu(tmpa)** type complexes. The increase of the onset potential could be expected from the Hammett parameter of the corresponding complexes as this correlates to the $E_{1/2}$ of the complexes. As opposed to fast reduction of H_2O_2, we found that **Cu₂(btmpa)** is a highly selective catalyst for the O_2 to H_2O_2 reduction due to hindered H_2O_2 over-reduction. There is no clear explanation why the selectivity differs significantly from **Cu(tmpa)** with the current understanding of the H_2O_2 reduction mechanism. Interesting to note, is that **Cu₂(btmpa)** had the highest $E_{1/2}$ of the $Cu^{I/II}$ of all complexes studied in Chapters 4 and 5 while this had no clear effect on the onset potential, rate or selectivity of O_2 and H_2O_2 reduction with respect to the findings of Chapter 5. Clearly, the difference in rigidity leading to a different geometry has a large impact on electron transfer rates and therefore on the rate of catalysis. Whereas the observed differences in rate and electron transfer induced by the electronic differences of the complexes in Chapter 5 were small, **Cu₂(btmpa)** has a far slower electron transfer due to geometrical constraints that has a large impact on catalysis with respect to **Cu(tmpa)**. In general, the **Cu(tmpa)** type complexes of Chapter 5 displayed fast O_2 and H_2O_2 reduction. The trigonal bipyramidal Cu^{II} geometry and the easy transition to a tetragonal geometry of the corresponding Cu^I complex makes that the Cu^{II} to Cu^I reduction occurs via fast electron transfer. The flexibility of the pyridine arms of the tmpa ligand facilitate the coordination and release of the tertiary amine to establish these two preferred geometries. On the other hand, the btmpa ligand of **Cu₂(btmpa)** has a strained bipyridine moiety. The rigidity of this moiety leads to an elongation of both of the Cu–N bonds of the bipyridine to avoid steric hindrance between the two Cu centers of **Cu₂(btmpa)**. This leads to a distorted octahedral geometry which is not the optimal geometry for Cu^{II}. In addition, a transition to a tetragonal geometry, preferred for Cu^I, is more cumbersome. As a result, the electron transfer to form the Cu^I complex is slow. In turn, the slow electron transfer

significantly lowers the O_2 reduction rate and diminished the H_2O_2 over-reduction. Steric hindrance cannot explain the difference in reactivity because H_2O_2 and O_2 can be considered as comparable in size. An explanation might be that the reorganization required for the reduction of H_2O_2 is more complex than the reorganization of O_2 which encompasses O_2 coordination after Cu^{II} to Cu^{I} reduction to form the superoxo radical species. In O_2 and H_2O_2 reduction, the strain of the btmpa ligand slows down any required reorganization, but may have a larger impact on H_2O_2 catalysis where reorganization might entail more than merely the reduction of Cu^{II} to Cu^{I}. Another option would be that any radical species generated due to the splitting of the O–O bond of H_2O_2 degrades the ligand of **Cu$_2$(btmpa)**. However, this should lead to a quick depletion of the catalytic activity which is not observed and therefore less likely. In contrast, **Cu(tmpa)** type complexes have an open site available due to the tetragonal geometry of the Cu^{I} complex where coordinated H_2O_2 is not in close proximity with any of the pyridines. Overall, the ability of **Cu(tmpa)** (and related complexes) to adopt a trigonal bipyramidal Cu^{II} complex and easily transition to a tetragonal Cu^{I} complex allows for very fast O_2 and H_2O_2 reduction to form H_2O. The rate can mildly be improved by placing electron withdrawing groups on the ligand. Mostly, catalysis will be mass-transport limited. On the other hand, for selectively obtaining H_2O_2, steric hindrance caused by a rigid moiety in the ligand seems to be important. As a consequence, O_2 reduction to H_2O_2 will be kinetically hindered instead of mass transport limited and thus requires more catalyst material.

The stability of molecular complexes is always seen as a problem since decomposition of the parent complex can kill the activity, or any observed reactivity might be incorrectly linked to the structure of the complex. Of note, the production of H_2O_2 uses anthraquinones as redox mediator which only have a few turnovers but is still considered as acceptable since >90% of H_2O_2 is prepared via this inefficient process. Chapters 2 and 3 emphasize that thorough studies with multiple methods are required to observe and characterize any active species arising from the decomposition driven deposition of material on the electrode. Even though the molecular systems studied were not the active species, they did form a deposit on the electrode that was active. Interestingly, we found that the ligands used still could influence the activity of the complexes (Chapter 2) and prevent corrosion of the active species under the studied conditions (Chapter 3). This shows that the effect of ligands might still perturbate the activity and stability of heterogeneous bulk catalysts. As discussed in Chapter 1, ligands are actively used to improve the reactivity of, for example, nanoparticles by utilizing the knowledge obtained from catalytic studies with molecular systems. Moreover, the results from Chapter 4

accentuate that the negative consequences of catalyst decomposition (in this case H_2O_2 over-reduction) can be counteracted. First of all, knowledge about the decomposition is vital. Not only in this thesis, but also in other reports, it is shown that copper complexes are prone to decompose to Cu^0 deposits. An important aspect is the binding strength of the ligand. The complex discussed in Chapter 3 has a ligand which has only one chelating site per copper atom and thus readily loses its ligand to form Cu^0. On the other hand, the complexes in Chapter 4 and 5 have three to four chelating sites per copper atom that greatly enhances the stability. Due to the higher binding strength of the ligand, Cu^0 deposits are less likely to form and can be removed during bulk electrolysis by applying high stripping potentials and thereby retain the high Faradaic efficiency for H_2O_2 production by **Cu₂(btmpa)** (Chapter 4). In conclusion, the research presented in this thesis concerns the assessment of the stability of molecular complexes, identification of the active species, and uncovering factors that improve the reactivity of molecular systems in electrocatalytic reactions. Together, the research allows for a better understanding of the mechanism to improve electrocatalysts that are important for the future energy infrastructure.

6

Appendix A

<u>Supplementary information for Chapter 2:</u>
The influence of the ligand in the iridium mediated
electrocatalytic water oxidation

A.1   Cyclic voltammetry of iridium picolinate series

To study the picolinate complexes with cyclic voltammetry (CV), a glassy carbon (GC) electrode (0.07 cm²) was used. The electrode was in contact with the electrolyte via a hanging meniscus configuration. The electrolyte is a 0.1 M phosphate buffer of pH 7 that is strengthened to 0.5 M ionic strength with additional NaClO$_4$. A 1 mM catalyst concentration was used. Figure A.1 shows the first scan of the CVs of the different catalysts. The more electron donating complexes **4-OH1** and **6-OH1** have an earlier onset for the irreversible anodic wave at 1.55 V. The other complexes have an anodic wave starting at 1.65 V. This onset was consistently found at the same potential over several measurements (Figure A.3) with freshly polished GC working electrodes in the same catalyst solution. The magnitude of the maximum current reached at 2.1 V differs slightly among the catalysts (Figure A.1). In contrast to the onset, the magnitude of the current fluctuates significantly as became evident from several separate measurements (Figure A.3). This discrepancy in CVs is observed for the entire range of the iridium (hydroxyl)picolinate complexes. Any difference in the CV of the complexes lies within the experimental error. The hanging meniscus configuration is not the reason for the discrepancy as two of the three measurements shown in Figure A.3 show identical capacitive double layer currents but distinct maximum currents. As became clear from the electrode-rinse-test (Figure A.2) and the EQCM experiments (Figure 2.2), the complexes deposit material on the electrode. Electrodeposition, catalyst degradation (Figure A.4), oxygen evolution (Figure 2.1) and GC oxidation (Figure A.7) simultaneously
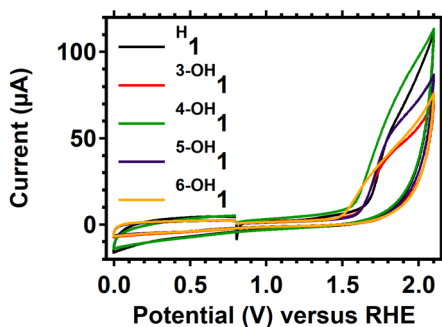
Figure A.1. Shown are the first scans of the cyclic voltammogram taken at 0.1 V/s with a glassy carbon working electrode. A 1 mM complex solution was used in combination with a 0.1 M phosphate buffer of pH 7 with an ionic strength of 0.5 M by adding NaClO$_4$ as supporting electrolyte.

contribute to the magnitude of the anodic current. This complexity results in large error margins for the magnitude of the current.
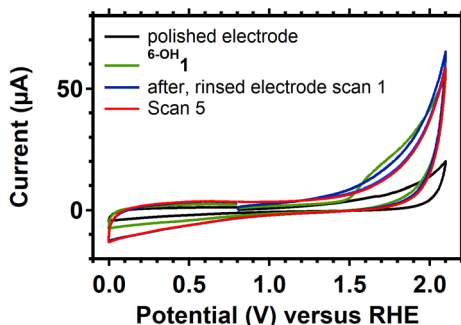
Figure A.2. The cyclic voltammograms of a GC electrode in a pH 7 phosphate buffer before (polished electrode, black line), during (green) and after (blue and red) it has been tested in electrolyte containing 1 mM of **6-OH1**. The CVs before and after were obtained in a catalyst free electrolyte. The electrode was rinsed copiously with Milli-Q grade water before the CVs in blue and red were obtained. All CVs were taken at a 0.1 V/s scan rate.
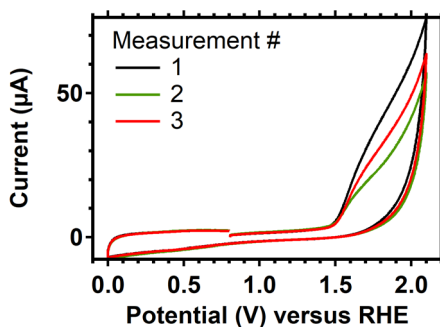
Figure A.3. The first scans are shown of three separate cyclic voltammetry measurements of a 1 mM **6-OH1** solution in a pH 7 phosphate buffer taken at a 0.1 V/s scan rate. The glassy carbon working electrode was polished before each measurement and used in a hanging meniscus configuration. The same electrolyte containing **6-OH1** was used for each measurement.

A.2   *Post*-electrolysis spectroscopy studies.

A.2.1   NMR

^{1}H NMR spectra were recorded of the D_2O based electrolyte used in the bulk electrolysis experiment of **4-OH1** (Figure A.4). For comparison, the spectrum of 4-hydroxypicolinate was recorded by adding NaOH to a mixture of 4-hydroxypicolinic acid and D_2O to be able to dissolve the ligand. The electrolyte spectrum before bulk electrochemistry shows three peaks corresponding to coordinated picolinate ligand as the spectrum has shifted with respect to metal-free ligand due to the electron withdrawing effect of iridium (III). Furthermore, two peaks can be linked to the Cp* ligand indicating the presence of at least two iridium complexes in the solution. The iridium complex with the weakly coordinating nitrate might be in equilibrium with an iridium complex where the nitrate is exchanged for a water or phosphate in solution. After 6 hours of bulk electrolysis, the major peaks are still present. The picolinate ligand seems unaffected. However, new peaks have risen in the region of the Cp* ligand. Two additional peaks can be observed. In a region slightly more downfield, three more peaks can be observed. Though close to
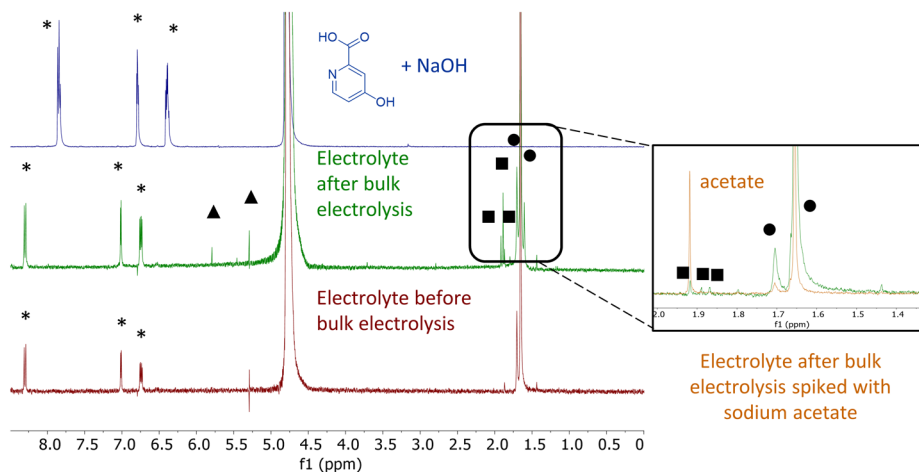
Figure A.4. ^{1}H NMR spectra of the deprotonated 4-hydroxypicolinic acid ligand (blue spectrum) and the electrolyte of the bulk electrolysis experiment before (red spectrum) and after (green spectrum) containing **4-OH1**. All spectra are recorded in D_2O. The asterisks indicate the signals corresponding to the (coordinated) 4-hydroxypicolinate ligand. The circles correspond to Cp* coordinated to iridium. The squares indicate possible degradation products of Cp*. The triangles indicate unknown compounds. The inset shows a part of the ^{1}H NMR spectrum of the electrolyte after bulk electrolysis before (green) and after (orange) it has been spiked with sodium acetate.

the region of Cp*, these latter peaks are usually associated with acetate and/or other decomposition products of Cp*.[1-18] Specifically, the peak at 1.92 ppm corresponds to acetate as it increases in intensity after the solution has been spiked with sodium acetate (inset Figure A.4). Two more unknown peaks are observed at relatively high chemical shifts.

A.3 UV-vis

Minor changes are observed in the UV-vis spectrum of the electrolyte solution before and after bulk electrolysis was employed (Figure A.5). The overall spectrum of a 10 times diluted electrolyte solution seems to be lower in intensity after the bulk electrolysis experiment. This drop might be caused by a slight osmotic-driven dilution of the electrolyte solution during 6-hour experiment. The Luggin of the reference electrode was filled with catalyst-free solution and was in direct contact with the bulk solution. Thus, diffusion and dilution could have taken place over the course of the experiment of 6 hours. The fact that no spectral shifts were observed indicates that the majority of the solution is unaffected and still contains $^{4-OH}\mathbf{1}$. Moreover, the lack of absorption above 450 nm indicates that there are no iridium oxide nanoparticles in solution which usually absorb around 580 nm.[19-21]
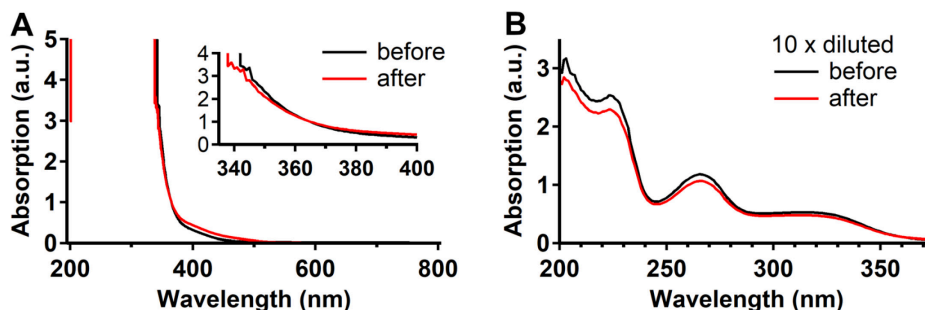
Figure A.5. UV-vis spectra of the electrolyte solution used for the bulk-electrolysis experiment containing 1 mM of $^{4-OH}\mathbf{1}$ before and after the bulk electrolysis was performed. A) shows the full spectrum of the undiluted electrolyte. The inset is a zoom of the region between 330 and 400 nm. B) shows the UV-vis spectrum of electrolyte that was diluted 10 times with D_2O. The spectra are recorded in a quartz crystal cuvet with 10.0 mm path length.

A.4   CV of electrode
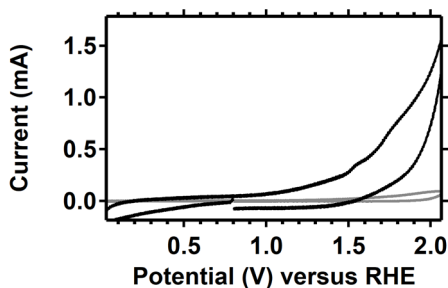
Figure A.6. CV of the large surface area GC electrode (0.79 cm²) in 0.1 M phosphate buffer of pH 7. The CV at a scan rate of 0.1 V/s was taken before (grey line) and after (black line) the electrode was used for performing bulk electrolysis at 1.95 V for 6 hours in the presence of **4-OH1**.

A.5   Chronoamperometry experiments of 1 − 5

Chronoamperometry allows for studying the current over time at a fixed potential. This way, any activation/deactivation process becomes more visible and better comparisons can be made. The amperograms at potentials of 1.8, 1.9, 2.0 and 2.1 V of complexes **1 − 5** which were recorded for 1 hour are shown in Figure A.7. These were taken with a freshly polished, but not pre-anodized GC electrode. The currents that are produced by the complexes are minimal and just barely above the current produced by GC alone (Figure A.7). Also, these amperograms showed clearly that the GC electrode is oxidized at these potentials which has a large influence on the shape of the amperogram of complexes **1 − 5** as well. Moreover, random artefacts are observed. For example, the current produced by **3-OH1** suddenly increases to a higher plateauing current halfway the measurement at 2.1 V (Figure A.7D and Figure A.8). This feature was not observed in a second measurement of a fresh solution of **3-OH1** with a freshly polished electrode (Figure A.8). Therefore, the electrode was pre-anodized for 25 minutes at 2.1 V before the amperometry measurements (Figure A.9) were taken to construct Figure 2.3. In these amperograms, artefacts such as in Figure A.8 were not observed anymore. In addition, it was found that the current would steadily increase over the period of 30 minutes in the potential window of 1.8 to 1.95 V as indicated by the green lines in Figure A.9. However, above potentials of 1.95 V, the potential either decreases immediately or decreases after an initial maximum was reached as indicated by the red lines in Figure A.9. These potential windows correlate with the potential windows of the kink in the plots of Figures 3A, B, C and E.
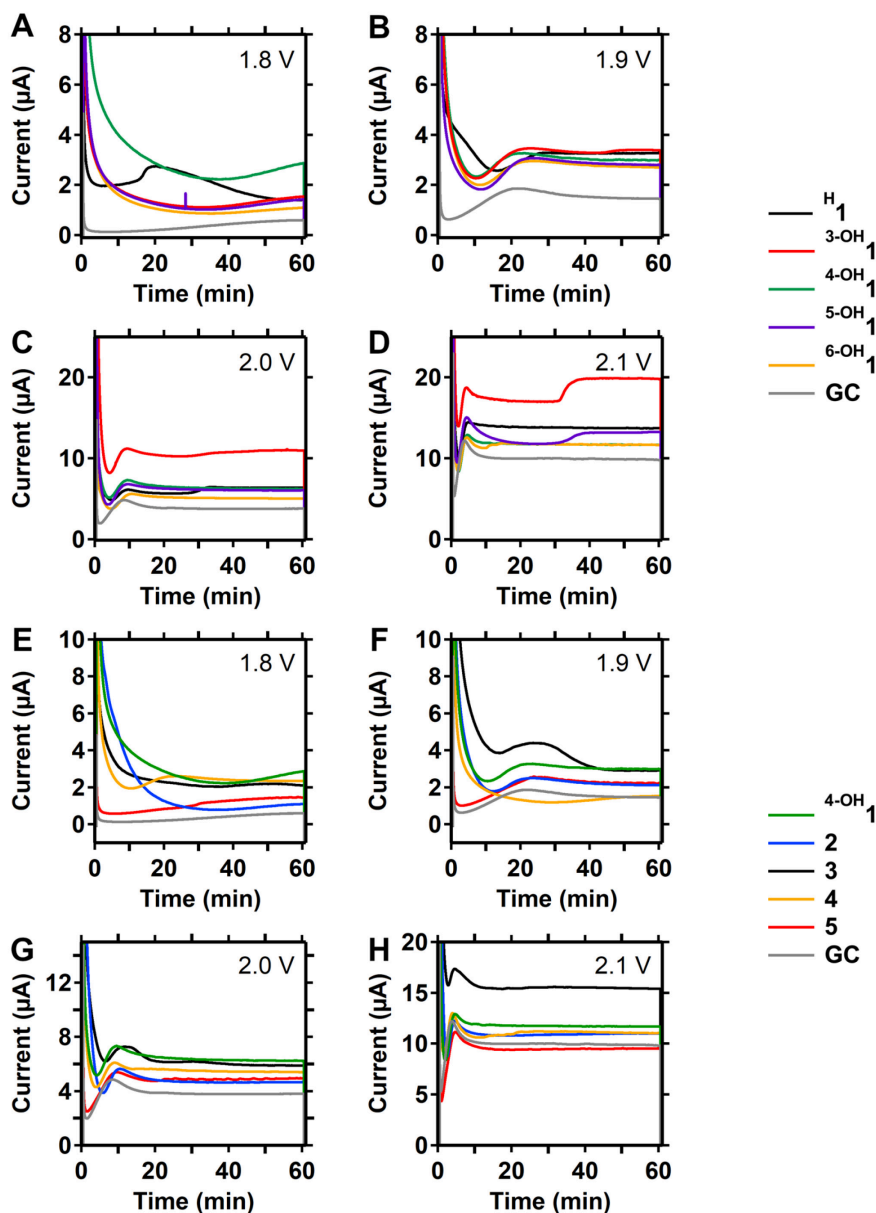
Figure A.7. The CA experiments of the iridium (hydroxy)picolinate complex series in a phosphate buffer electrolyte of pH 7 (A-D). The GC work electrode was fixed at a potential of 1.8, 1.9, 2.0 or 2.1 V versus RHE for 1 hour. E-H show the amperograms of **2** - **5** as well as that of $^{4\text{-OH}}$**1** for reference. The response of bare GC without any catalyst present in the electrolyte is indicated by the grey lines in all plots. For ^{H}**1**, a concentration of 0.4 mM was used whereas the other complexes were studied at 1 mM concentrations. The GC electrode was mechanically polished before each measurement.
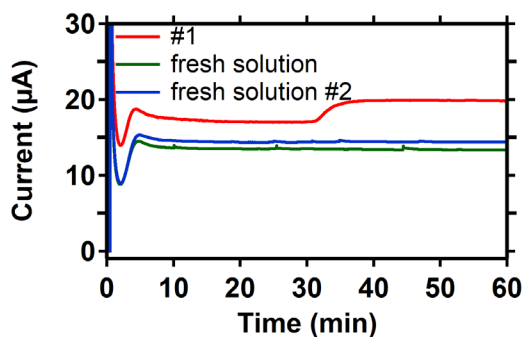
Figure A.8. Amperogram of $^{3\text{-}OH}$**1** with a 2.1 V applied potential and a GC as electrode. The red line depicts a measurement where a sudden increase in current is observed after 1800 seconds as is also displayed in Figure A.7D. The measurement was repeated with a fresh solution of $^{3\text{-}OH}$**1** that is depicted with the blue line. The green line depicts a second measurement of the fresh solution with a freshly polished electrode.
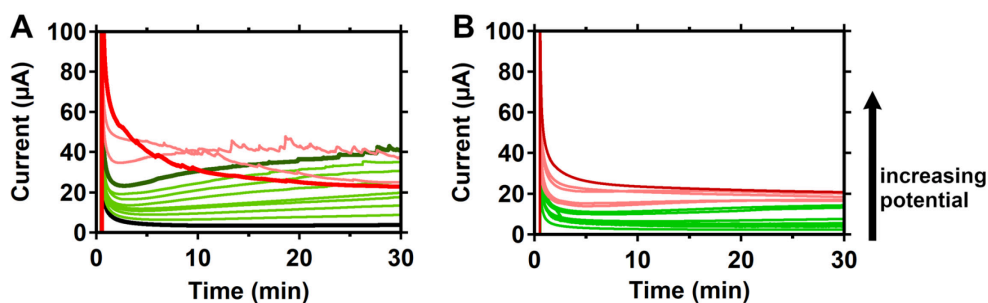
Figure A.9. The uncorrected amperograms of $^{3\text{-}OH}$**1** (A) and $^{4\text{-}OH}$**1** (B). The green lines depict the potential window where the current steadily increases over time (1.8 −1.95 V) whereas the red lines indicate the potential window where the current steadily decreases after reaching a maximum (1.95 − 2.1 V). These regions correspond to the regions indicated in Figure 2.3.

A.6 X-Ray Photoelectron Spectroscopy characterization
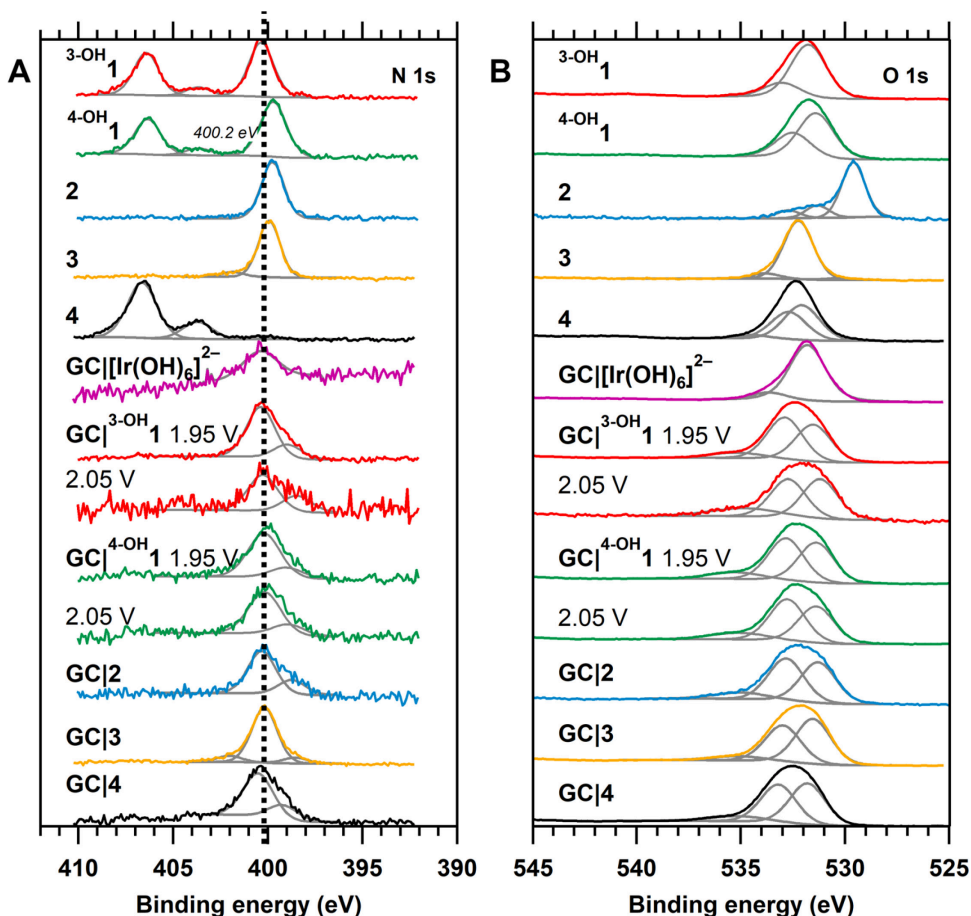
Figure A.10. N 1s (A) and O 1s (B) XPS spectra of **GC|³⁻ᴼᴴ1** (red) and **GC|⁴⁻ᴼᴴ1** (green) that were prepared at 1.95 V or 2.05 V and **GC|2** (blue), **GC|3** (orange) and **GC|4** (black) that were prepared at 1.95 V. Also included are the spectra of the parent complexes compounds ³⁻ᴼᴴ1 (red), ⁴⁻ᴼᴴ1 (green) 2 (blue), 3 (orange) and 4 (black). The deconvolution of the spectra is shown in grey.
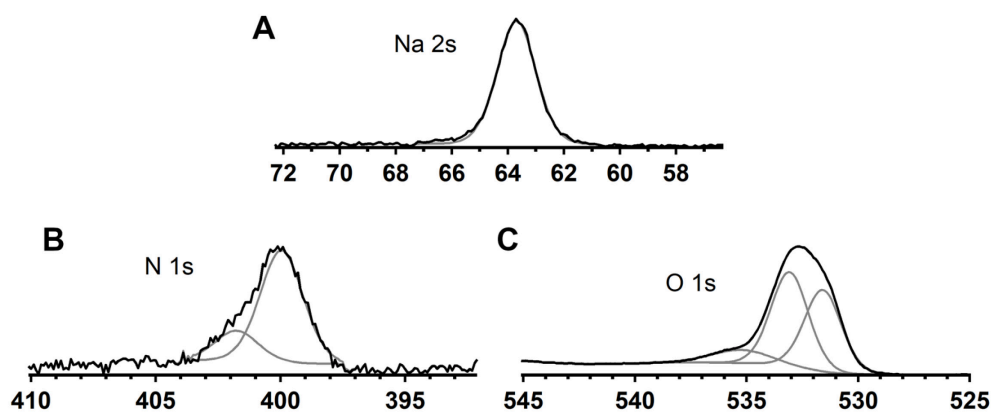
Figure A.11. XPS spectra of the Na 2s (A, same region as Ir 4f), N 1s (B) and O 1s (C) regions of the surface of a GC electrode that was anodized by performing chronoamperometry at 2.1 V in a 0.1 M phosphate buffer (pH 7) for 25 minutes.

A.7 Chronoamperometry and CV experiments of [Ir(OH)$_6$]$^{2-}$ and colloidal IrO$_x$ solutions
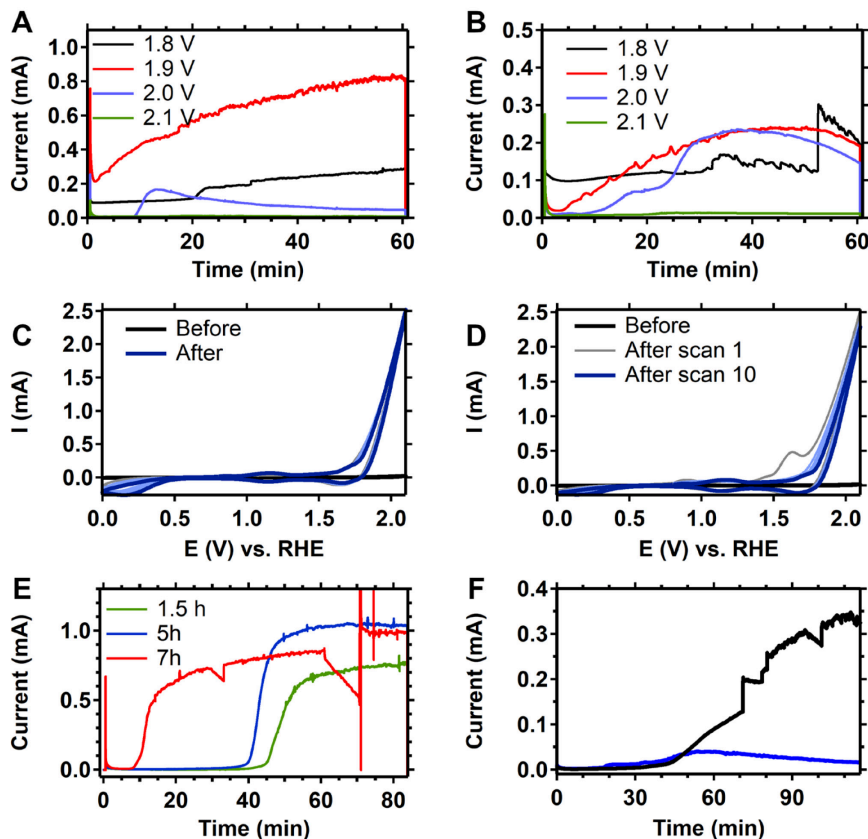
Figure A.12. Amperograms of the current generated when a glassy carbon electrode was held at 1.8 V (black), 1.9 V (red), 2.0 V (blue) or 2.1 V (green) versus RHE for 1 hour in a solution containing 1 mM [Ir(OH)$_6$]$^{2-}$ (A, one day old solution) or a colloidal solution of IrO$_x$ nanoparticles (B) with a 1 mM iridium concentration. Also displayed are the CVs of the glassy carbon work electrode in a iridium-free 0.1 M phosphate buffer solution before and after amperometry was performed for [Ir(OH)$_6$]$^{2-}$ (C) and IrO$_x$ nanoparticles in solution (D). Measurements taken at 1.95 V with an anodized GC electrode with a fresh solution of [Ir(OH)$_6$]$^{2-}$ show the lag time between the start of the measurement and the increase in current (E). These measurements were taken 1.5 hours (green), 5 hours (blue) and 7 hours (red) after the preparation of the [Ir(OH)$_6$]$^{2-}$ solution. The spikes are due to bubble formation on the electrode. (F) The influence of 1 mM 4-hydroxypicolinic acid (blue) present in a 1 mM [Ir(OH)$_6$]$^{2-}$ solution as ligand at 1.95 V with a pre-anodized glassy carbon electrode. In black, the amperogram for the same batch of [Ir(OH)$_6$]$^{2-}$ solution without ligand is shown. Both solutions were measured simultaneously 2 hours after preparation. The ligand was added 30 minutes before measurement to allow for deoxygenation of the solution by purging with argon.

A.8   NMR of $^{3\text{-},4\text{-},5\text{-},6\text{-OH}}\mathbf{1}$

These ^{1}H NMR spectra in DMSO-d_6 are from the iridium complexes $^{3\text{-OH}}\mathbf{1}$, $^{4\text{-OH}}\mathbf{1}$, and $^{6\text{-OH}}\mathbf{1}$ that have been prepared by a different synthetic route than previously reported.[22] This new synthetic route allowed for easy removal of silver contamination. The ^{1}H NMR spectra all correspond to the previously published spectra that were reported for the synthetic route using [Cp*IrCl$_2$]$_2$ as precursor instead of $\mathbf{4}$.
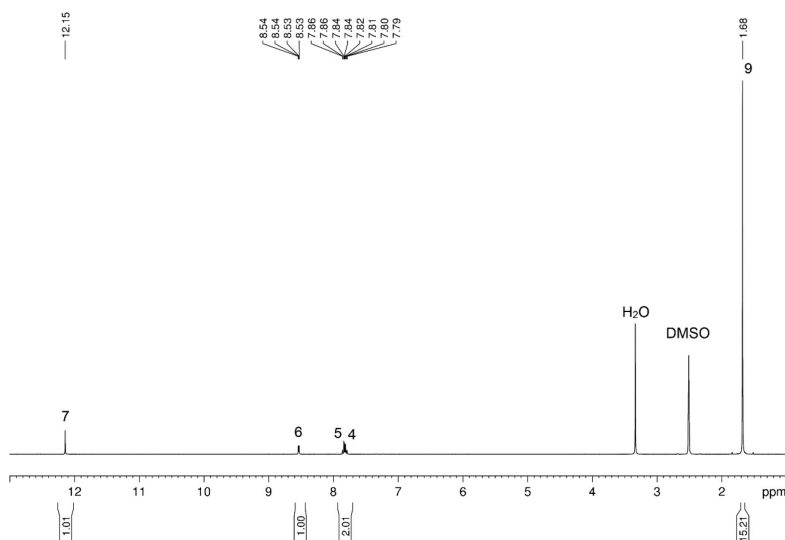
Figure A.13. ^{1}H NMR of $^{3\text{-OH}}\mathbf{1}$ in DMSO-d_6 prepared via the alternative synthetic route using $\mathbf{4}$ as precursor.
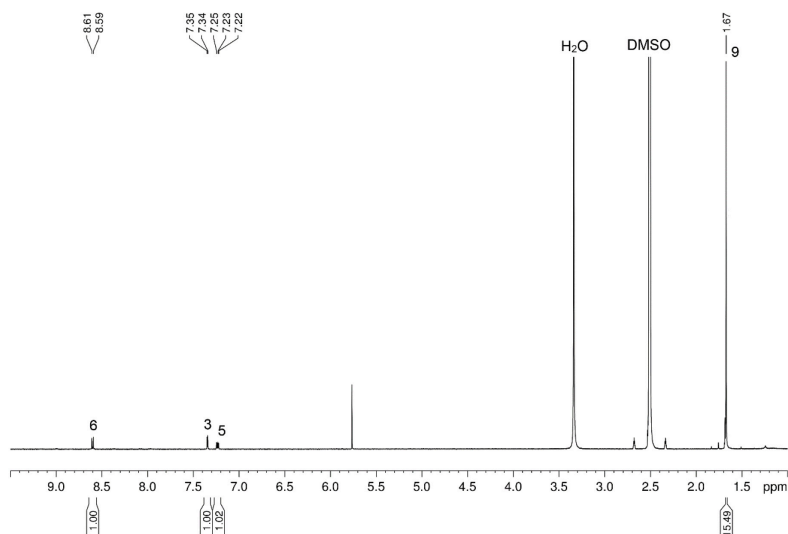
Figure A.14. ¹H NMR of ⁴⁻ᴼᴴ**1** in DMSO-d₆ prepared via the alternative synthetic route using **4** as precursor.

A
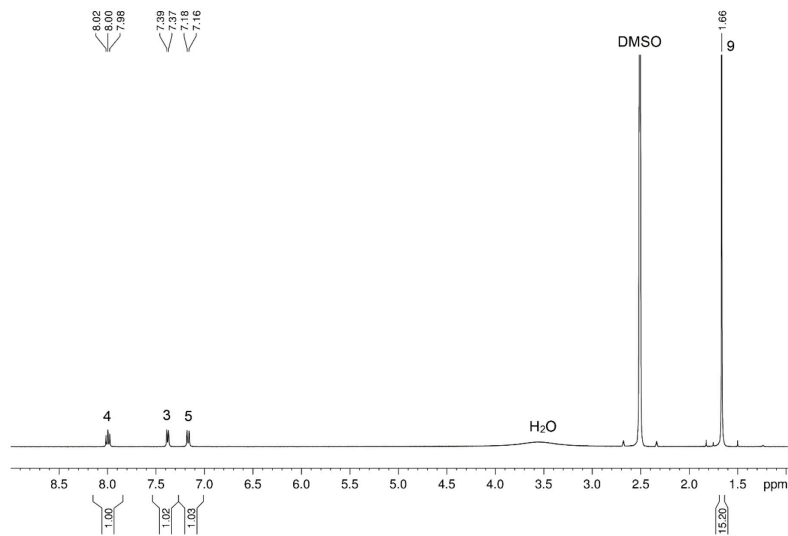
Figure A.15. ¹H NMR of ⁶⁻ᴼᴴ**1** in DMSO-d₆ prepared via the alternative synthetic route using **4** as precursor.

A.9 References

1. Savini, A.; Belanzoni, P.; Bellachioma, G.; Zuccaccia, C.; Zuccaccia, D.; Macchioni, A., *Green Chem.* **2011,** *13,* 3360–3374.
2. Wang, C.; Wang, J.-L.; Lin, W., *J. Am. Chem. Soc.* **2012,** *134,* 19895–19908.
3. Zuccaccia, C.; Bellachioma, G.; Bortolini, O.; Bucci, A.; Savini, A.; Macchioni, A., *Chem. - Eur. J.* **2014,** *20,* 3446–3456.
4. Blakemore, J. D.; Schley, N. D.; Olack, G. W.; Incarvito, C. D.; Brudvig, G. W.; Crabtree, R. H., *Chem. Sci.* **2011,** *2,* 94–98.
5. Grotjahn, D. B.; Brown, D. B.; Martin, J. K.; Marelius, D. C.; Abadjian, M.-C.; Tran, H. N.; Kalyuzhny, G.; Vecchio, K. S.; Specht, Z. G.; Cortes-Llamas, S. A.; Miranda-Soto, V.; van Niekerk, C.; Moore, C. E.; Rheingold, A. L., *J. Am. Chem. Soc.* **2011,** *133,* 19024–19027.
6. Zuccaccia, C.; Bellachioma, G.; Bolaño, S.; Rocchigiani, L.; Savini, A.; Macchioni, A., *Eur. J. Inorg. Chem.* **2012,** *2012,* 1462–1468.
7. Hong, D.; Murakami, M.; Yamada, Y.; Fukuzumi, S., *Energy Environ. Sci.* **2012,** *5,* 5708–5716.
8. Blakemore, J. D.; Mara, M. W.; Kushner-Lenhoff, M. N.; Schley, N. D.; Konezny, S. J.; Rivalta, I.; Negre, C. F. A.; Snoeberger, R. C.; Kokhan, O.; Huang, J.; Stickrath, A.; Tran, L. A.; Parr, M. L.; Chen, L. X.; Tiede, D. M.; Batista, V. S.; Crabtree, R. H.; Brudvig, G. W., *Inorg. Chem.* **2013,** *52,* 1860–1871.
9. Hintermair, U.; Sheehan, S. W.; Parent, A. R.; Ess, D. H.; Richens, D. T.; Vaccaro, P. H.; Brudvig, G. W.; Crabtree, R. H., *J. Am. Chem. Soc.* **2013,** *135,* 10837–10851.
10. Codolà, Z.; M. S. Cardoso, J.; Royo, B.; Costas, M.; Lloret-Fillol, J., *Chem. - Eur. J.* **2013,** *19,* 7203–7213.
11. Savini, A.; Bucci, A.; Bellachioma, G.; Rocchigiani, L.; Zuccaccia, C.; Llobet, A.; Macchioni, A., *Eur. J. Inorg. Chem.* **2014,** *2014,* 690–697.
12. Ingram, A. J.; Wolk, A. B.; Flender, C.; Zhang, J.; Johnson, C. J.; Hintermair, U.; Crabtree, R. H.; Johnson, M. A.; Zare, R. N., *Inorg. Chem.* **2014,** *53,* 423–433.
13. Thomsen, J. M.; Sheehan, S. W.; Hashmi, S. M.; Campos, J.; Hintermair, U.; Crabtree, R. H.; Brudvig, G. W., *J. Am. Chem. Soc.* **2014,** *136,* 13826–13834.
14. Zhang, T.; deKrafft, K. E.; Wang, J.-L.; Wang, C.; Lin, W., *Eur. J. Inorg. Chem.* **2014,** *2014,* 698–707.
15. Lewandowska-Andralojc, A.; Polyansky, D. E.; Wang, C.-H.; Wang, W.-H.; Himeda, Y.; Fujita, E., *Phys. Chem. Chem. Phys.* **2014,** *16,* 11976–11987.
16. Corbucci, I.; Ellingwood, K.; Fagiolari, L.; Zuccaccia, C.; Elisei, F.; Gentili, P. L.; Macchioni, A., *Catal. Today* **2017,** *290,* 10–18.
17. Wan, X.; Wang, L.; Dong, C.-L.; Menendez Rodriguez, G.; Huang, Y.-C.; Macchioni, A.; Shen, S., *ACS Energy Lett.* **2018,** *3,* 1613–1619.
18. Graeupner, J.; Hintermair, U.; Huang, D. L.; Thomsen, J. M.; Takase, M.; Campos, J.; Hashmi, S. M.; Elimelech, M.; Brudvig, G. W.; Crabtree, R. H., *Organometallics* **2013,** *32,* 5384–5390.
19. Zhao, Y.; Hernandez-Pagan, E. A.; Vargas-Barbosa, N. M.; Dysart, J. L.; Mallouk, T. E., *J. Phys. Chem. Lett.* **2011,** *2,* 402–406.
20. Zhao, Y.; Vargas-Barbosa, N. M.; Hernandez-Pagan, E. A.; Mallouk, T. E., *Small* **2011,** *7,* 2087–2093.
21. Hintermair, U.; Hashmi, S. M.; Elimelech, M.; Crabtree, R. H., *J. Am. Chem. Soc.* **2012,** *134,* 9785–9795.
22. Menendez Rodriguez, G.; Bucci, A.; Hutchinson, R.; Bellachioma, G.; Zuccaccia, C.; Giovagnoli, S.; Idriss, H.; Macchioni, A., *ACS Energy Lett.* **2017,** *2,* 105–110.

A

Appendix B

<u>Supplementary information for Chapter 3:</u>
Pinpointing the active species of the Cu(DAT)
catalyzed oxygen reduction reaction

B.1 EPR and SQUID of Cu(DAT) powder

A **Cu(DAT)** powder was obtained by removing water under reduced pressure of a 6.6 mM aqueous solution of a 1:1 mixture of $Cu(OTf)_2$ and DAT. Electron paramagnetic resonance (EPR) spectroscopy (Figure B.2) was employed to check whether the powder agrees upon the structure of **Cu(DAT)** in solution. A broad peak at g = 2.16 was observed as well as the weak signal for the forbidden $M_s = \pm 2$ transition both indicating the presence of the dinuclear $Cu_2(\mu\text{-}DAT)_2$ core. Moreover, SQUID data (Superconducting Quantum Interference Device) of the same **Cu(DAT)** powder was obtained (Figure B.2). The χ_m *versus* T plot with χ_m being the magnetic susceptibility per two Cu^{II} ions. A maximum at 102.5 K can be found which is characteristic of two antiferromagnetically coupled Cu^{II} sites that are closely spaced and have a diamagnetic S = 0 state. Some paramagnetic impurity was found (estimated at 2.4% when a pure spin center with g = 2.0 is assumed) which was most likely corresponding to a mononuclear $[Cu^{II}(DAT)]^{2+}$ species. By correcting the data for this small impurity, the data for **Cu(DAT)** could be obtained and fitted to find the *J*-coupling constant, isotropic g-factor, and temperature independent (orbital) paramagnetism value of -115.8 cm^{-1}, 2.11, and 5.2×10^{-4} cm^3 mol^{-1} respectively which fall in the range of other triazole-bridged copper complexes. The small intermolecular *J*-coupling of 1.0×10^{-4} cm^{-1} could exclude the presence of polymeric chain structures in the solid state. These results confirm that the **Cu(DAT)** powder that was used for XPS analysis has the same electronic structure as the **Cu(DAT)** complex in solution.
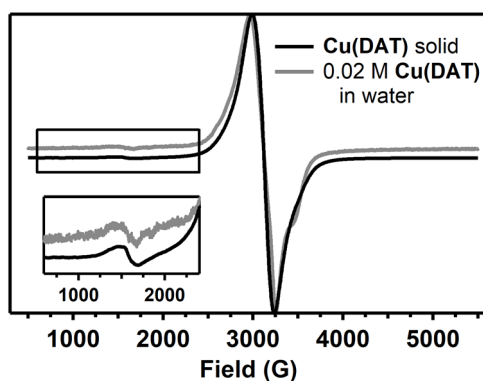
Figure B.1. In black, the normalized EPR spectrum of the **Cu(DAT)** powder depicted. The spectrum was obtained at 9.35 GHz at 77 K. For comparison, the normalized EPR spectrum of **Cu(DAT)** in water (Figure 3.2) is depicted in grey. The inset depicts a zoom of the spectrum between 600 and 2400 Gauss.
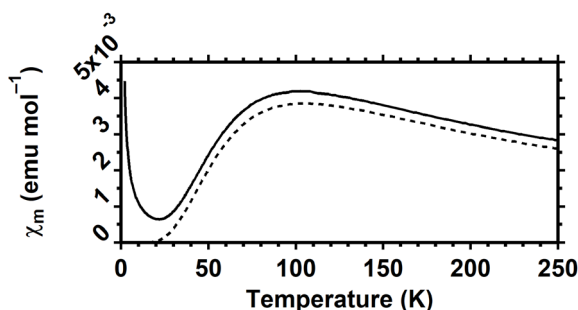
Figure B.2. SQUID data of the **Cu(DAT)** powder (solid) and the extracted spectrum where the influence of paramagnetic impurity was excluded (dashed).

B.2 Long-term stability of Cu(DAT) solutions

The stability of a **Cu(DAT)** solution was monitored by UV-vis over time (Figure B.3). Before the first spectrum was taken, two solutions were prepared: a 5 ml 0.1 M $NaClO_4$ solution containing 13.2 mM $Cu(OTf)_2$ and 5 ml of a 0.1 M $NaClO_4$ solution containing 13.2 mM 3,5-diamino-1,2,4-triazole (DAT). These solutions were mixed and within a minute, the first UV-Vis spectrum was taken. Slowly, the absorption at 380 nm was observed to increase. After 10.75 hours, the absorption at 380 nm reached a maximum and the absorption between 600 and 1000 nm had shifted. In addition, precipitation had formed in the solution. In the following hours, the absorption at 380 nm was found to decrease. Clearly, the **Cu(DAT)** solution is

B
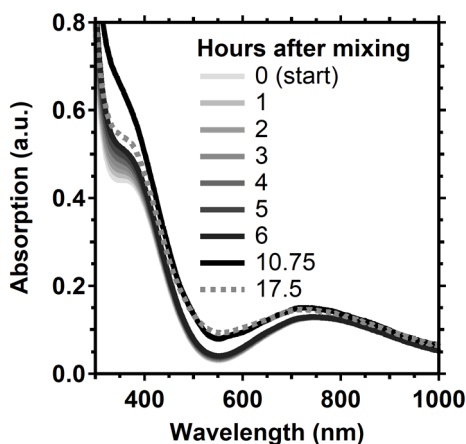
Figure B.3. UV-vis spectra recorded over the course of 17.5 hours of a 0.1 M $NaClO_4$ solution containing 6.6 mM of a 1:1 mixture of $Cu(OTf)_2$ and DAT. The evolution in time is illustrated with the color change from light grey to black. The grey dotted line represents the spectrum after 17.5 hours.

not stable over long periods of time. Therefore, all experiments were performed within 0-4 hours after preparation of the **Cu(DAT)** solution when only minor changes are observed in the UV-vis spectrum.

B.3 pH titrations on Cu(DAT)

pH titrations were performed to study the influence of the pH on the complex as the triazole ligand might be protonated (pK_a of HDAT$^+$ is 4.4) or deprotonated (pK_a of DAT is 12.1).[1-3] An acidic titration on a 0.1 M NaClO$_4$ solution containing 30 mM of a 1:1 mixture of Cu(OTf)$_2$ and DAT was performed with 1.0 M HClO$_4$ (Figure B.4A). A perchlorate solution was used in order to resemble the conditions of electrochemical measurements. At the inflection point, 2.1 equivalents of acid with respect to Cu$_2$(μ-DAT)$_2$ are transferred. This equals 1.05 equivalents with respect to the ligand DAT. At the inflection point, both of the coordinated DAT ligands of the Cu$_2$(μ-DAT)$_2$ core are protonated simultaneously with an estimated pK_a value of 3.5. The drop in pH is accompanied by a color change from green to light blue. The UV-vis spectrum of **Cu(DAT)** at pH 4.8 has two distinct absorptions at 380 nm and circa 740 nm (Figure B.4B). This latter signal has shifted to circa 800 nm in the UV-vis spectrum upon acidification of the **Cu(DAT)** solution to pH 1 using HClO$_4$. Simultaneously, the distinctive absorption at 380 nm almost completely
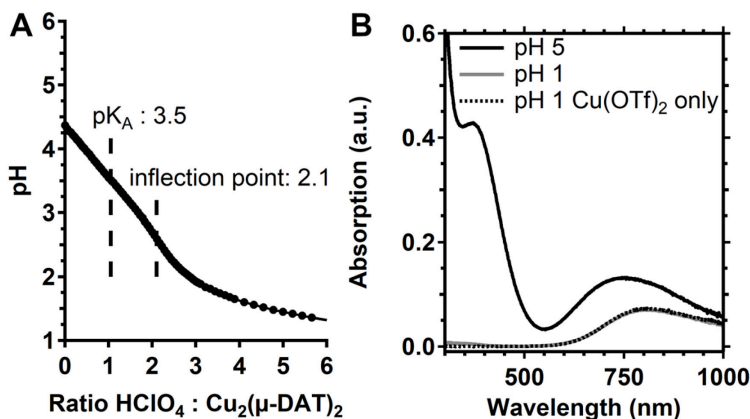
Figure B.4. (a) shows the pH titration with 1.0 M HClO$_4$ of a 0.1 M NaClO$_4$ solution containing 30 mM of a 1:1 mixture of Cu(OTf)$_2$ and DAT with 1.0 M HClO$_4$. The ratio is given with respect to the dinuclear Cu$_2$(μ-DAT)$_2$ core. (b) shows the UV-Vis spectrum of a 0.1 M NaClO$_4$ solution containing 6.6 mM of a 1:1 mixture of Cu(OTf)$_2$ and DAT (pH 5, black solid line). Also depicted are the spectra of a 0.1 M HClO$_4$ solution (pH 1) containing either 6.6 mM of a 1:1 mixture of Cu(OTf)$_2$ and DAT (grey solid line) or only 6.6 mM Cu(OTf)$_2$ (black dotted line).

disappeared. The UV-vis spectrum of **Cu(DAT)** at pH 1 was found to be qualitatively identical to the UV-vis spectrum of $Cu(OTf)_2$ in absence of DAT.

Starting from a 15 mM solution of a 1:1 mixture of $Cu(OTf)_2$ and DAT a titration with 1.1 M NaOH was performed under continuous stirring (Figure B.5). Small amounts of green precipitation were observed to form above pH 5.5 and increased in quantity as the pH further increased. At circa pH 12 a turbid solution was obtained. The titration with NaOH was stopped and immediately followed by a back titration with 1.0 M $HClO_4$. The back titration showed hysteresis around the inflection point. Moreover, the precipitation slowly disappeared while the pH was lowered and eventually a clear solution was obtained below pH 5. The observed hysteresis around the inflection point indicates that an additional process coupled to a deprotonation takes place. A coordinating H_2O is most likely deprotonated as one equivalent of NaOH is required to reach the inflection point. As a result, the anionic hydroxyl is now able to form an intermolecular bridge between complexes. Ultimately, this can lead to the formation of insoluble coordination polymers, which are frequently observed in case of aqueous copper complexes.[4-6]
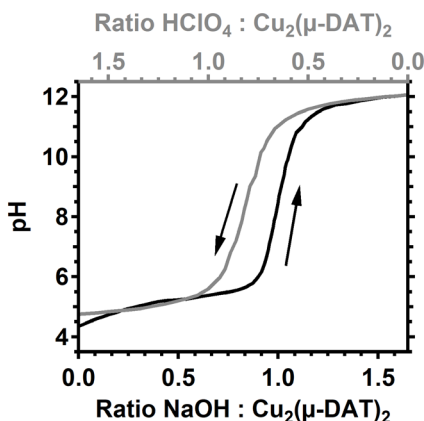
Figure B.5. pH titration of an aqueous 15 mM solution of a 1:1 mixture of $Cu(OTf)_2$ and DAT with 1.1 M NaOH (black line, bottom axis) and the back-titration with 1.0 M $HClO_4$ (grey line, top axis). The ratio is given with respect to the dinuclear $Cu_2(\mu\text{-DAT})_2$ core.

B.4 Copper and DAT titrations followed by UV-vis spectroscopy

In order to investigate the influence of different ligand to copper ratios, two titrations were performed in 0.1 M $NaClO_4$. First, 10 μL aliquots of a solution containing 0.42 M $Cu(OTf)_2$, 6.6 mM DAT, and 0.1 M $NaClO_4$ were added to a 2.5 ml solution of 6.6 mM DAT in 0.1 M $NaClO_4$. UV-vis spectra were recorded after every

addition (Figure B.6). As soon as $Cu(OTf)_2$ was added, the characteristic absorption at 380 nm as well as a broad absorption with a maximum at 720 nm corresponding to the d-d transition of Cu^{II} started to appear. While the $Cu(OTf)_2$ concentration was increased, the absorption at 380 nm increased and sharpened. Moreover, the d-d absorption not only increases but also shifts to 780 nm. The latter event is an indication for a change in ligand environment as this affects the d-d transition. An opposite shift is observed when a 0.42 M DAT solution containing 6.6 mM $Cu(OTf)_2$ and 0.1 M $NaClO_4$ is titrated to a 6.6 mM $Cu(OTf)_2$ solution in 0.1 M $NaClO_4$ (Figure B.7). In this case, the d-d band shifts to lower wavelengths most likely due to a larger ratio of coordinated DAT with respect to copper. The absorption at 380 nm quickly increases in intensity but is eventually overlapped by a large absorption in the UV area.
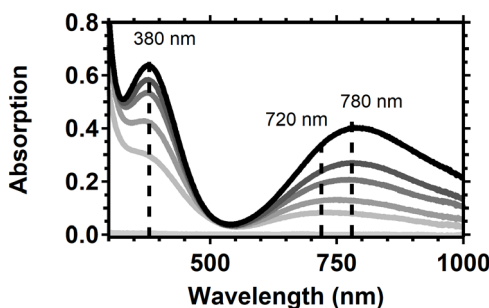
Figure B.6. UV-vis spectra of the titration of $Cu(OTf)_2$ to a 6.6 mM DAT solution in 0.1 M $NaClO_4$. In the order of increasing darkness are depicted the spectra of 0, 0.5, 1, 2, 3 and 4 equivalents of $Cu(OTf)_2$ with respect to DAT.

Titrations were also performed at pH 1 to see the effect of protonated DAT (Figures B.8 and B.9). When $Cu(OTf)_2$ was titrated to a DAT solution in 0.1 M $HClO_4$, the absorption corresponding to the d-d absorption increased in intensity but did not shift (Figure B.8). The maximum was found at 800 nm which corresponds to a $Cu(OTf)_2$ only solution at pH 1 (Figure B.4). A slight absorption can be observed at 355 nm but only becomes significant when the amount of DAT was increased up to 11 equivalents with respect to $Cu(OTf)_2$ (Figure B.9). This indicates that an infinite small amount of $HDAT^+$ still coordinates but hardly has a change on the ligand environment of copper, as the d-d transition at 800 nm does not shift nor changes in intensity.
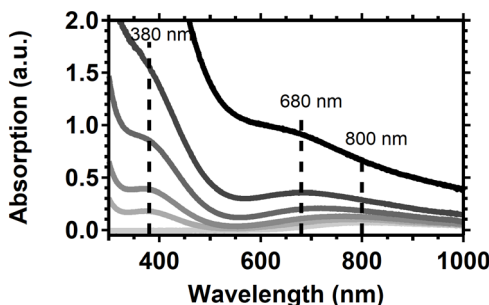
Figure B.7. UV-vis spectra of the titration of DAT to a 6.6 mM Cu(OTf)$_2$ solution in 0.1 M NaClO$_4$. In the order of increasing darkness are depicted the spectra of 0, 0.5, 1, 2, 3 and 4 equivalents of DAT with respect to Cu(OTf)$_2$.
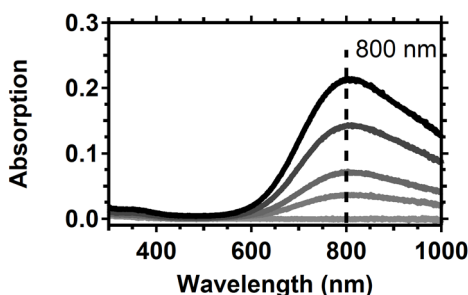
Figure B.8. UV-vis spectra of the titration of Cu(OTf)$_2$ to a 6.6 mM DAT solution in 0.1 M HClO$_4$. In the order of increasing darkness are depicted the spectra of 0, 0.5, 1, 2, and 3 equivalents of Cu(OTf)$_2$ with respect to DAT.

B

B.5 Influence of MES buffer on Cu(DAT)

It was found that the combination of **Cu(DAT)** and a phosphate or Britton-Robinson buffer led to precipitation of **Cu(DAT).** Hence, 0.03 M of 2-(*N*-morpholino)ethanesulfonic acid (MES) was investigated as a buffer, since it has a pK_a of 6.15 and thus a useful buffering range close to pH 4.8.[7, 8] Moreover, no immediate precipitation was observed in combination with **Cu(DAT)**. Although it has been reported that MES is not likely to coordinate to Cu^{II},[9] a deviation in the UV-vis spectrum was observed implying that some coordination of MES does take place (Figure B.10). The absorption belonging to the d-d transition shifts while the absorption at 380 nm increases significantly. Coordination can be expected for a complex such as **Cu(DAT)** with labile ligands in the coordination sphere but the Cu$_2$(μ-DAT)$_2$ core remains intact as illustrated by the 380 nm absorption and the identical EPR spectra of **Cu(DAT)** in the presence and absence of MES (Figure B.11).
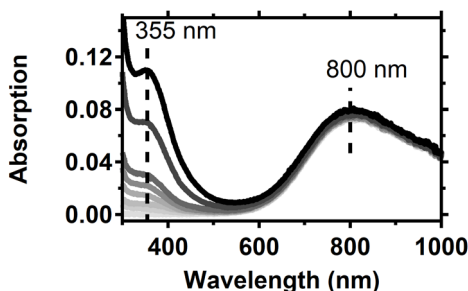
Figure B.9. UV-vis spectra of the titration of DAT to a 6.6 mM Cu(OTf)$_2$ solution in 0.1 M HClO$_4$. In the order of increasing darkness are depicted the spectra of 0, 0.5, 1, 2, 3, 4, 8 and 11 equivalents of DAT with respect to Cu(OTf)$_2$.
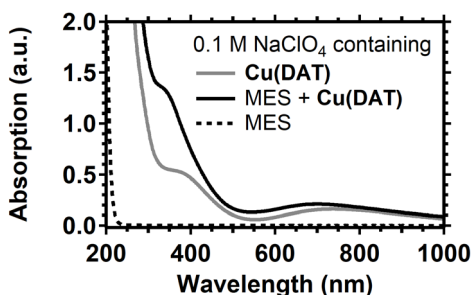
Figure B.10. The UV-vis spectra of a 0.1 M NaClO$_4$ solution with 6.6 mM of a 1:1 mixture of Cu(OTf)$_2$ and DAT (**Cu(DAT)**, grey solid line), 0.03 M MES buffer (dotted black line) and a mixture of both (solid black line).
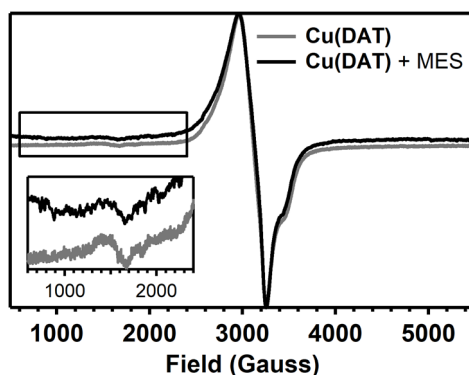
Figure B.11. In grey, the normalized EPR spectrum of a 6.6 mM **Cu(DAT)** solution (Figure 3.2, taken at 9.36 GHz) is shown. The black lines show the normalized EPR spectrum of 6.6 mM **Cu(DAT)** + 0.03 M MES (taken at 9.34 GHz. The inset shows a zoom of the spectrum between 600 and 2400 Gauss. Both spectra were taken at 77 K.

B.6 Electrochemical Quartz Crystal Microbalance experiments

For the sensitive microbalance experiments a sensitivity coefficient relating the frequency to mass can be determined by the electrodeposition of Pb^0 as is described elsewhere.[10] However, frequency changes might not solely depend on mass changes as for example the viscoelasticity and surface roughness of the deposition also have an effect on the frequency.[11]

A separate electrochemical quartz crystal microbalance (EQCM) measurement was performed for a solution containing 6.6 mM of only DAT. In the potential window of 0.0 to 1.0 V an anodic peak is during cyclic voltammetry (CV) observed accompanied by a negligible frequency change. When the potential window is broadened to 1.2 V it becomes clear that the oxidation that has an onset at 0.9 V *versus* the reversible hydrogen electrode (RHE) is part of an oxidation that produces significant currents above 1.0 V (Figure B.12). The initial positive sweep is followed by a negative sweep where a broad reductive peak between 0.9 and 0.4 V *versus* RHE can be observed. Accordingly, the oxidation starting at 0.9 V is linked to the oxidation of DAT but does not lead to signification deposition.

The electrochemical deposition of material by **Cu(DAT)** can also be induced by chronoamperometry. Applying a fixed potential of 0.2 V on a gold electrode induces a steady decrease of frequency, thus increase of mass, of the electrode (Figure B.13). Figure B.14 shows that the ORR activity of the electrodeposition induced by chronoamperometry (^{CA}Au|**Cu(DAT)**) shows the same current profile on gold as the deposition generated by cyclic voltammetry (^{CV}Au|**Cu(DAT**, 30 cycles between 0 and 1 V at 100 mV/s). Also, for both ^{CV}Au|**Cu(DAT)** and ^{CA}Au|**Cu(DAT)** the activity increases by circa 30% in the course of 40 scans. The difference in absolute current might be caused by the difference in the amount of deposited material. During modification with cyclic voltammetry, part of the deposition is stripped above 0.8 V whereas during chronoamperometry the potential is held at 0.2 V.

B
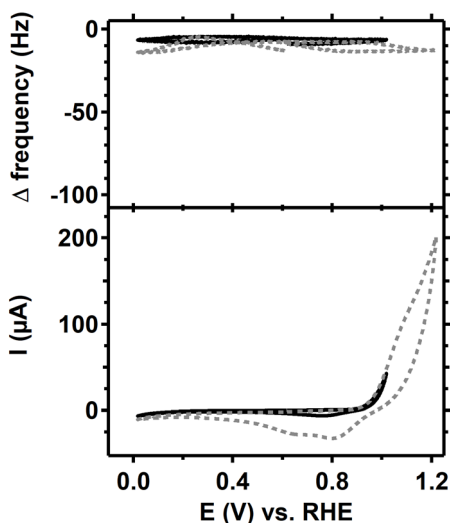
Figure B.12. A cyclic voltammogram combined with a quartz crystal microbalance experiment of a 0.1 M NaClO$_4$ solution (pH 4.4) containing 6.6 mM DAT measured at a 10 mV/s scan rate. The voltammograms were recorded between 0 and 1 V (solid black line) or 1.3 V (dotted grey line).
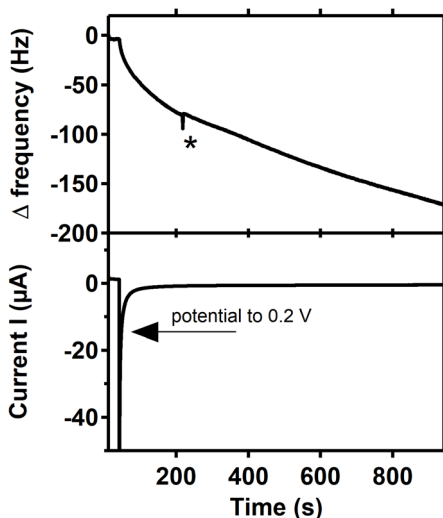
Figure B.13. A quartz crystal microbalance experiment combined with chronoamperometry. A gold electrode in a 0.1 M NaClO$_4$ (pH 4.8) solution containing 6.6 mM of a 1:1 mixture of Cu(OTf)$_2$ and DAT was modified by chronoamperometry. For the first 30 seconds, the potential was held at 0.8 V. Next, the potential was set at 0.2 V for 15 minutes. The current response is displayed in the bottom panel while the corresponding frequency change is displayed in the top panel. The asterisk (*) depicts an artifact.
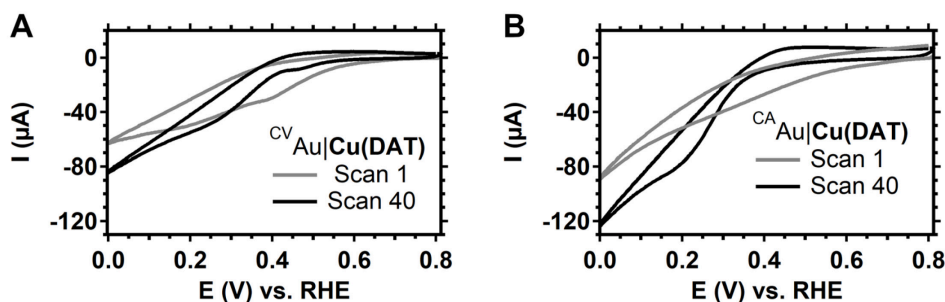
Figure B.14. Cyclic voltammograms at a scan rate of 100 mV/s of modified gold electrodes in an oxygen-purged 0.03 M MES buffer in a 0.1 M NaClO$_4$ solution (pH 5.2). The electrodes were either pre-modified by cyclic voltammetry (a) or chronoamperometry (b) in a **Cu(DAT)** solution. For clarity, only the first (light grey) and last (40th, black) scans are shown.

The deposition formed by **Cu(DAT)** can readily be stripped off by performing CV in a potential window up to 1.3 V (Figure B.15). A gold electrode was modified by repeated CV scans in an 0.1 M NaClO$_4$ electrolyte containing **Cu(DAT)**. The EQCM measurement shows that the intensity of the oxidative peak at 0.8 *versus* RHE drastically increases above 1.0 V and is accompanied by a severe decrease in mass indicating loss of material. Subsequent scanning in this broader potential window shows that deposition formed in the cathodic region is readily stripped above 1.0 V so build-up of material on the electrode does not take place anymore.
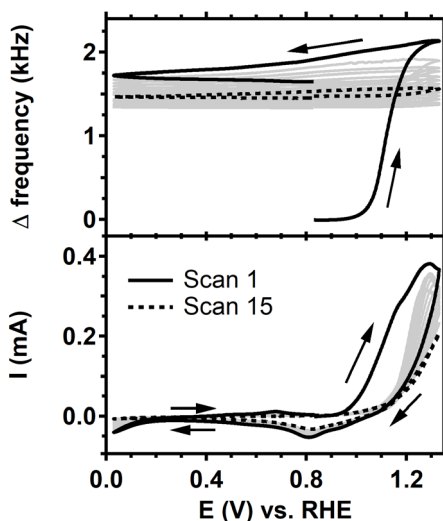
Figure B.15. Stripping of the deposition of a modified gold electrode in a 0.1 M NaClO$_4$ (pH 4.8) solution containing 6.6 mM of a 1:1 mixture of Cu(OTf)$_2$ and DAT by EQCM combined with cyclic voltammetry at a 10 mV/s scan rate. The material was deposited on the electrode by performing CV for 15 scans between 0 and 1 V at a 10 mV/s scan rate in the same electrolyte prior to stripping.

B.7 Cyclic voltammetry in the presence of Cu(DAT) with gold and pyrolytic graphite electrodes

A gold disk electrode was modified using the same procedure as the EQCM experiments were performed: a CV was taken in a 6.6 mM solution of a 1:1 ratio of Cu(OTf)$_2$ and DAT in a 0.1 M NaClO$_4$ electrolyte solution. 30 cycles at a 100 mV/s scan rate were performed to obtain the modified electrode ^{CV}Au|**Cu(DAT)**. Compared to unmodified gold, the onset is at slightly higher potentials and larger currents are acquired. Also, the ring shows less current implying better selectivity. However, the activity drops over repetitive scanning. Most likely, the deposition cannot bind strong enough on gold to perform rotating ring disk electrode (RRDE) experiments with high rotation rates. In contrast, when a stationary gold electrode is used, the activity increases upon repetitive potential cycling (Figure B.14 and B.19) similar to the behavior of PG|**Cu(DAT)** (Figure 3.4). As gold is active in the same potential window for the ORR (Figure B.16), any attributions to active species cannot be made unambiguously when gold is used. Therefore, pyrolytic graphite (PG) was
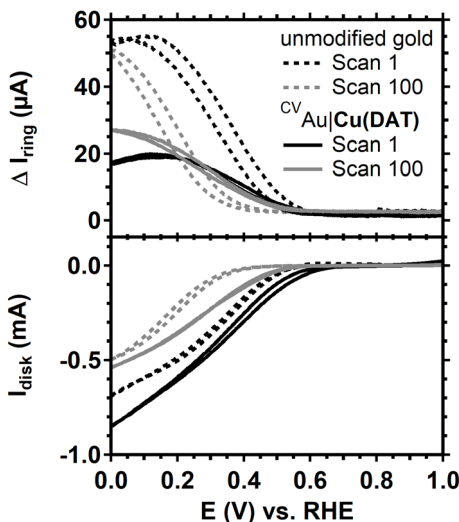
Figure B.16. RRDE experiment with a gold disk electrode (0.196 cm²) in an oxygen-purged 0.1 M NaClO$_4$ solution containing 0.03 M MES buffer (pH 5.2). The cyclic voltammogram of the gold disk which was rotated at 2000 rpm (bottom panel) and the current response of the platinum ring that was set at a potential of 1.2 V (top panel) are depicted. The dotted lines correspond to an unmodified gold disk while the solid lines correspond to the modified electrode ^{CV}Au|**Cu(DAT)**. In black, the first scan is shown while the grey lines show the last (100th) scan. The CV was taken at a 100 mV/s scan rate.

used as electrode as it shows qualitatively the same electrochemistry for **Cu(DAT)** as with gold (Figure B.17).
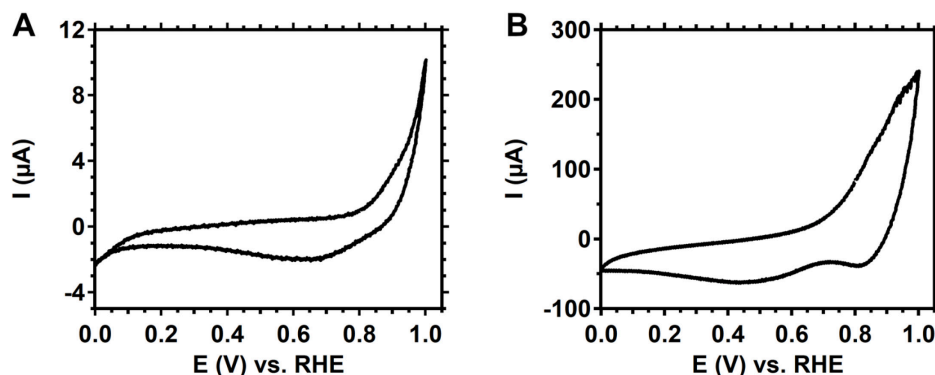
Figure B.17. Cyclic voltammograms that are recorded at a 25 mV/s scan rate in a 0.1 M NaClO$_4$ (pH 4.8) solution with 6.6 mM of a 1:1 ratio of Cu(OTf)$_2$ and DAT with (a) gold and (b) pyrolytic graphite (PG) working electrodes.

B.8   Koutecky-Levich analysis

The linear fits in Figure B.18A show that the limiting current for dioxygen reduction at different rotation rates behaves according to the Koutecky-Levich equation (see Chapter 1).[12] The Levich equation (Eqn. 1.7) can be simplified to Equation B.1 with *B* being the Levich constant. This constant was determined by performing rotating ring disk electrode (RRDE) experiments with a platinum disk electrode, as platinum is known to be a 4-electron dioxygen reduction catalyst. *B* can be calculated using the slope of the Koutecky-Levich plot as the following equation holds (Equation B.2):[13]

$$I_L = 0.62nFAD_O^{2/3}C_O\nu^{-1/6}\omega^{1/2} = BnA\omega^{1/2} \qquad \textbf{Eqn. B.1}$$

$$slope = \frac{1}{BnA} \qquad \textbf{Eqn.B.2}$$

For the platinum electrode the slope, *n* (4) and *A* (0.196 cm^2) are known, so *B* could be determined and used to calculate *n* for the modified PG electrode for which *A* (0.12 cm^2) and the slope are known as well. *n* was calculated to be 1.2 indicating that dioxygen is reduced to mainly superoxide and partly peroxide species.
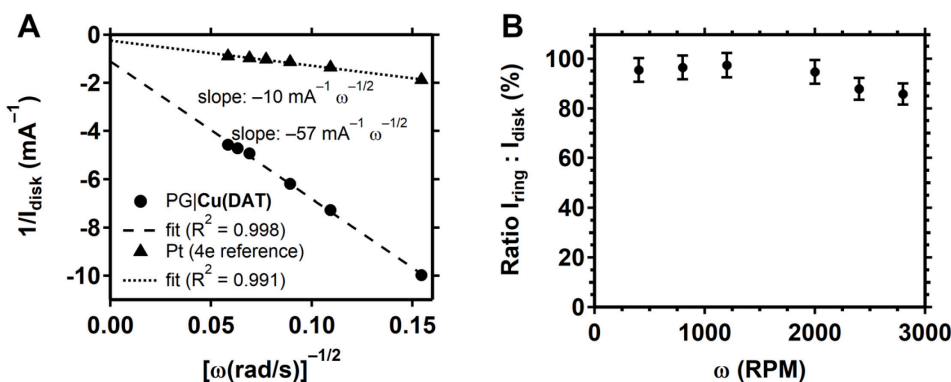
Figure B.18. (a) shows the Koutecky-Levich plot of the inverse of the average limiting current between 0.40-0.42 V of PG|**Cu(DAT)** (rounds, Figure 3.4B) versus the inverse square root of the rotation rate and the result of a linear fit. Also shown is the inverse of the average limiting current between 0.30 and 0.35 V for a Pt disk electrode (triangles) used as calibration for the Levich equation in oxygen-saturated 0.1 M NaOH. (b) shows the ratio of the average limiting current of the ring to the average limiting current of PG|**Cu(DAT)** between 0.40 and 0.42 V versus the rotation speed in 0.1 M NaOH. The ratio was corrected for the collection efficiency (22%) of the ring that was determined with the $[Fe(CN)_6]^{4-}/[Fe(CN)_6]^{3-}$ redox couple.

B.9   XPS analysis of C 1s and N 1s regions of modified gold and pyrolytic graphite electrodes

For X-ray photoelectron spectroscopy (XPS) analysis (Figure B.19, B.20 and Table B.1), the following procedures were followed to obtain ^{CV}Au|**Cu(DAT)** and ^{CA}Au|**Cu(DAT)**. EQCM gold electrodes were used in a similar set-up as the EQCM experiments. Sample ^{CV}Au|**Cu(DAT)** was prepared with cyclic voltammetry by performing 30 CV scans between 0 and 1 V at a 100 mV/s scan rate in a 0.1 M NaClO$_4$ solution containing 6.6 mM of a 1:1 ratio of Cu(OTf)$_2$ and DAT at pH 4.8. Sample
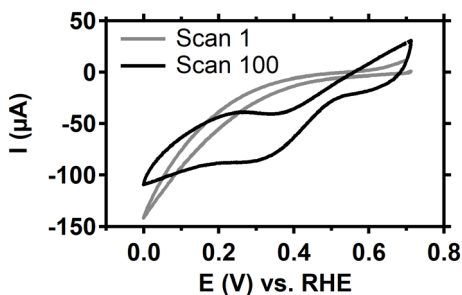
Figure B.19. Cyclic voltammogram of ^{Cat}Au|**Cu(DAT)** directly after the modification in an oxygen purged 0.1 M NaClO$_4$ solution containing 0.03 M MES buffer at a pH of 5.2. 100 cycles at a 100 mV/s scan rate were performed.

^{CA}Au|**Cu(DAT)** was prepared potentiostatically by applying 0.2 V for 15 minutes. The whole set-up was stationed in a glove bag under an N_2 atmosphere to prevent contact with air upon removal of the electrode from the EQCM cell. The electrodes were rinsed with Ar purged water and dried under high vacuum before XPS analysis.

^{Cat}Au|**Cu(DAT)** was prepared with cyclic voltammetry by performing 30 CV scans between 0 and 1 V at a 100 mV/s scan rate in a 0.1 M $NaClO_4$ solution containing 6.6 mM of a 1:1 ratio of $Cu(OTf)_2$ and DAT at pH 4.8. Next, the electrode was put in an oxygen-saturated 0.03 M MES buffer (pH 5.2) in 0.1 M $NaClO_4$. 100 CV cycles between 0 and 1 V at a 100 mV/s scan rate were performed. The ORR onset was observed to increase after repetitive scanning up to 100 scans (Figure B.19) as was also observed with RRDE experiments on PG|**Cu(DAT)**.

PG|**Cu(DAT)** was prepared in a regular electrochemical set-up by performing 90 CV scans between 0 and 1 V at a 100 mV/s scan rate in a 0.1 M $NaClO_4$ solution containing 6.6 mM of a 1:1 ratio of $Cu(OTf)_2$ and DAT at pH 4.8. 90 instead of 30 CV scans were used to increase the intensity of the XPS signal. The electrode was rinsed with N_2 purged water and dried under high vacuum. Care was taken to prevent contact with air during handling and transferring the electrode into the XPS apparatus.
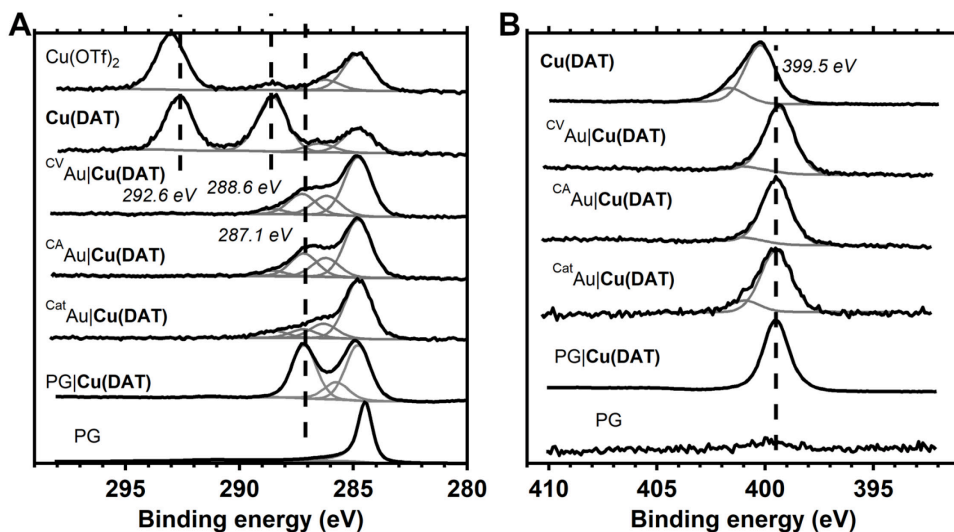
Figure B.20. C 1s (A) and N 1s (B) XPS spectra (black lines) of the modified electrodes ^{CV}Au|**Cu(DAT)**, ^{CA}Au|**Cu(DAT)**, ^{Cat}Au|**Cu(DAT)**, PG|**Cu(DAT)** and the reference compounds **Cu(DAT)**, $Cu(OTf)_2$ and PG electrode. In grey, the deconvolution is depicted.

Table B.1. The C : Cu ratio of several carbon species with respect to the total amount of copper of the modified electrodes [CV]Au|**Cu(DAT)**, [CA]Au|**Cu(DAT)**, [Cat]Au|**Cu(DAT)** and the reference compounds **Cu(DAT)** and Cu(OTf)$_2$ as determined by XPS.

Corresponding carbon species (eV)[a]	Cu(OTf)$_2$	**Cu(DAT)**	[CV]Au|**Cu(DAT)**	[CA]Au|**Cu(DAT)**	[Cat]Au|**Cu(DAT)**
293.0 (OTf$^-$)	1.6				
292.6 (OTf$^-$)		2.0			
288.6 (DAT)		2.2			
286.2			1.1	1.2	
287.2			1.4	1.2	
288.5			0.3	0.3	
286.4					1.9
287.7					1.1
289.1					0.7

[a]The ratio of the carbon species at 284.8 eV is omitted as this mostly corresponds to adventitious carbon for these samples.

B.10 Influence of DAT on the ORR activity of copper electrodes

B

To study the electrochemical effect of DAT on a copper surface, a copper disk was modified by cyclic voltammetry similar to the modification of PG to obtain PG|**Cu(DAT)**. A copper disk electrode was modified by cyclic voltammetry between 0 and 1 V *versus* RHE in a 0.1 M NaClO$_4$ solution containing 6.6 mM DAT to obtain Cu|DAT. Notably, oxidation of copper occurs above 0.5 V thus the scan rate was adjusted to 250 mV/s to reduce the corrosion time of the copper disk per cycle. The amount of scans was increased to 75 to maintain the same total modification time of 10 minutes. Figure B.21 shows the ORR activity studied with RRDE experiments of Cu|DAT compared to PG|**Cu(DAT)**. Cu|DAT was studied at both pH 5.2 and pH 13. In both cases, the CV of the disk differs significantly from PG|**Cu(DAT)**. Also, the shape of the CV of Cu|DAT stabilized after repetitive CV cycling. Figure B.22 shows a comparison of the ORR activity of Cu|DAT as compared to an unmodified copper disk electrode. At pH 5.2, the shape of the CV of Cu|DAT is more similar to copper than to PG|**Cu(DAT)** (Figure B.21). However, the surface modification did lead to some differences in the CV of the disk. Furthermore, some ring current can be
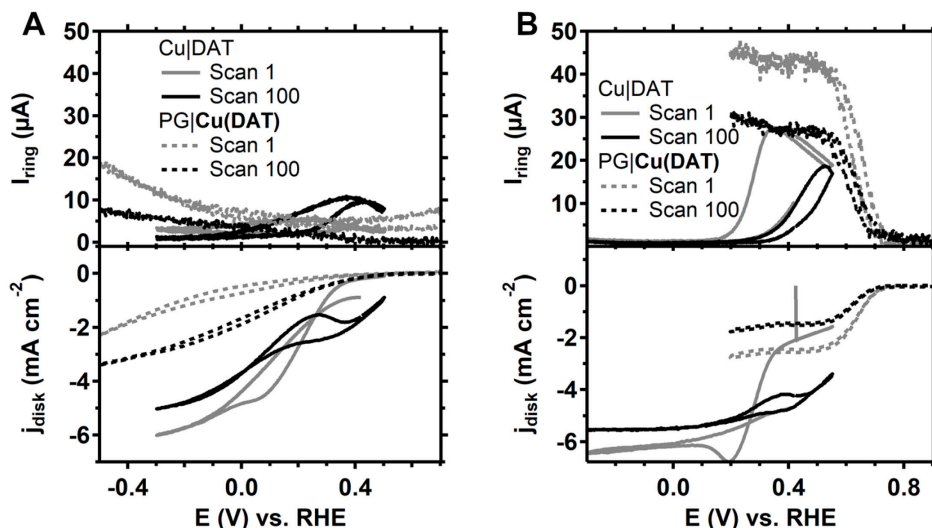
Figure B.21. RRDE experiment of Cu|DAT in an oxygen-saturated electrolyte (solid line). Cu|DAT was studied in both 0.03 M MES in 0.1 M NaClO$_4$ at pH 5.2 (A) and 0.1 M NaOH at pH 13 (B). For comparison, the results of PG|**Cu(DAT)** (Figure 3.4) are depicted as well (dotted lines). Current densities are given for the disk as the surface from Cu|DAT (0.196 cm²) is different from PG|**Cu(DAT)** (0.12 cm²). The CV was taken at a 100 mV/s scan rate while the disk was rotated at 2000 RPM.

observed for Cu|DAT whereas unmodified copper does not show any ring current. At pH 13 the shape of the last CV of Cu|DAT and unmodified copper are more comparable than at pH 5.2.

Possibly, the modified layer of Cu|DAT is quickly stripped off during the ORR experiments, because the shape of the CV of Cu|DAT resembles the CV of unmodified copper. Therefore, the ORR activity of unmodified copper was also studied in electrolytes containing 6.6 mM DAT at pH 5.2 and pH 13 (Figure B.23) with RRDE. At both pH 5.2 and pH 13, the CV of the copper electrode did not change after repetitive potential cycling in contrast to the PG|**Cu(DAT)** electrode. Also, larger currents are observed in the case of the copper electrode. Experiments in combination with a ring could not be performed because DAT is oxidized above 0.9 V (Figure B.12). Moreover, the copper electrode is oxidized above 0.5 V thus limiting the potential window wherein CV was performed. Notably, the solution slowly developed a yellow color in the course of the ORR experiments that were performed at pH 13. Most likely, DAT is slowly disintegrated due to the combination of electrochemistry and high pH. A pH 13 solution containing DAT not subjected to electrochemical measurements remained colorless.
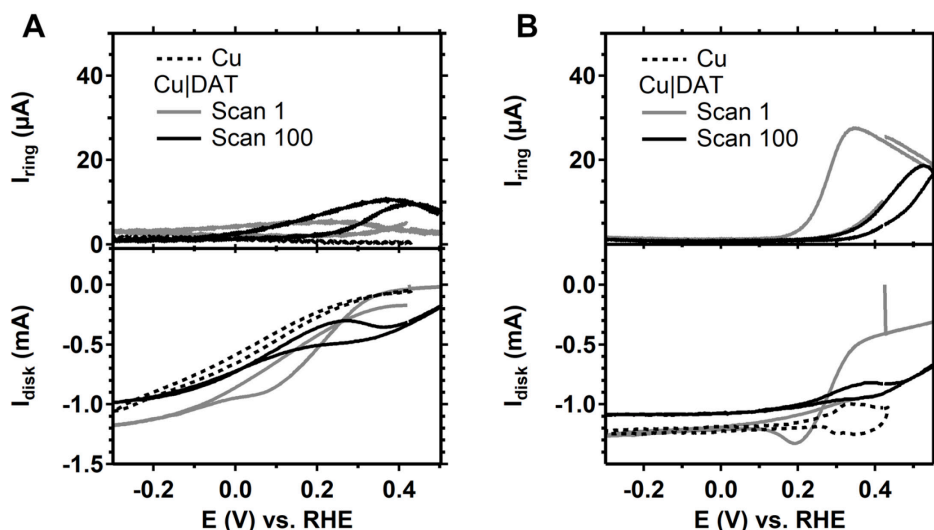
Figure B.22. RRDE experiment with unmodified Cu (black dotted lines) and modified Cu|DAT disk electrodes (solid lines) in an oxygen-saturated electrolyte. Both the electrodes were studied in a 0.03 M MES in 0.1 M NaClO$_4$ at pH 5.2 (A) and 0.1 M NaOH at pH 13 (B). The CV was taken at a 100 mV/s scan rate while the disk was rotated at 2000 RPM. In B the ring current during the CV of the unmodified Cu disk was not monitored.
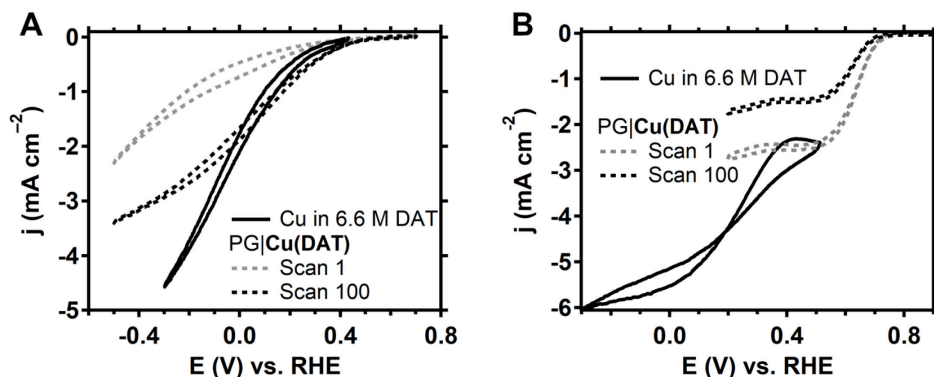
Figure B.23. Rotating disk electrode experiments of a copper electrode (0.196 cm²) in an oxygen-saturated electrolyte containing 6.6 mM DAT (black solid line). The copper electrode was studied in both 0.03 M MES in 0.1 M NaClO$_4$ at pH 5.2 (A) and 0.1 M NaOH at pH 13 (B). For comparison, the results obtained with PG|**Cu(DAT)** (Figure 3.4) are depicted as well (dotted lines). Current densities are given as the surface from PG|**Cu(DAT)** (0.12 cm²) is different from the copper electrode (0.196 cm²). The CV was taken at a 100 mV/s scan rate while the disk was rotated at 2000 RPM.

B.11 RRDE and XPS experiments of Vulcan|Cu(DAT)

Vulcan|**Cu(DAT)** was prepared according to the reported procedure[14] from DAT and $CuSO_4 \cdot 5H_2O$ (≥99.995% trace metal basis, Sigma Aldrich) by mixing 1.00 g Vulcan XC-72R (Cabot) with 0.200 g $CuSO_4 \cdot 5H_2O$ (99.995%, Sigma Aldrich) in 20 ml water and sonicating the mixture for 2 hours to obtain a viscous suspension. Next, a solution of 0.159 g DAT in 10 ml water was added dropwise to the stirred suspension. After addition of DAT, the mixture was left stirring for an additional 20 hours. Subsequently, the black solids were collected through filtration. The remaining black paste was further dried in a vacuum oven at 90 °C for 3.5 hours. Following, the brittle solid was pulverized with pestle and mortar to obtain Vulcan|**Cu(DAT)** which was further analyzed by XPS (Figure B.24 and B.25).
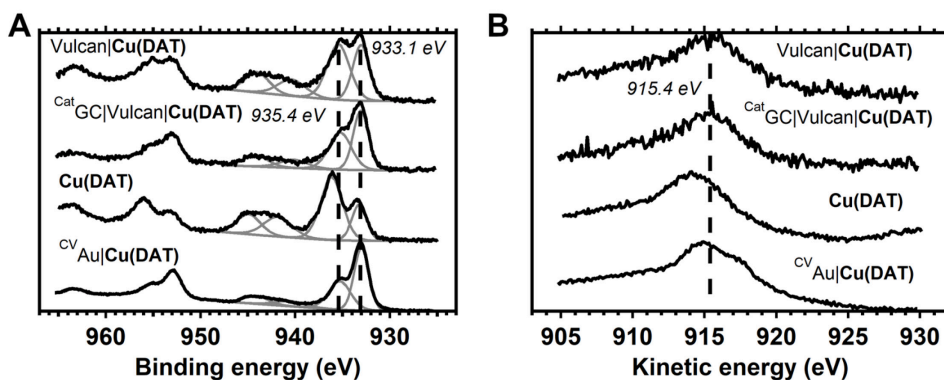
Figure B.24. XPS spectra (black lines) of the modified electrodes ^{CV}Au|**Cu(DAT)** and ^{Cat}GC|Vulcan|**Cu(DAT)** and the reference compounds Vulcan|**Cu(DAT)** and **Cu(DAT)**. In grey, the deconvolution of the $Cu2p_{3/2}$ region is depicted. A shows the Cu 2p region of the spectra and B shows the Cu $L_3M_{4,5}M_{4,5}$ Auger spectra.

A GC disk electrode (0.196 cm²) was modified by dropcasting Vulcan|**Cu(DAT)** on the electrode as previously reported.[14] The onset for oxygen reduction with GC|Vulcan|**Cu(DAT)** was found to correspond to the reported onset (Figure B.26).[14] In addition, GC|Vulcan|**Cu(DAT)** was tested under the same conditions as PG|**Cu(DAT)** in a pH 5 MES buffer (Figure B.27). GC|Vulcan|**Cu(DAT)** is clearly more active and seems to achieve limiting currents within the potential window. The 100th scan is displayed for both modified electrodes. For PG|**Cu(DAT)**, the 100th scan corresponds to the most active scan. For GC|Vulcan|**Cu(DAT)**, a minimal decrease in activity is observed over the course of 100 scans. These results indicate that the substrate plays an a very important role in the oxygen reduction activity.
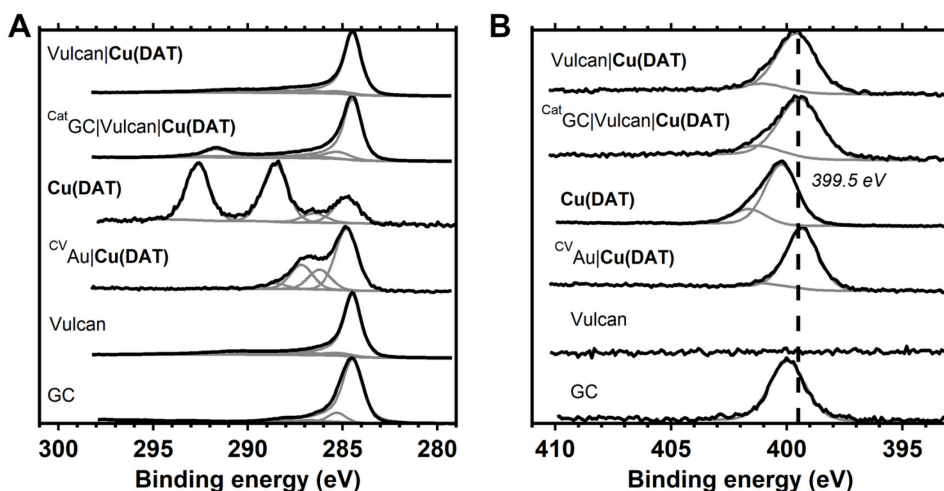
Figure B.25. C 1s (A) and N 1s (B) XPS spectra (black lines) of the modified electrodes ^{CV}Au|**Cu(DAT)** and ^{Cat}GC|Vulcan|**Cu(DAT)** and the reference compounds **Cu(DAT)** and Vulcan|**Cu(DAT)** as well as bare GC and Vulcan. In grey, the deconvolution is depicted.
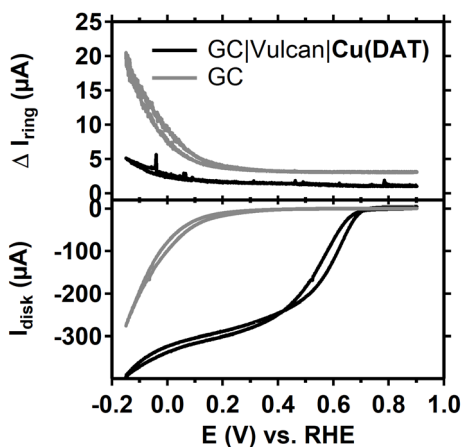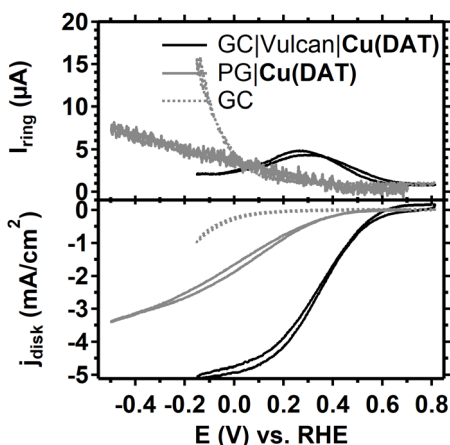
B

Figure B.26. RRDE experiment of GC|Vulcan|**Cu(DAT)** disk in an oxygen-saturated pH 7 Britton-Robinson buffer in 0.1 M $NaClO_4$. The solid black lines depict the disk (bottom graph) and ring (top graph) current responses. The grey solid lines depict the current response when a freshly polished GC disk was used. The CV was performed at a 5 mV/s scan ate while the ring was set to 1.2 V and the disk rotated at 1600 rpm.

Figure B.27. RRDE experiment of GC|Vulcan|**Cu(DAT)** disk (0.196 cm²) in an oxygen-saturated pH 5.2 MES buffer in 0.1 M NaClO₄. The solid black lines depict the disk (bottom graph) and ring (top graph) current responses of the 100th scan. The grey dotted lines correspond to a freshly polished GC disk. The grey solid lines belong to the 100th scan of a PG|**Cu(DAT)** disk (0.12 cm². The CV was performed at a 100 mV/s scan ate while the ring was set to 1.2 V and the disk rotated at 2000 rpm.

Another GC electrode (0.07 cm²) was modified by dropcasting Vulcan|**Cu(DAT)**. With this electrode (CatGC|Vulcan|**Cu(DAT)**), 103 CV cycles between 0.9 and 0 V at a 100 mV/s scan rate were performed in an oxygen purged pH 7 Britton-Robinson buffer in 0.1 M NaClO₄. After performing oxygen reduction, the electrode was rinsed with water and dried under a soft stream of air. XPS measurements were performed to analyze the composition of CatGC|Vulcan|**Cu(DAT)** after catalysis (Figures B.24 and B.25). Within the Cu 2p region both CatGC|Vulcan|**Cu(DAT)** and Vulcan|**Cu(DAT)** show similarities with CVAu|**Cu(DAT)** and CAAu|**Cu(DAT)**. Copper species with Cu 2p$_{3/2}$ binding energies of 933.1 and 935 eV are observed for all samples (Figure B.24A). Also, the Auger parameter in the Cu L$_3$M$_{4,5}$M$_{4,5}$ spectrum has a kinetic energy of 915.4 eV for all species (Figure B.24B). Two species are observed in the N 1s region for both Vulcan|**Cu(DAT)** and CatGC|Vulcan|**Cu(DAT)** with BEs of 399.5 eV and 401.2 eV (Figure B.25B). The (unpolished) GC electrode also contains a N 1s species, but this is different from Vulcan|**Cu(DAT)** species. Most importantly, the reference **Cu(DAT)** powder was found to differ from Vulcan|**Cu(DAT)** implying that the complex **Cu(DAT)** is not present in Vulcan|**Cu(DAT)** when it is prepared according to the literature procedure.[14] This is further supported by the (too) low nitrogen to copper ratio (Table 3.1). Moreover, the C 1s region is very different from **Cu(DAT)** and CVAu|**Cu(DAT)** (Figure B.25A). This is due to the use of Vulcan and GC which

B

are both carbon based materials and thus their strong signals overlap all other signals. Here, the most important species for both Vulcan|**Cu(DAT)** and ^{Cat}GC|Vulcan|**Cu(DAT)** is the graphitic sp^2 carbon with a BE of 284.5 eV. The carbon species with a BE of 291.6 eV in ^{Cat}GC|Vulcan|**Cu(DAT)** might correspond to the π-π* transition shake-up of graphite and does not correspond to **Cu(DAT)**. Also, the carbon composition is different compared to ^{cv}Au|**Cu(DAT)**.

The negligible change of the copper composition between Vulcan|**Cu(DAT)** and ^{Cat}GC|Vulcan|**Cu(DAT)** and the large resemblance with ^{CV}Au|**Cu(DAT)** indicate that most of the catalytic active sites of Vulcan|**Cu(DAT)** have not performed ORR due the diffusion limitation of oxygen. Figure B.28 shows the corresponding CV response. Clearly, most of the oxygen near the catalytic surface has been reduced in only the first scan as the following scans show a far lower current response. Purging the electrolyte after scan 3 with O$_2$ for a brief moment did lead to a slight increase of ORR current in the first following scan.
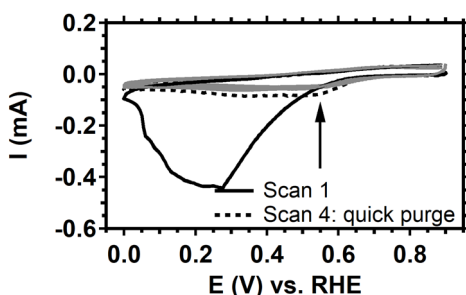
Figure B.28. ORR response of ^{Cat}GC|Vulcan|**Cu(DAT)** that was analyzed by XPS hereafter. CV was performed between 0.9 and 0 V for 103 cycles with a scan rate of 100 mV/s in a pH 7 Britton-Robinson buffer in 0.1 M NaClO$_4$. After scan 3, the potential cycling was halted to re-purge the electrolyte with O$_2$ before continuing the potential cycling.

B.12   References

1.   Antolini, L.; Fabretti, A. C.; Gatteschi, D.; Giusti, A.; Sessoli, R., *Inorg. Chem.* **1991**, *30*, 4858–4860.
2.   Fabretti, A. C., *J. Crystallogr. Spectrosc. Res.* **1992**, *22*, 523–526.
3.   Kröger, G. F.; Freiberg, W., *Z. Chem.* **1965**, *5*, 381–382.
4.   Zhang, T.; Wang, C.; Liu, S.; Wang, J.-L.; Lin, W., *J. Am. Chem. Soc.* **2014**, *136*, 273–281.
5.   Gomez, V.; Benet-Buchholz, J.; Martin, E.; Galan-Mascaros, J. R., *Eur. J. Inorg. Chem.* **2014**, *2014*, 3125–3132.
6.   Boland, Y.; Tinant, B.; Safin, D. A.; Marchand-Brynaert, J.; Clerac, R.; Garcia, Y., *CrystEngComm* **2012**, *14*, 8153–8155.
7.   Good, N. E.; Winget, G. D.; Winter, W.; Connolly, T. N.; Izawa, S.; Singh, R. M. M., *Biochemistry* **1966**, *5*, 467–477.
8.   Kandegedara, A.; Rorabacher, D. B., *Anal. Chem.* **1999**, *71*, 3140–3144.
9.   Mash, H. E.; Chin, Y.-P.; Sigg, L.; Hari, R.; Xue, H., *Anal. Chem.* **2003**, *75*, 671–677.
10. van der Ham, C. J. M.; Işık, F.; Verhoeven, T. W. G. M.; Niemantsverdriet, J. W.; Hetterscheid, D. G. H., *Catal. Today* **2017**, *290*, 33–38.

B

11.	Buttry, D. A.; Ward, M. D., *Chem. Rev.* **1992,** *92*, 1355–1379.

12.	Bard, A. J.; Faulkner, L. R., *Electrochemical Methods: Fundamentals and Applications*. Wiley: New York, 2000.

13.	Boulatov, R.; Collman, J. P.; Shiryaeva, I. M.; Sunderland, C. J., *J. Am. Chem. Soc.* **2002,** *124*, 11923–11935.

14.	Thorum, M. S.; Yadav, J.; Gewirth, A. A., *Angew. Chem. Int. Ed.* **2009,** *48*, 165–167.

B

Appendix C

<u>Supplementary information for Chapter 4:</u>
A selective molecular dinuclear copper oxygen
reduction catalyst for the electrochemical synthesis
of H_2O_2 at neutral pH

C.1   UV-vis of Cu₂(btmpa) and H₂O₂
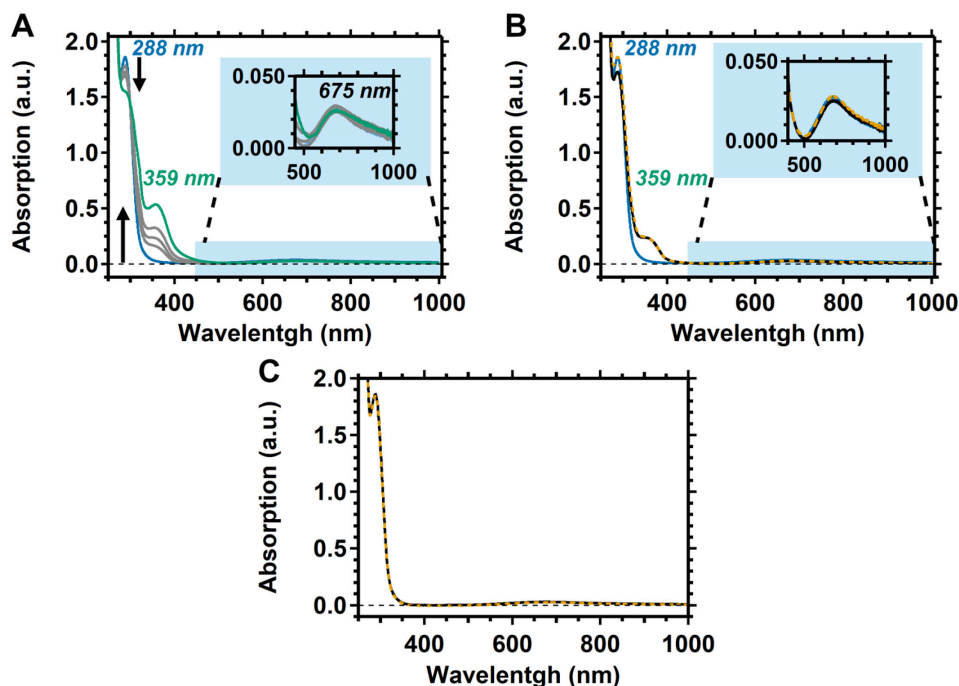
Figure C.1. UV-Vis of 0.15 mM **Cu₂(btmpa)** in phosphate buffer. A fresh solution (blue trace) spiked with 1.13 mM H₂O₂ was monitored over the course of a week (green trace) (A). B shows a fresh and 8 hour old solution (blue and black trace, respectively) with H₂O₂ and an 8 hour old **Cu₂(btmpa)** solution after performing O₂ reduction at 0.0 V (orange dashed). A fresh (black) and 1 week old solution of **Cu₂(btmpa)** (orange dashed) without H₂O₂ is shown in C.

C.2   EPR and SQUID of Cu₂(btmpa)

The electron paramagnetic resonance (EPR) spectra of **Cu₂(btmpa)** were measured in water, 0.1 M phosphate buffer and dimethyl formamide (Figure C.2). In water and phosphate buffer, broad peaks were observed and two g values could be extracted from the simulation: $g_{||}$ = 2.21 and $g_{\perp}$ = 2.08 for water and $g_{||}$ = 2.23, $g_{\perp}$ = 2.06 for phosphate buffer though the latter simulation was less accurate. The spectra and g values are very similar but minor discrepancies suggest that phosphate coordination slightly changes the geometry around the copper cores though pH effects are not excluded. In dimethyl formamide, a clear splitting pattern arising from coupling to the copper core was observed. The g values of dimethyl formamide are $g_{||}$ = 2.23 (A_{Cu} = 500 Hz) and $g_{\perp}$ = 2.06, equal to the phosphate buffer sample.

This might indicate that both dimethyl formamide and phosphate have a similar influence on the geometry. Because $g_{||} > g_{\perp}$, the single occupied molecular orbital (SOMO) is the $d_{x^2-y^2}$ orbital since there is significant orbital mixing in the z-direction ($g_{||} = g_z$). This is the case in, for example, an elongated (distorted octahedron).[1] Hence, the geometry of **Cu₂(btmpa)** in aqueous and dimethyl formamide solutions is in close resemblance to the previously published crystal structures.[2] The obtained g tensors are clearly different from the mononuclear **Cu(tmpa)** complex ($g_{||}$ = 2.00, $g_{\perp}$ = 2.19) indicating a significant difference in geometry.[3] In the case of **Cu(tmpa)**, $g_{||} < g_{\perp}$, pointing to d_{z^2} as SOMO and a trigonal bipyramidal geometry of the complex.[1] Overall, it seems that both copper centra of **Cu₂(btmpa)** can be seen as independent and produce the same EPR signal. There is no antiferromagnetic coupling as was also observed with SQUID (superconducting quantum interference device, Figure C.3). Interestingly, the g value for both copper centra was found to be 1.85 from the powder SQUID spectra which indicates that they are identical but have a lower value than determined from the frozen solution EPR spectra. It has to be noted that g values from EPR are
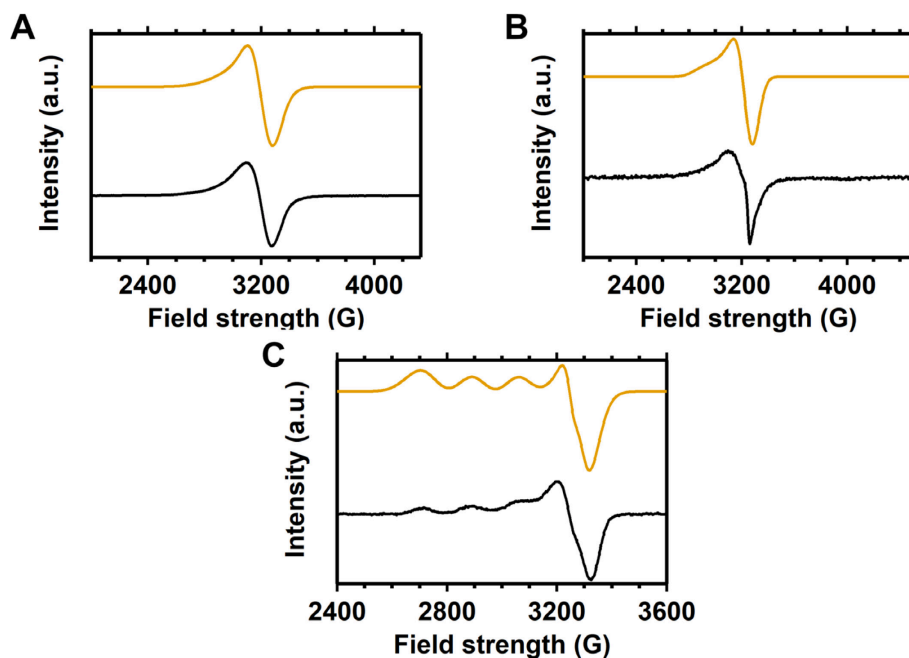
Figure C.2. EPR spectra (black lines) of 0.6 mM **Cu₂(btmpa)** in water (A, 9.342 GHz), phosphate buffer (B, 9.344 GHz) and dimethyl formamide (C, 9.352 GHz). The simulated spectra are shown in orange. Spectra were obtained at 77 K with frozen solutions.

generally more accurate than g values obtained from fitted SQUID data. From the SQUID data it can also be concluded that there is a small ferromagnetic coupling between the two copper centra of 34 cm⁻¹. From the data, no conclusive evidence for the coordination of the copper centra with respect to each other can be given. On the other hand, the coupling does indicate that the two copper centra have a minor influence on each other.
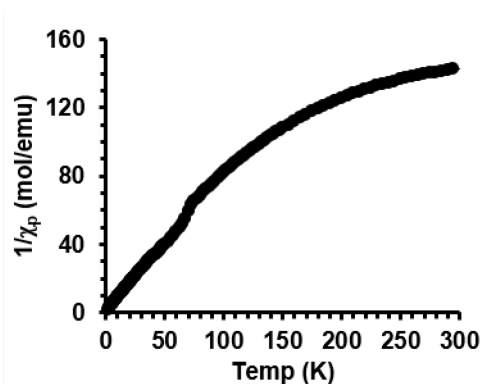

Figure C.3. SQUID spectrum of **Cu₂(btmpa)** powder.

C.3   The collection efficiency of H₂O₂ of Pt

For reliable rotating ring disk electrode (RRDE) measurements, the collection efficiency has to be stable throughout the measurement. That way, the percentage of H₂O₂ and the electron transfer number (n) can be determined using equations C.1 and C.2 respectively where $N_{H_2O_2}$ is the collection efficiency for H₂O₂. Usually, this collection efficiency can be determined with a one-electron redox couple such as the [Fe^{II}CN₆]⁴⁻/[Fe^{III}CN₆]³⁻ and equation C.3 where N_{CE} is the collection efficiency. However, H₂O₂ oxidation on Pt is not always diffusion limited. As a result, the H₂O₂ collection efficiency ($N_{H_2O_2}$) can be different from the N_{CE} determined with the Fe$^{II/III}$ redox couple.[4] Phosphate buffer and PtO$_x$ formation at 1.2 V can significantly influence the amount of active sites thereby changing the potential where diffusion limited H₂O₂ oxidation is obtained on a Pt ring.[5-11] To study what factors influence $N_{H_2O_2}$, several chronoamperometry measurements were performed with the RRDE setup using a GC disk as work electrode in O₂ purged 0.1 M phosphate buffer of pH 7. The GC electrode is a 100% selective catalyst at moderate potentials in the freshly polished state.[12]

$$\%H_2O_2 = \frac{2 \times (\frac{i_{ring}}{N_{H_2O_2}})}{i_{disk} + (\frac{i_{ring}}{N_{H_2O_2}})} \times 100\%$$ **Eqn. C.1**

$$n = \frac{4 \times i_{disk}}{i_{disk} + (\frac{i_{ring}}{N_{H_2O_2}})}$$ **Eqn. C.2**

$$N_{CE} = \frac{|i_{ring}|}{|i_{disk}|}$$ **Eqn. C.3**

To start, we studied the influence of the disk potential (Figure C.4). The ring and disk currents were stable at disk potentials (0.1, 0.0, and −0.1 V) where low current is obtained (Figure C.4A). The corresponding collection efficiencies are lower than the theoretical value of 24% for this specific setup (Figure C.4B). The maximum collection efficiency can be achieved by not only mechanically polishing the Pt ring, but also electropolishing the ring to remove any poisoning substances from the Pt
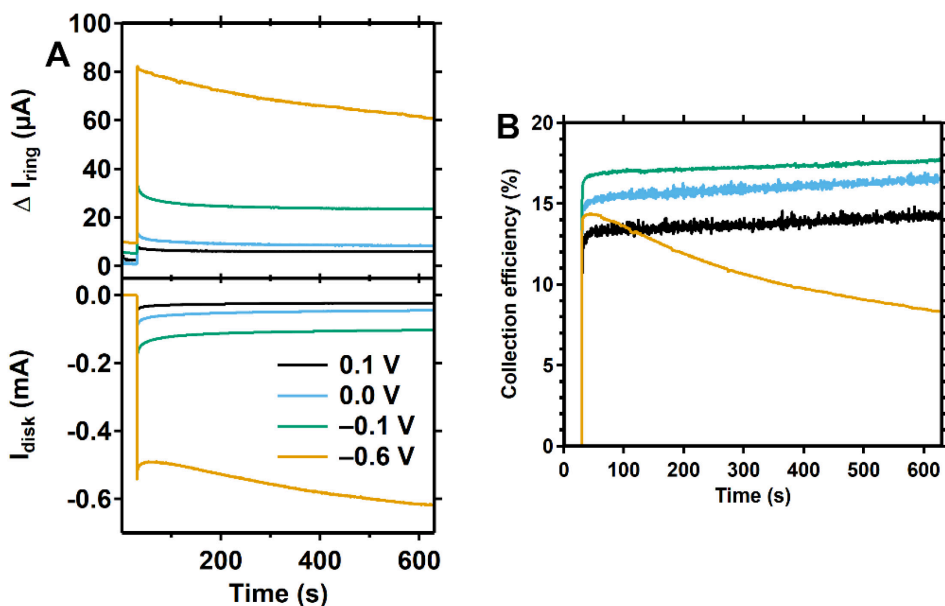
Figure C.4. RRDE Chronoamperometry of O_2 reduction by a GC disk at various potentials (A, bottom panel), the response of the Pt ring (A, top panel), and the calculated collection efficiency of the ring for H_2O_2 (B). The ring was kept at 1.2 V. The disk was rotated at 1600 rpm. All electrodes were polished before the measurement. O_2 purged 0.1 M phosphate buffer of pH 7 was used.

surface. However, we found that such a clean Pt surface is very susceptible for (re-)poisoning and therefore the collection efficiency will drop quickly over the course of the experiment. When merely mechanical polish is applied, the collection efficiency shows a minor incline over the course of the 10 minute experiment (Figure C.4B) and is therefore more useful. Nevertheless, only a low amount of H_2O_2 is produced at these potentials since the disk current is low. The disk produces up to 6 times more current at -0.6 V. Interestingly, the disk current increases over the course of 10 minutes whereas the ring current decreases at that potential. As the ratio ring to disk current decreases rapidly, the calculated collection efficiency (Figure C.4B) decreases from 14 to 8% over the course of 10 minutes at -0.6 V disk potential. Two explanations are possible. First, the selectivity of O_2 to H_2O_2 might not be 100% at this potential but instead an increasing part of the current might be attributed to the over-reduction of H_2O_2 to H_2O. The second explanation is that the Pt ring surface is affected by H_2O_2 and therefore less able to oxidize H_2O_2.

To study whether the Pt surface is affected by H_2O_2, we performed two RRDE amperometry measurements at 0.0 V for 10 minutes. First, a freshly polished GC and Pt ring were used (Figure C.5). After the first 0.0 V measurement, amperometry at -0.6 V was performed for 10 minutes in order to expose the Pt ring to a large amount of H_2O_2. Finally, another 0.0 V amperogram was recorded for 10 minutes. The disk current at 0.0 V for the last measurement is lower than it the freshly polished state, but more stable at -45 μA. The current of the freshly polished GC decreases to circa -50 μA after 10 minutes. On the other hand, the ring current has significantly dropped from circa 10 μA to 5 μA in the 0.0 V measurement after the -0.6 V measurement. Moreover, the ring to disk ratio, and consequently the calculated collection efficiency, drops significantly over the 10 minute experiment from 15 to 9%. In conclusion, the Pt ring is somehow affected and cannot consistently oxidize H_2O_2 after being exposed to larger amounts of H_2O_2. Indeed, earlier reports have shown that H_2O_2 inhibits H_2O_2 oxidation by Pt at high (>1 mM) H_2O_2 concentration as the process is a mix of diffusion and kinetical parameters.[13] Therefore, the application of RRDE for the detection of H_2O_2 remains limited to situations where a low amount of H_2O_2 is produced and/or a qualitative one where only the detection is important. Quantification of H_2O_2 in situations with larger amounts of H_2O_2 is limited under these conditions.
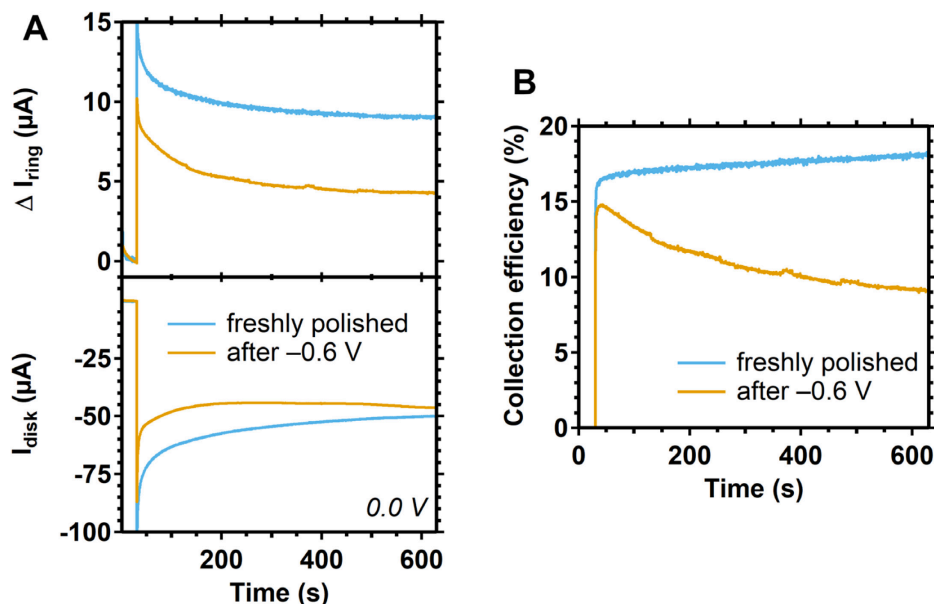
Figure C.5. RRDE chronoamperometry of O_2 reduction at 0.0 V for 10 minutes (A, bottom panel), the Pt ring response (A, top panel) with a freshly polished GC an Pt ring (blue) and after an experiment that produced high amounts of H_2O_2 (orange). The corresponding calculated collection efficiencies (or ring to disk ratios) are shown in B. Prior to the yellow measurement, an amperogram at −0.6 V was recorded for 10 minutes. The ring was kept at 1.2 V. The same conditions as in Figure C.4 were used.

C.4 Electrochemical H_2O_2 reduction by Cu_2(btmpa)

Over-reduction of H_2O_2 to H_2O is a possibility that could lower the H_2O_2 selectivity. Therefore, H_2O_2 reduction by **Cu_2(btmpa)** under argon atmosphere was studied by CV (Figure C.6). The reduction of different concentrations of H_2O_2 was studied under rotating and non-rotating conditions. Indeed, there is reducing current observed indicating that H_2O_2 is reduced by the complex. A positive order in H_2O_2 is expected for the rate determining step because the reducing current increases with the H_2O_2 concentration. Interestingly, no peak current under non-rotating and no diffusion limited current under rotating conditions could be obtained even at high concentrations of H_2O_2. Only at 1.2 mM, a peak current and limiting current seem to be reached. However, these disk currents of 50 μA are low and not close to 200 μA which is the diffusion limited current for H_2O_2 reduction under these conditions.[4] Overall, the reduction of H_2O_2 by **Cu_2(btmpa)** is a slow, kinetically limited reaction. Therefore, O_2 reduction to H_2O_2 by **Cu_2(btmpa)** can

reach a high selectivity in this potential window. However, this selectivity may decrease significantly when the concentration of H_2O_2 rises during long experiments.
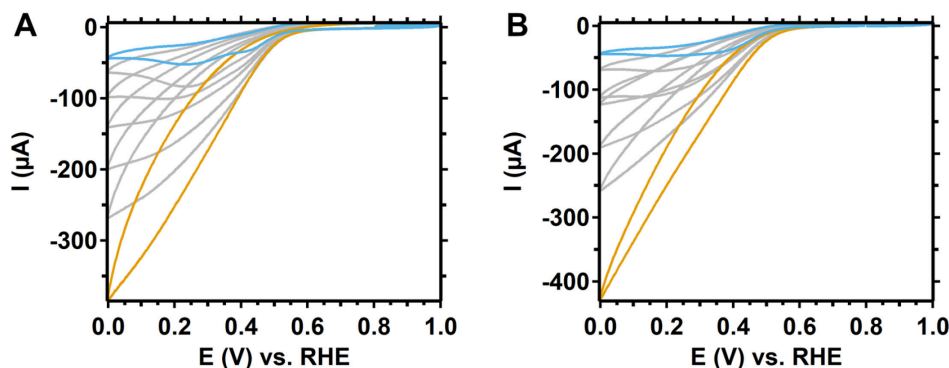

Figure C.6. Cyclic voltammograms of H_2O_2 reduction by 0.15 mM **Cu₂(btmpa)** under argon atmosphere with a non-rotating (A) and rotating (B, 1600 rpm) GC electrode (0.196 cm²). H_2O_2 concentrations of 1.2 (blue), 2.1, 4.2, 8.4, 14.1, 25.2, and 47.4 mM (orange) were tested in 0.1 M phosphate buffer of pH 7. Scan rates of 100 mV/s (A) and 50 mV/s (B) were used.

C.5   Cu⁰ deposit on electrode

After 7 hours of continuously applying 0.0 V in a **Cu₂(btmpa)** solution, a clear copper-colored deposit will form (Figure C.8). Frequent intervals at 0.8 V might help to strip this deposit. However, there is an additional process already from the start of the measurement: during the first half hour of amperometry at 0.0 V a significant increase in current is observed. Moreover, in the first 2 hours of amperometry with 0.8 V intervals, the magnitude of the current at the end of each cycle is regained at the start of the next cycle after the interval (Figure 4.5). Apparently, the deposit causing this increase in current cannot be simply removed by applying 0.8 V. On the other hand. an electrode that was held in a **Cu₂(btmpa)** solution only for the first half hour and subsequently rinsed with water did not retain its activity. When this electrode was put in catalyst-free electrolyte after rinsing to compare the activity with a polished GC electrode, the current drops significantly to −0.08 mA and is equal the current of the polished GC (Figure C.7). This in in contrast to what happens when the electrode stays in catalyst solution (Figure 4.5). In that case, the current remains −0.37 mA even after briefly applying a potential of 0.8 V. The rinsing of the electrode is the extra step that removed most of the deposit on the electrode. When the rinsed electrode was tested for an additional 5 hours, the current steadily increased to −0.27 mA. It did not reach the level of an electrode that permanently resides in a **Cu₂(btmpa)** solution (−0.83 mA) but it did follow a
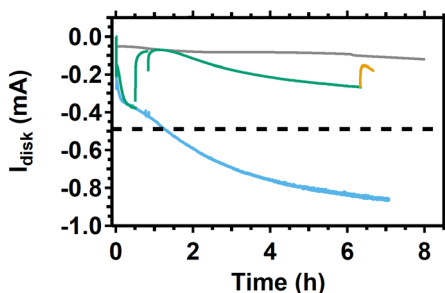
Figure C.7. Rotating (1600 rpm) disk electrode experiment at 0.0 V of a glassy carbon electrode in O$_2$ saturated electrolyte in absence (grey) or in presence (blue) of **Cu$_2$(btmpa)**. The green trace was in presence of **Cu$_2$(btmpa)** for 30 minutes after which the electrode was rinsed and tested in a catalyst-free electrolyte. The orange trace is a 20 minute measurement recorded after the electrode (green trace) was briefly held at 0.8 V. 0.1 M phosphate buffer of pH 7 was used. Catalyst concentration was 0.15 mM.

similar current profile. Also, the polished GC does not show this behavior (Figure C.7). These results seem to point to a small residue of **Cu$_2$(btmpa)** still residing on the electrode even after the rinse. Although the EQCM data show that the potential-dependent adsorption is reversible on gold electrodes, the carbon based GC electrode might have a stronger affinity with **Cu$_2$(btmpa)**. Especially in the first half hour of amperometry, catalyst accumulation on the electrode enhances the number of active sites. At 0 V, **Cu$_2$(btmpa)** is still significantly kinetically limited. In this case, an increase in active sites would indeed increase the catalytic current. The 0.8 V intervals do not lead to significant desorption of **Cu$_2$(btmpa)** perhaps aided by the continuous supply of fresh catalyst by the rotation of the electrode. Rinsing with water on the other hand, did remove most catalyst. The small residue that would still be present was then subjected to 0.0 V for 5 hours. In that time window, this residue can form Cu^0 which explains why the current steadily
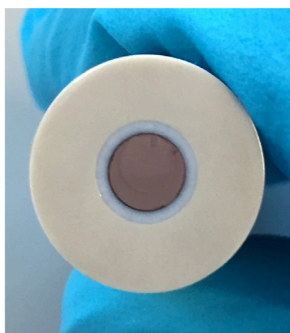

Figure C.8. Picture of the copper-colored deposit on a GC electrode after 7 hours of amperometry at 0.0 V in presence of **Cu$_2$(btmpa)**.

increases more than that of a polished GC (Figure C.7). Indeed, after applying a short 0.8 V interval, the current significantly decreased to −0.15 mA which indicated the stripping of Cu^o (Figure C.7).

C.6 Intercepting H_2O_2 during long term chronoamperometry

To study long term H_2O_2 production with a rotating ring disk electrode setup, we performed amperometry at 0.0 V in 20 minute intervals for a period of 8.5 hours. In the 10 second intervals, potentials of 0.55 V applied at the Pt ring to reduce accumulated PtO_x and 0.8 V at the disk to strip Cu^o were applied. Additionally, a 30 second baseline measurement was included in the interval procedure after 3 hours by holding the 0.8 V potential at the disk while setting the ring to 1.2 V. Consequently, no H_2O_2 is produced at the disk and only H_2O_2 that is already present in the solution is detected at the Pt ring. The results of this measurement are shown in Figure C.9 including the schematic overview of the measurement procedure. With the additional ring data, it is clear that H_2O_2 is formed at the disk. When the
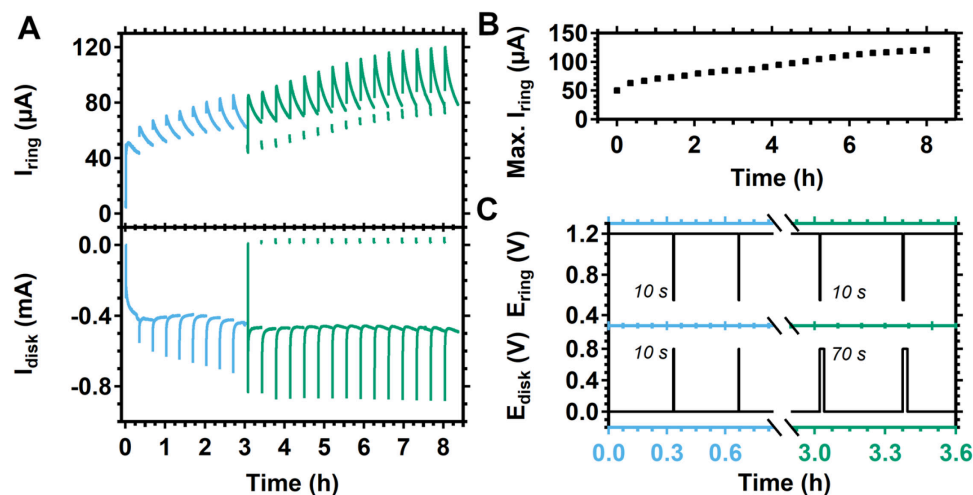
Figure C.9. RRDE chronoamperometry measurement of O_2 reduction at 0.0 V by **Cu₂(btmpa)** over the course of 8.5 hours with an interval every 20 minutes (A) with the disk (bottom) and ring current (top). The maximum ring current reached every 20 minutes is depicted in B and the potential *versus* time plot in C for the blue and green marked areas of A. During the short interval (10 seconds), accumulated PtO_x on the ring could be reduced and Cu^o on the disk could be stripped by a potential of 0.55 V and 0.8 V, respectively. After 3 hours, the disk potential was kept at 0.8 while the ring was set to 1.2 V for 1 minute to establish a baseline ring current.

measurement starts, the ring current immediately rises to 50 µA which (with a pre-determined N_{CE} of 18.3% for this measurement) corresponds to a 91% selectivity for H_2O_2. However, the ring current decreases to 45 µA and the selectivity drops to 72% over the course of 20 minutes. Every 20 minute cycle, the maximum of the ring current was reached in the first minute of the measurement after which the current decreased. As discussed before, the ring current can also decrease because of PtO_x formation and/or exposure to high amounts of H_2O_2. Indeed, the ring current increased to 65 µA after the first interval wherein the potential of the ring was briefly set to 0.55 V demonstrating that the decrease in ring current is mostly caused by these events and not (entirely) by a decrease in selectivity of H_2O_2 production. This was found to be the case for every 20 minute measurement. From that, we conclude that H_2O_2 is produced throughout the measurement with a high selectivity. Remarkably, 100% H_2O_2 production should only lead to a maximum current of 60 µA at the ring. Already in the second 20 minute cycle the maximum ring current is 65 µA. This indicates that H_2O_2 from the solution is oxidized as well. The maximum ring current increased every 20 minute cycle (Figure C.9B) which is expected if H_2O_2 is accumulating in the solution. Hence, a baseline measurement was added to the interval procedure after 3 hours to establish the ring current before H_2O_2 is produced at the disk. The baseline current after 3 hours was 50 µA and increased over time to circa 80 µA showing that H_2O_2 is accumulating in the solution. Interestingly, the disk current hardly increases and remains stable after 3 hours. Moreover, the increase during each 20 minute cycle is not less pronounced as was found in measurements without the Pt ring electrode (Figures 4.5 and C.10). Most likely, the continuous re-oxidation of a part of the formed H_2O_2 and the H_2O_2 from the solution will limit the concentration of H_2O_2 in the solution. In turn, this would indicate that high H_2O_2 concentrations would lead to faster Cu^0 deposition and more over-reduction of H_2O_2 thereby increasing the current rapidly during each 20 minute cycle.

C.7 The influence of interval measurements on the Faradaic efficiency

As described, Cu^0 deposition can become a problem and negatively affect the Faradaic efficiency. Two experiments were performed to check whether an interval measurement would increase the Faradaic efficiency by briefly applying a potential of 0.8 V every 20 minutes. The results are plotted in Figure C.10. Notably, the Faradaic efficiency decreases over time in both the continuous as well as the interval
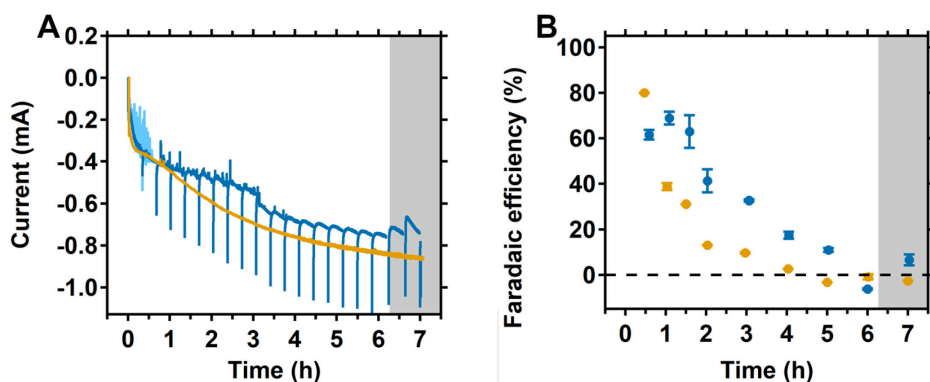
Figure C.10. Rotating disk measurement at 0.0 V of O_2 reduction by **Cu$_2$(btmpa)** over the course of 7 hours (A) and the corresponding Faradaic efficiency (B). Each datapoint is the efficiency of the period since the preceding datapoint. A continuous measurement (orange) and an interval measurement (blue) were monitored. A potential of 0.8 V was briefly applied during the intervals. The spikes are an artefact of (re-)applying 0.0 V. In the grey area, the 0.8 V interval time was extended to 4 minutes. The same conditions as Figure 4.5 were used.

measurement. The efficiency of the continuous measurement is lower than the interval measurement, apart from the first 30 minutes. In these first 30 minutes, the Faradaic efficiency for H_2O_2 is high: 80% for the continuous and 62% for the interval-experiment. The lower Faradaic efficiency for the interval experiment could be explained from the high current noise in these 30 minutes. The measurement
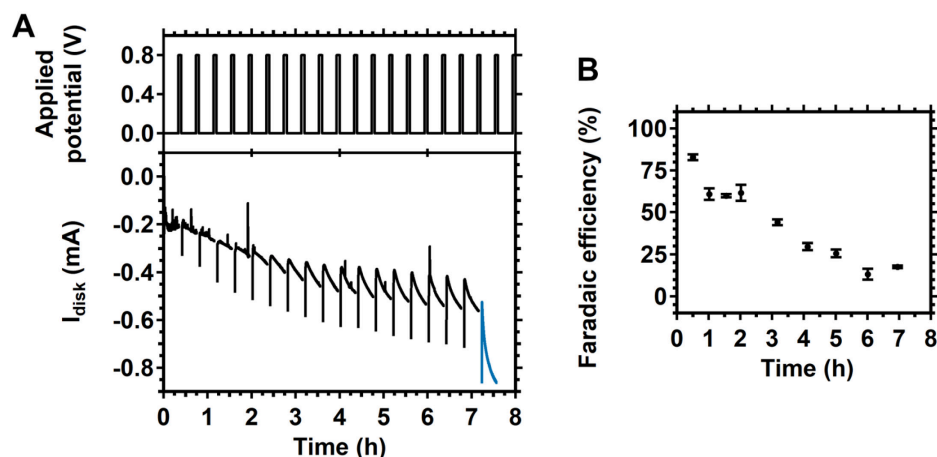
Figure C.11. Rotating disk measurement at 0.0 V of O_2 reduction by **Cu$_2$(btmpa)** (A) and the corresponding Faradaic efficiency (B). The full 8 hours of the measurement of Figure 4.6 is depicted. Before the last 20 minutes (blue line in A), the H_2O_2 concentration was manually increased 5 times.

suffered from O_2 bubbles blocking the surface during continuous purging which resulted in current spikes and a higher overall charge that passed the electrode. After 30 minutes, the set-up of the disk electrode was slightly changed to overcome this problem. As a result, the Faradaic efficiency increased to 69% in the next 30 minutes. This in sharp contrast to the continuous experiment. There, the efficiency dropped to 39%. 1.5 hours after the start, it dropped even further to 31% while the interval measurement still had an efficiency of 63%. Clearly, the 0.8 V interval could strip away Cu^o thereby keeping the Faradaic efficiency high. This is also reflected in the disk current which was lower for the interval experiment than for the continuous experiment. The latter used more charge for the full 4 electron reduction to water. Nonetheless, the Faradaic efficiency dropped significantly for the interval experiment as well after 2 hours. After 6 hours, the calculated efficiency was negative because there had been a decrease in the H_2O_2 bulk concentration. This happened for the continuous measurement already after 5 hours. When the calculated selectivity is negative, more H_2O_2 is converted to H_2O than that H_2O_2 is produced from O_2. For the continuous experiment this was expected because of the slow build-up of Cu^o, but not for the interval experiment. The 30 second 0.8 V interval was apparently not enough to strip all the formed Cu^o. Therefore, the interval time was increased to 4 minutes after 6 hours of amperometry (marked by the grey area in Figure C.10). As a result, the Faradaic efficiency went back to a positive value of 6%

Table C.1. The concentration of H_2O_2 as measured by the enzyme based photometric method for Figure C.11. The volume of the solution changed continuously during the measurement as aliquots were taken. Errors are as standard errors.

Hours after start	Faradaic efficiency[a] (%)	Concentration H_2O_2 (mM)	Volume of electrolyte (ml)
00:30	83 ± 2 (3)	0.040 ± 0.001	33.6
01:01	61 ± 3 (3)	0.077 ± 0.003	32.0
01:33	60 ± 1 (3)	0.124 ± 0.001	30.7
02:01	62 ± 5 (3)	0.166 ± 0.006	29.2
03:10	44 ± 2 (3)	0.273 ± 0.007	27.6
04:07	30 ± 2 (4)	0.340 ± 0.009	26.2
05:01	26 ± 3 (4)	0.41 ± 0.01	24.9
06:01	13 ± 3 (5)	0.45 ± 0.02	23.4
06:57	18 ± 1 (3)	0.503 ±0.005	21.9

[a]The Faradaic efficiency corresponds to the period between measurements, not the total Faradaic efficiency since the start of the measurement. Number between brackets is the amount of measurements that was performed.

and the disk current decreased. The bulk H_2O_2 concentration went up from 15.6 to 16.7 mg/l which is 0.5 mM of H_2O_2. Overall, these experiments show that Cu^0 deposition affects the Faradaic efficiency but this can be counteracted by applying a potential at which Cu^0 will strip from time to time.
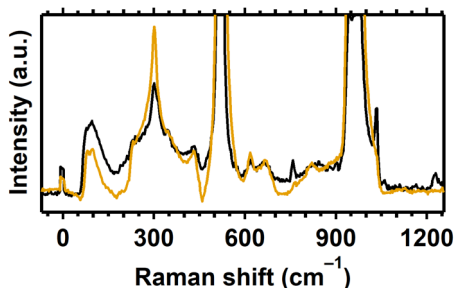
C.8   Raman of Cu₂(btmpa) and H₂O₂

Figure C.12. Raman spectra of a dropcasted solution of 3 mM **Cu₂(btmpa)** (fresh, black) and of a **Cu₂(btmpa)** solution with 22 mM H_2O_2 (orange, 9 days old). The solutions were dropcasted on a silicon wafer.

C.9   References

1.   Garribba, E.; Micera, G., *J. Chem. Educ.* **2006,** *83*, 1229.
2.   Lee, D.-H.; Murthy, N. N.; Karlin, K. D., *Inorg. Chem.* **1997,** *36*, 5785–5792.
3.   Karlin, K. D.; Hayes, J. C.; Juen, S.; Hutchinson, J. P.; Zubieta, J., *Inorg. Chem.* **1982,** *21*, 4106–4108.
4.   Langerman, M.; Hetterscheid, D. G. H., *Angew. Chem. Int. Ed.* **2019,** *58*, 12974–12978.
5.   Ross, P. N.; Andricacos, P. C., *J. Electroanal. Chem. Interfacial Electrochem.* **1983,** *154*, 205–215.
6.   Zhang, Y.; Wilson, G. S., *J. Electroanal. Chem.* **1993,** *345*, 253–271.
7.   Hall, S. B.; Khudaish, E. A.; Hart, A. L., *Electrochim. Acta* **1999,** *44*, 4573–4582.
8.   Hall, S. B.; Khudaish, E. A.; Hart, A. L., *Electrochim. Acta* **2000,** *45*, 3573–3579.
9.   Evans, S. A. G.; Elliott, J. M.; Andrews, L. M.; Bartlett, P. N.; Doyle, P. J.; Denuault, G., *Anal. Chem.* **2002,** *74*, 1322–1326.
10.   Katsounaros, I.; Schneider, W. B.; Meier, J. C.; Benedikt, U.; Biedermann, P. U.; Auer, A. A.; Mayrhofer, K. J. J., *Phys. Chem. Chem. Phys.* **2012,** *14*, 7384–7391.
11.   Jiang, K.; Back, S.; Akey, A. J.; Xia, C.; Hu, Y.; Liang, W.; Schaak, D.; Stavitski, E.; Nørskov, J. K.; Siahrostami, S.; Wang, H., *Nat. Commun.* **2019,** *10*, 3997.
12.   Song, C.; Zhang, J., Electrocatalytic Oxygen Reduction Reaction. In *PEM Fuel Cell Electrocatalysts and Catalyst Layers: Fundamentals and Applications*, Zhang, J., Ed. Springer London: London, 2008; pp 89–134.
13.   Hall, S. B.; Khudaish, E. A.; Hart, A. L., *Electrochim. Acta* **1998,** *43*, 579–588.

Appendix D

<u>Supplementary information for Chapter 5:</u>
Mechanistic insight from structure–activity studies in the electrochemical oxygen reduction by substituted tris(2-pyridylmethyl)amine copper complexes

D.1 Electrochemistry of 3^{NO_2}

The nitro complex **3^{NO_2}** is, on paper, a very interesting complex since the nitro group has the highest Hammett parameter of all substituents studied here.[2] This high electron withdrawing effect would shift the redox couple significantly and perhaps influence the rate of O_2 reduction. Under argon atmosphere and the same conditions as the other complexes, a sharp reduction starting at 0.4 V was observed with a peak current that was *circa* one order of magnitude higher than expected for a Cu$^{I/II}$ redox couple (Figure D.1). Moreover, no corresponding oxidation was observed. On the other hand, a redox feature at 0.8 V appeared after having scanned below 0.4 V. This feature slowly fades when a narrow potential region was scanned (Figure D.1). The linear relationship between the E$_{1/2}$ and the Hammett parameter that was found for the other complexes (Figure 5.2) would predict a E$_{1/2}$ at circa 0.35 V for **3^{NO_2}**. For this reason, and in combination with the fact that the 0.8 V redox couple is not visible in the first scan, we conclude that the redox feature at 0.8 V does not correspond to the Cu$^{I/II}$ redox couple of the **3^{NO_2}** complex. It has been reported that 4-nitropyridine can electrochemically be reduced to a hydroxylamine with a total of 6 electrons.[3] Reduction to NH$_2$ is not expected as the CV's of **3^{NH_2}** (Figure 5.1) and **3^{NO_2}** do not match. However, the formed reduced pyridines might be redox active[3] and have some (quasi-)reversible feature that might be linked to the high redox feature at 0.8 V. The redox chemistry of **3^{NO_2}** is interesting, but disturbs a good assessment of any catalytic properties since the bulk electrolyte will always contain unreacted **3^{NO_2}**.

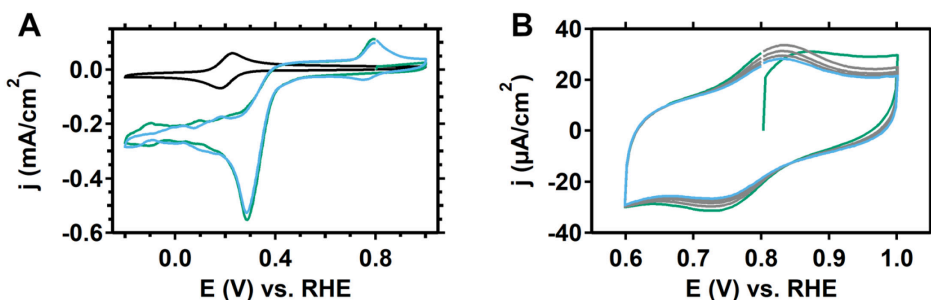**Figure D.1.** Cyclic voltammogram under argon atmosphere of **3^{NO_2}** (green: 1st and blue: 2nd scan) with **1** (black) for comparison (A). B shows 5 scans of the 0.8 V feature of **3^{NO_2}** after the CV in A was recorded (green first and blue last scan). Different size electrodes were used (0.07 cm^2 for **1** and 0.196 cm^2 for **3^{NO_2}**. The wobbly current response of the first scan in A is due to turbulence created by purging the electrolyte with argon. Data of **1** was adapted from reference 1.

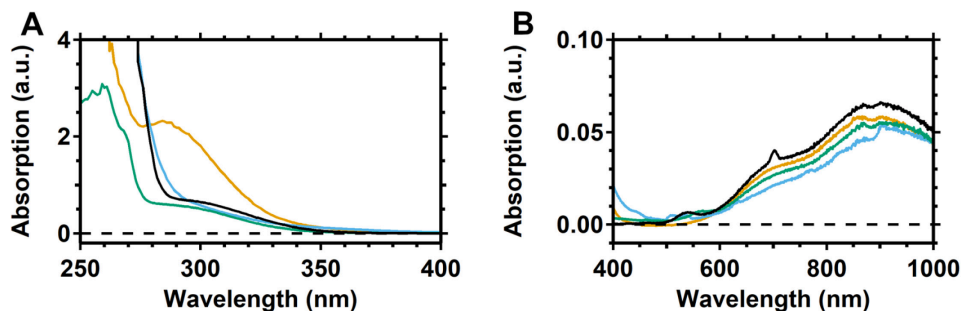## D.2 UV-vis of 2^{Cl}, 2^{CF3}, 3^{NO2}, and 3^{NH2}

Figure D.2. UV-vis spectra of 3^{NH2} (blue), 3^{NO2} (orange), 2^{Cl} (green), and 2^{CF3} (black) of 0.3 mM solutions of these complexes in 0.1 M phosphate buffer of pH 7.

D.3 Deposition by 3^{NH2}

The complex 3^{NH2} could not be purified by crystallization and small remnants of the copper salt Cu(OTf)$_2$ or other impurities may be present in the electrolyte after the *in-situ* formation of the complex. These impurities lead to extra oxidation and reduction peaks in the cyclic voltammograms (Figure D.3) that become visible at low scan rates under argon atmosphere. When the potential was scanned down to −0.2 V, extra oxidative peaks, that grow in current with each consecutive scan, became visible at circa 0.45, 0.55 and 0.70 V (Figure D.3A). In addition, a small reductive peak at 0.4 V was visible after the first scan. In a following scan where the potential was not scanned below 0.0 V, the oxidative peaks disappeared except for the peak at 0.55 V. In addition, the reductive peak at 0.40 V remained. The oxidative peaks are most likely stripping peaks belonging to a Cu^0 deposit that is formed below 0.0 V.

During O$_2$ and H$_2$O$_2$ reduction by 3^{NH2}, a broad oxidative feature can be observed (Figure D.3B and D.3C). In addition, after prolonged scanning the O$_2$ reduction under rotating conditions at potentials as low as −0.6 V revealed two different reductive peaks at 0.4 and 0.5 V. Interestingly, these peaks are accompanied by a spike in ring current as well. On the forward scan to lower potentials, the spike in the ring current is at 0.5 V whereas it can be found at 0.55 V at the backward going scan. This reduction cannot be related to deposit formation since the formed species passes the ring so it must be in solution. It is not known to what species these reductive peaks belong to. However, these peaks only show after prolonged scanning at potentials below −0.6 V, so it is expected that these species do not interfere in the first scan of a CV, especially not in the forward going scan to lower

potentials. The deposition process does take place and affects the CV. However, scanning not lower than 0.0 V will minimize the influence.
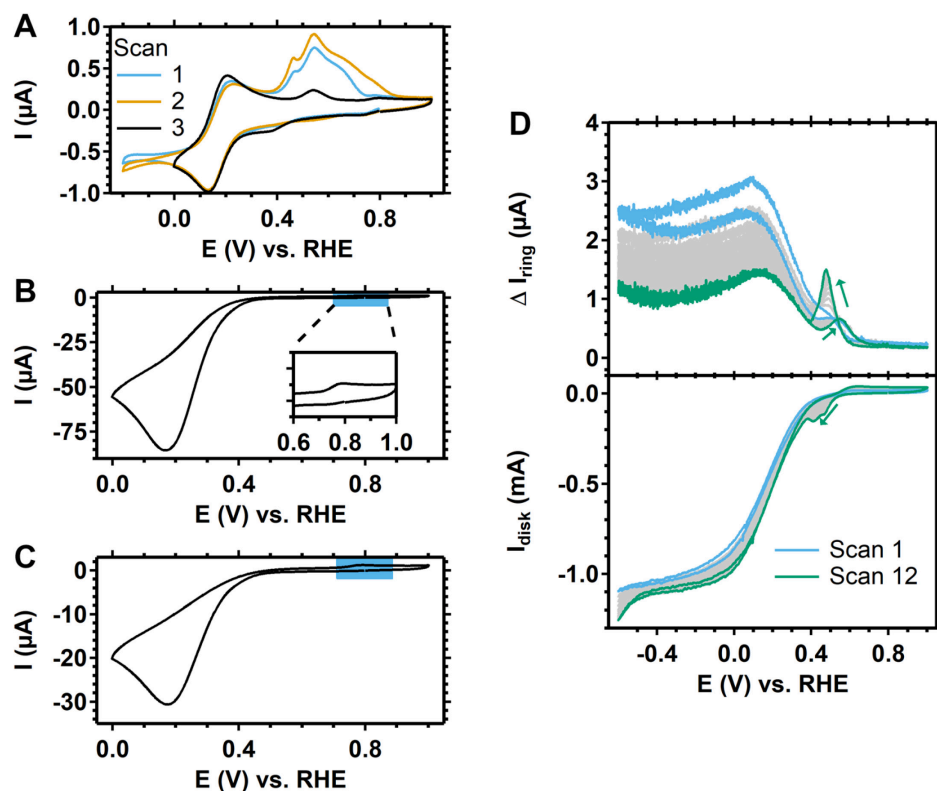

Figure D.3. (A) CVs of 3^{NH2} under argon atmosphere for which the lower potential of the potential window of the third CV scan was narrowed from −0.2 V to 0.0 V. (B) CV of 3^{NH2} in the presence of O_2. (C) CV of 3^{NH2} in the presence of H_2O_2 under argon atmosphere. (D) CVs of 3^{NH2} with a RRDE setup in O_2 atmosphere with the disk current in the bottom and the ring current in the top panel. The ring potential was 1.2 V throughout the measurement. All CVs were recorded with 0.3 mM catalyst concentration in 0.1 M phosphate buffer of pH 7. Scan rates were 10 (A), 50 (D), and 100 mV/s (B and C).

D.4 Laviron plots of 2^{Cl}, 2^{CF3}, and 3^{NH2}
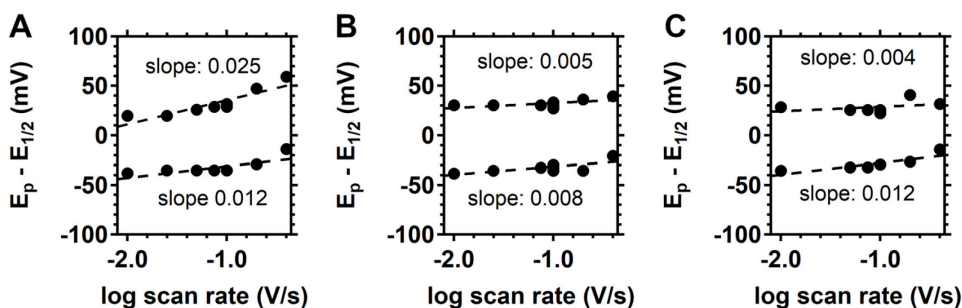
Figure D.4. Laviron plots of the cathodic and anodic peak positions of 2^{Cl} (A), 2^{CF3} (B), 3^{NH2} (C), and the slopes of linear fits (dashed lines).

D.5 Experimental error in O$_2$ reduction

As with any experiment, there are experimental errors that lead to slight differences between measurements. Under non-rotating conditions, we found that the onset for O$_2$ reduction by the **1** and **2**^{Cl} complexes could differ by *circa* 50 to 75 mV (Figure D.5). This is higher than under rotating conditions (Figure D.6). To investigate whether any onset shifts would be an effect of rotating the electrode, the electrodes were rotated above and below rotation speeds that allow for a diffusion limited current.[4] When rotating too slowly, a peak current is visible. For **1**, varying the rotation speed did not lead to 50 − 75 mV onset potential shifts (Figure D.6) as was the case under non-rotating conditions (Figure D.5). However, the onset is at slightly lower potentials at lower rotation speeds. An explanation for the larger experimental error/onset shift under non-rotating (or very low speed rotating)
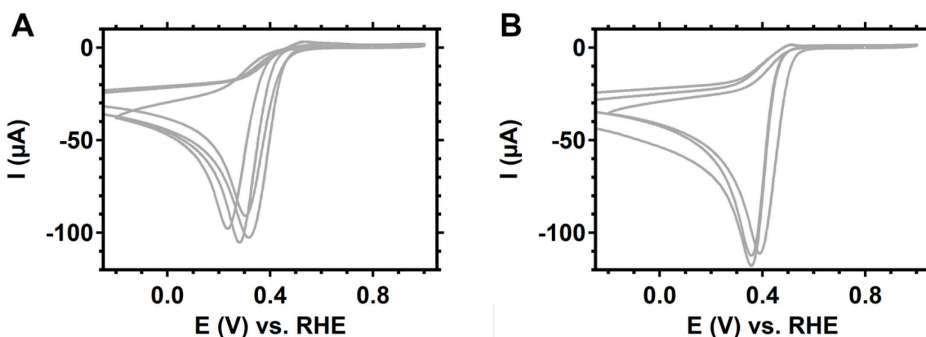

Figure D.5. The first scan of the CV of different experiments of O$_2$ reduction by **1** (A) and **2**^{Cl} (B) with a freshly polished GC electrode (0.07 cm^2) recorded at 100 mV/s in a 0.1 M phosphate buffer of pH 7.

conditions is that electrochemistry is highly dependent on diffusion and thus on turbulence caused by pre-experiment purging of O_2, electrode dipping or other reasons.[4] When rotating fast enough, the effects of turbulence are diminished.
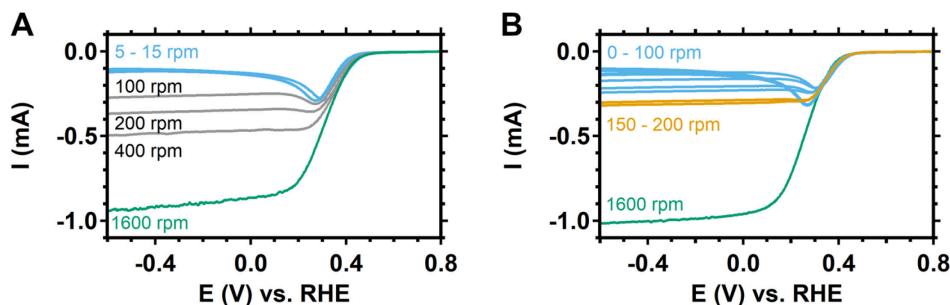

Figure D.6. LSV's of several measurements of O_2 reduction by **1** (A) and 2^{Cl} (B) with a freshly polished GC electrode (0.196cm²) recorded at 50 mV/s in a 0.1 M phosphate buffer of pH 7 at different rotation speeds.
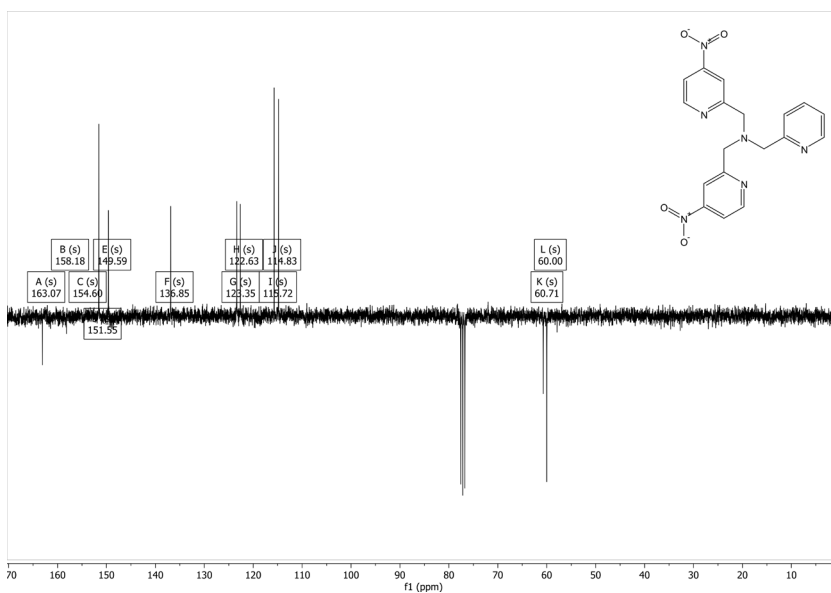
D.6   NMR spectra 6 and 7
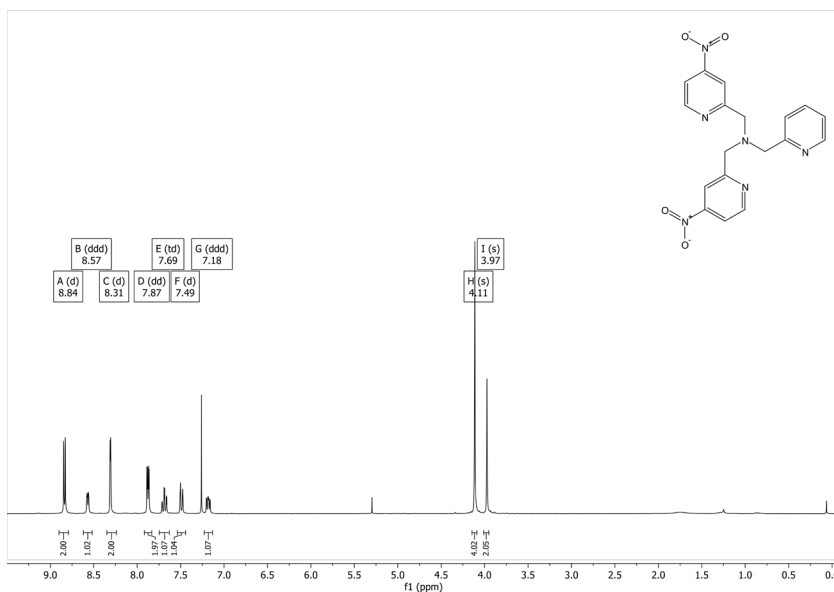
Figure D.7. ¹H NMR of **6** in CDCl$_3$ recorded at 300 MHz. Solvent residual peak (7.26 ppm) and DCM (5.30 ppm) are visible as well.

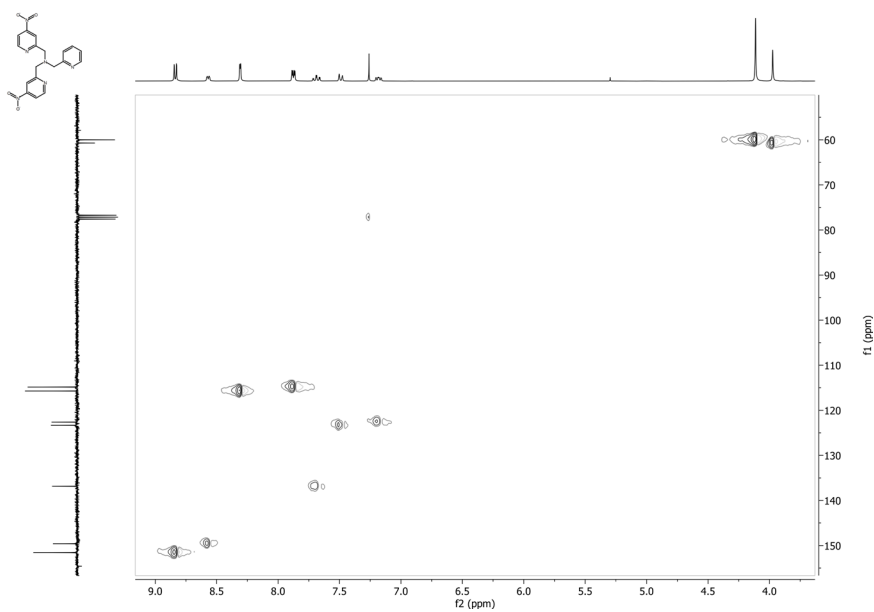**Figure D.8**. ^{13}C APT **6** in CDCl$_3$ recorded at 75 MHz. Solvent residual peak is found at 77.16 ppm.

Figure D.9. COSY of **6** in CDCl$_3$.
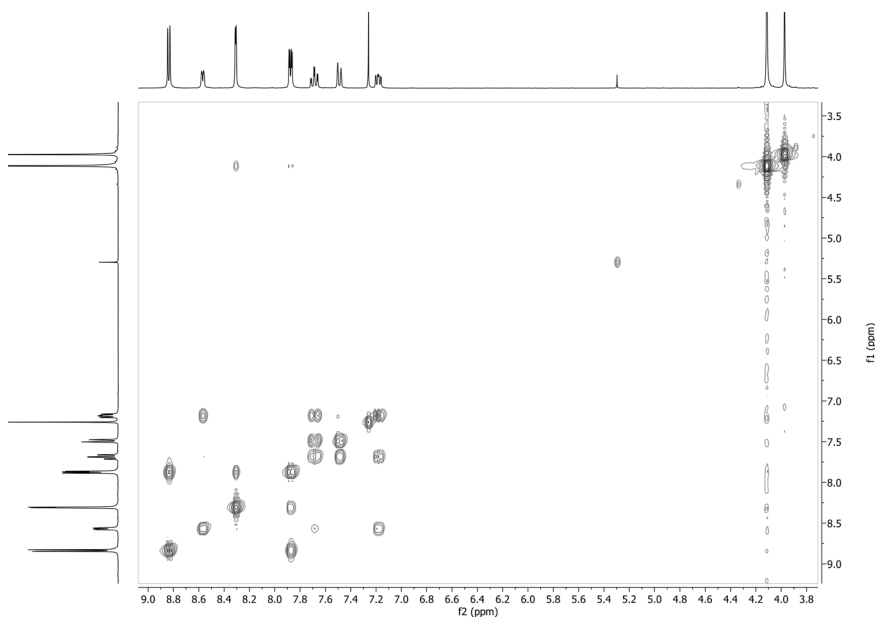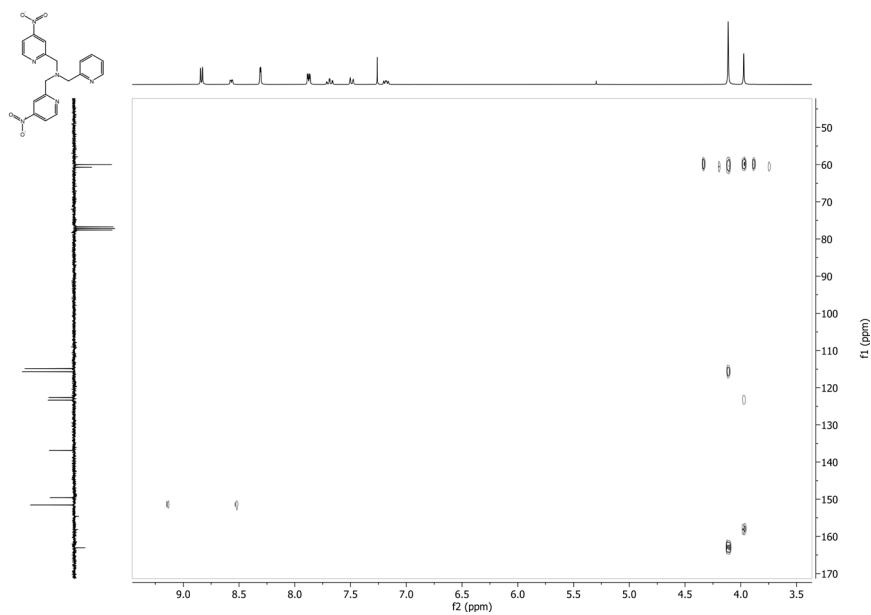
Figure D.10. HSQC of **6** in CDCl₃.
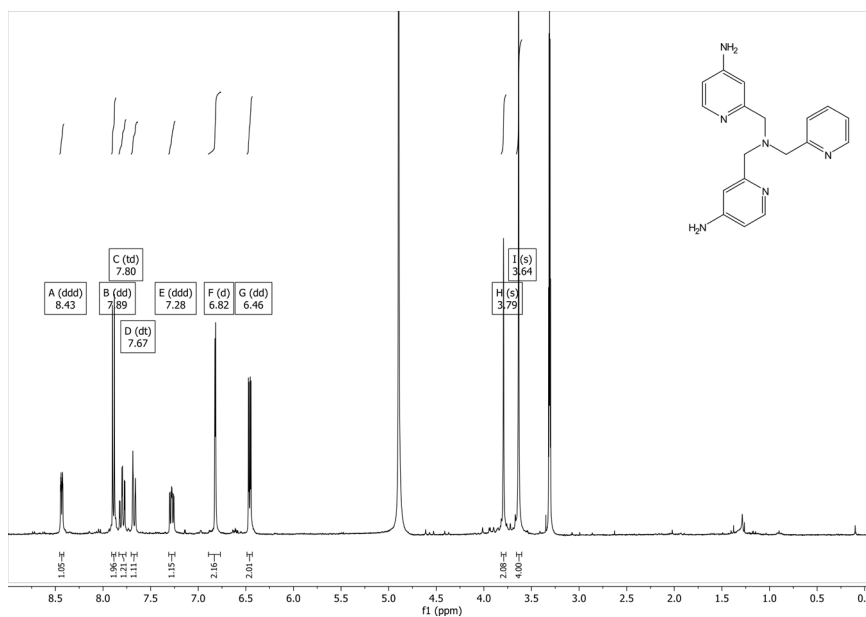

Figure D.11. HMBC of **6** in CDCl₃.

D

Figure D.12. ¹H NMR of **7** MeOD recorded at 300 MHz. Solvent residual peak (3.31 ppm) and H₂O (4.89 ppm) are visible as well.
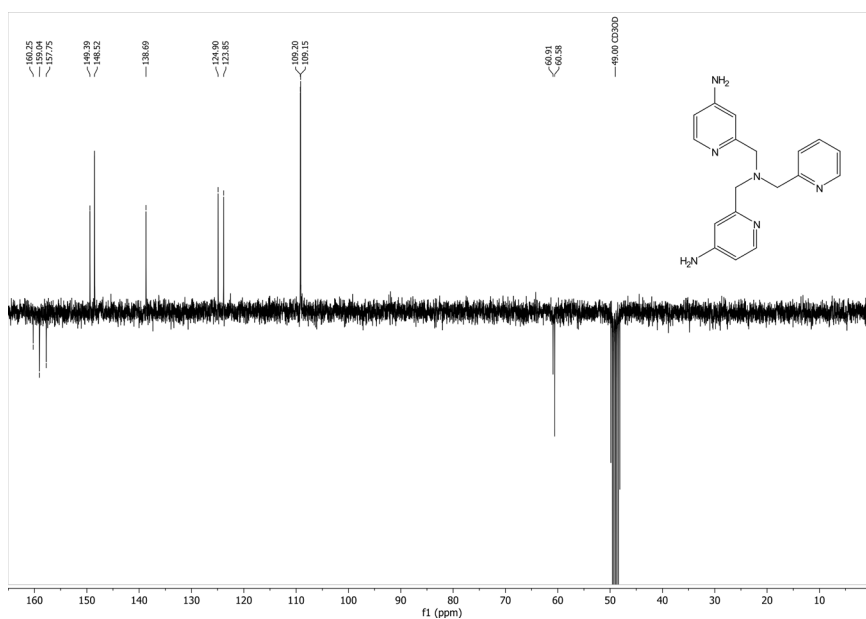

Figure D.13. ¹³C APT of **7** in MeOD recorded at 75 MHz. Solvent residual peak is found at 49 ppm.
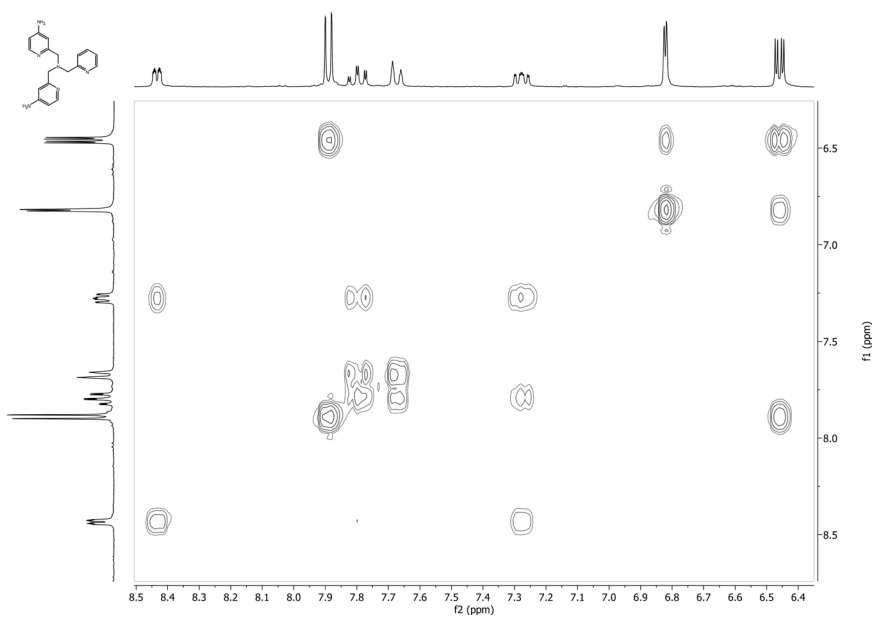
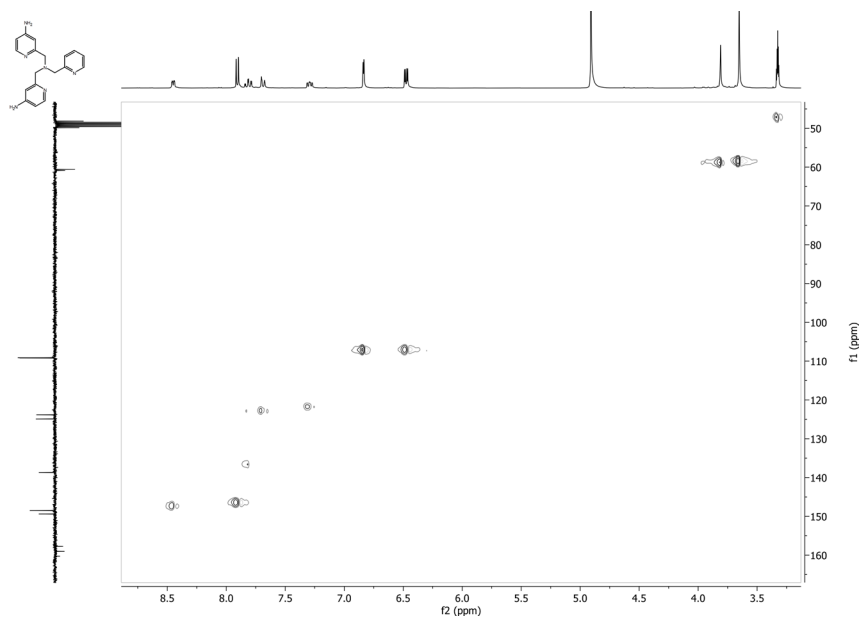**Figure D.14**.COSY of **7** in MeOD.

Figure D.15. HSQC of **7** in MeOD.
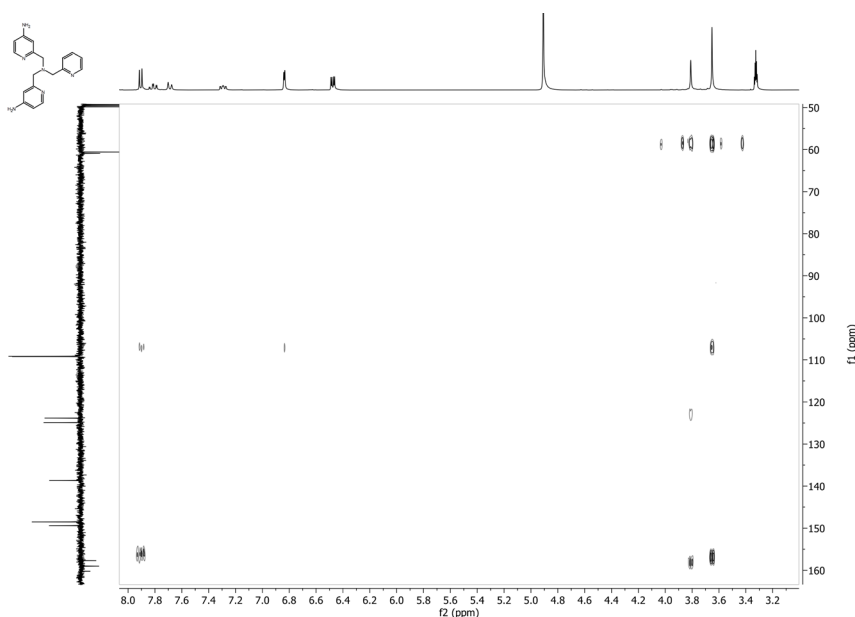
Figure D.16. HMBC of **7** in MeOD.

D.7   References

1.   Langerman, M.; Hetterscheid, D. G. H., *Angew. Chem. Int. Ed.* **2019,** *58*, 12974–12978.
2.   Hansch, C.; Leo, A.; Taft, R. W., *Chem. Rev.* **1991,** *91*, 165–195.
3.   Laviron, E.; Meunier-Prest, R.; Vallat, A.; Roullier, L.; Lacasse, R., *J. Electroanal. Chem.* **1992,** *341*, 227–255.
4.   Bard, A. J.; Faulkner, L. R., *Electrochemical Methods: Fundamentals and Applications*. Wiley: New York, 2000.

D

Samenvatting en conclusie

De rol en analyse van moleculaire systemen in elektrokatalyse

S.1 Samenvatting

De opslag van energie is een belangrijk onderdeel van het verduurzamen van onze energie-infrastructuur. De elektriciteit die opgewekt wordt door duurzame energiebronnen zoals wind- en zonne-energie, kan bijvoorbeeld worden opgeslagen met behulp van de elektrolyse van water in waterstof (H_2) en zuurstof (O_2). Waterelektrolyse kan echter nog niet alle processen vervangen die op dit moment fossiele brandstoffen gebruiken (zie hoofdstuk 1). De huidige technologie kan namelijk nog niet op de daarvoor benodigde schaalgrootte toegepast worden. De halfreactie waarmee H_2O omgezet wordt in O_2, en andersom, is de grootste oorzaak van het verlies van energie bij het produceren en het gebruik van H_2 als brandstof. Zelfs de beste katalysatoren halen alleen een hoge stroomdichtheid als deze ver van de evenwichtspotentiaal werken. Onderzoek naar moleculaire complexen voor deze elektrokatalytische reacties draagt bij aan het vinden van efficiëntere katalysatoren. Moleculaire complexen kunnen onder andere als modelsysteem dienen voor het katalytische centrum van enzymen. Het enzym laccase kan bijvoorbeeld O_2 reduceren naar H_2O dichtbij de evenwichtspotentiaal van 1.23 V doordat het enzym een katalytisch centrum met 3 koperatomen bevat. Enkele van de in dit proefschrift onderzochte kopercomplexen zijn daarom geïnspireerd op laccase. Daarnaast kunnen synthetische aanpassingen van het ligand de katalytische activiteit en/of selectiviteit van moleculaire complexen veranderen. Hiermee wordt inzicht in het katalytisch mechanisme verkregen om mogelijk de katalysator verder te verbeteren. Een nadeel van moleculaire complexen is dat deze gemakkelijk ontleden ten opzichte van heterogene katalysatoren. Vaak leiden een snelle liganduitwisseling en/of ligandafbraak door zeer reactieve tussenproducten tot de ontleding van de katalysator. De afbraak van het complex leidt in sommige gevallen tot de afzetting van metallische lagen of metaaloxides op de electrode. In dit proefschrift wordt de activiteit, selectiviteit en stabiliteit van moleculaire complexen daarom onderzocht met meerdere elektrochemische technieken in combinatie met allerlei andere karakterisatie technieken. Met name de combinatie van meerdere technieken is van belang om een zo goed mogelijk beeld te vormen en daardoor verkeerde interpretaties zo veel mogelijk te voorkomen (zie ook hoofdstuk 3). Snelheidsconstanten worden bijvoorbeeld bepaald met de *foot of the wave analysis* (FOWA) of de *current enhancement* methode. De FOWA analyseert de stroom aan het begin van de katalytische piek. De *current enhancement* methode gebruikt de verhouding tussen de maximale katalytische stroom en de maximale stroom van de reductie/oxidatie van de katalysator in afwezigheid van het substraat. De roterende

ring-schijf elektrode (RRDE) techniek wordt gebruikt om de selectiviteit van de reactie te bepalen. De O_2-reductiereactie leidt bijvoorbeeld tot H_2O of H_2O_2 als product. H_2O_2 kan vervolgens op de ringelektrode gedetecteerd worden om de productverhouding te bepalen. Andere technieken om kwantitatief de productdistributie te meten, zoals een titratie, completeren de RRDE-techniek. De stabiliteit van complexen wordt gemeten met een elektrochemische kwartskristal microbalans (EQCM). Met de EQCM-techniek wordt de mate van depositie van materiaal op de elektrode gemeten. De depositie wordt verder gekarakteriseerd met behulp van spectroscopische technieken zoals röntgenfoto-elektronenspectroscopie (XPS).

In hoofdstukken 2 en 3 worden moleculaire complexen besproken die degraderen tot een depositie op de elektrode. De depositie bleek de actieve katalysator voor, respectievelijk, wateroxidatie en zuurstofreductie. Daarnaast wordt besproken wat het effect van het ligand van het oorspronkelijke complex op de katalytische activiteit van de depositie is. In hoofdstukken 4 en 5 worden moleculaire kopercomplexen besproken die de zuurstofreductiereactie katalyseren. Het effect van synthetische aanpassingen van het ligand van deze complexen op de elektrokatalyse bleek te resulteren in een andere selectiviteit (Hoofdstuk 4) en/of een verschillende katalytische aanvangspotentiaal en activiteit (Hoofdstuk 5).

De beste katalysatoren voor het oxideren van water naar zuurstof zijn iridiumoxides. Deze katalysator wordt veel toegepast in de elektrolytische cellen, maar heeft een significante overpotentiaal nodig om voldoende stroom te genereren. Daarnaast is iridium zeer duur en schaars. Dit is de reden voor de interesse in de modificatie van liganden van moleculaire iridiumcomplexen die de efficiëntie van deze katalysatoren verhogen. Vele van deze studies gebruiken oxidatieve reagentia zoals $((NH_4)_2[Ce(NO_3)_6])$ en $NaIO_4$ zodat katalysatoren H_2O oxideren naar O_2. In een eerdere studie is wateroxidatie door enkele iridiumcomplexen met hydroxylpicolinaat en Cp* (pentamethylcyclopentadienyl) liganden bestudeerd met het gebruik van de eerdergenoemde reagentia. Ook bleek uit deze eerdere studie dat de zogeheten omzettingsfrequentie (TOF) een direct verband heeft met de aanwezigheid en locatie van een hydroxylgroep op het hydroxylpicolinaat ligand. In hoofdstuk 2 is de elektrochemische studie van de iridiumcomplexen met hydroxylpicolinaat liganden beschreven. Onderzoek met behulp van EQCM toonde aan dat deze complexen een depositie geven op de electrode en XPS werd gebruikt om deze depositie te karakteriseren. Daarnaast werden na een bulkelektrolyse-experiment met behulp van ^{1}H-kernspinresonantiespectroscopie (NMR) afbraakproducten gevonden in het elektrolyt die aantoonden dat het Cp*-ligand

S

degradeert onder katalytische condities. Ten eerste bleek dat de XPS-spectra van de deposities onderling slechts kleine verschillen hadden. De invloed van het ligand op de elektronische omgeving van het iridiumion bleek groter te zijn in het moleculaire complex dan in de depositie die het complex genereerde. Ten tweede bleek de wateroxidatieactiviteit van deze verschillende deposities onderling nauwelijks te verschillen. De structuur van het oorspronkelijke complex en de katalytische activiteit van de corresponderende depositie hadden onderling geen duidelijke relatie. Ten derde vormt het ligandloze $[Ir(OH)_6]^{2-}$ een depositie die wateroxidatiestromen van twee ordegroottes hoger produceert ten opzichte van alle geteste iridiumcomplexen met liganden. Deze observaties golden niet alleen voor de eerdergenoemde iridiumcomplexen met hydroxylpicolinaat liganden, maar ook voor enkele andere eerder bestudeerde iridiumcomplexen met en zonder het Cp*-ligand. Deze resultaten leidden tot de conclusie dat alle bestudeerde iridiumcomplexen ontleden tot een klein IrO_x cluster dat waarschijnlijk slechts uit enkele iridiumatomen en ligand (of ligandresidu) bestaat. Het ligand(residu) lijkt de wateroxidatieactiviteit van iridium te verlagen, maar onze studies suggereerden dat het ligand ook katalysatordegradatie vermindert alsmede de aggregatie van iridiumatomen voorkomt. De laatste eigenschap komt goed van pas in elektrolytische cellen om de hoeveelheid benodigd iridium te verlagen.

Brandstofcellen zijn in staat om elektriciteit op te wekken uit de reactie van H_2 met O_2 naar H_2O. Ook hier is de efficiëntie gelimiteerd door de halfreactie waarin O_2 gereduceerd wordt naar H_2O. De huidige gebruikte katalysatoren kunnen namelijk O_2 alleen met hoge stroomdichtheid reduceren als deze ver van de evenwichtspotentiaal van 1.23 V opereren. Zoals eerder beschreven, kan het enzym laccase wel O_2 dichtbij 1.23 V reduceren met behulp van het trinucleaire kopercentrum. Op basis daarvan zijn in het verleden vele moleculaire koperkatalysatoren ontworpen en getest om de activiteit van laccase te proberen evenaren. Het dinucleaire kopercomplex **Cu(DAT)** met twee 3,5-diamino-1,2,4-triazool (DAT) liganden werd hierin als maatstaf gebruikt. Eerder onderzoek suggereerde namelijk dat dit complex O_2 met de laagste gerapporteerde overpotentiaal en de hoogste activiteit van alle kopercomplexen reduceert. Het is belangrijk te vermelden dat het actieve, heterogene katalytische deeltje werd verkregen door het ligand, een koperzout en koolstof-gebaseerd substraatmateriaal te mengen zonder dat aangetoond werd dat het complex **Cu(DAT)** aanwezig en/of gevormd was. Omdat de structuur van de actieve katalysator niet geheel opgehelderd was, is de elektrokatalytische activiteit van **Cu(DAT)** onderzocht waarbij werd uitgegaan van het homogene complex (zie hoofdstuk 3). Het oorspronkelijk

gerapporteerde **Cu(DAT)** complex bleek echter een precipitatie te geven. Om deze precipitatie te voorkomen, zijn niet-coördinerende anionen gebruikt in het koperzout en elektrolyt. Daarom is het elektrochemisch onderzoek is verricht met het homogene C**u(DAT)** complex dat gekarakteriseerd is met elektron paramagnetische resonantie (EPR) en UV-vis spectroscopie. EQCM-metingen wezen uit dat **Cu(DAT)** niet stabiel is onder elektrochemische condities doordat het een depositie vormt. Met XPS-analyses is deze depositie gekarakteriseerd als metallisch Cu⁰. Daarnaast is met XPS- en EPR-spectroscopie aangetoond dat het eerder gerapporteerde actieve deeltje (het mengsel van ligand, koperzout en koolstofsubstraat) niet **Cu(DAT)** was, maar gelijk is aan de depositie dat **Cu(DAT)** vormt onder elektrochemische omstandigheden. Het triazoolligand van **Cu(DAT)** bleek corrosie van een metallische koperelektrode te verhinderen bij oxidatieve potentialen waar normaal Cu⁰-oxidatie plaatsvindt. Dit verklaart waarom de depositie, gevormd door **Cu(DAT)**, geen oxidatieve strippieken had in het katalytische potentiaalgebied. Ondanks dat **Cu(DAT)** niet stabiel bleek, laten deze resultaten wel zien dat het ligand een positieve invloed heeft op de elektrokatalyse. Daarnaast benadrukken deze resultaten dat de karakterisering van een actief deeltje zeer belangrijk is om te voorkomen dat de katalytische activiteit die gevonden wordt met onstabiele moleculaire complexen als algemene maatstaf wordt gebruikt voor andere moleculaire complexen.

De elektrokatalytische reductie van O_2 kan zowel een vier-elektronreductie naar H_2O als een twee-elektronreductie naar H_2O_2 zijn. H_2O_2-productie door elektrochemische O_2-reductie is een veelbelovend alternatief voor de huidige bulkproductie methode via het antrachinonproces. Het huidige proces is verantwoordelijk meer dan 90% van de wereldwijde productie van H_2O_2 terwijl het een zeer energie-intensief en vervuilend productieproces is. Mede om die reden is het dinucleaire kopercomplex **Cu₂(btmpa)** bestudeerd dat het btmpa-ligand heeft (btmpa = 6,6'-bis[[bis(2-pyridylmethyl)amino]methyl]-2,2'-bipyridine). Het complex wordt als twee gefuseerde mononucleaire **Cu(tmpa)** (tmpa = tris(2-pyridylmethyl)amine) complexen gezien waarbij de kopercentra gelinkt zijn via een bipyridine. Van **Cu(tmpa)** is eerder aangetoond dat het O_2 kan reduceren met een TOF in de ordegrootte van 10^6 s⁻¹. Het complex doet dat via een stapsgewijs mechanisme waarin als eerste O_2 wordt gereduceerd naar H_2O_2 alvorens dit verder wordt gereduceerd naar H_2O. In hoofdstuk 4 is beschreven dat het dinucleaire complex **Cu₂(btmpa)** volledig andere eigenschappen heeft dan **Cu(tmpa)** waardoor ook de elektrochemie beïnvloed wordt. Het Cu^{I/II}-redoxkoppel van **Cu₂(btmpa)** is 0.3 V positiever dan **Cu(tmpa)** doordat de bipyridine minder

elektrondonerend is richting de Cu^{II} centra. Daarnaast is de O_2-reductie trager dan **Cu(tmpa)**, maar de H_2O_2-(over)reductie is grotendeels verhinderd waardoor de selectiviteit voor de productie van H_2O_2 tot 90% was zoals uit RRDE-metingen naar voren kwam. De Faraday-efficiëntie werd verder bestudeerd in lange bulkelektrolyse-experimenten met een roterende-schijf-elektrode. Onze observaties lieten zien dat de RRDE-opstelling niet geschikt is voor het bepalen van de Faraday-efficiëntie. Voor de bepaling van de Faraday-efficiëntie is daarom gebruik gemaakt van een op fotometrie-gebaseerde methode die de H_2O_2-concentratie kan bepalen met behulp van een peroxidase-enzym. Daarmee is aangetoond dat de Faraday-efficiëntie tot 80% is in het eerste halfuur van bulkelektrolyse bij 0.0 V. In de eerste 20 tot 30 minuten neemt de katalytische stroom langzaam toe. Het complex adsorbeert namelijk aan de elektrode bij lagere potentialen zoals met EQCM-metingen is aangetoond. Daarnaast kon overreductie van H_2O_2 voorkomen worden waardoor de Faraday-efficiëntie tussen de 60 en 70% bleef gedurende 2 uur. Bij hogere H_2O_2-concentraties neemt de kans toe dat **Cu₂(btmpa)** degradeert tot Cu^0. De Cu^0-depositie die daarmee gevormd wordt, reduceert H_2O_2 verder naar O_2. Om dat te voorkomen, zijn tijdens de bulkelektrolyse regelmatig korte intervallen aangebracht waarbij de potentiaal kortstondig op 0.8 V is gezet. Het onderzoek van hoofdstuk 4 is de eerste uitgebreide studie naar H_2O_2-productie door een moleculair systeem en laat zien dat optimalisatie van potentialen en strip-intervallen bijdraagt aan het optimaal benutten van de intrinsieke hoge selectiviteit van moleculaire systemen.

Het mononucleaire **Cu(tmpa)** complex werd ook als inspiratie gebruikt voor het onderzoek in hoofdstuk 5. In dit hoofdstuk wordt het effect van elektrondonerende (EDG) en elektronzuigende (EWG) groepen op de activiteit van **Cu(tmpa)** beschreven. NH_2 (EDG), Cl en CF_3 (EWG) groepen werden geplaatst op de *para*-positie van de coördinerende pyridines van het tmpa ligand. Het elektronische effect van zulke groepen kan het best beschreven worden met de Hammett-parameter. Als eerste is aangetoond dat de Hammett-parameter van de verschillende complexen een lineaire correlatie heeft met de $E_{1/2}$ van het $Cu^{I/II}$-redoxkoppel. Als tweede bleek dat de aanvangspotentiaal van O_2-reductie niet verandert door de invloed van deze EDG en EWG ondanks dat de $E_{1/2}$ van de complexen tot wel 100 mV was verschoven. Ten derde bleek dat de katalytische snelheid toeneemt door de invloed van de Cl-groepen, maar dat CF_3-groepen geen invloed hebben op de katalytische snelheid in vergelijking met het ongesubstitueerde **Cu(tmpa)** complex. De reductie van Cu^{II} naar Cu^I en het daaropvolgende coördineren van O_2 aan het gereduceerde complex om tot het Cu^{II}–$O_2^{•-}$

superoxocomplex te komen, is een zeer snel proces op de tijdschaal van een cyclisch voltammogram omdat de TOF rond de 10^6 s^{-1} is. Daarom is het waarschijnlijk dat het gereduceerde Cu^I-complex een kortlevend tussenproduct is dat in een snel evenwicht is met zowel Cu^{II} en Cu^{II}–O$_2$$^{\bullet-}$. Vandaar dat het aannemelijk is dat Cu^{II} naar Cu^{II}–O$_2$$^{\bullet-}$ als snelheidsbepalende stap geobserveerd wordt waarbij deze stap de E$_{1/2}$ bepaalt. Omdat het elektron hierbij eindigt in een orbitaal op het superoxide en dus op afstand zit van de moleculaire orbitalen van het ligand, heeft het ligand weinig invloed hebben op de thermodynamische E$_{1/2}$. De snelheidsconstante hangt nog steeds af van de bindingsconstante van O$_2$ aan het complex waarvoor *π-backbonding*, de elektrondonatie van het complex naar O$_2$ via π-bindingen, een rol speelt. De invloed van de substituenten op de reductie van H$_2$O$_2$ is aanzienlijk anders dan op de O$_2$-reductie. EWG verhogen zowel de aanvangspotentiaal als de snelheid van reductie. Dit is een ongebruikelijk resultaat, omdat een verhoging van de aanvangspotentiaal meestal gepaard gaat met een verlaging van de katalytische reductiesnelheid, maar het komt wel in enkele gevallen voor. Opmerkelijk genoeg bleek dat de hoogste reductiesnelheid wederom werd bereikt door Cl-groepen te gebruiken. In tegenstelling tot de CF$_3$-groep, kan Cl elektronen delokaliseren vanuit de p-orbitalen en kan daardoor secundaire elektronische effecten teweegbrengen zoals bijvoorbeeld de eerdergenoemde *π-backbonding* welke waarschijnlijk niet volledig beschreven door de Hammett-parameter. De structuur-activiteitstudie van dit hoofdstuk laat zien dat dit soort type studies waardevolle informatie geven over het mechanisme en over hoe de reactiviteit van moleculaire systemen verbeterd kan worden.

S.2   Conclusie en toekomstperspectief

De hoge mate waarin moleculaire complexen synthetisch aangepast kunnen worden, geeft verschillende mogelijkheden om elektrokatalytische reacties te controleren. Het **Cu(tmpa)** complex diende als inspiratie voor hoofdstuk 4 en 5. Synthetische aanpassingen aan het tmpa-ligand resulteerden in een andere geometrie (hoofdstuk 4) of de andere elektronische eigenschappen (hoofdstuk 5). Dat resulteerde ook in verschillende katalytische activiteit voor O$_2$- en H$_2$O$_2$-reductie. Het gebruik van EWG op **Cu(tmpa)** complexen versnelt de reductie van H$_2$O$_2$ en verhoogt de katalytische aanvangspotentiaal. De Hammett-parameter van deze substituenten correleert direct met de E$_{1/2}$ van de complexen en is daarmee een goede indicatie voor het verhogen van de aanvangspotentiaal. In tegenstelling tot deze snelle H$_2$O$_2$-reductie, bleek het dinucleaire complex **Cu$_2$(btmpa)** juist een zeer

selectieve katalysator te zijn voor de O_2- naar H_2O_2-reductie doordat de H_2O_2-overreductie grotendeels gehinderd is. Hiervoor is geen eenduidige verklaring te geven, omdat het mechanisme van H_2O_2-reductie door **Cu(tmpa)** nog niet (volledig) bekend is. Interessant genoeg bleek de $E_{1/2}$ van **Cu₂(btmpa)** het hoogste te zijn van alle bestudeerde complexen in hoofdstukken 4 en 5, terwijl dit geen eenduidig effect had op de aanvangspotentiaal, de snelheid of selectiviteit van O_2-reductie. De rigiditeit binnen het ligand leidt duidelijk wel tot een verandering van de geometrie van het dinucleaire complex ten opzichte van **Cu(tmpa)**. Dit zorgde voor een aanzienlijk langzamere elektronoverdracht. **Cu(tmpa)** en de afgeleide complexen uit hoofdstuk 5 hebben juist snelle O_2- en H_2O_2-reductiesnelheden. De trigonaal bipirimidale geometrie van deze Cu^{II}-complexen kan makkelijk veranderen naar de tetraëdrische geometrie van het Cu^{I}-complex doordat de pyridine-armen van het tmpa-ligand zeer flexibel zijn en het tertiaire amine gemakkelijk kan coördineren of losgaan van het centrale koperatoom. Dit zorgt voor een snelle elektronoverdracht. **Cu₂(btmpa)** heeft echter een rigide bipyridine in het btmpa ligand dat leidt tot een verstoorde octaëdrische geometrie om sterische hinder te vermijden. Dit is echter niet de optimale geometrie voor Cu^{II} en hindert een overgang naar de tetraëdrische geometrie voor Cu^{I} waardoor de elektronoverdracht dus langzaam is. Daardoor zijn ook de O_2-reductie langzaam en de H_2O_2-reductie flink gehinderd. Sterische hinder kan niet het verschil tussen O_2- en H_2O_2-reductie verklaren, omdat deze substraten vergelijkbaar in grootte zijn. Een mogelijke verklaring is dat de reorganisatie meer complex is wanneer H_2O_2 coördineert dan wanneer O_2 coördineert. De rigiditeit van de bipyridine kan de reorganisatie vertragen wat dus een groter effect zou hebben op H_2O_2 reductie, omdat voor O_2 reductie alleen de geometrische Cu^{I} naar Cu^{II} een rol speelt. Radicale tussenproducten, die vrijkomen bij de reductie van H_2O_2, kunnen het btmpa ligand oxidatief degraderen. Dit zou echter leiden tot een snel verminderde katalytische activiteit. Omdat dit niet is geobserveerd, is deze verklaring niet aannemelijk. **Cu(tmpa)** complexen hebben daarentegen een open plek die ver van het ligand gepositioneerd is met weinig sterische hinder. Daarnaast leidt de snelle elektronoverdracht tot een snelle H_2O_2-reductie. De katalyse is voornamelijk bepaald door een massatransportlimitatie en veranderingen aan het ligand brengen maar kleine verbeteringen te weeg. Een rigide onderdeel van het ligand is nodig om H_2O_2 te verkrijgen. Als gevolg hiervan is de O_2-reductie wel significant langzamer. Meer katalysator is daarom nodig, omdat het proces vooral kinetisch gelimiteerd is.

De ontleding van onstabiele moleculaire complexen kan de katalytische activiteit stoppen. Daarnaast kan de activiteit die geobserveerd wordt, wordt ten

onrechte aan het complex toegeschreven worden. Dit zijn twee belangrijke nadelen van moleculaire complexen. Interessant om te noemen, is dat de productie van H_2O_2 antrachinon vergt dat maar enkele cyclussen stabiel blijft voordat het ontleedt. Toch wordt meer dan 90% van alle wereldwijde H_2O_2 op deze manier geproduceerd. Hoofdstukken 2 en 3 benadrukken dat intensieve studies met meerdere methoden benodigd zijn om de ontleding van moleculaire complexen te detecteren en bestuderen. Ondanks dat de bestudeerde moleculaire complexen niet actief waren, gaven deze wel een katalytisch actieve depositie op de elektrode. Uit het onderzoek van hoofdstuk 2 bleek dat liganden nog steeds een kleine invloed op de katalyse hadden en het ligand uit hoofdstuk 3 voorkomt de corrosie van Cu^{II}. Dit laat ook zien dat liganden nog steeds de activiteit en stabiliteit van heterogene systemen kan verbeteren. Zoals ook besproken in hoofdstuk 1, worden liganden zelfs gebruikt om de reactiviteit van bijvoorbeeld nanodeeltjes te sturen met de kennis die met moleculaire systemen opgedaan is. Daarnaast kunnen de negatieve gevolgen van katalysatordegradatie ook deels voorkomen worden met de juiste kennis over mogelijke degradatieprocessen (zie hoofdstuk 4). Kopercomplexen zijn bijvoorbeeld zeer vatbaar voor ontleding naar Cu^0 waarbij de bindingsconstante van het ligand een grote rol speelt. Het complex uit hoofdstuk 3 heeft bijvoorbeeld maar één plek waar een koperatoom bindt en kan daarom dus gemakkelijk uit elkaar vallen. De complexen van hoofdstukken 4 en 5 hebben meerdere bindingsplekken per koperatoom en verbeteren daar dus de stabiliteit mee. Dit leidt tot een vermindering van de ontleding van het complex tot Cu^0. Daarnaast zorgen korte intervallen van hogere potentialen ervoor dat het gevormde Cu^0 gestript wordt (zie hoofdstuk 4). Het strippen van Cu^0 leidt tot een behoud van de hoge selectiviteit voor H_2O_2. De conclusie van het onderzoek in dit proefschrift is dat de identificatie van het actieve katalytische deeltje, studies naar de stabiliteit van complexen onder elektrokatalytische condities en het bestuderen van factoren die de reactiviteit van moleculaire complexen beïnvloeden tezamen een goede basis geven om mechanismes te bestuderen. Dit resulteert in kennis om op verschillende manieren katalysatoren te verbeteren en zal daarom zeer belangrijk zijn voor toekomstige energie-infrastructuur.

S

Curriculum vitae

Bas van Dijk was born the 2nd of September 1992 in Heemskerk, The Netherlands. In 2010, he graduated *cum laude* from the Kennemer College, Beverwijk obtaining his VWO diploma. Next, he started studying chemistry at the University of Amsterdam. In 2013, he performed a research internship in the Synthetic Organic Chemistry group under the supervision of Dr. Roel Klein Nijenhuis in the groups of Prof. Dr. Jan van Maarseveen and Prof. Dr. Henk Hiemstra about the synthesis of biomarkers for naturally occurring ladderanes which was in collaboration with Prof. Dr. Jaap Sinninghe Damsté from the Royal Netherlands Institute for Sea Research (NIOZ). In the same year, he obtained his Bachelor of Science degree *cum laude* and continued with the joint MSc program Chemistry at the University of Amsterdam and the Vrije Universiteit Amsterdam. A second internship was performed in the group of Prof. Dr. Ir. Jarl-Ivar van der Vlugt under the supervision of Dr. Linda Jongbloed on the topic of (catalytically) selective C–H activation through supramolecular pre-organization. Subsequently, Bas received his Master of Science in chemistry in 2015. During his studies, Bas occupied the position of treasurer in the board of the study association *Amsterdams Chemisch Dispuut* in 2012-2013 and co-organized a study trip to the Czech Republic that encompassed visits to the Charles University in Prague, the Institute of Organic Chemistry and Biochemistry in Prague, and the chemical company Synthos in Kralupy nad Vltavou.

In January 2016, Bas started as a PhD candidate in the group of Dr. Dennis Hetterscheid. The research was performed in the labs of the Catalysis and Surface Chemistry (CASC) and Metals in Catalysis, Biomimetics and Inorganic Materials (MCBIM) research groups. During his PhD, Bas collaborated with Dr. Longfei Wu and Prof. Dr. Jan Philipp Hofmann from the Technical University Eindhoven on the spectroscopical analysis of various electrodeposits. In addition, Bas collaborated with Dr. Gabriel Menendez Rodriguez and Prof. Dr. Alceo Macchioni from the University of Perugia, Italy on the electrochemical study of molecular iridium complexes for water oxidation. Another collaboration was performed with Austin Herzog and Prof. Dr. Kenneth Karlin from the John Hopkins University, United States of America on the electrochemical analysis of molecular copper complexes. Various results of the studies included in this thesis were presented at (inter)national conferences including oral presentations at the 2017 edition of the *Netherlands Catalysis and Chemistry Conference* (NCCC) and 2019 edition of the *CHemistry as*

INnovative Science (CHAINS) national conferences as well as poster presentations at the Reedijk Symposium (2016), NCCC (2016, 2018, 2019, 2020), CHAINS (2016), and the International Symposium on Homogeneous Catalysis in 2018. Next to research, Bas assisted in several (practical) courses for undergraduate students and supervised the internships of one Bachelor level and two Master level students. In 2020, Bas assisted the Master programs for *Chemistry* and *Life Science and Technology* of Leiden University with the scheduling of courses and final talks of (literature) internships of students. During the PhD research, Bas also completed several courses including *Catalysis: An Integrated approach* organized by the Netherlands Institute for Catalysis Research, *Physical Methods in Inorganic Chemistry* and *High Impact Writing* both organized by the Holland Research School of Molecular Chemistry, and graduate school courses organized by Leiden University: *Communication in Science*, *Effective Communication*, *Scientific Conduct*, and *Time management and Self-management*.

List of publications

B. van Dijk, J. P. Hofmann, and D. G. H. Hetterscheid. Pinpointing the active species of the Cu(DAT) catalyzed oxygen reduction reaction, *PCCP*, **2018**, 20, 19625–19634

B. van Dijk, G. Menendez Rodriguez, L. Wu, J. P. Hofmann, A. Macchioni, and D. G. H. Hetterscheid. The Influence of the Ligand in the Iridium Mediated Electrocatalyic Water Oxidation, *ACS Catalysis,* **2020**, 10, 4398–4410

L. Wu, N. Y. Dzade, N. Chen, **B. van Dijk**, S. Balasubramanyam, A. Sharma, L. Gao, D. G. H. Hetterscheid, E. J. M. Hensen, A. A. Bol, N. H. de Leeuw, and J. P. Hofmann. Cu Electrodeposition on Nanostructured MoS_2 and WS_2 and Implications for HER Active Site Determination, *J. Electrochem. Soc.,* **2020**, 167, 116517

N.W.G. Smits, **B. van Dijk**, I. de Bruin, S. L. T. Groeneveld, M. A. Siegler, and D. G. H. Hetterscheid. Influence of Ligand Denticity and Flexibility on the Molecular Copper Mediated Oxygen Reduction Reaction, *Inorg. Chem.*, **2020**, 59, 16398–16409

B. van Dijk, R. Kinders, and D. G. H. Hetterscheid. A selective molecular dinuclear copper oxygen reduction catalyst for the electrochemical synthesis of H_2O_2 at neutral pH, *in preparation*

B. van Dijk, A. E. Herzog, K. D. Karlin, and D. G. H. Hetterscheid. Mechanistic insight from structure–activity studies in the electrochemical oxygen reduction by substituted tris(2-pyridylmethyl)amine copper complexes, *in preparation*

Acknowledgements

The research that laid the foundation for this thesis has been greatly supported by many people that helped me in different ways. Their help is greatly appreciated since they not only strengthened the research, but also my skills as researcher.

The obvious person to start with is Dr. Dennis Hetterscheid. I am thankful that you had trust in me to pursue my PhD in your group. I have learned a great set of skills from you to strengthen my approach to research and how to present it. The most important thing I learned from you is to have a mindset that can see a positive note in every experimental result. I also appreciated the fact that your door was always open for small brainstorm sessions. I would also like to thank Prof. Dr. Marc Koper and the CASC groups for feedback on my research, access to the equipment, and access to their extended knowledge in electrochemistry. In addition, the feedback and help from Prof. Dr. Lies Bouwman and the MCBIM group, special mention to Hans, are greatly appreciated in the field of synthesis and molecular inorganic chemistry as well as being able to make use of the lab and instruments. The "Minions" Konstantin, Koen, Martijn, Silvia, Nicole, Michiel, Shengxiang, Daan, Andrey, Kyra, Dana, Ross, Jan, and Phebe gave me a warm welcome from the start and I really appreciate all your help, the discussion, and the fun times we had. I valued the relaxed atmosphere in which anyone feels comfortable sharing their results and critically discuss due to which my work, but also that of others, significantly improved. A special thanks to Koen since you were the one that introduced me to proper electrochemistry and a special thanks to Daan and Michiel, my paranymphs.

During the past few years, many collaborations have been established and I would like to thank Prof. Dr. Jan Philipp Hofmann and Dr. Longfei Wu for the XPS measurements which has been a significant contribution to the research throughout this thesis. In addition, Prof. Dr. Alceo Macchioni and Dr. Gabriel Rodriguez Menendez are thanked for the collaboration which resulted in a nice publication (Chapter 2). Prof. Dr. Kenneth Karlin and Austin Herzog are thanked for their collaboration by supplying complexes for Chapter 5. Michiel Langerman is kindly thanked for supplying a complex for Chapter 5 as well. The effort of Dr. Andrey Konovalov for the SQUID measurements of Chapter 3 and 4 is also greatly appreciated. The students I supervised also aided my research by exploring new